Nonlocal manipulation on Si(111)-7x7 using the scanning tunnelling microscope, from charge injection to decay

Etheridge, Henry

Award date:
2021

Awarding institution:
University of Bath

Nonlocal manipulation on Si(111)-7×7 using the scanning tunnelling microscope, from charge injection to decay

submitted by

Henry George Etheridge

for the degree of Doctor of Philosophy

of the

University of Bath

Department of Physics

2020

Summary

In this thesis we aim to develop further understanding of the mechanisms leading to the nonlocal manipulation of adsorbed aromatic molecules on a Si(111)-7 $\times$ 7 surface. The injection of either electrons or holes into the surface above a bias threshold results in the manipulation of molecules up to tens of nanometers away from the injection site. We use the tip of a scanning tunnelling microscope (STM) as both a tunable source of hot charge carriers, as well as an imaging tool with atomic-scale resolution. While far slower than the timescale of the manipulation process at room temperature, this allows for observation of the distribution of aromatic molecules on the surface before and after nonlocal charge injection.

The nonlocal manipulation process can be separated into three distinct steps, each of which occurs identically and independently for each individual charge carrier; charge injection, charge transport, and molecular manipulation. In this thesis we focus on the charge transport step, the link between the nonlocal process and light emission from the same system, and the manipulation step itself.

To isolate the charge transport process, the radial extent of nonlocal manipulation has been measured at two injection biases and across a range of charge injection times from 1 to 500 s (i.e., varying the number of injected charge carriers). For sufficient injection duration, the manipulated spot-size is described by purely diffusive transport of the injected charge carriers. This sets a practical limit on the maximum size of the nonlocal effect, which is constrained by the surface diffusive properties and feasible injection duration. Conversely, at the lower limit of injection times, the radius of manipulation is observed to plateau with a radius between 6 and 10 nm, conforming to an initial non-manipulative ballistic transport regime prior to the diffusive transport.

Secondly, we consider similarities in the onset biases between nonlocal manipulation and light emission from the same system, alongside constant emission spectra, which suggest a common origin for the two mechanisms. We demonstrate that the nonlocal manipulation, and hence photon emission, is not mediated by a localised surface plasmon decay process, and instead that light emission occurs after the charge transport step of nonlocal manipulation. The probability of both outcomes follows a similar exponential increase with increasing bias above the shared threshold, between +2.0 and +2.7 V, suggesting that both processes follow an identical pathway prior to manipulative relaxation or light emission.

To observe the final manipulation step, we consider the outcome, rather than only the distribution, of nonlocal manipulation. Previous investigation into the outcome of local

manipulation demonstrated a bias invariance of the final manipulation step. Here we expand this to nonlocal manipulation, thus demonstrating that the molecular manipulation occurs from a common energy state for each injected charge carrier, independent of the injection bias above or below the nonlocal threshold. For electron injection, the nonlocal branching ratio is observed to be a similar order of magnitude to the local branching ratio. Additionally, we observe a similar probability of manipulation per charge-molecule interaction across both local and nonlocal manipulation. This suggests that the manipulation step occurs identically for both local and nonlocal manipulation, with only the addition of a charge transport step in nonlocal manipulation altering the outcome.

Finally, we discuss the effect of varying the adsorbate molecule on the manipulation step. While changing the adsorbate from a lighter (toluene) to a heavier (bromobenzene) aromatic molecule has no effect on the manipulation for electron injection, for hole injection the relative probability of desorption is suppressed. This is in agreement with the differing manipulation processes between the injected charges; surface-mediated electron injection proceeds mostly independent of the adsorbate molecule, while molecule-mediated hole injection is dependent on the mass of the adsorbate.

Acknowledgements

I would like to thank my supervisor, Dr Peter Sloan, for his enthusiasm and support during this PhD process. Without his assistance, the project would have never made it this far. Thank you to Dr. Kristina Rusimova and Dr. Rebecca Purkiss, who taught me how to use the STM, answered my questions, and were available for discussion. Thank you to the technical staff, Paul, Jenny, Isabel, Martin, Wendy, for helping me find what I needed, build things I couldn't, and generally allow any of the experimental work to actually happen.

Finally, thank you to my parents for supporting me throughout my entire time at Bath and for letting me live back at home during these last few months, especially my Mother for happily reading through hundreds of pages of draft thesis. Thank you to my brother, Alex, for letting me escape to Birmingham. And to my girlfriend, Katherine, for your encouragement throughout the PhD, but most of all for still being here after nearly four years of STM and STM-adjacent rambling.

Contents

1 Introduction **1**

1.1 Thesis overview . . . 3

1.2 Declaration of work . . . 4

2 Scanning probe microscopy and quantum tunnelling **5**

2.1 Scanning probe microscopy . . . 6

2.2 Scanning tunnelling microscopy . . . 7

2.2.1 One-dimensional finite potential barrier model . . . 8

2.2.2 Quantifying the lateral resolution . . . 12

2.2.3 Density of states and the tunnel current . . . 12

2.2.4 Fermi's golden rule and finite temperature effects . . . 18

2.3 STM operation . . . 19

2.3.1 Constant current STM imaging . . . 21

3 Atomic manipulation with the STM **23**

3.1 Inelastic electron tunnelling induced manipulation . . . 24

3.2 Nonlocal atomic manipulation via IET . . . 30

4 Benzene derivatives on Si(111)-7×7 **37**

4.1 The Si(111)-7×7 reconstructed surface . . . 38

4.2 Adsorption of small benzene derivatives . . . 41

4.3 Local and nonlocal manipulation on Si(111)-7 × 7 . . . 45

5 Achieving atomic-resolution STM images **49**

5.1 Sample preparation . . . 50

5.2 Tip preparation . . . 55

5.2.1 Electrochemical etching . . . 55

5.2.2 Annealing . . . 60

5.2.3 In vacuo tip fixing . . . 62
5.3 Tip-sample Approach . . . 64
5.4 Noise . . . 66
5.5 Dosing . . . 68
5.5.1 Freeze-pump-thaw purification . . . 70
5.5.2 Verifying the dosing gas . . . 72

6 Automation of local and nonlocal injection procedures 75
6.1 Drift correction . . . 77
6.2 Piezo creep . . . 78
6.3 Injection overview . . . 79
6.4 Automated molecule finder . . . 80
6.5 Injection . . . 84
6.5.1 Local . . . 85
6.5.2 Nonlocal . . . 85
6.5.3 Drift during injection . . . 88

7 Data analysis 91
7.1 Local injection analysis . . . 92
7.2 Nonlocal injection analysis . . . 93
7.2.1 Manual molecule Finder . . . 93
7.2.2 Tip Position . . . 96
7.2.3 Radial analysis . . . 97
7.3 Thermal manipulation of benzene derivatives . . . 98
7.3.1 Correction for the thermal manipulation of toluene . . . 99
7.3.2 Thermal manipulation of bromobenzene . . . 102

8 Models of nonlocal manipulation 107
8.1 Introduction and experimental methodology . . . 110
8.2 Radial distribution of desorption . . . 113
8.2.1 Dealing with contamination . . . 115
8.2.2 Nonlocal manipulation half radius . . . 116
8.2.3 Tunnelling current dependence . . . 117
8.2.4 Bias dependence . . . 121
8.2.5 Charge carrier dependence . . . 127
8.3 Diffusion from an instantaneous point source . . . 133
8.3.1 Derivation of the half radius . . . 136
8.3.2 Discussion . . . 138

8.4 Ballistic-diffusive transport . . . 144
8.5 Localised surface plasmon induced manipulation . . . 148
8.5.1 Localised surface plasmons . . . 150
8.5.2 Results and discussion . . . 153
8.6 Linking nonlocal manipulation and light emission . . . 159
8.6.1 Relative probability per injected electron . . . 162
8.7 Conclusions . . . 165

9 Measuring the outcome of local and nonlocal manipulation 167
9.1 Local toluene branching ratio . . . 169
9.2 New adsorbate molecule selection . . . 173
9.2.1 Larger benzene-like adsorbates on Si(111)-7×7 . . . 177
9.2.2 Discussion and conclusions . . . 180
9.3 Local manipulation of bromobenzene . . . 180
9.3.1 Binding site dependence: middle versus corner . . . 181
9.3.2 Results . . . 182
9.3.3 Discussion and conclusions . . . 186
9.4 Further linking local and nonlocal manipulation . . . 190
9.5 Measuring the branching ratio in nonlocal manipulation . . . 193
9.5.1 Diffusion and no-manipulation half radii . . . 197
9.5.2 Maximum diffusion probability . . . 199
9.5.3 Conclusions . . . 201
9.5.4 Results . . . 201
9.5.5 Nonlocal toluene branching ratio . . . 203
9.5.6 Nonlocal BrPh branching ratio . . . 205
9.5.7 Discussion . . . 206
9.6 Conclusions . . . 207

10 Summary and conclusions 209

A The nanometre limits of ballistic and diffusive hot-hole mediated nonlocal molecular manipulation 213

B Common source of light emission and nonlocal molecular manipulation on the Si(111)-7×7 surface 220

Bibliography 231

Chapter 1

Introduction

Understanding the femtosecond-scale dynamics of high-energy charge carriers across a surface provides an avenue for greater control over microscale and nanoscale systems. For example, photogenerated hot charge carriers with energy between 1 and 3 eV, equivalent to a visible or near-infrared photon, are fundamental to solar cells. The efficiency of such devices is practically limited by, among other things, the transport characteristics of the hot charges prior to thermalisation, even for nanostructure devices [1]. Through direct measurement of the immediate hot electron charge dynamics, from generation to decay, greater understanding and thereby control of the system could be developed. This would allow for the engineering of surfaces with expanded carrier lifetimes, leading to an increase in the maximum capture efficiency, potentially breaking the Shockley-Queissier limit for solar cells [2]. However, observing or extracting real time information from a hot charge carrier is difficult due to the extremely short lifetime and length scale of the particle prior to thermalisation, usually occurring over the order of a femtosecond.

The scanning tunnelling microscope (STM) is both a source of tunable hot charge carriers as well as a microscope with atomic resolution. The STM can also, by way of the hot charge carriers, induce atomic manipulation; for example allowing the desorption of specific molecules beneath the tip [3], the manual positioning of individual atoms or molecules on a surface [4], and can induce chemical reactions [5]. It should be noted that the manipulation in these examples is restricted to the tunnel junction and so tells little about the underlying hot electron dynamics which are far faster than an STM can resolve. Additionally, the present methods generally require time-intensive

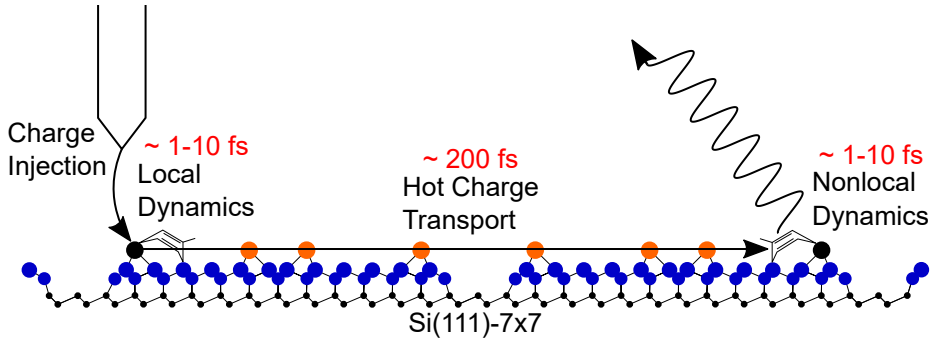

Figure 1-1: The lifetime of a hot charge carrier injected from an STM tip into the surface states of a Si(111)-7 × 7 surface. The charge will eventually thermalise, inducing local or nonlocal dynamics including light emission, phonon excitation or manipulation of adsorped molecules.

atom-by-atom manipulation which means that increasing the scope towards large-scale manufacturing is, from a practical point of view, out of reach.

Previous work within the atomic manipulation group at the University of Bath has investigated the nonlocal manipulation of aromatic molecules on the Si(111)-7 × 7 reconstructed surface via the injection of both hot holes and hot electrons from the tip of an STM [6–9]. It has been shown that the injected charges are not confined to the tunnel junction directly beneath the tip, and instead each injected charge carrier may, as a part of the decay process, result in the manipulation of a molecule on the surface many nanometres away from the injection site [7]. By considering that the discrete manipulation events occur probabilistically, with a rate determined partially by the nature of the charge carrier injection and subsequent transport, and injecting a large number of charge carriers, the dynamics of each individual injected charge can be inferred. This nonlocal manipulation has been shown to be a hot charge mediated effect, the dynamics of which can be separated into several categories, shown in figure 1-1; including the charge injection itself, the transport of the hot charge across the surface, and the final thermalisation via mechanisms including molecular manipulation and light emission. Each of these steps has previously been investigated and will be described in more detail within. This nonlocal mechanism provides a route to expand the serial one-at-a-time nature of conventional scanning probe microscope (SPM) manufacturing, albeit losing the atomic scale control.

The main results of this thesis aim to confirm previously derived models, showing that they are more robust than just the initial reports, whilst further developing them. The former is primarily achieved by increasing the parameter space tested and showing that

the results can be sufficiently explained within the scope of nonlocal charge transport. Additionally we show that explicit values can be extracted from the broader model, separating it into several key components, most notably relating to the probability of the final manipulation step for an individual charge carrier. Finally, we attempt to further demonstrate the link between local and nonlocal manipulation, showing that the ratio of desorption to diffusion of a manipulated molecule is similar across both regimes. This will demonstrate that the final manipulation step is common and thus only the initial injection and any subsequent transport processes vary, suggesting further routes to deconvolve the hot charge transport into its constituent parts from this state-of-the-art atomic manipulation experiment.

1.1 Thesis overview

This thesis can be split into 3 main topics; a review of STM and relevant theory leading to atom-scale resolution imaging and atomic manipulation, details of the experimental aspects and data analysis required to produce the STM images as well as the nonlocal manipulation experiments, and the scientific results of the experiments. Additionally, appendices present the papers published based on the work within; including [10], which is composed of experimental results and analysis from chapter 8, and [11], which utilises the analysis of section 8.6.1.

STM and atomic manipulation

The initial chapters aim to provide a detailed overview of the theoretical and practical background necessary for the experimental work of the later chapters of this thesis. In chapter 2 a brief overview of SPM is given, with particular attention paid to STM; including an introduction to the theory of quantum tunnelling. This is then followed by a theoretical and practical discussion of atomic manipulation, both locally and non-locally, in chapter 3, and our specific surface and surface-molecule systems in chapter 4; namely benzene derivatives chemisorbed onto the Si(111)-7 $\times$ 7 surface.

Experimental procedure

A significant advantage of our experimental system is the largely automated experiments and analysis using software developed in-house, which allows the collection of large sets of data with minimal human oversight or intervention. Several chapters are dedicated to describing the processes behind achieving high quality STM images at room temperature, including the production of tips and dosed samples. Chapter 6.5

describes in detail the automated injection processes for both local and nonlocal parameter experiments. Chapter 7 provides an explanation of the data analysis process, both in terms of identifying and differentiating molecules and adatom sites from STM images of the surface, as well as further data analysis.

Scientific results

Chapter 8 focuses primarily on nonlocal manipulation due to the injection of high energy holes at biases above the nonlocal threshold. Here, the radial extent of the nonlocal effect is observed whilst varying the number of injected charge carriers via the injection duration, from which the charge transport step is further quantified.

Acknowledging the similarities between nonlocal manipulation and STM charge injection induced light emission, chapter 8 additionally considers an alternative mechanism for nonlocal manipulation. In this model the decay of localised surface plasmons mediate both light emission and the distribution of nonlocal manipulation.

Chapter 9 aims to compare local and nonlocal manipulation with the ultimate goal being to indicate a common final decay step between both manipulation regimes. Previous results have suggested the the ratio of desorption to diffusion for local manipulation is invariant across a range of injection parameters [12]. Here, we attempt to expand this branching ratio to extract a similar value from nonlocal manipulation experiments.

Finally, chapter 10 provides an overview of the results presented in this work.

1.2 Declaration of work

The majority of this thesis discusses results from experiments performed by myself with supervision by Dr Peter Sloan at the University of Bath. For this thesis, operation of the STM itself has been undertaken primarily independently, including daily operation, tip and sample preparation, as well as troubleshooting issues. A large portion of the procedures and software used have been developed by Dr Sloan and prior PhD students, however, especially with regards to the injection and analysis software, these programs were altered or rewritten as necessary to achieve the intended experiments or analysis.

It should be noted that several sections of this thesis use data provided by Dr Kristina Rusimova from her previous work as a PhD student with Dr Sloan. Unless otherwise stated, these data were provided as raw STM images with all further analysis performed by myself.

Chapter 2

Scanning probe microscopy and quantum tunnelling

Scanning probe microscopy (SPM) techniques provide a method to image surfaces with resolution far greater than traditional optical microscopy. Rather than allow for direct visualisation of the surface, in each of these techniques the structure beneath a nanoscale tip is inferred from a measured tip-sample interaction. In this chapter several forms of SPM are briefly introduced with the main focus on scanning tunnelling microscopy (STM), the primary experimental technique used within this thesis. The purpose of this chapter is to provide an overview of the theory behind STM, it aims to link the measured current across the STM tip-sample junction to the atom-scale structure of the surface which results in the surface images able to be produced by this technique.

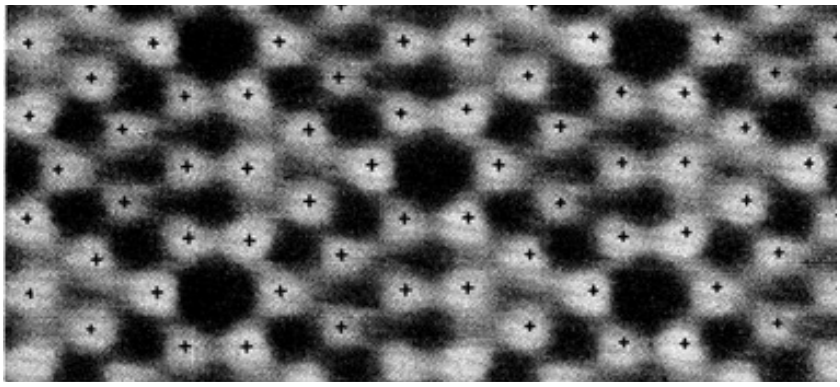

Figure 2-1: STM image used for the initial characterisation of the Si(111)-7×7 surface [14]. The crosses atop bright adatom sites in the STM image indicate the determined adatom positions in the developed model.

2.1 Scanning probe microscopy

SPM consists of a family of structurally similar surface imaging techniques. By rastering (i.e. moving it line by line up an area) an extremely sharp tip with a radius of curvature usually of the order of nanometres across a surface and measuring a localised interaction across the junction between the tip and the sample, it is possible to construct an overall image of the topography of a surface. The measured interaction depends on the type of SPM used and whether it is electrostatic forces for atomic force microscopy (AFM), near-field light for scanning near-field optical microscopy (SNOM), tunnel current for scanning tunnelling microscopy (STM), or otherwise, the overall process remains the same.

The invention of the STM, the first form of SPM realised, was by Binnig and Rohrer in the early 1980s [13] and demonstrated real-space images of a surface at atomic resolution, a feat for which they received (part of) the Nobel prize in physics in 1986. Over the years, STM has been shown to be a powerful surface characterisation tool, with pictures of a surface, shown in figure 2-1, immediately proving a great aid in determining surface structures [14]. This technique can, however, be used for considerably more than just imaging; for example the STM can be used to measure electronic states within the surface via scanning tunnelling spectroscopy [15], move atoms around [4], or even induce chemical reactions [5]. It should be noted that STM is fundamentally limited by the requirement of a conducting sample, without which no current can flow, so no tunnel current can be measured and no surface image can be formed.

Other techniques do not have such a limitation. For example, in AFM the electrostatic force between nearby atoms is translated into a measured force between a cantilevered tip and the sample [16]; electron flow is not required. As a result AFM has become an invaluable tool in the characterisation of biological structures, which are mainly insulators [16], in addition to its use imaging insulating nanoscale structures and surfaces. In this thesis STM is used as more than an inert imaging device. While AFM can be used to manipulate molecules on surfaces [17], the forces involved are all extremely short ranged and manipulation is limited to within the tip-sample junction [18].

The more recent development of qPlus AFM, in which a stiff quartz oscillator is used as the cantilever arm of an AFM, allows for simultaneous non-contact AFM and STM with submolecular resolution [19, 20]. Such a system allows for the simultaneous measurement of electrical, using STM, and mechanical, using AFM, properties of a material [21, 22], as well as induce manipulation via charge injection [23, 24]. QPlus AFM/STM provides a useful tool for characterising and manufacturing conductive structures or molecules, decoupled from the underlying surface layer. It is, however, the electronic structure of a surface that is of great importance to many areas and so an understanding of the electronic properties, that can be discerned from STM alone, is extremely relevant.

2.2 Scanning tunnelling microscopy

The leading principle behind the STM is the measurement of a current between the tip and the sample surface across a nanoscale gap. In classical mechanics such a barrier inhibits the flow of any current unless the energy of the particles is greater than the height of the barrier, in which case the particles will be always be transmitted. Quantum mechanically, however, transmission or reflection occur probabalistically dependent on the relative energy levels of the particle and the barrier. As the height of the barrier is dependent on the tip-sample separation, changes in the topography of the surface as the tip is rastered across it will result in corresponding changes in the measured current. However this assumes a surface with a uniform density of states. A large part of the apparent physical corrugations in an STM image are, instead, due to changes in the local charge density, for example due to a change in the local surface atom. It is much more accurate to describe an STM image as a real space contour map of the local density of states of a surface.

The total tip-sample tunnelling results in a complex many particle system, in which a vast number of electrons at numerous energy levels and initial positions in both the

tip and the sample may or may not transition, and thereby contribute to the tunnel current. As such a full theoretical approach to the tunnel current is not reasonable. Instead, through a series of approximations, a number of models have been used to derive key characteristics of the system. In this section, a brief introduction to quantum tunnelling theory is developed using a one-dimensional finite potential barrier model to describe the fundamental operation of an STM, leading to estimate equations describing both the expected resolution and tunnel current. In addition, Bardeen's model of tunnelling, which allows calculation of the tunnel current in a three-dimensional system, is qualitatively described. Finally, finite temperature effects are considered. Note, however, this is not a complete overview of model STM theory, and a comprehensive review can be found elsewhere [15, 25]. In each subsequent case elastic tunnelling, such that electrons do not lose energy in the tunnelling process, is assumed. While this is a reasonable approximation for passive STM scanning and the inelastic channel is usually assumed to be minor, inelastic tunnelling is extremely relevant to manipulation induced by the STM.

2.2.1 One-dimensional finite potential barrier model

In a simple model, the tip-vacuum-surface junction can be described by a one dimensional metal-insulator-metal junction, such that the barrier to tunnelling can be approximated as a rectangular potential. In the simplest form of this approximation there are only two available states; one in the tip and one in the sample, and only one electron. For an electron with energy E and mass m described by a wavefunction $\psi(z)$, with z the distance from the tip towards the sample surface, and assuming a gap of width a with potential U_0 where $U_0 > E$, shown in figure 2-2, the potential across the junction U is only dependent on whether the electron is within the barrier region,

$$U(z) = \begin{cases} 0, & z < 0 \\ U_0, & 0 < z < a \\ 0, & z > a, \end{cases} \tag{2.1}$$

As such, the probability of transmission can be calculated using the one-dimensional time-independent Schrödinger equation (TISE),

$$\frac{\hbar^2}{2m}\frac{\partial^2\psi(z)}{\partial z^2} = [U(z) - E]\,\psi(z). \tag{2.2}$$

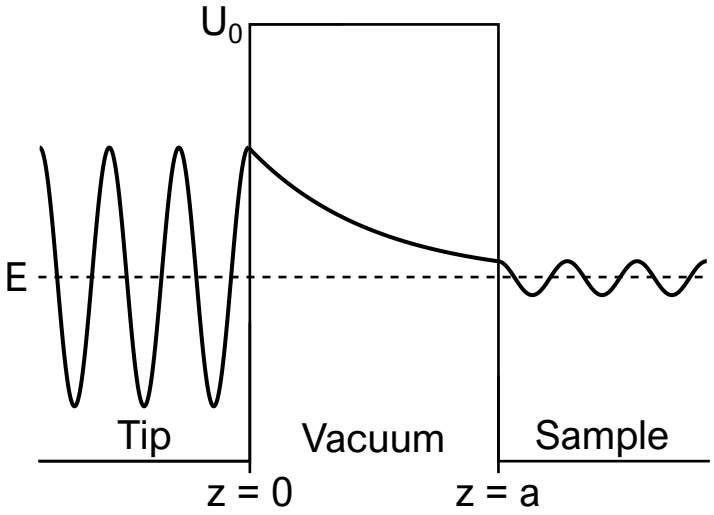

Figure 2-2: The one dimensional finite potential barrier model applied to the junction of an STM. In quantum mechanics, an electron travelling from the left to the right has a probability of tunnelling through a barrier with potential greater than the energy of the particle, $U_0 > E$.

We initially assume the solution of a plane wave with wavevector k travelling from the left side of the junction to the right, $\psi = e^{ikz}$. Thus from equation (2.2),

$$k = \sqrt{\frac{2m}{\hbar^2}\left[E - U(z)\right]}. \tag{2.3}$$

Outside of the vacuum region the potential barrier is zero, so

$$k = \sqrt{\frac{2m}{\hbar^2}E} \tag{2.4}$$

and the wavefunction has the form of a regular oscillating wave. Within the vacuum barrier $U = U_0$, and as the energy of the electron is less than the energy of the barrier the solution to equation (2.2) within the barrier region,

$$k = \sqrt{\frac{2m}{\hbar^2}\left[E - U_0\right]}, \tag{2.5}$$

is complex. This results in a real, exponentially decaying wavefunction within the barrier; $\psi = e^{\kappa z}$ where $\kappa = -ik$.

In addition to the right-travelling wave, a second solution to the equation results in a left-travelling wave, $\psi = e^{-ikz}$. Both inside and outside the barrier region the solutions to this second wave have the same forms as the right-travelling wave, and the overall

solution is a linear superposition of the two waves,

$$\psi(z) = \begin{cases} A\mathrm{e}^{ikz} + B\mathrm{e}^{-ikz}, & z < 0 \\ C\mathrm{e}^{-\kappa z} + D\mathrm{e}^{\kappa z}, & 0 < z < a \\ F\mathrm{e}^{ikz} + G\mathrm{e}^{-ikz}, & z > a, \end{cases} \tag{2.6}$$

in which A, B, C, D, F and G are complex eigenvalues for which the solutions remain. Note that these left-travelling waves can be considered the reflected portion of the incident right-travelling waves. As there is no barrier to reflect from in the rightmost region and in this model there is no incoming particle from the right, $G = 0$.

In all space the wavefunction of a particle is expected to be finite, continuous and differentiable. As such, we are able to apply boundary conditions between each of the constituent parts of equation (2.6) and thereby the relative values of the prefactor constants can be calculated. However, only the relative amplitudes of the incident (A) and transmitted (F) waves are relevant in calculating the transmission probability. Assuming a sufficiently large barrier, such that $\kappa a \gg 1$, and the incident amplitude $\mid A \mid^2 = 1$, the transmission probability

$$T = \mid F \mid^2 = \frac{16k^2\kappa^2}{\left(k^2+\kappa^2\right)^2}\mathrm{e}^{-2\kappa a} = \frac{16E(U_0 - E)}{U_0^2}\mathrm{e}^{-2\kappa a} \tag{2.7}$$

$$\propto \mathrm{e}^{-2\kappa a}. \tag{2.8}$$

In figure 2-3 the relation between the transmission probability and both a and E are shown, with constants set to reasonable values for the W-Si(111) junction of an STM. In this simplified model, the tunnelling current across the tip-sample junction is shown to be exponentially dependent on the width of the junction. This exponential dependence results in the atomic resolution of the STM as small, linear changes in the gap size will result in exponential changes in the measured tunnel current. In addition, the largest contribution of the tunnel current will occur between the surface and the foremost atoms on the tip apex which are closest to the surface; assuming a well tapered tip, further atoms will only slightly contribute to the tunnel current.

In STM the tip and the sample are usually made from metallic or metal-like materials with different work functions, ϕ, such that the energy to excite an electron from the surface to the vacuum differs on either side of the gap. Considering again a purely classical system, the only electrons able to enter the vacuum region are those emitted from the surface via excitation with energy sufficient to overcome the work function. Similarly, in the quantum mechanical system the work function acts as the potential

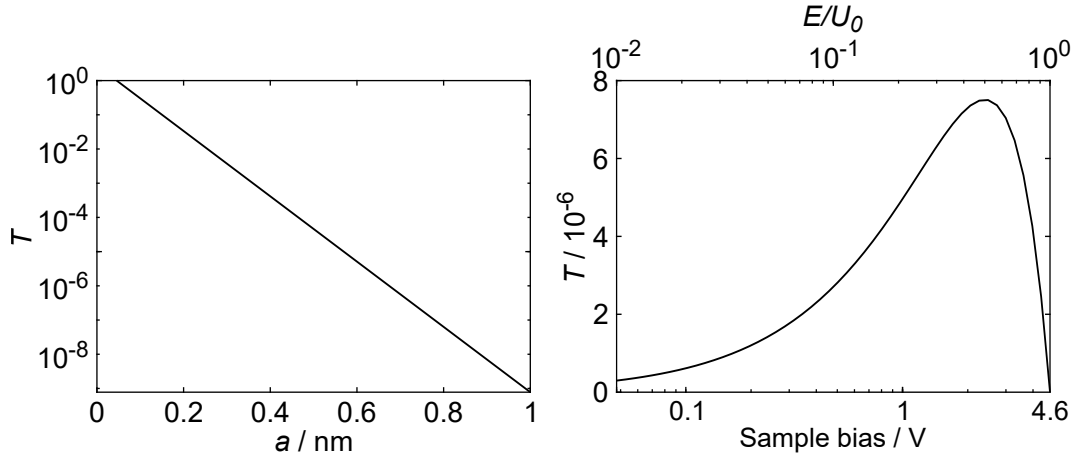

Figure 2-3: Transmission probability T of an electron across a one-dimensional finite potential barrier as a function of (left) the barrier width a and (right) the sample bias or electron energy E compared to the barrier potential U_0, as described by equation (2.7). Constants have been set to reasonable values for tunnelling between a tungsten tip and a Si(111) surface in an STM; with $U_0 = 4.60$ eV in both graphs [26], $E = 1$ eV in the left graph and $a = 0.6$ nm in the right graph [12].

barrier. That is, on either side of the junction $U_0(z = 0) = \phi_t$ and $U_0(z = a) = \phi_s$. As the work function of the two materials differ whilst the potential at each point across the gap is continuous, the potential barrier across the junction must equally change; $U_0 = U_0(z, \phi_t, \phi_s)$. This is commonly approximated as resulting in a trapezoidal potential profile. The square-potential model can be expanded, for example using the semi-classical Wentzel-Kramers-Brillouin (WKB) approximation in which the total barrier is considered a series of infinitesimal rectangular barriers [27, 28].

In the case of our system with a tungsten tip and a Si(111)-7×7 sample, the work function at either side of the barrier are extremely similar; 4.60 eV for Si(111) compared to 4.55 eV for polycrystaline tungsten [26]. As such, for situations in which the injection bias is small compared to the work function, $eV \ll \phi$, the system can be somewhat reasonably approximated as a rectangular potential. Note however that transmission increases exponentially with a linear decrease in the barrier height, and so a slight overestimate in the barrier height due to the applied voltage will result in a correspondingly large underestimate in the transmission probability. In figure 2-3, the transmission probability tends to zero as the injection bias approaches the work function of the material. This is due to limitations of the model. In reality, electrons with energy above the work function are able to travel through the potential barrier region without tunnelling and so the transmission probability will instead increase at higher biases.

2.2.2 Quantifying the lateral resolution

Based on this simple model the lateral resolution of an STM can be quantified. Modelling the apex of the tip as a parabola approximating a sphere with a radius R, such that the radius of the tip is far larger than the tip-sample separation, a, results figure 2-4. In this case, a movement of Δz laterally across the surface results a change in a of

$$\Delta a \approx \frac{\Delta z^2}{2R}. \tag{2.9}$$

Therefore, assuming the results of the purely planar model at each point on the surface of the tip,

$$\Delta T(\Delta z) \propto \exp\left(-2\kappa \frac{\Delta z^2}{R}\right). \tag{2.10}$$

As before assuming that $eV \ll \phi$ and thus

$$\kappa \approx \sqrt{\frac{2m\phi}{\hbar^2}}, \tag{2.11}$$

using $\phi = 4.6$ eV results $\kappa \approx 10$ nm^{-1}. The manufacture of tips for use with our STM is to be discussed in chapter 5, here we assume the tips have a radius of approximately 10 nm [29, 30]. When $\Delta z^2 = R/\kappa$, the probability of transmission for each electron will drop by a factor of e^{-2}, which is roughly an order of magnitude. This result suggests that the majority of transmission will occur from the tip to the sample within a circle of radius ≈ 1 nm on the tip, notably far lower than the radius of the tip itself. Correspondingly, the transmission will be primarily limited to a similar area on the the surface, thus resulting in an approximate lateral resolution of the order of 1 nm.

In reality, however, STM are observed to have an actual resolution well above the value calculated with this model and imaging surfaces with atomic resolution is possible. For example, a line profile from an STM image of a Si(111)-7 $\times$ 7 surface is displayed in figure 2-5. Multiple distinct peaks can be observed, each corresponding to an atom on the surface. Atoms on the Si(111)-7$\times$7 surface are separated by approximately 0.6 nm [31], hence as each clear peak in figure 2-5 is separated by less than this value, individual atoms can be discerned in an STM image.

2.2.3 Density of states and the tunnel current

In the previous model, an electron travelling from negative or positive z will experience the same potential barrier and so the probability of tunnelling in either direction will be equal. Additionally, no assumption has been made about the relative rates of incident

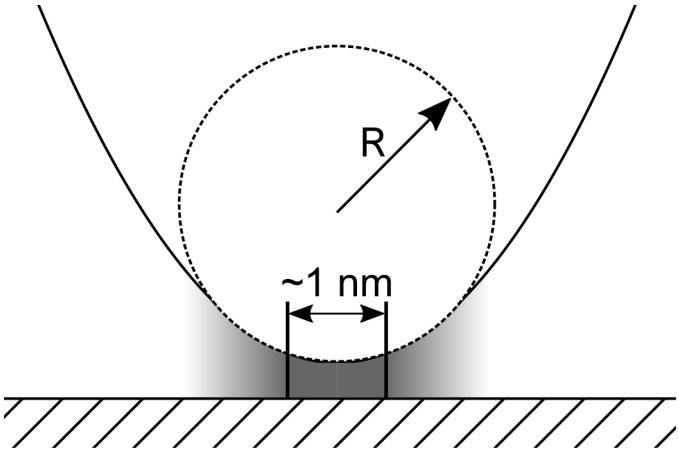

Figure 2-4: An estimation of the lateral resolution of an STM by approximating the tip as a parabola in the one dimensional finite potential barrier model. For a tip with a radius R of 10 nm, such that R is much greater than the tip-sample separation, the tunnel current is almost entirely concentrated within a region of approximately 1 nm diameter.

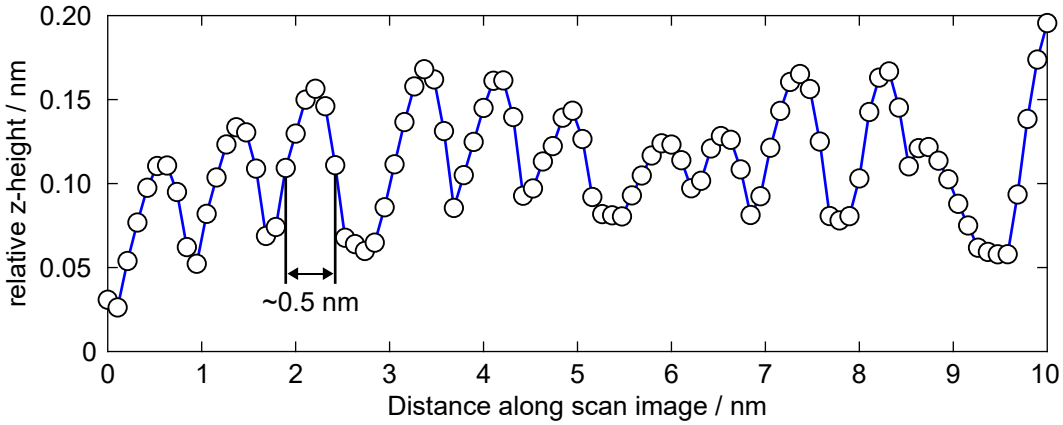

Figure 2-5: A single STM line profile, showing the change in height of the tip as it passes across the surface, from a 10×10 nm image of a Si(111)-7×7 surface with the tip-sample separation recorded at each marker. Each clear peak can be discerned with a horizontal resolution of less than 0.5 nm.

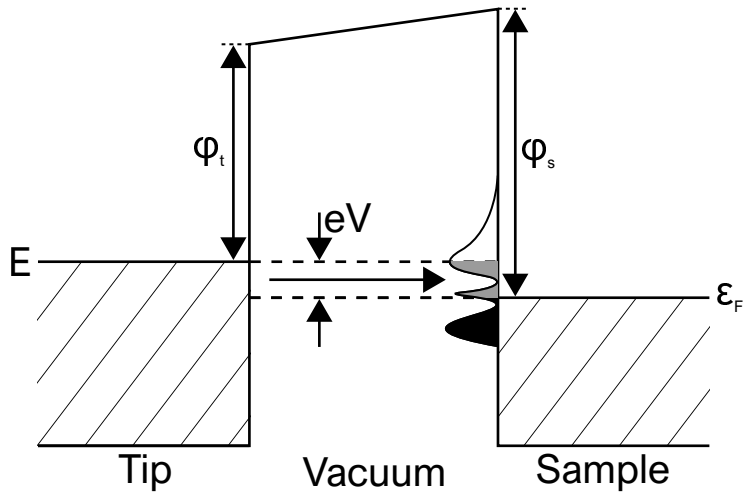

Figure 2-6: Quantum tunnelling across a one dimensional vacuum barrier. A negative bias, V, is applied to the tip whilst the sample is grounded, which results in an offset in the Fermi level of the tip, E, by eV. Electrons in the tip in states with energy between ϵ_F and E are able to tunnel across the junction into the empty states of the sample at a rate proportional to the LDOS of the sample. The height and shape of the potential barrier is dependent on the work function of the tip, ϕ_t, and the sample, ϕ_s, relative to the Fermi level, which is here approximately by a trapezoid.

electron tunnelling attempts (i.e. relating to the $\mid A \mid^2$ term removed from equation (2.7)) from the tip or the sample. An assumption of equal rates of tunnelling attempts suggests that the flow of charge across the gap will be equivalent in either direction and the net current will be zero. According to the Pauli exclusion principle, for an electron to successfully tunnel across the barrier, an unoccupied state at the same energy level is required on the other side. With no applied potential the Fermi levels of both the sample and the tip will be equivalent and there will be no available states, here assuming 0 K temperature. In an STM a bias is applied across the junction. An applied bias of $-V$ to the tip will raise the maximum occupied state by eV above the neutral level, raising the Fermi level of the tip, ϵ_F, with respect to the sample. In this case, electrons in the states between ϵ_F and $\epsilon_F - eV$ will be occupied in the tip, but not in the sample. Hence tunnelling can occur and a nonzero tunnel current will be measured, as shown in figure 2-6.

In a material, the number of available states is not homogeneously distributed throughout all possible energy levels. Instead, the number of states can be considered as a continuous distribution function with a specific density of states at each energy. Thus the tunnelling current from the tip to the sample with a bias eV across the junction, noting that the tunnelling current will be proportional to the transition probability for

each electron,

$$I \propto \sum_{E_n=\epsilon_F-eV}^{\epsilon_F} \mid \psi_n(z=0) \mid^2 \mathrm{e}^{-2\kappa a}, \tag{2.12}$$

in which $\psi_n(z=0)$ is the wavefunction of an electron in a state at energy E_n at the apex of the tip. While in general the density of states is defined as an average across a material, an STM is able to image a surface with subatomic resolution and hence a more localised measure is useful. For a sufficiently small applied bias the density of states can be considered to be approximately constant between ϵ_F and $\epsilon_F - eV$, resulting in a quantity known as the local density of states (LDOS), ρ_s, defined as the number of electrons per unit energy per unit volume at a given point on the surface and a given injection bias. At position $\vec{r}$ on the surface,

$$\rho_s(\vec{r}, \epsilon_F) \equiv \frac{1}{eV} \sum_{E_n=\epsilon_F-eV}^{\epsilon_F} \mid \psi_n(\vec{r}) \mid^2 . \tag{2.13}$$

Hence equation (2.12) can be re-expressed in terms of the LDOS of the sample beneath the tip,

$$I \propto V \rho_s e^{-2\kappa a}. \tag{2.14}$$

As it is this quantity that the STM effectively measures, images produced by an STM are not perfect recreations of the topography of a surface which, anyway, is not clearly defined at the atomic scale.

Equation (2.14) suggests that the tip height should be linearly proportional to the negative log of the tunnel current. Due to the proportionality, however, it gives no information about the absolute separation between the tip and the surface beneath. This relationship can be displayed by measuring the change in the measured tip height as the tunnel current is varied, which is shown in figure 2-7. At a set current and bias the tip height, according to equation (2.14), will be constant, however the absolute tip-sample separation is hard to measure using an STM. Instead, by considering the change in tip height at different currents at the same position on the surface the value of κ and hence, using equation (2.11), ϕ can be determined from the gradient. This figure shows the change in tip height Δa between passive scanning parameters (1 V, 100 pA) and injection parameters (here -2.1 V) with varying tunnel current I. While in each individual measurement in figure 2-7 the tip is stationary, positioned above an unoccupied adatom site on a Si(111)-7×7 surface, note that the exact position of the tip with respect to the adatom will vary. Thereby the LDOS of the surface beneath the tip will vary, resulting in slight variations in the exact tip height at each current. Using

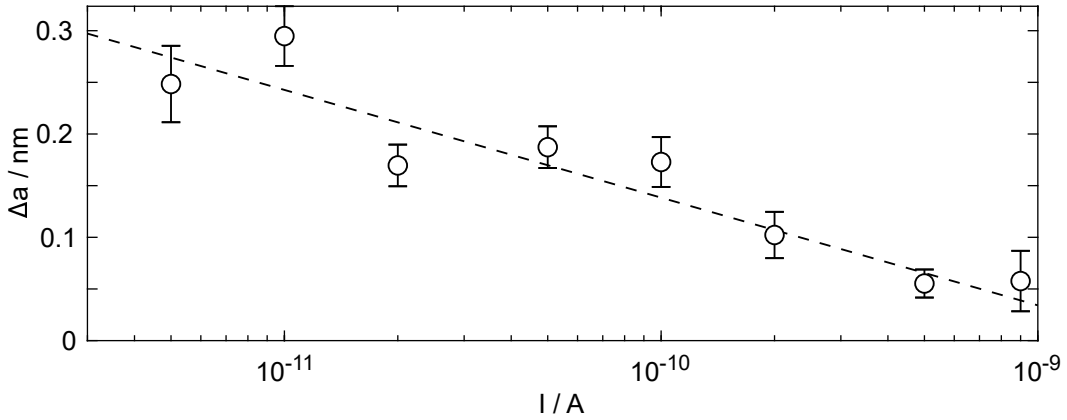

Figure 2-7: The change in the tip-sample separation Δa between passive scanning parameters (1 V, 100 pA) and experimental injection parameters at -2.1 V with varying tunnel current I between 5 and 900 pA. Error bars show standard error of the mean across a minimum of 6 measurements at each current. The dashed line shows a weighted least squares fit, with the gradient $\Delta a / \ln(I) = -0.045 \pm 0.008$ nm.

the gradient of the fit shown in figure 2-7 results $\phi = 4.7 \pm 1.7$ eV, in good agreement with the 4.60 eV value used above [26]. Note, however, that the injection bias here is similar in magnitude to ϕ, so the tunnelling characteristics will diverge from the simple model discussed here.

That the STM is a measure of the LDOS at a constant Fermi level on a surface can result in a number of interesting properties when imaging certain systems. Consider for example the simultaneous AFM and positive bias STM images of a Si(111)-7 $\times$ 7 surface dosed with benzene (a system to be discussed in more detail in chapter 4) by Majzik et al. [32] shown in figure 2-8. In this figure it is observed that the STM and AFM images show different apparent structures at the sites with chemisorbed benzene molecules. In the AFM image benzene molecules are observed as protrusions from the surface, whilst in the STM image they are observed as dark sites, similar to vacant adatoms.

This can be explained in terms of the LDOS of the surface. In the chemisorption process the bonds formed between the Si adatom and the benzene molecule have the effect of saturating the empty dangling bond electron states at the adatom, thus reducing the LDOS available for tunnelling and thereby reducing the tunnelling current between the tip and the adatom according to equation (2.14). However, κ will be reduced as tunnelling through something is easier than tunnelling through vacuum, so the presence of the adsorbate makes it harder by reducing the LDOS but makes it easier by reducing the effective barrier. In this case the reduction in the LDOS has the larger effect,

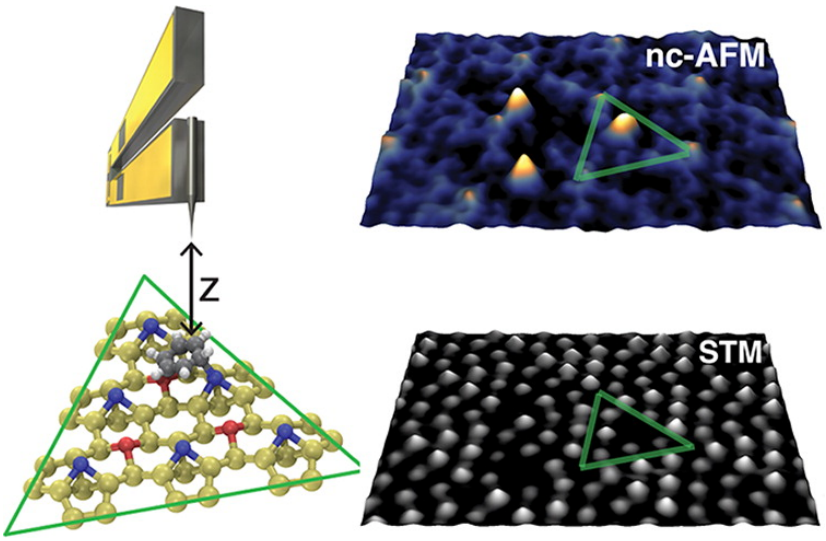

Figure 2-8: A schematic diagram (Left) of the simultaneous measurement of STM and non-contact AFM images (right) of a Si(111)-7×7 surface dosed with benzene at 0.05 V. At most points on the surface the AFM and STM images roughly correlate, however at the position of a chemisorbed benzene molecule the AFM displays a clear bright spot whereas the STM image shows a dark site similar to a vacancy. The green triangle represents the same half unit cell in all three images, with a benzene molecule chemisorbed to a middle adatom. From [32].

and so, to reach the requisite tunnel current, the STM tip must approach the surface such that tunnelling primarily occurs between the tip and deeper lying states. The chemisorbed molecule effectively increases the width of the barrier, which is visualised as an indent on the surface, much like an absent adatom. Chemisorbed molecules will have a different distribution of density of states than the clean surface, and so at higher or lower biases adsorbates may instead appear brighter than adatoms. As such, for surfaces with variable electron density, for example here due to chemisorbed molecules, an STM image will not directly correlate with the geometric positions of surface atoms or molecules.

In addition, the quantum mechanical behaviour of electrons can result in interference effects visible in STM images. For example, the presence of defects including step edges and vacancies is observed to result in Friedel oscillations [33], such as those visible on the Cu(111) surface shown in figure 2-9 [34]. In this image standing waves are clearly visible propagating both radially from vacant sites or linearly from step edges. In such a system the defects act as scattering sites for surface electrons, resulting in a perturbation of the electron gas and, thereby, oscillations in the electron wavefunction. Near the Fermi level such charge density waves affect the LDOS across the surface,

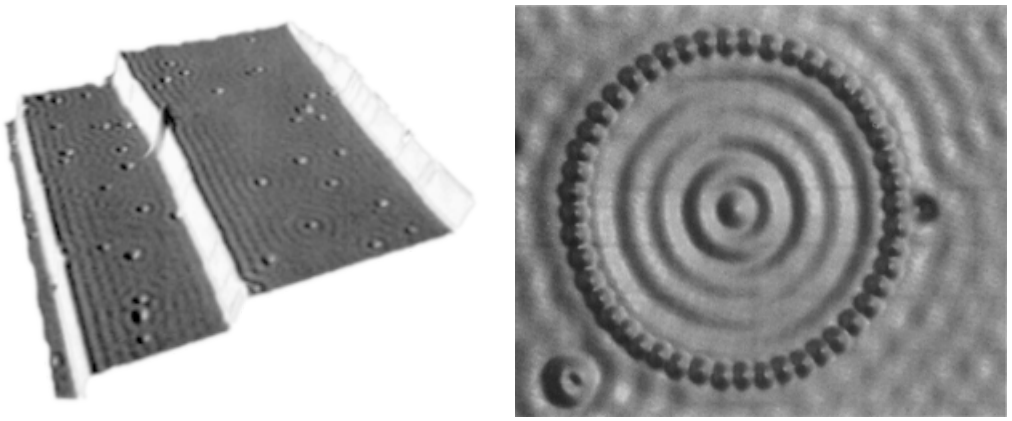

Figure 2-9: (Left) 50×50 nm^2 STM image at 0.1 V, 1 nA of the Cu(111) surface. Step edges and vacancies on the surface result in oscillations in the surrounding LDOS with a periodicity of approximately 1.5 nm. From [34], edited for clarity. (Right) The quantum corral. Standing waves in the electron gas due to quantum interference effects can be observed in the STM image of a ring of Fe atoms on a Cu(111) surface. From [37].

leading to the observed oscillations in the STM image of figure 2-9. The wavelength of such oscillations is dependent on the energy of the electron gas and can be measured by taking the Fourier transform of the STM image. Using this analysis properties of the electron gas can be indirectly measured, such as the dispersion relation and the band structure of the surface material [35, 36]. By positioning atoms into a ring on a surface these quantum mechanical effects can be observed as the quantum corral, for example that shown for Fe atoms on a Cu(111) surface in figure 2-9 [37]. This pattern is, essentially, a visualisation of a standing wave in a 2 dimensional infinite square well, with the Cu surface electrons reflecting from the Fe adatoms, and is well described by the relevant solution to the Schrödinger equation.

2.2.4 Fermi's golden rule and finite temperature effects

In the above simplified model only the LDOS of the surface have been considered to contribute towards the tunnelling current. Whereas, in reality, the rate of tunnelling will be dependent on the LDOS of both the tip and the sample. Assuming that the tip is perfectly stable, only the surface LDOS will vary as the tip is rastered across the surface, however the overlap of the states will still vary dependent on both systems. Bardeen developed a model of metal-insulator-metal junctions such that either side of the junction, and each electron, is considered independently whilst assuming a weakly coupled system [38]. Further assuming weak tunnelling between one electrode and the other and a small applied bias compared to the work functions of the materials, the

total wavefunction for an electron in any state of either side can be considered nearly independently. Thus the tunnelling probability is dependent only on the wavefunction plus a small perturbation from the wavefunction of the other electrode. A complete derivation of this result, as well as a discussion of situations in which the model is reasonable, can be found in [38]. The key result of this model is that the rate of electron transfer for an electron in any state can be approximated by Fermi's golden rule; such that the rate of transition is proportional to the available post-transition DOS. Hence, in an STM the tunnel current will be proportional to the LDOS of both the tip and the sample.

As the temperature of the system is reduced towards zero Kelvin, the occupation of states will tend towards the discrete step-change occupation assumed above. That is, all states below the Fermi level are completely filled whilst all states above are completely empty. As a result, tunnelling can only occur in one direction across the junction; from the more negatively charged surface to the more positively charged surface, and the total number of states can be considered without mention of occupation. At finite temperature T, however, the state occupation at energy E will be distributed about the Fermi level according to the Fermi-Dirac distribution,

$$f(E-\epsilon_F) = \frac{1}{1+\exp\left(\frac{E-\epsilon_F}{k_b T}\right)}, \tag{2.15}$$

in which k_B is the Boltzmann constant. Filled and vacant states will therefore exist, meaning that tunnelling can occur in either direction as shown in figure 2-10. At sufficiently low temperature, the Fermi-Dirac distribution can be approximated as a Heaviside step function and the above equation will return to the zero-temperature form. At finite temperatures, however, the measured LDOS is effectively the result of contributions from a range of LDOS surrounding the Fermi energy of both the tip and the sample, and the ability of the STM to precisely probe specific energy levels is reduced.

2.3 STM operation

Fundamentally, the imaging process of each SPM technique is the same, primarily consisting of the tip-sample junction and a method of measuring the specific interaction whilst moving the tip across the surface. The movement process generally uses piezoelectric motors; these are crystals which expand or contract by a well defined amount under an applied electric field, such that the tip is rastered across the surface by varying

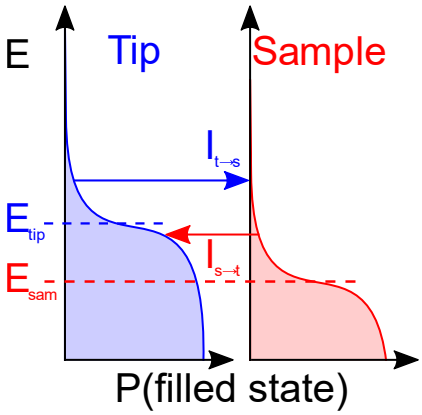

Figure 2-10: The Fermi-Dirac distribution about the Fermi level of both the tip and the sample of an STM at finite temperature, with a negative bias applied to the tip. Tunnelling can occur between filled (shaded) and empty (unshaded) states in either the tip or the sample, such that current will flow in both directions.

the field applied to x- and y-axis controlling piezos. A diagram of the system used in this thesis is shown in figure 2-11.

In the case of STM, the tip is brought close enough to the surface that a tunnel current can be measured whilst a bias is applied across the tip and the sample. As the interaction is exponentially dependent on the separation, the tip is required to be brought extremely close to the sample, usually within 1 nm. It is important, however, to prevent the tip from making contact with the surface. If the tip ever touches the surface it is quite likely that the apex of the tip will irreversibly change and high resolution STM imaging may be lost. Similar to the x-y control, a piezo-motor controls the z-height of the tip relative to the surface.

Prior to measurement, the tunnel current is passed through a preamplifier to reduce the effects of electrical noise, discussed in section 5.4, and allow the current to be measured by the control electronics. In our system, a Nanonis SPM controller is used to measure the tunnel current as well as to control the position and height of the tip via the piezo-motors and apply a bias to the sample. The output of the controller, including traces of the tip height across the surface, is then transferred via a high resolution digital-analogue-converter (DAC) to a computer, allowing for analysis of the images. Nanonis software on the computer can additionally be used to manually or programmatically control the Nanonis controller, allowing for manual or automated experiments such as those described in chapter 6.5.

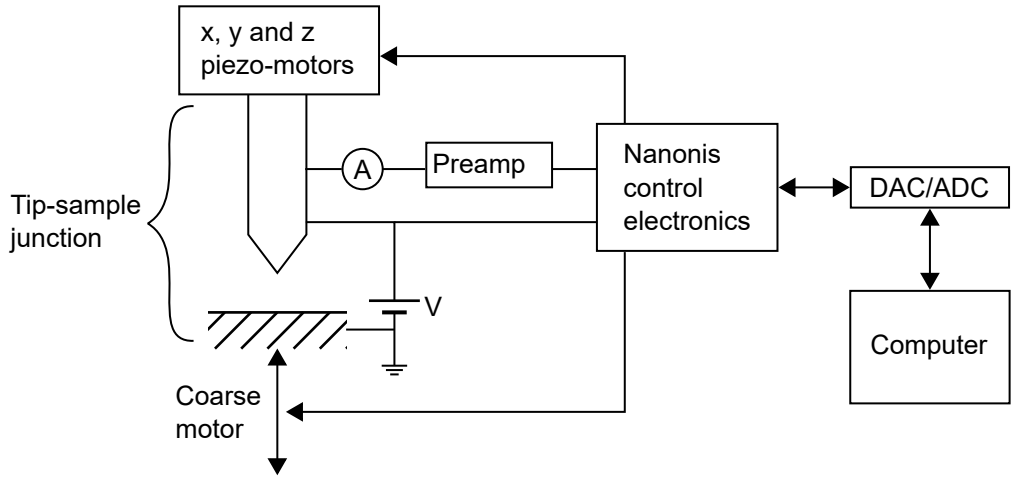

Figure 2-11: The tip-sample junction and control electronics of the STM. A Nanonis SPM control system controls the position of the tip and the sample, applies a bias and measures an amplified current across the junction, as well as providing communication with a computer.

2.3.1 Constant current STM imaging

In an STM scan at any position on the surface, any two of the three primary measurable parameters can be adjusted by controlling the third; the tip-sample bias, the tip height (i.e. the piezo-motor extension), and the tunnel current. STM imaging is generally operated in constant current mode, an outline of which is shown in figure 2-12, such that a feedback loop acts to maintain a constant current across the tip-sample junction during scanning. As changing the applied bias will affect the LDOS on the surface and thereby the STM image, this is achieved by adjusting the tip height to counter any measured changes in the current. Thus in constant current STM the tip height trace is approximately a real-space map of the LDOS of the sample.

As the tip is scanned across the surface the LDOS will change, and so the measured tunnel current will itself change; assuming a simple one-atom basis system the LDOS will be higher when the tip is positioned above a surface atom and lower elsewhere. The current is amplified by the preamplifier and measured by the Nanonis controller, which responds by retracting or expanding the z-height piezo-motor as necessary to maintain the tunnel current. The magnitude of the response, as well as the time between adjustments can be controlled using the Nanonis software. If the magnitude of the response is too high or the time between adjustments too small, the tip will overcorrect resulting in a sharp, unnatural z-height trace as the tip rapidly bounces towards and away from the surface. This may additionally result in contact between

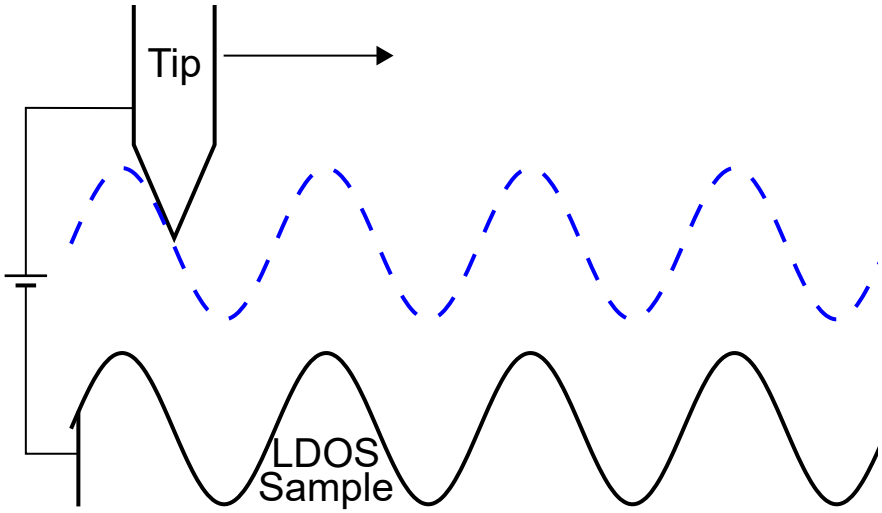

Figure 2-12: The constant current mode of STM operation. By varying the extension of the z-height piezo-motor, the tip apex follows the contours of the LDOS of the surface (black) as it is rastered across. With the tip following the dashed blue path, the tunnel current is maintained.

the tip and the sample. Corrections that are too small or a response that is to slow will limit the resolution of the STM images, as the tip height will not be adjusted sufficiently quickly to follow the corrugations of the surface.

Chapter 3

Atomic manipulation with the STM

The STM was primarily developed for its use as an atomic-scale resolution microscope, although it was soon discovered that the technique could be used to move atoms across the surface with atomic precision. This was disadvantageous for microscopy and initially limited to extremely weakly interacting systems and individual atoms at low temperatures. Despite this, STM atomic manipulation allowed the formation of artificial structures [4] and the visualisation of quantum effects [39] at the nanoscale. More recently, STM manipulation has resulted in more complex systems, including working electronic components such as switches [40], transistors [41] and diodes [42] able to operate at room temperature. Utilising the electrical properties of individual molecules, this route offers the potential for the manufacture of complete bespoke circuits at the nanoscale, far below that offered by traditional manufacturing techniques. Additionally, of primary interest to this thesis, manipulation of molecules far from the injection site allows the indirect observation of the manipulation and charge transport dynamics themselves.

In this section an overview of the mechanisms behind the atomic manipulation processes are discussed. Initially focusing on local atomic manipulation, where the manipulation is limited to molecules directly within the junction beneath the tip, additional detail is included with respect to nonlocal atomic manipulation.

3.1 Inelastic electron tunnelling induced manipulation

The earliest observed form of atomic manipulation with the STM involved the unintended manipulation of individual particles as the tip was scanned across the surface. In weakly interacting systems it was realised that the presence of the tip induces sufficient tip-particle forces to either push or pull adsorbates. By manually controlling the position of the tip, this process could be exploited and the positions of the adsorbates could be altered almost at will. With the tip at passive scanning parameters, the interaction between the tip and the adsorbate molecules is weak enough to rarely induce manipulation. To manipulate an adsorbate, the tip is brought towards the surface (i.e. increasing the tunnel current) when directly above the requisite atom, resulting in the tip being closer to the particle and thereby a stronger tip-adsorbate interaction occurs. Assuming an initial attractive interaction (for example Van der Waals forces), as the tip is then moved laterally across the surface the molecule will experience a force towards the tip and may follow the tip by moving from one adsorption site to the next. The tip can then be retracted, and the particle should remain in the new position. It should be noted that this lateral manipulation requires a relatively uniform surface and extremely weak surface-molecule interactions; examples of lateral manipulation are mainly restricted to metal surfaces and low temperatures [4, 39].

The STM tip is also a source of hot charge carriers which tunnel across the vacuum barrier and into the surface-particle system beneath (or alternately the reverse; with charge carriers tunnelling from the surface-particle to the tip). In section 2 it was assumed that the tunnelling process is an elastic process such that no energy is lost by the charge carrier after tunnelling, however this is not always the case. Instead a small portion of the injected charge can undergo inelastic electron tunnelling (IET), with a pathway leading to the transfer of energy from the tunnelling charge carrier to the particle within the junction and resulting in a corresponding excitation. Thus tunnelling can induce electronic or mechanical (e.g. promoting vibrational modes) excitation of the underlying particle, potentially leading to the breaking of one or more surface-adsorbate bonds and thereby manipulation. Assuming each bond between the surface and the adsorbate is broken, the particle is then able to desorb. However, depending on the injection parameters and the surface-molecule system, IET can result in numerous outcomes including diffusion or dissociation of the adsorbate molecule [43].

The processes that result in desorption due to this excitation can be separated into two main categories; dynamics induced by (single) electronic transition (DIET) and, less commonly, dynamics induced by multiple electronic transitions (DIMET) [44], potential

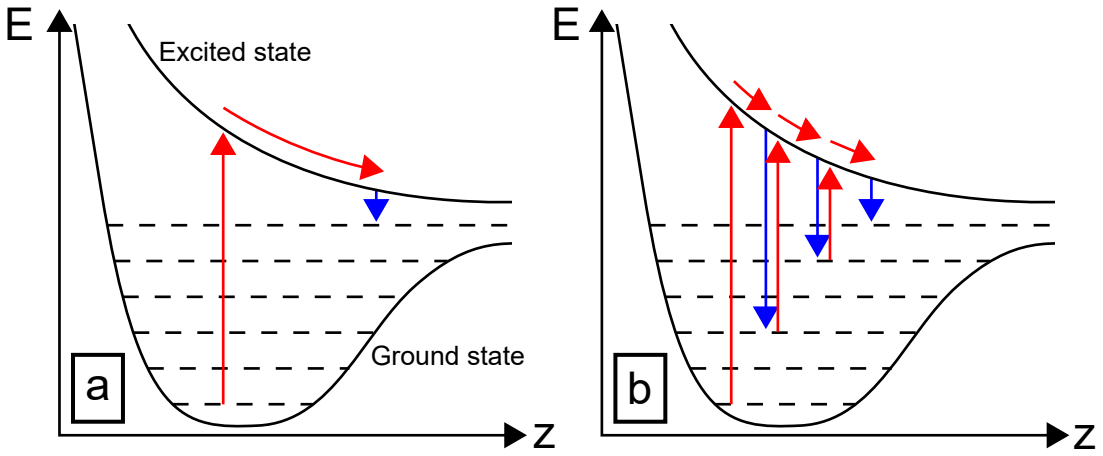

Figure 3-1: (a) DIET and (b) DIMET models of manipulation, showing the potential energy surface as a function of the z-height of the adsorbate for a system with a repulsive excited state. In (a) the excited state lifetime is long enough that after relaxation the adsorbate has sufficient energy to overcome the barrier to desorption. Whereas in (b), after relaxation the system enters a vibrationally excited state with a long lifetime compared to the excitation rate. This excitation-relaxation repeats until the system has sufficient energy to overcome the potential barrier.

energy surfaces of which are shown in figure 3-2. Such processes are fundamentally similar, and both have traditionally been modelled using either the Menzel-Gomer-Redhead (MGR) [45] or the Antoniewicz [46] models depending on the direction of the excited state potential; repulsive or attractive respectively [47]. In both models, the system is treated as one-dimensional with respect to the distance of the centre of mass of the adsorbate from the underlying substrate with two distinct multilevel states; an initially occupied ground state and an initially unoccupied excited state. IET here results in the excitation of the adsorbate from the bottom of the ground state to the excited state and, depending on the shape of the potential surface, a corresponding force on the particle towards or away from the substrate. This force leads to a physical shift in the position of the adsorbate. The adsorbate will eventually transition back to the ground state, maintaining the altered position and momentum such that the particle will be in a vibrational excited state within the ground state [48]. With a sufficient excited state lifetime, the particle can gain enough kinetic energy during the excitation and relaxation steps to overcome the barrier to desorption. Essentially, energy is transferred from the tunnelling electron into a surface-adsorbate vibrational mode.

DIET mechanics, shown in figures 3-1b and 3-2, occur when the kinetic energy transferred during the excited state is sufficient to independently overcome the energy barrier

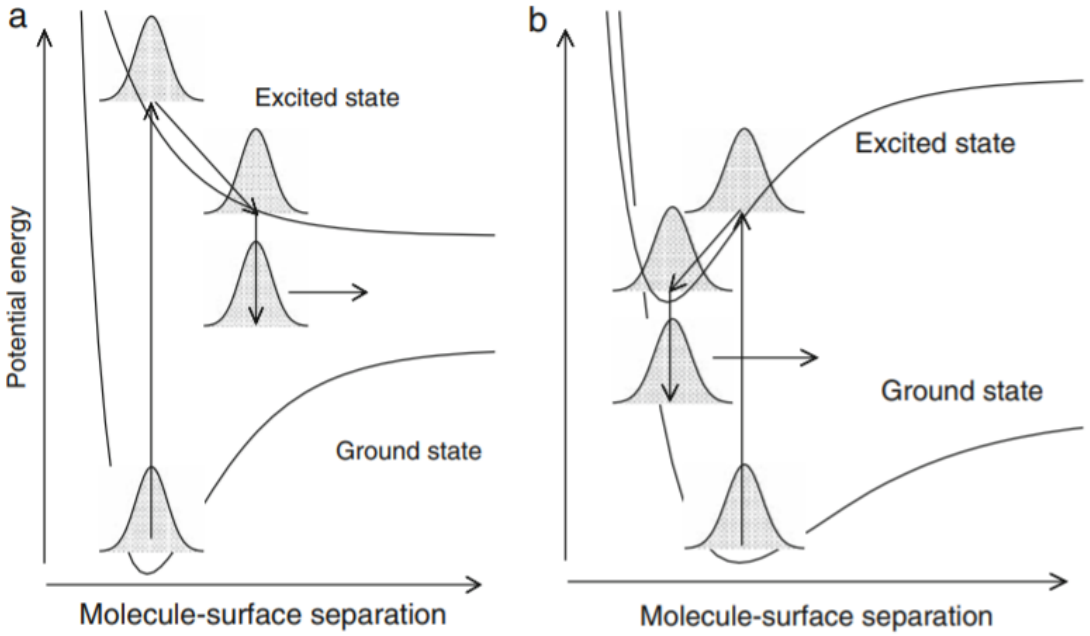

Figure 3-2: Models of DIET. Potential energy surfaces experienced by a particle initially adsorbed onto a substrate. Inelastic electron tunnelling induces transition from the ground state to an excited state with a different equilibrium bond length, resulting in a force applied to the adsorbate. (a) MGR model in which the particle experiences a repulsive potential upon excitation. (b) Antoniewicz model in which the potential is attractive. When the particle relaxes to the ground state, it maintains kinetic and potential energy sufficient to overcome the desorption barrier. From [48].

to manipulation. Clearly, if the energy of the tunnelling charge is below the energy of the barrier, DIET cannot occur [49]. Additionally, if the excited state lifetime is short, the system will not gain enough kinetic or potential energy to overcome the barrier before relaxing back to the ground state. This effect is modelled in figure 3-3 [50], wherein an increased excited state lifetime results in a greater probability of desorption. As such, DIET is dependent on both the excited state lifetime in addition to the energy transferred from the hot charge carrier, which is clearly limited by the energy of the hot charge itself.

Conversely, in DIMET, shown in figure 3-1b, multiple tunnelling charges provide energy in succession such that manipulation can occur in situations where the energy transfer during the excited state is insufficient to induce desorption, even if the energy of each independent injected charge is below the manipulation threshold [44, 49]. In this case, IET occurs whilst the system is in the vibrationally excited ground state, wherein the particle will again transition to the excited state. Upon successive relaxation,

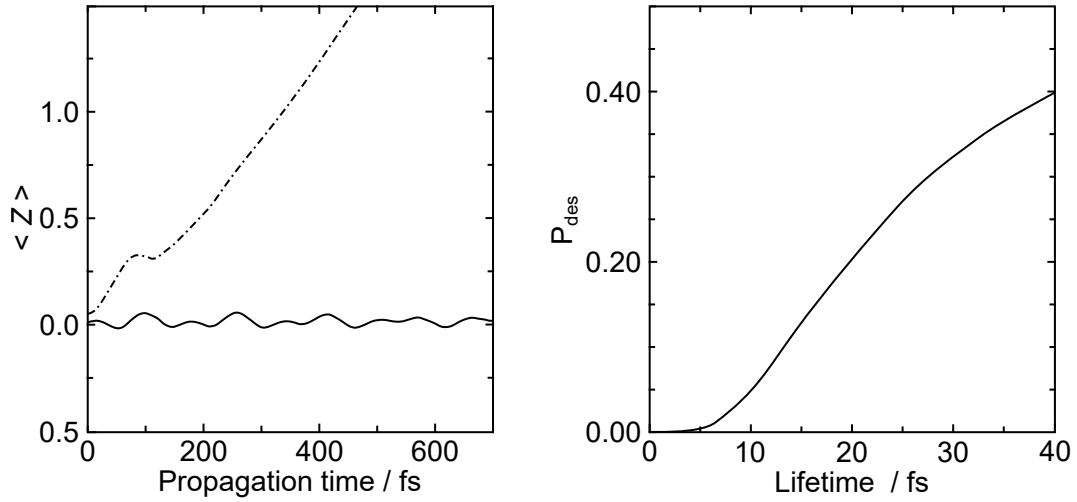

Figure 3-3: Theoretical model of the STM-induced desorption of benzene from a Si(100) surface. (Left) Mean surface-particle separation Z after 10 fs (solid line) or 40 fs (dot-dashed line) residence in the excited state. For short residence time the particle wave-packet relaxes into a low energy region within the ground state, with only low-amplitude vibrational motion remaining. Whereas the longer residence results in the particle relaxing into a highly repulsive region of the ground state. (Right) Probability of desorption as a function of the excited state residence time. Adapted from [50].

the particle will have gained further kinetic energy and may be in a higher energy vibrational excited state. This "vibrational ladder climbing" process [51] may repeat until the particle has sufficient energy to overcome the desorption barrier.

In certain systems both of these pathways to manipulation can occur, however the relative rates depend on several factors [43]. In situations in which the vibrationally excited state lifetime is short compared to the rate of injection of charge carriers, the probability of a charge carrier interacting with the particle in the vibrationally excited state is small and so the probability of DIMET is similarly small. In this case, any desorption via IET will only realistically occur due to DIET mechanics. Alternatively, if the lifetime of the excited state is long, such that the rate of IET is much greater than the relaxation rate of the particle, the dominant desorption mechanism may be DIMET [52, 53]. For example, at sufficient bias (0.4 V) the desorption of O_2 from a Pt(111) surface has been observed to occur at a rate per injected electron independent of the injection current [54], and thereby it is a DIET process with the energy of a single electron sufficient to induce desorption. Reduced injection biases necessitate multiple electrons and the vibrational ladder climbing process to induce desorption (requiring two electrons per desorption at 0.3 V and three at 0.2 V), hence we observe a transition from DIET to DIMET for injections below the 0.4 V threshold. In this case,

the vibrational excited state relaxation rate is sufficiently larger than the maximum injection current (4×10^{12} s^{-1} compared with 6×10^{11} s^{-1} respectively) so that the DIET process is favourable, given sufficient bias. It should be noted, however, that the rates are comparable, and hence DIMET processes are possible and favoured below the threshold bias. Conversely, in a system with an excited state lifetime far shorter than the charge injection rate, a sharp threshold bias below which little manipulation occurs is observed [9, 55].

The dominant pathway can be determined by measuring the rate of manipulation with respect to the rate of hot charge injection r_e, which in STM will be proportional to the tunnel current during injection I,

$$r_e = \frac{I}{e}, \tag{3.1}$$

in which e is the elementary charge. Assuming here a one charge DIET process, each IET event will be independent and the rate of manipulation will be linear and directly proportional to the rate of charge injection. Whereas in the multi-charge DIMET process, the probability of a hot charge interacting with the vibrationally excited state will depend on both r_e and the number of excitation-relaxation events n required to induce desorption. Assuming that the probability of each injection exciting the adsorbate is itself independent, the total rate of manipulation will depend on a power law relation with the rate of charge injection, r_e^n [49]. Thus in the case of STM, the rate of manipulation due to IET

$$R \propto I^n, \tag{3.2}$$

and the average number of IET events per desorption can be measured. It is important to note that experimental factors, such as the specific tip structure, as well as the large inherent statistical variation in desorption yield measurements, have previously resulted in difficulties accurately estimating the charge dependence [56].

Alongside desorption and other mechanical manipulation pathways, IET may also result in the dissociation or tautomerisation of an adsorbate molecule, or the formation of individual bonds between molecular complexes [5, 57]. These pathways are similar in form to the pathway to desorption, however with the vibrational excited state providing energy to overcome an alternative barrier with an energy threshold less than the threshold to desorption. For example, using IET from a combined qPlus AFM/STM to induce the reversible formation of a chemical bond between an Au adatom and an organic a perylene-3,4,9,10-tetracarboxylic dianhydride (PTCDA) admolecule [58]. The I-V spectra of the transition, showing a distinct change between the two states, as well as STM images of the orbital structures of the states of the complex and singly

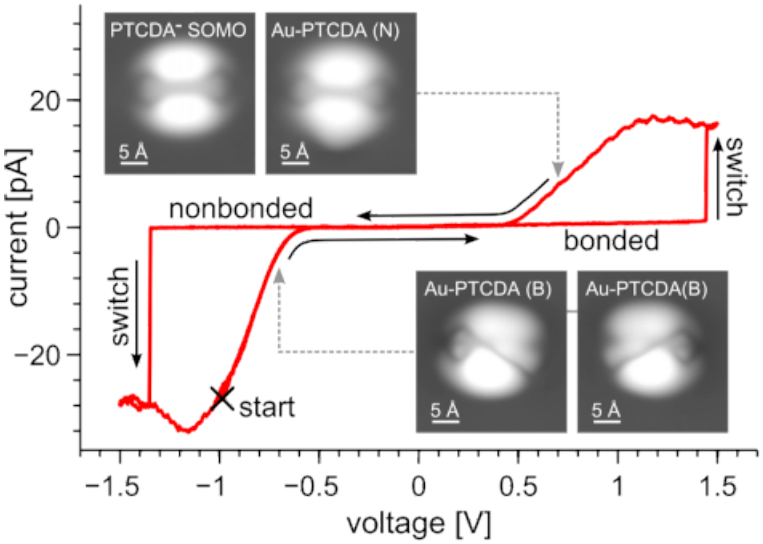

Figure 3-4: I-V spectrum of the switching cycle of an electronically isolated Au-PTDCA complex, initially in the bonded Au-PTCDA(B) state, measured above the centre of the complex with arrows indicating the direction of the applied voltage cycle. While the bonded state showed no peak at positive bias prior to switching at ≈ 1.4 V, the unbonded Au-PTCDA(N) state showed no peak at negative bias. Insets show STM images of PTCDA (labelled PTCDA$^-$ SOMO) and the different states of an Au-PTCDA complex at the dI/dV peaks, recorded at $I = 5$ pA and $V = +0.8$ V for PTCDA, $V = +0.7$ V for Au-PTCDA(N), and $V = -0.7$V for Au-PTCDA(B). From [58].

occupied PTDCA$^-$ are shown in figure 3-4. In this case the atom-molecule system is electronically decoupled from a conductive Cu substrate via a thin, insulating NaCl film, providing stability for both the excited and neutral complex states. To induce the bond formation (or dissociation), the tip is initially positioned at a nonspecific point above the complex, with the Au ion close to the PTCDA, and the applied sample bias is increased to -1.5 V (1.5 V for dissociation). The bond breaking and formation were both accompanied by an approximately two orders of magnitude increase in the tunnel current, providing a clear signal for the transition. The switching process has been found to be mediated by the long lifetime of the electron or hole attached to the Au-PTDCA complex, and hence results in a stable and reliable switching bias, varying by less than 0.1 V [58]. Thereby this mechanism presents a route towards utilising IET in the construction of individual atomic-scale switches.

3.2 Nonlocal atomic manipulation via IET

In the previously discussed local manipulation, the surface beneath the adsorbate is generally only a passive substrate on top of which the manipulation process occurs. However in many cases, manipulation is not limited to directly within the tunnel junction. Instead, molecules many nanometres away from the injection site can be manipulated by a single charge injection event. In this case, prior to manipulation the charge carrier will be transported across the surface. While the aforementioned local manipulation can be considered a two step process, charge injection followed by manipulative decay, nonlocal manipulation adds an additional middle charge transport step as well as further limiting the available initial injection states. Charge carriers are only able to exist within available surface transport states in nonlocal manipulation, and so surface dynamics begin to play an important role in the distribution and requisite parameters for the IET induced manipulation. This nonlocal mechanism has been observed on a number of surfaces, primarily including metals [59–62] and metal-like surfaces such as graphene [63] and certain reconstructed semiconductors, most notably silicon and germanium [64–66]. Note that the Si(111)-7 $\times$ 7 surface, and nonlocal manipulation therein, is to be discussed in detail in section 4 and as such will only be briefly mentioned here.

Examples of nonlocal manipulation by charge transport through a metal surface includes the dissociation of CH_3SSCH_3 molecules adsorbed onto an Au(111) substrate into two CH_3S fragments observed by Maksymovych et al. [59], clearly visible in figure 3-5a. In this mechanism, the application of an increased bias, with a threshold of 1.4 V, between the tip and the surface whilst the tip position is maintained results in the dissociation of adsorbates up to 100 nm away from the injection site. This process was shown to be primarily mediated by the tunnelling charges as injections with the tip effectively retracted from the surface by greater than 1 nm, with the tip positioned on an extruding cluster, had little effect on the overall manipulation radius, despite a much reduced electric field strength. In figure 3-5b, the rate of manipulation as a function of the injection current shows that this dissociation is a one electron process in analogy with equation (3.2). However in nonlocal manipulation experiments the direct number of injected electrons per manipulation cannot be measured, instead here the overall surface coverage of undissociated CH_3SSCH_3 molecules both before and after injection have been considered. The extraction of manipulation rates and probabilities from static before-and-after injection STM images is used in this thesis, and is discussed in more detail in chapters 8 and 9. Additionally, accounting for the geometric increase in the surface area with radius, the rate of manipulation R was shown to decay

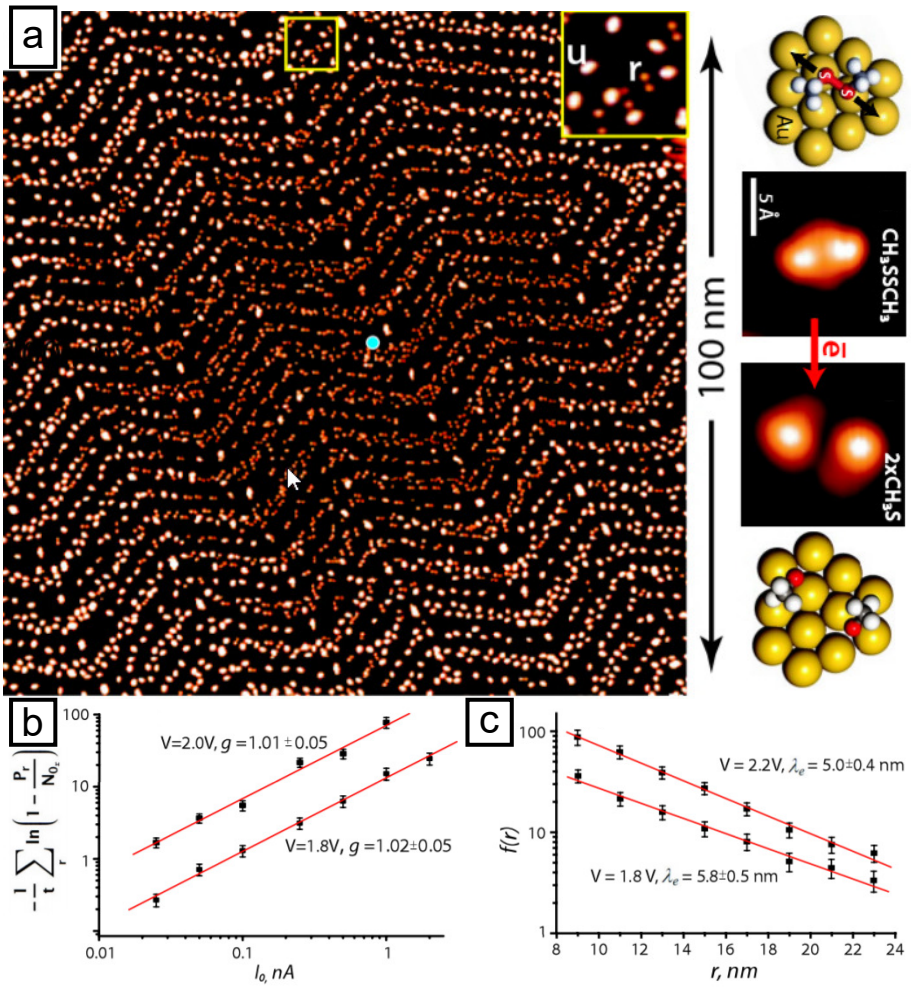

Figure 3-5: Nonlocal dissociation of CH_3SSCH_3 molecules on an Au(111) surface due to injection of electrons from an STM [59]. (a) A large STM image of the system after a 2.5 V, 1.0 nA, 200 ms injection showing a dissociated region surrounding the injection site (blue circle). (b) The rate of manipulation per injected electron as a function of the injection bias. The total number of injected charges is maintained across the data by varying the injection duration. The linear scaling suggest that the nonlocal dissociation is a one electron process at both 1.8 V and 2.0 V. (c) Attenuation as a function of the distance from the injection site, showing an exponential decay in the manipulation probability with increasing distance.

exponentially with distance from the injection site r, $R \propto \exp(-r/\lambda)$, with a length scale λ of approximately 6 nm at both an injection bias of 1.8 V and 2.2 V (figure 3-5c). Maksymovich et al. note that whilst the Au(111) surface has an available unoccupied surface state at 1.5 eV, the observed threshold voltage of approximately 1.4 V suggests this is not clearly the nonlocal transport state.

After cleaving, the new surface of crystalline materials contains a number of unsaturated dangling bonds into the vacuum. In metals, the strongly delocalised electron gas usually results in little distortion in the general structure of the surface compared to the bulk in the majority of cases [67, 68]; that is, the surface relaxes with atoms displaced from the bulk position but no change in, for example, surface periodicity. However in certain metals and semiconductors the cleaved surface system is especially energetically unfavourable, and in many cases, results in a large rearrangement of the surface into a lower energy state. This process results in a marked difference in the electronic structure of a number of surfaces compared to the bulk material, even if compared with the theoretical state of an unreconstructed surface [68], leading to the presence of clearly defined surface states which decay exponentially perpendicular to the surface. Depending on the distribution of the dangling bonds of the reconstruction, certain reconstructed semiconductor surfaces result in surface states with free electron like properties. These surface states allow for long range transport of the injected hot charge carriers, and thereby nonlocal manipulation effects.

An example of nonlocal manipulation through a reconstructed semiconductor surface is the reversible hopping of a bistable hydrogen atom between neighbouring adatom sites on the Si(100)-2×1:H surface at 5 K induced by nonlocal charge injection [66], visible in figure 3-6. Desorbing the H atom from a single adatom site results in a clear bright spot due to the increased LDOS of the unsaturated dangling bond, and allows for the neighbouring H atom to transition between the two sites in the same dimer. Bellec et al. demonstrate that this transition can be induced both by local and nonlocal charge injection. In the former (figures 3-6d-e), the STM tip is positioned on top of the initial position of the H atom and a negative voltage is applied with the tip height feedback loop switched off. The H transition between the two available sites ("hopping") can then be observed as a discrete step in the tunnel current. In this manner it was shown that the yield of the hopping process per injected carrier is current independent and therefore a one electron process with a threshold voltage of approximately -2.4 V; a value corresponding to the energy of Si-Si bond surface states. This process is shown to be an extremely localised effect; with the tip positioned 0.3 nm away from the H atom, at the position of the exposed Si adatom, the hopping yield is reduced by a factor of

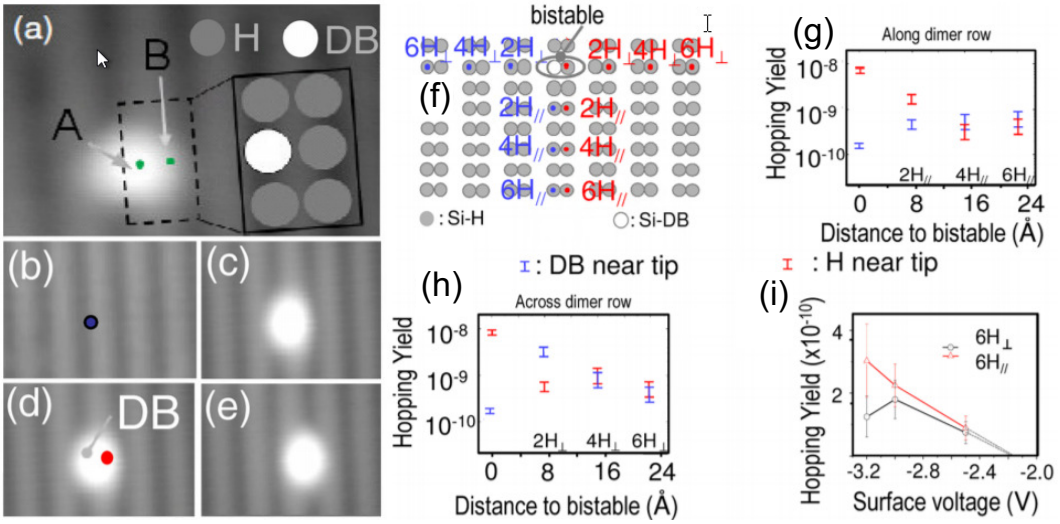

Figure 3-6: Nonlocal charge injection induced hopping of H atoms on the Si(100)-2×1 surface between neighbouring adatom sites [66]. (a) An STM image of the surface structure, with a bright unsaturated dangling bond (DB) at one site. (b-c) IET induced desorption of a single H atom, with a +2.5 V charge injection into the blue dot between images. (d-e) Local IET induced hopping. -2.5 V injection at the red dot, on top of the H occupied site of the dimer pair, here results in the movement of the H atom to the unoccupied site. (f) Positions of nonlocal injections to induce H hopping relative to the adatom sites. (g-h) Hopping yield per injected charge carrier along or across the dimer row. (i) Nonlocal hopping yield as a function of injection bias both along and across the dimer row.

40. This is explained as being due to a decrease in the available DOS between -2 and -3 eV at the position of the Si dangling bond compared to the Si-H bond.

Conversely, nonlocal manipulation was observed when the tip was initially positioned at distant Si-H sites (figure 3-6f) with a comparable yield both along and perpendicular to the dimer rows (figures 3-6g-h). In this case hopping could not be directly measured as steps in the tunnel current, instead only by imaging a change in the partially dehydrogenated dimer before and after injection. At neighbouring dimers the hopping yield was identified to be increased nearer the H occupied side of the manipulated dimer, whereas at more distant sites this effect was not seen. As with local injection, the hopping yield for nonlocal injection was observed to increase for biases more negative than the threshold bias of approximately -2.4 V (figure 3-6i). This suggests a similar electronic excitation process in both regimes, with the nonlocal manipulation relating to the transport of the injected charge carriers through the Si-Si bond surface state and the final manipulation step being shared.

Note, however, that in [66] the nonlocal manipulation was only measured over a radius up to 2.3 nm away from the injection site. This corresponds with an extremely short carrier lifetime within the surface transport state. In comparison, nonlocal manipulation on the Si(111)-7 × 7 and the Ge(001) surfaces have been observed to occur over much larger radii. Takagi et al. demonstrate the creation and annihilation of topological defects on the Ge(001)-$c(4\times2)$, figure 3-7a, and Ge(001)-$p(2\times2)$, figure 3-7b, surfaces due to STM injection at distances up to 100 nm from the injection site at 80 K [64, 69]. By scanning either surface at a controlled bias, defect pairs can be formed on a dimer row beneath the tip with the region between the defects defined by the alternate superstructure conformation [70] (positive sample bias above 0.8 V for -$p(2\times2)$ formation on a -$c(4\times2)$ surface and negative sample bias below -0.7 V for -$c(4\times2)$ formation on -$p(2\times2)$). Scanning at biases between the transformational values was not observed to affect the surface conformation. Charge injection into the surface distant to the defect region can then induce the one dimensional propagation or annihilation of the kink perpendicular to the dimer-row axis, depending on the injection bias and the local superstructure at the injection site, as can be seen in figure 3-7c. Both locally and nonlocally the defect formation process is suggested to be due to IET of the injected charge carriers, with the nonlocal manipulation mediated by hot charge transport in surface electronic states [64, 70].

Propagation of the injected charge carriers is additionally shown to vary between holes and electrons, with electrons undergoing a greater rate of relaxation and thereby a shorter length scale of the nonlocal effect perpendicular to the dimer-row axis, which is visible in figure 3-7d [69]. It is suggested that this is due to a large anisotropy observed in the electron surface transport state, with a strong dispersion in the dimer-row direction and little dispersion in the dimer-axis direction, resulting in stronger inelastic scattering perpendicular to the dimer-row axis by a factor of greater than 10 [64]. Conversely the hole transport surface state is nearly isotropic, and only a factor 2 difference in the manipulation between the two axes is observed, figure 3-7e.

For electron injection at low current ($<$ 2 nA) the rate of motion of the kink (i.e. here transformation from -$c(4\times2)$ to -$p(2\times2)$) is shown to be linearly dependent on the current, visible in figure 3-8a, thereby suggesting the transition between the two conformation states is a one electron process [70]. At these low currents, the rate of decay of the vibrational excited state at 80 K is much faster than the excitation rate and so a vibrational ladder climbing effect is not observed [71]. However at greatly increased currents ($>$ 100 nA) an additional multiple electron pathway is introduced, even at injection biases below the previous threshold values, with each individual injection

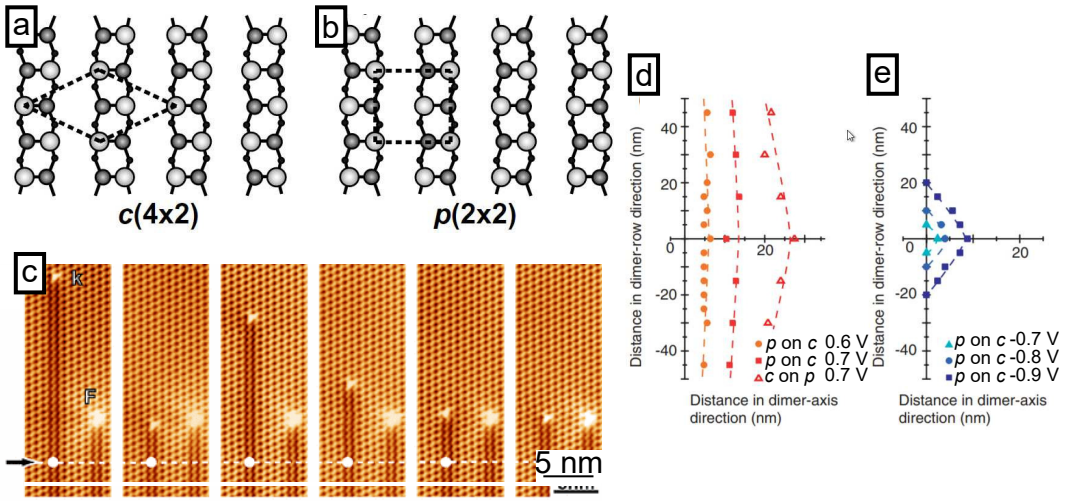

Figure 3-7: (a-b) A schematic model of the Ge(001) surface structure in the buckled dimer model [70], with the larger, lighter atom in the figures geometrically above the darker atom, in the two observed configurations. (c) STM images of the same -$p(2\times2)$ kink on a -$c(4\times2)$ surface between charge injections with varying bias located at the white marks on the dashed white line [69]. The right defect-fixed kink was used as a reference point. (d-e) Distance from the injection site at which the probability of kink motion is 0.5 at positive (d) and negative (e) surface bias [64].

exciting a vibrational state of the system as in figure 3-1b [72]. At sufficient current this alternate pathway results in the excitation of a dimer rocking mode between the two potential superstructures akin to a local temperature increase to above 250 K. After the bias pulse, the local system rapidly cools to below the rocking mode threshold thus potentially leaving a kink in the surface, visible in figures 3-8c-d. Unlike the previous one electron process, this structure transition pathway does not have a preferential direction of kink expansion which, in figure 3-8, results in a distributed web of -$c(4\times2)$ surface structure. As before these kinks act as scattering sites for electrons in the surface transport state, and thereby the radius of the nonlocal effect is limited to a maximum range of approximately 10 nm for both axes in the increased current regime.

Hence the rate and length scale of nonlocal manipulation across these surfaces is shown to be strongly dependent on the structure of the surface itself, alongside the characteristics of the injected charges. Through measurement of both the distribution (in chapter 8) and result (in chapter 9) of nonlocal manipulation, in this thesis we aim to further isolate the charge transport step. By allowing for more direct measurement of the hot charge dynamics within the surface, we aim to provide a route to the direct control of nonlocal manipulation through the engineering of surface properties. While the above local and nonlocal manipulation examples are generally limited to cryogenic

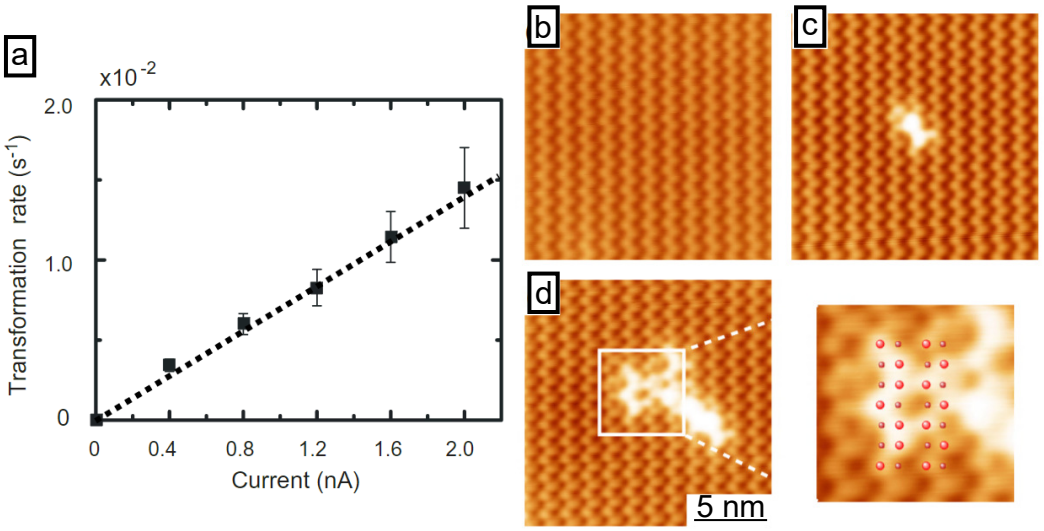

Figure 3-8: (a) The rate of configuration switching from -$c(4 \times 2)$ to -$p(2 \times 2)$, induced by scanning a pure -$c(4 \times 2)$ surface at a surface bias of -0.8 V, as a function of the tunnel current [70]. (b-d) STM images of a -$p(2 \times 2)$ surface after an injection of 1 s duration at the centre of the image; (b) 0.5 V at 80 nA, (c) 1.6 V at 180 nA, (d) 1.6 V at 560 nA [72].

temperatures, and the stability and control this affords, in this thesis we use a room temperature system. Hence we show that through nonlocal manipulation experiments, surface properties can be determined in the unfavourable conditions more reminiscent of real-world applications.

Chapter 4

Benzene derivatives on Si(111)-7×7

The primary surface of interest within the atomic manipulation group at the University of Bath is the the 7×7 reconstruction of Si cleaved along the (111) plane. This Si surface has been extensively studied in terms of the spatial and electronic structure, molecular adsorption and desorption, and, key to this thesis, hot charge transport. In this section the surface is introduced in more detail, with a focus on the electronic structure that allows for the nonlocal IET induced manipulation of adsorbed benzene derivatives, which forms the experimental work of the later sections. Additionally, the choice of adsorbate molecule is discussed. While previous work within the group has used benzene, chlorobenzene or toluene, in this thesis experiments are primarily performed with bromobenzene.

4.1 The Si(111)-7×7 reconstructed surface

The arrangement and properties of the Si(111)-7 × 7 surface are well described by the Dimer Adatom Stacking fault (DAS) model first proposed by Takayanagi et al. [73] and developed from, among a large body of other work, the STM images shown in figure 2-1 [13]. In this model, which is visible in figure 4-1, each surface unit cell consists of 12 adatoms in the top layer, 6 restatoms in the second layer, and 9 dimers and an unoccupied corner hole site at each corner in the third layer. The system can be further differentiated into two triangular half unit cells separated by dimers, one unfaulted and one faulted, with the adatom and restatom sites evenly and symmetrically distributed between the two halves. In the faulted half a stacking fault exists between the second and third layers which results in a misalignment between the faulted surface and the bulk structure. This reconstruction reduces the number of dangling bonds post-cleaving, with each adatom saturating three atoms in the restatom layer. In the top three layers of the supercell there are 102 atoms (12 adatoms, 42 atoms in the restatom layer and 48 atoms in the third layer), yet only 19 dangling bonds (12 at adatoms, 6 at restatoms and one at the corner hole) compared to the one-per-surface-atom in the unreconstructed 1 × 1 surface. Note, however, that the 7 × 7 reconstruction alters the position of atoms many layers into the surface and not merely the top few layers [74].

Despite the semiconducting nature of bulk silicon, the Si(111)-7 × 7 surface has metallic conductive properties [75]. During the reconstruction, charge transfer occurs between the adatoms and underlying surface atoms, with the 12 adatoms donating 7 electrons and saturating the otherwise half-filled orbitals of the 6 restatoms and the corner hole site of each unit cell [76,77]. This results in 5 valence electrons remaining in the adatom orbitals, which are responsible for a metal-like adatom band. In figure 4-2 the metallic adatom surface state, U_1/S_1, can be observed to straddle the Fermi level. The partial occupation of this surface state leads to the Fermi level of the surface being pinned at 0.65 eV above the valence band maximum for both p- and n- type Si, for all but extreme doping [78, 79]. The 0.65 eV value is within the 1.1 eV bandgap of the underlying bulk silicon, which means the surface states are well decoupled from the substrate [80, 81]. Both the physical position and the metallic nature of the adatoms lead to the well defined and bright signal observed when imaging the 7 × 7 reconstruction with the STM at low positive bias (i.e. tunnelling of electrons from the tip into the unoccupied surface state near the Fermi level).

In figure 4-2, three surface resonances are displayed in addition to the metallic state U_1/S_1 localised to the adatom dangling bonds. It should be noted that whilst sur-

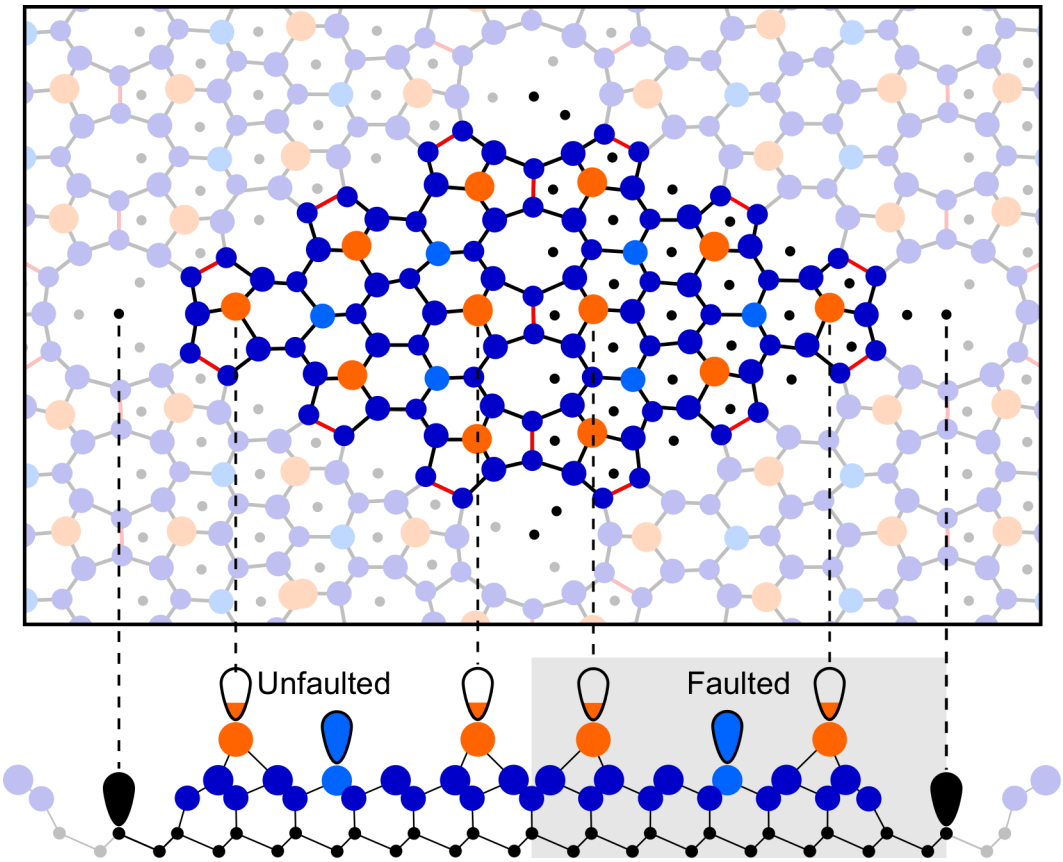

Figure 4-1: Atom arrangement in the Dimer-Adatom-Stacking fault (DAS) model of the Si(111)-7 $\times$ 7 reconstructed surface. In both images the central highlighted section contains a single unit cell, surrounded by (red) dimer bonds between atoms in the third layer. (Top) A top down view of the surface, with the decreasing height of each atom indicated by decreasing circle size. (Bottom) A cross-sectional view through the longest diagonal of the unit cell. Unsaturated dangling bonds are located at the adatoms (orange circles), whilst saturated dangling bonds are located at restatom sites (light blue) and corner holes. In the faulted half of the unit cell, the (black) bulk atoms are misaligned with the higher (blue) surface atoms and can be seen in the top-down view.

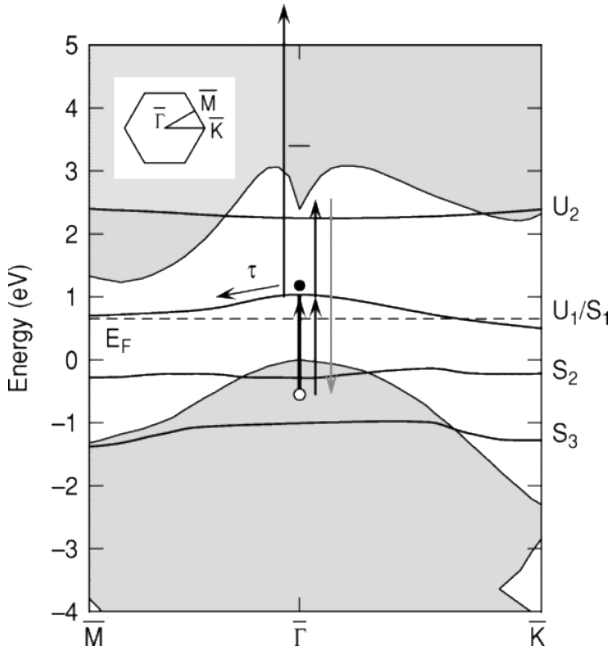

Figure 4-2: The electronic structure of the Si(111)-7 × 7 reconstruction, in comparison to the projected bulk bands (shaded areas). S_x and U_x refer to occupied and unoccupied surface states respectively. The dashed line E_F labels the energy at which the Fermi level of the surface is pinned due to the presence of the metallic adatom surface state U_1/S_1 with respect to the bulk valence band maximum. The Brillouin zone (top left inset) refers to the unit cell of an unreconstructed Si(111) surface. From [81].

face states formally refer exclusively to electron states located entirely within the bulk band gap, in this thesis the term is additionally used to refer to the metastable surface resonances that overlap with underlying bulk states [48]. The fully occupied S_2 state at approximately -0.8 eV from the Fermi level relates to the saturated dangling bonds of the surface restatoms [82, 83]. Additional states, namely the occupied S_3 and unoccupied U_2 states in the figure, originate from Si-Si back-bonds between the adatoms and atoms in the restatom layer. By scanning at sufficient positive (or negative) bias, electrons (or holes) are able to tunnel from the tip into the higher energy unoccupied (occupied) states, thereby increasing the available LDOS. In STM images, however, due to the exponential dependence of the tip-sample separation on the tunnel current, the physically closer and electrically more prominent adatoms generally dominate the tunnelling signal [84]. Alternate surface states can however be directly observed using scanning tunnelling spectroscopy, in which each state can be discerned at the relevant energy level from the dI/dV spectra at a point on the surface [85].

At low positive biases the adatoms on both halves of the unit cell appear almost identically; this can be seen in figure 4-3a. In negative bias scans, however, the two half unit cells can be clearly discerned; with the faulted half brighter than the unfaulted half, figure 4-3b. Additionally, adatoms on each half unit cell can be further differentiated into two categories depending on their position within the cell [86]. Those nearest the corner holes are deemed corner sites and those between corner sites are middle sites, as labelled in figure 4-3c , with the corner hole sites appearing brighter in negative bias STM images. Therefore, in the analysis of this thesis, we consider a total of 4 distinct adatom sites within each unit cell; unfaulted corner (UC), unfaulted middle (UM), faulted corner (FC) and faulted middle (FM), along with the corner hole site.

4.2 Adsorption of small benzene derivatives

The adsorption of benzene and certain benzene derivatives, for example chlorobenzene and toluene, to the Si(111)-7×7 surface results in a stable chemisorbed structure which has been the focus of a large number of experimental and theoretical studies [87–98]. In the chemisorption process, which, other that a slight change in the binding energy [99], is almost identical across a range of aromatic molecules [100–102], the cyclical ring is broken with the adsorbing molecule forming Si-C covalent bonds between either side of the phenyl ring and an adjacent adatom-restatom pair on the surface. This results in a 2,5-cyclohexadiene-like, di-σ bonded bridge structure, with the bridging molecule in a "butterfly-like" configuration with 2 carbon atoms in each "wing" [90] as visible in figure 4-4b-c . For toluene and chlorobenzene, the molecule chemisorbs preferentially

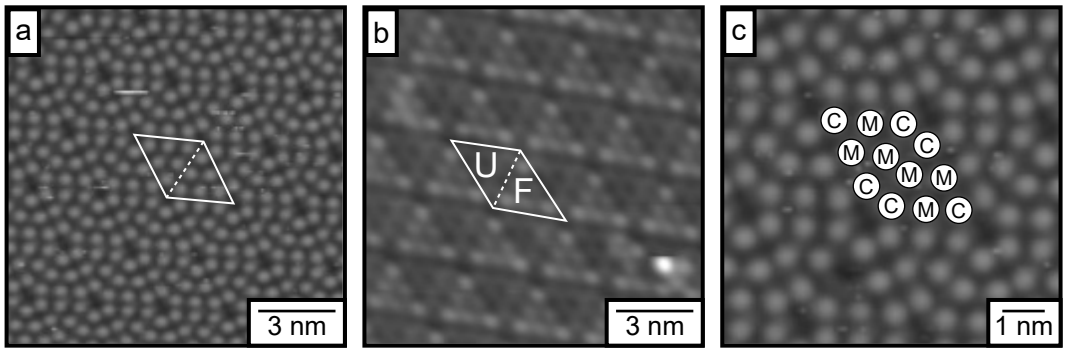

Figure 4-3: Si(111)-7 × 7 surface images at 100 pA and (a,c) 1 V or (b) -1 V bias. The white outline in (a,b) indicates a single unit cell, with the two halves separated by the dashed line. In (b) the two halves of the unit cell are differentiable; at negative bias the faulted half of the unit cell (F) appears brighter than the unfaulted half (U). In (c) the middle (M) and corner (C) adatom sites are labelled.

with the additional functional group (i.e. CH_3 and Cl respectively) positioned at the adatom-side of the surface.

During the chemisorption process the dangling bond of the involved surface adatom is saturated while the overall structure of the surface is not affected. Additionally, the bridging molecule does not have an electronic state near the Fermi energy of the system [104]. Hence, when imaging a dosed surface using an STM, the overall -7 × 7 structure remains, however individual adatom sites appear to be missing with the dark sites indicating the presence of an adsorbate molecule, as in figure 4-4d. At higher positive biases, depending on the tip-apex state, electronic states of the adsorbates may be imaged as bright regions along the axis of the molecule. This technique allows for further characterisation of the adsorbate species [103,105], as demonstrated in figure 4-4e. The chemisorbed state has a long lifetime, with benzene molecules retaining a fixed position on the surface for upwards of 2000 s at room temperature [89], which allows for the tracking of individual molecules on the surface across multiple STM images.

After exposure of the surface to adsorbate molecules, the probability of a site becoming occupied is not homogeneous. Instead, faulted sites are preferentially occupied, and within each half of the unit cell the middle sites are somewhat preferred over the corner sites [89]. Chemisorption is a local mechanism, with molecules binding directly to the surface beneath, such that chemisorption immediately after the initial surface-adsorbate interaction results in a relatively random distribution [88]. Here, however, each adsorbate molecule initially enters a weakly bound physisorbed precursor state

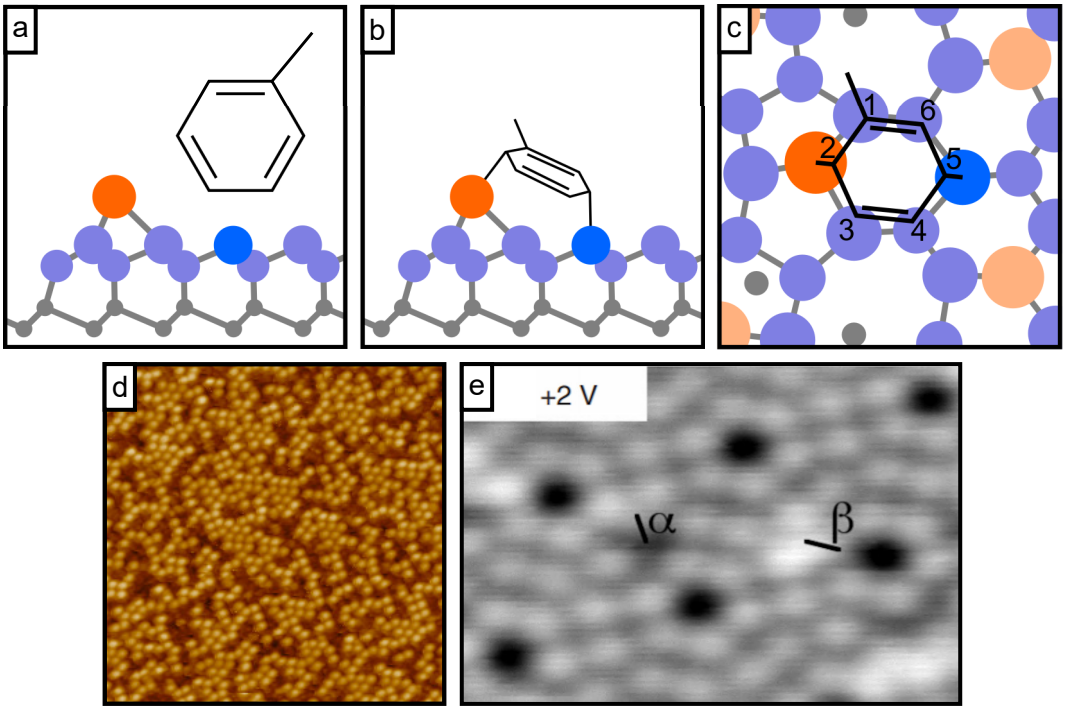

Figure 4-4: (a) A diagram of the chemical structure of toluene, consisting of a benzene ring with an additional CH_3 group, and the undosed Si(111)-7 × 7 surface as in figure 4-1. (b-c) Side and top view of the di-σ bonding configuration of chemisorbed toluene. (d) A 25×25 nm STM image (1 V, 100 pA) of the Si(111)-7 × 7 surface dosed with toluene, such that the adatoms at adsorbate sites (e.g., the bright orange adatom in (b-c)) appear dark. (e) From [103]. An increased bias (2 V, 50 pA) 6×4 nm STM image of chlorobenzene dosed Si(111)-7×7, such that the orientation of the chemisorbed chlorobenzene molecules (with α bonded to a middle adatom and β to a corner adatom) can be observed.

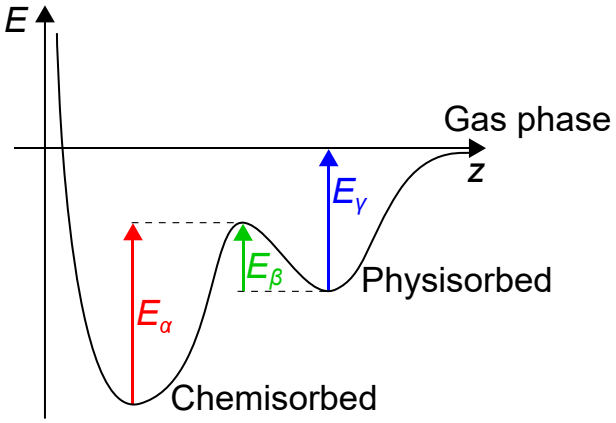

Figure 4-5: A sketch of the potential energy surface E as a function of the distance z from the surface for the bound states of an aromatic molecule on Si(111)-7 $\times$ 7. The molecule is able to transition, for example, from the chemisorbed state to the physisorbed state by overcoming an energy barrier E_α.

[88,106]. The potential energy surface of a molecule across the available states is shown in figure 4-5. While the chemisorbed state is stable and immobile, the physisorbed state is not, and molecules are able to translate across the surface. Prior to chemisorption the adsorbates will randomly explore the potential landscape of the surface, with a lower barrier to transition corresponding to a greater probability of chemisorption and the observed difference in the site-specific coverage.

In the physisorbed state the molecule is attracted to the surface merely by a weak van der Waals attraction [68]. The lifetime of the precursor state at room temperature is extremely short, of the order of 100 ps [107], however at low temperatures molecules within the physisorbed state are much less likely to overcome the energy barrier to either chemisorption or desorption and can be observed in STM images [106]. At higher surface coverage, the distribution of chemisorption is additionally limited by the number of restatom binding sites available within each half unit cell; with a maximum occupancy primarily constrained by the three restatom sites. As a result heavily dosed surfaces will have a more even distribution across the available sites; in fact, the unfaulted half unit cell is rarely observed to be occupied at low surface concentration [89].

Chemisorbed molecules may also transition from the chemisorbed state to the physisorbed state upon achieving sufficient energy to overcome the transition barrier. This energy may be provided by a variety of mechanisms; including thermally, in which case the rate is temperature dependent [108], by electronic excitation via the inelastic decay of a hot charge carrier, photoexciation [109], or through a combination of excitation mechanisms [110, 111]. Upon excitation and subsequent breaking of the

two covalent Si-C bonds via a DIET process [7, 102] the molecules will, as in the initial adsorption process, exist in the physisorbed state with a short, temperature-dependent lifetime. Again, in this state the molecules are free to move laterally across the surface, and will eventually either desorb from the surface entirely, entering the gas phase, or re-chemisorb at a new adatom-restatom site. Molecules diffusing via the physisorbed state have been measured to have an average diffusion length of 2.3 nm prior to re-chemisorption, however in 24 % of occasions the diffusing molecule transitions only to a neighbouring site [89].

4.3 Local and nonlocal manipulation on Si(111)-7×7

IET induced desorption of benzene derivatives may be induced, as discussed in section 3.1, via charge injection from the STM, a process which has been extensively studied within the atomic manipulation group at the University of Bath. In this case, the inelastic tunnelling of a charge carrier from the STM tip or the decay of a hot charge carrier after transport through a surface state, results in manipulation of surface molecules. While the former mechanism results in the manipulation being constrained to molecules directly within the tunnel junction, the latter mechanism allows molecules many nanometers from the tip to be manipulated, the results of which are shown in figure 4-6. The final manipulation process for both local and nonlocal manipulation are identical [9], which is discussed in more detail in section 9.4, such that the only observable distinctions between the two mechanisms are the distribution of manipulation and the requisite injection parameters for manipulation to occur.

Local manipulation experiments allow for the direct measurement of manipulation characteristics. By injecting from directly above a molecule, the charge carrier can interact with the target adsorbate without needing to access a surface state within which it can travel. The injected carrier is therefore not required to be at a sufficient energy to enter such a state, only that it has sufficient energy to induce manipulation. In this case, the manipulation thresholds are expected to depend primarily on the final manipulation step itself. While electron injection induced local manipulation of toluene on this surface occurs above a threshold bias of +1.4 V [9], nonlocal manipulation is measured to occur only above approximately +2.0 V for either chlorobenzene [7, 102] or toluene [11]. Only local manipulation is observed for injections between +1.4 V and +2.0 V. Charge carriers with energy below the local threshold do not have sufficient energy to induce manipulation upon interaction with an adsorbate.

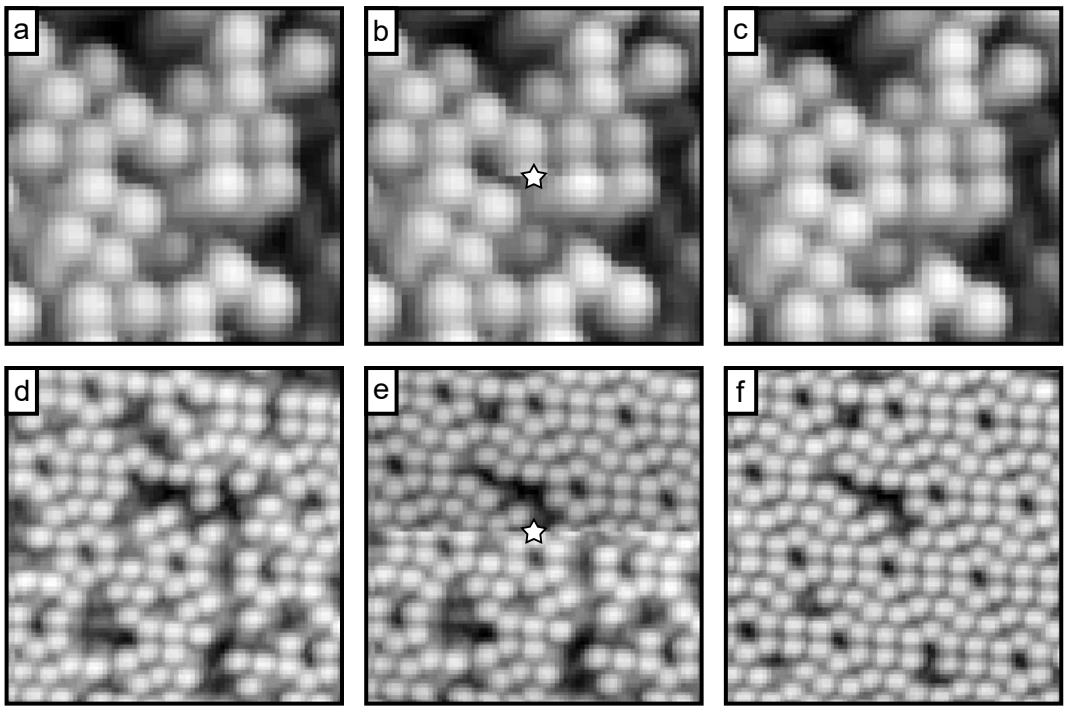

Figure 4-6: Manipulation of bromobenzene on Si(111)-7 × 7 via STM charge injection into the position of the star in (b) and (e). (a-c) 5×5 nm STM images before (a), during (b) and after (c) local manipulation with injection at -1.3 V, 5 pA. (d-e) 10×10 nm STM images surrounding nonlocal manipulation at -1.6 V, 900 pA. Images from results presented in chapter 8

Within each surface state the length scale of nonlocal manipulation is voltage invariant, with charge carriers undergoing an ultrafast decay to the bottom of the state prior to diffusion [8, 95]. For electron injection, the nonlocal manipulation threshold is greater than the unoccupied back-bond surface state U_2 at +1.6 V above the Fermi level in figure 4-2; the lowest lying surface state above the local manipulation threshold. The measured threshold instead corresponds to charge transport through an adatom back-bond surface resonance primarily located at the corner holes and restatom sites at approximately +2.0 V [7] (labelled for consistency as U_3 in, e.g., reference [11]). The energy level of this resonance has been identified using both scanning tunnelling spectroscopy [9] and two-photon photoemission spectroscopy [112]. Above a second threshold at +2.7 V the length scale and probability of nonlocal manipulation increases, which has been linked to the onset of (U_4 [11]) bands within the bulk structure [95].

Similarly, hole injection mediated nonlocal manipulation occurs above a threshold bias of -1.2 V, although the length scale and probability of manipulation dramatically increase above -1.6 V. These values correspond to the onset of the S_3 back-bond surface state with a peak at -1.6 V, and the onset of the S_4 state with a peak at -2.2 V respectively [8, 96, 102]. Regardless of the injected charge carrier or injection bias, nonlocal manipulation is isotropic and neither grain boundaries nor steps affect the distribution of manipulation [7].

For electron injection, both local and nonlocal desorption have been shown to be one-electron DIET processes, such that the injection current is independent of the manipulation probability per injected charge carrier, as described by equation (3.2) [6, 12, 52]. For hole injection, however, the rate of manipulation of a local molecule is only observed to linearly depend on the injection current at low current. Instead, for increased current (e.g. in [12] above approximately 10 pA for a -1.3 V injection) the rate of manipulation appears to plateau [12]. The presence of the tip near the molecule provides an additional pathway for the excited state of the molecule to decay through, reducing the excited state lifetime and, thereby, the manipulation probability [12]. As the injection current is increased, the tip will approach the surface according to the principles of quantum tunnelling, and the magnitude of the tip-molecule overlap state will increase accordingly. This additional pathway does not affect the DIET or DIMET characteristics of the interaction, and the manipulation process itself is expected to remain a one-election DIET process, as observed for low-current injections, despite the change in manipulation probability with varying injection current.

In 2PPE, an initial pump laser excites electrons from the valence band of the surface, before incidence of a second, delayed probe laser results in the emission of photoelec-

trons. By measuring the kinetic energy of the emitted electrons, alongside knowledge of the work function of the surface and the energy of the lasers, the exact energy of the electron in the excited surface state can be measured. In energy-resolved 2PPE the energy of the pump laser is varied such that the excited electron will occupy different surface states, whereas in time-resolved 2PPE the separation between the pump and probe is altered, from which the lifetime of excited states can be determined. Within a range of pump energies (+3.60 to +3.80 eV), on Si(111)-7 $\times$ 7 there is an immediate ($\sim$ 40 fs [81, 113]) relaxation of the excited charge to the bottom of the surface state (identified as U_2 in reference [112]) measured at 1.94 ± 0.15 eV [112]. The similarity between this energy level and the +2.0 V threshold for nonlocal electron-injection mediated manipulation suggests that this is the same charge transport state for such manipulation [95]. The lifetime of the hot charge prior to relaxation towards the bottom of the surface transport state has also been inferred from STM manipulation experiments [8], which are discussed in more detail in section 8.4. Here, manipulation due to the injection of holes between -1.2 and -2.3 V into the S_3 (above -1.6 V) or S_4 (-1.6 V and below) surface states were determined to occur following an initial 10 fs ballistic transport period. Using 2PPE the lifetime of a hot charge carrier within the transport state, prior to the excited charge relaxing into a lower energy state, can also be measured. Ichibayashi et al. show the transition to occur with a timescale of 180 fs for hot electrons, before diffusely scattering into the conduction band minimum at +0.5 eV [113]. This state is well below the +1.4 eV threshold to manipulation, and hence after relaxation charge carriers are unable to induce manipulation.

While the chemisorption process occurs without dissociation of the adsorbate for small benzene derivatives at the aforementioned biases, upon excitation with higher energy charge carriers the molecule has been observed to dissociate, leaving clear, bright adsorbate species neighbouring dark, occupied adatoms in subsequent STM images [52, 92]. Unlike the desorption processes, this has a nonlinear dependence on the injection current suggesting a DIMET process. For example, dissociation of chlorobenzene at +3 V results in a two electron process ($n = 1.8 \pm 0.3$) [52].

Chapter 5

Achieving atomic-resolution STM images

STM imaging is extremely sensitive to the tip-sample junction. Both the macroscopic and microscopic structure of the tip will greatly affect the resultant images; atomic-resolution is only achievable with a high quality tip. Even when atoms can be discerned, unstable or otherwise improper tips can prevent reliable experimentation or correct analysis of results. Samples must form the correct reconstructed surface, whilst being free of defects and other contaminants which may prevent imaging, damage the tip, or result in incorrect statistics. Production and transfer into vacuum can take up to several days, which means that trial and error testing of new components is an extremely inefficient process. Hence it is important to be able to reliably manufacture high quality components.

In this chapter, experimental techniques necessary for the production of components used in our STM are described. This includes the preparation and transfer of Si(111)-7×7 surfaces into vacuum, as well as the daily cleaning, adsorbate dosing procedure, and a brief discussion of surface quality. Additionally, the in-house STM tip manufacturing process is described, including the initial ex-vacuo electrochemical etching as well as further tip cleaning and techniques to improve the quality of the STM images. The general process for sample and tip production as well as dosing is identical to that used previously [7], however here it is described in detail.

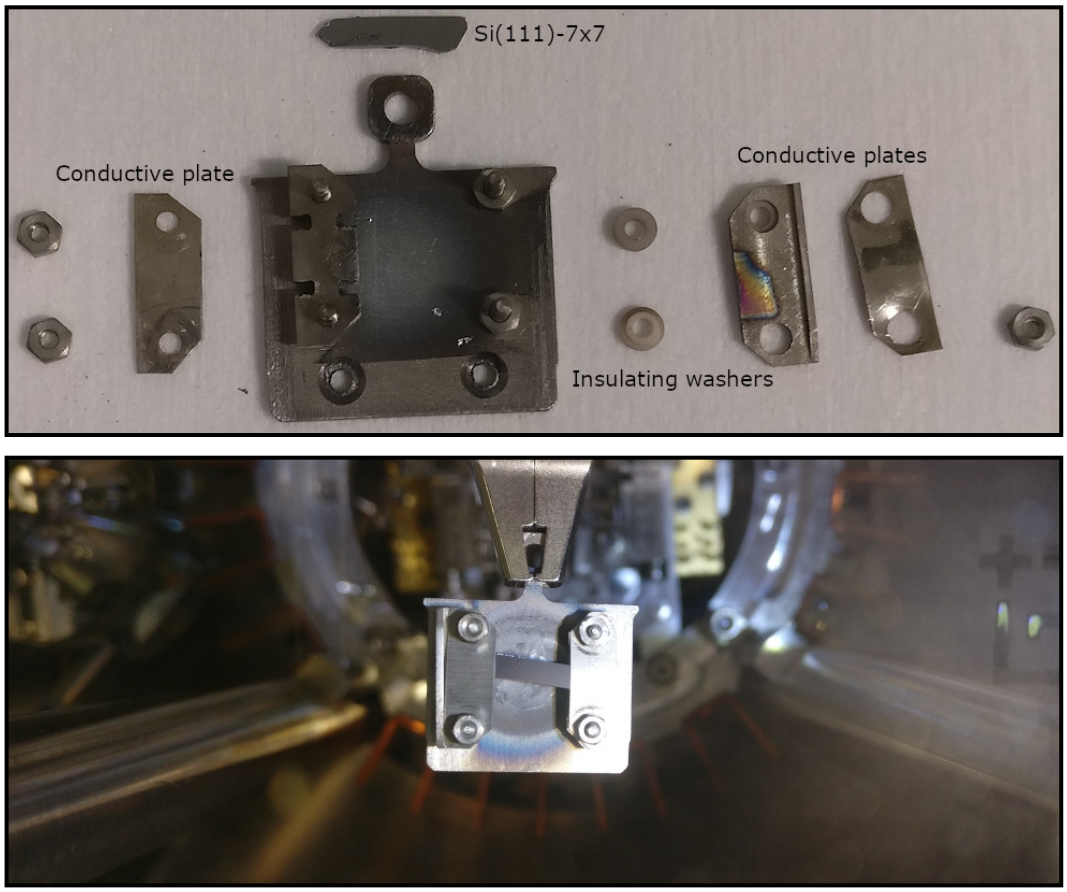

Figure 5-1: (Top) A deconstructed sample holder. The Si sample is mounted such that one side (left in images) is electrically connected to the Ta base plate, whilst the right side is disconnected from the plate via ceramic washers. (Bottom) Assembled sample holder inside the STM chamber. The Si(111)-7×7 crystal bridges the gap between the two sides, such that a current can flow across the crystal by applying a voltage between the base plate and the conductive plate on the right-hand side.

5.1 Sample preparation

In this thesis Si(111)-7×7 samples (n-type, phosphorous doped, 0.001-0.002 Ωcm from Pi-KEM) were used as the surface of interest. Prior to use, the samples were cleaned, mounted and degassed in order to ensure a clean surface able to be imaged in the STM. Initially outside of the vacuum chamber, individual pre-cut Si(111)-7×7 crystals are cleaned with isopropanol before being mounted on a sample holder, shown in figure 5-1.

It is important to note that tools or components coming into contact with the sample cannot be steel, instead tantalum sample holders and molybdenum or plastic tools,

cleaned via sonication for several minutes in an isopropanol bath, are used. The reason for this is that small quantities of nickel can result in an extreme restructuring of the surface due to long range bonding between subsurface Ni atoms and first-, second-, or third-nearest neighbour Si adatoms [114]. This results in a transition from the 7×7 reconstruction to an altered $\sqrt{19} \times \sqrt{19}$ nickel silicide surface at the high annealing temperatures required for a clean 7×7 surface [115]. Additionally, due to the high diffusion coefficient of Ni in bulk Si, further attempts to thermally clean the crystal will only promote diffusion of surface Ni into the bulk, resulting in nanoscale islands of nickel silicide [116].

The sample holder is structured to allow a current to be passed through the sample, allowing direct, resistive heating of the sample within the vacuum chamber. This is achieved by isolating the sample from the holder-base via ceramic washers, only presenting a bridge between two metallic contacts through the sample as shown in figure 5-1. To ensure electrical connection with the contacts and isolation from the base-plate, the resistance across the sample is tested prior to being placed in vacuum, with an expected value of approximately 4 Ω.

The sample is introduced to the ultra-high vacuum in two stages. Initially it is placed into the load-lock at atmospheric pressure, where it is pumped by a roughing pump backed turbomolecular pump to a pressure of approximately 1×10^{-6} mbar. Then it is transferred, via the transfer arm, to the ultra-high vacuum prep chamber where it is positioned in the sample heating stage. This stage is connected to an external power supply and sample heating is controlled via an automated LabVIEW program.

As a result of being out of vacuum, both the sample and the sample plate will contain contaminants that must be degassed prior to scanning. This is achieved by an initial long duration, (relatively) low temperature heating, to a maximum temperature of approximately 660°C, sufficient to enhance the Arrhenius rate of desorption of contaminants from the surface (primarily water vapour), whilst below the melting point of the passivating SiO_2 layer [117]. To limit the increase in the pressure of the system, this initial baking is performed in several stages with the current through the sample increased periodically as the pressure of the prep chamber reduces towards approximately 10^{-9} mbar. The maximum current during baking is determined by measuring the temperature of the sample during the bake with an optical pyrometer, which is calibrated to the emissivity of Si ($\approx$0.65 at 600°C [118]). Once the temperature is calibrated the sample is left to bake for several hours until the pressure plateaus.

To obtain an imageable surface, the sample must then be heated briefly ("flashed") from room temperature to temperatures sufficient to remove surface contaminants (N_2, He, H, etc.) but for a duration short enough to prevent the surface from melting. Flashes to a surface temperature of approximately 1200°C, as measured on an optical pyrometer, for 10 s are used here. Once this higher current is calibrated, a new sample is then flashed approximately 20 times to remove the contaminants, waiting for the sample to cool between each flash. Finally, to promote the formation of large areas of the 7×7 reconstruction, the sample is annealed from 960°C. During the flashing process the valve between the STM chamber and the prep chamber is shut to prevent contamination of the STM by material released from the sample.

In ultra-high vacuum the formation of the oxide layer occurs very slowly, however over time it will form. As such, a shortened version of the flashing-annealing routine is repeated daily, with fewer flashes used to prevent undue strain on the crystal which can result in the formation of defects [119]. The same sample heating LabVIEW program is used to control this process and an example is shown in figure 5-2. Occasionally during this process the pressure in the chamber will increase dramatically due to the release of gasses from the sample. If the pressure increases above a set level, usually set to 1×10^{-9} mbar, the heating current is immediately switched off and that specific flash is discounted and is repeated once the sample has cooled. After the daily flashing, the surface is transferred from the heating stage in the prep chamber to the STM head using the wobble stick.

Assuming the sample is not visibly melted, for example as shown in figure 5-3d, the quality of the surface and the flashing and reconstruction currents must then be verified by imaging the surface. A sufficiently usable sample should have large areas of clean Si(111)-7×7, with few dark sites or defects. Several examples of good and bad surfaces are shown in figure 5-3. There are, in essence, three courses of action for a poor surface. If, for example, the undosed surface is covered in a large number of dark sites, roughly more than 0.1 per unit cell (figure 5-3b), this is likely to be the result of an insufficient flashing temperature leading to contaminants remaining on the surface after flashing. In this case the sample flashing currents should be recalibrated using the optical pyrometer, and the flashing process repeated. If, however, there are an unusable number of steps on the surface (figure 5-3c), no amount of additional flashing will reduce the issue and the sample must be replaced. Finally, if the surface scan does not result in a clear Si(111)-7×7 surface, this could either be a serious issue with the surface or the tip. Due to the nature of STM it is usually unclear which is the issue, and it is possible either or both could be the cause.

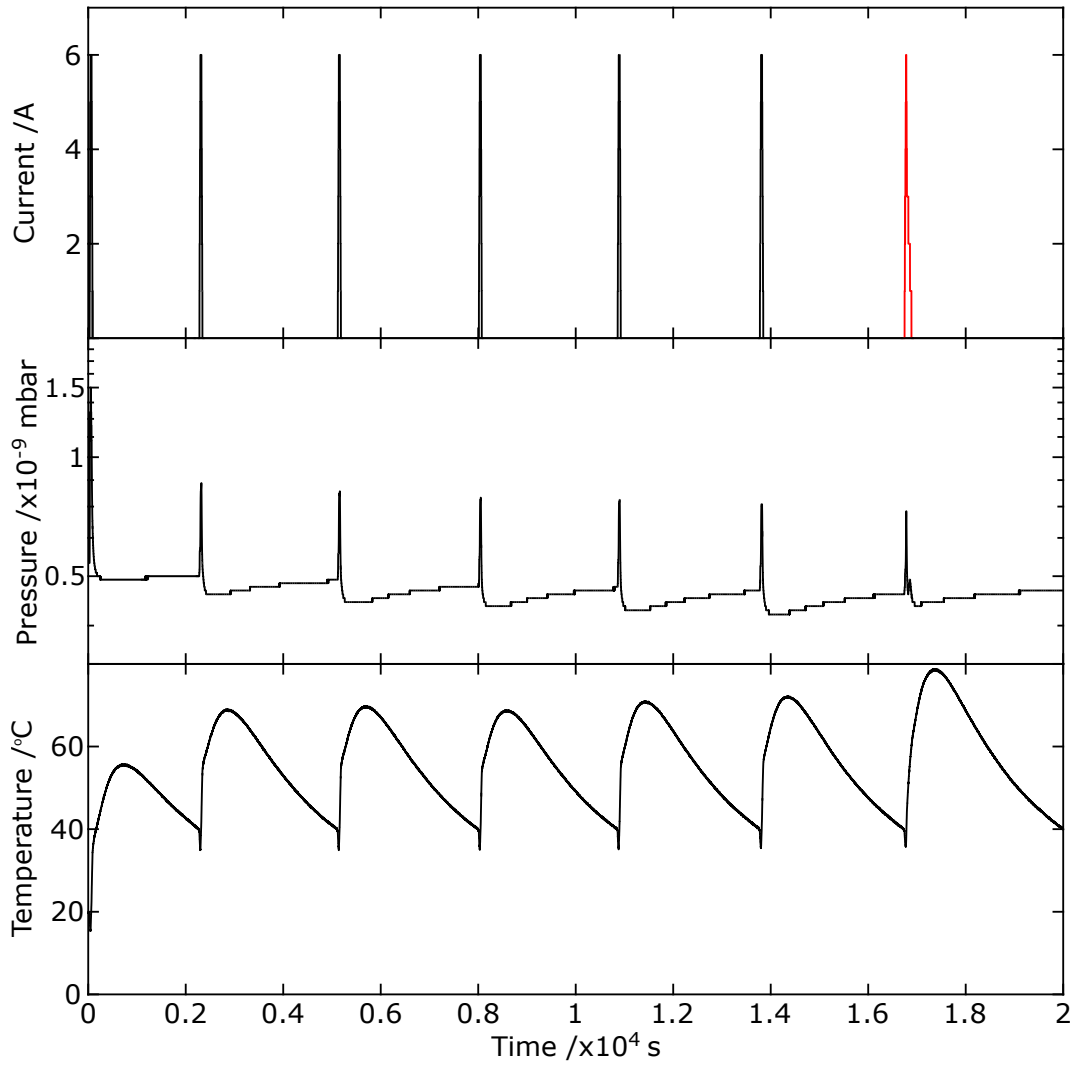

Figure 5-2: (Top) The current applied through the Si crystal during the flashing and annealing processes. Each flash here (black) consists of a 5.9 A 10 s pulse, heating the crystal to approximately 1200°C. In the final annealing pulse (red in top figure), after the flash the current is slowly stepped down from 3.4 A. (Middle) The pressure in the prep chamber during the same flashing process. If the pressure during a flash increases above a set value, here 1×10^{-9} mbar, the flash will be aborted and repeated. In this case, this has occurred for the first flash pulse. (Bottom) The temperature of the heating stage directly adjacent to the crystal. After each flash the LabVIEW program waits for the measured temperature to drop below 40°C before beginning the subsequent flash.

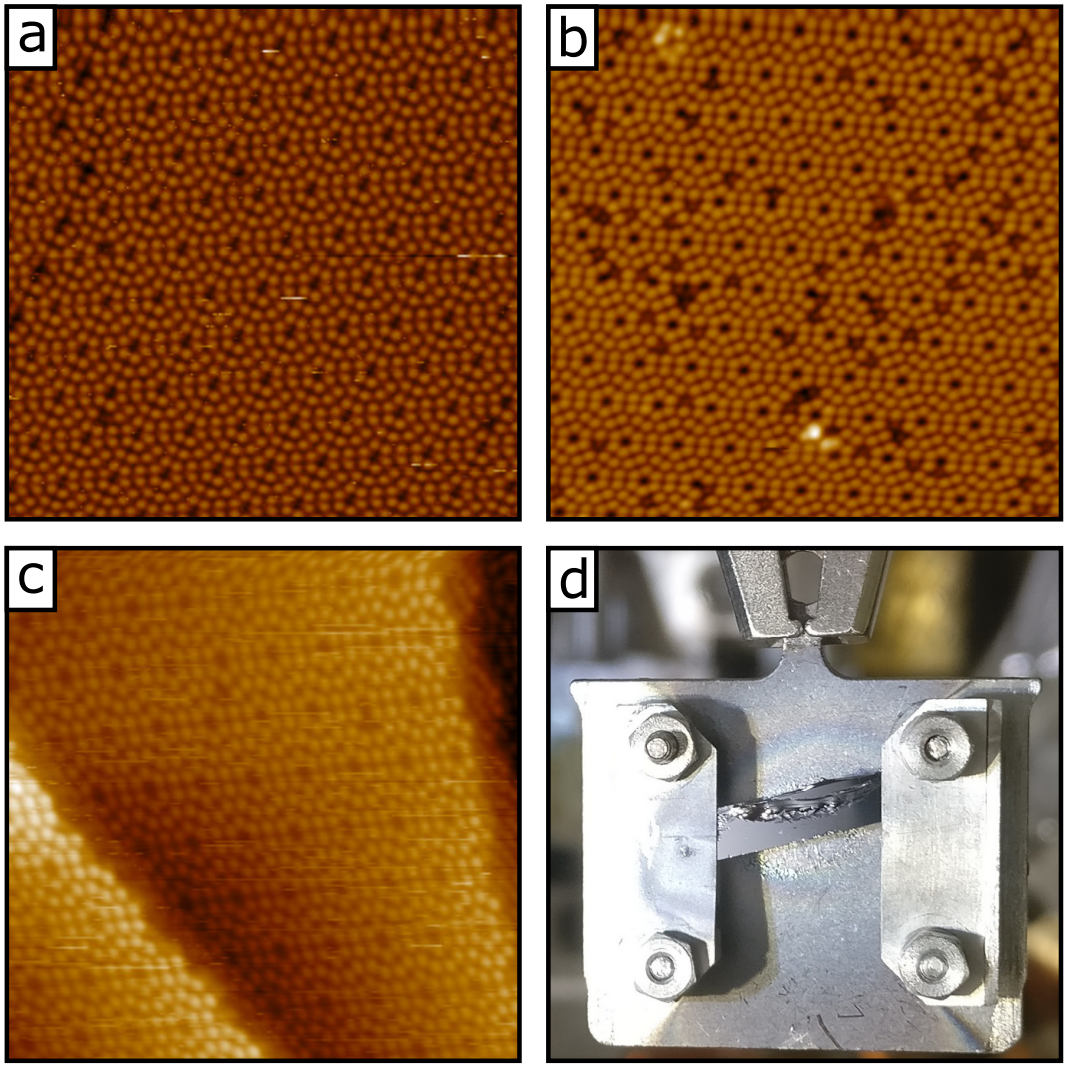

Figure 5-3: (a-c) Examples of 25×25 nm STM images of a Si(111)-7×7 surface after the calibration process. (a) A correctly calibrated sample, such that the underlying Si(111)-7×7 reconstruction is visible with only a small portion of sites occupied by contaminants. (b) An incorrectly calibrated surface, such that after the flashing process an increased proportion of sites are occupied. (c) A sample with a high step density. (d) A photograph of a partially melted sample.

5.2 Tip preparation

The resolution of an STM is ultimately limited by the tip [120]. A "good" tip allows for reproducible STM imaging at a variety of biases without discrete changes in the tunnel current, whereas imaging with a "bad" tip varies between instability and complete lack of tunnelling. The quality of the tip is defined by both the macroscale structure and the microscale apex. At the microscale, a theoretically perfect STM tip consists of a radially symmetrical taper leading to a single-atom point which acts as the dominant source of the tunnel current. An overly blunt apex (low aspect ratio) results in the contribution of multiple atoms on the tunnel current, and so corrugations on the STM image appear indistinct. In comparison an overly long apex (high aspect ratio) results in macroscopic issues, such as increased vibrations of the apex offsetting any improvement in scan quality.

A rudimentary STM tip can be quickly and easily manufactured from a wire using nothing more than wire cutters and brute force, however tips from this approach vary dramatically in quality. Transferring anything from atmosphere to vacuum is not a quick process and repeatedly opening the UHV chamber to higher pressures negatively affects the quality of the vacuum. Rather than attempting scanning with a large number of simple tips, instead a more reliable manufacturing process is used; this is described below.

The probes used in this thesis are produced from 99.95% pure tungsten wire with a diameter of 0.25 mm. While several different conductive materials can be used, W is an extremely hard and mechanically stiff material and as such is a perfect candidate. W, however, forms a surface oxide layer and so W tips cannot be used outside of a vacuum chamber. This layer must be removed before scanning by an additional annealing process otherwise the insulating layer effectively blunts the tip to the tunnel current, preventing good quality STM images and possibly resulting in crashing the tip.

5.2.1 Electrochemical etching

The initial production of atomically sharp apex tips from the W rods here consists of an electrochemical etching process described by Ibe et al. [29], an outline of which is shown in figure 5-4. A cut section of wire is lowered into 2 M NaOH solution in the centre of an Au ring and a 9 V bias is applied between the wire anode and the Au ring

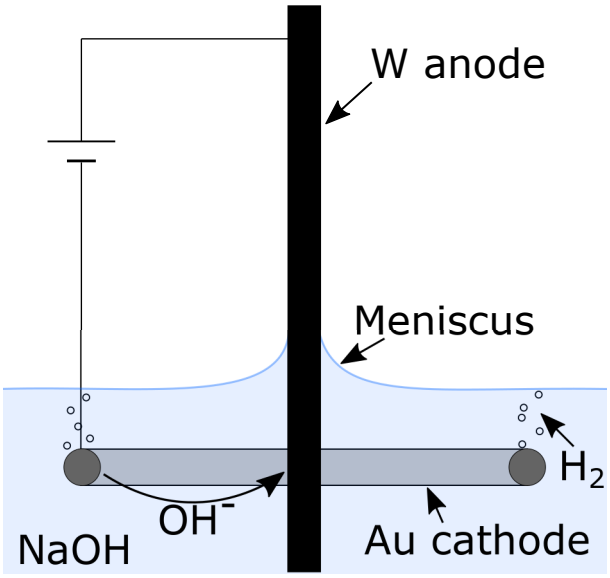

Figure 5-4: An overview of the etching process used in the formation of W tips for STM. The Au cathode consists of an unbroken ring suspended in the NaOH solution surrounding the W anode, submerged by several millimetres.

cathode. This results in a series of chemical reactions,

$$6\,H_2O + 6\,e^- \longrightarrow 3\,H_2(g) + 6\,OH^- \textbf{ (cathode)} \tag{5.1}$$

$$W(s) + 8\,OH^- \longrightarrow WO_4{}^{2-} + 4\,H_2O + 6\,e^- \textbf{ (anode)} \tag{5.2}$$

$$W(s) + 2\,H_2O + 2\,OH^- \longrightarrow WO_4{}^{2-} + 3\,H_2(g) \textbf{ (overall)}, \tag{5.3}$$

in which the reduction of water molecules results in H_2 gas visible as bubbles in the solution from the Au ring. The primary outcome of these reactions is the oxidation of the solid W rod to tungstate ions, resulting in the rod beneath the surface of the NaOH being etched away.

The surface tension of the NaOH solution results in the formation of a meniscus around the W rod. It is the shape of the meniscus that controls the resultant shape of the etched tip. Within the meniscus the concentration of hydroxide ions is lower as the ions are attracted towards the anode, and so the rate of etching is increasingly reduced higher up the meniscus. In figure 5-5a it can be observed that the rate of etching is also reduced further beneath the surface. This is both due to a similar concentration gradient of hydroxide ions, W nearer the cathode will be etched faster, but also to a protective layer of sinking, denser tungstate ions shielding the bottom end of the rod [29]. After sufficient etching, the weight of the lower section will overcome the

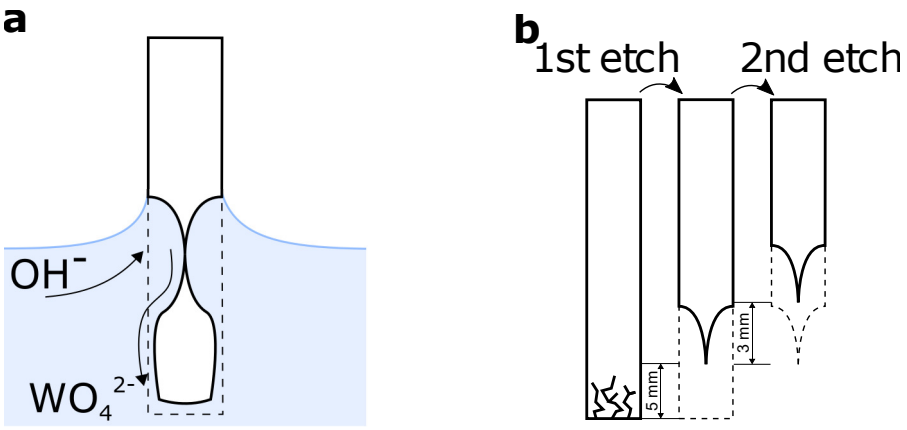

Figure 5-5: (a) A diagram of the W rod during the etching process, prior to the drop off of the lower section. The tungstate ions produced during the etching reaction sink, insulating the lower W and reducing the rate of the etching reaction beneath the Au ring. (b) The overall etching process consists of two individual etching steps, the first of which removes a damaged section of the rod, while the second results in the tip.

tensile strength of the rod at the thinnest point of the neck and the lower section will drop off, leaving the tip above. Here we repeat the etching step as shown in figure 5-5b, the first etch removing the mechanically damaged portion of the wire due to being cut with wire cutters and the second etch producing the tip.

The etching process will not automatically stop after the drop of the lower section, and further etching will only serve to blunt the tip. However, the drop-off results in the reduction of the effective size of the anode and, correspondingly, a reduction in the current through the circuit. The current through the circuit is measured and when a step change to below a threshold value, initially set to 4 mA, is observed the bias is stopped. An example of the measured current during etching is shown in figure 5-6. This cut off time strongly relates to the quality of the tip [29], and so this process is automated using a LabVIEW program connected to a nanosecond-response solid state transistor switch. Correctly setting this cut off threshold is important to producing high quality STM tips.

The complete etching process is described here. To reduce contamination, prior to etching the W rods as well as all tools are cleaned via sonication in an isopropanol bath for several minutes. A W rod is cut to length, including the additional length that will be lost due to drop-offs, and is attached to a tip holder allowing for manual height adjustment. The rod is then lowered towards the centre of the Au ring submerged by several millimetres in 2 M NaOH solution. Using the position at which a meniscus first forms as the zero point, the tip is then lowered into the solution. On the first

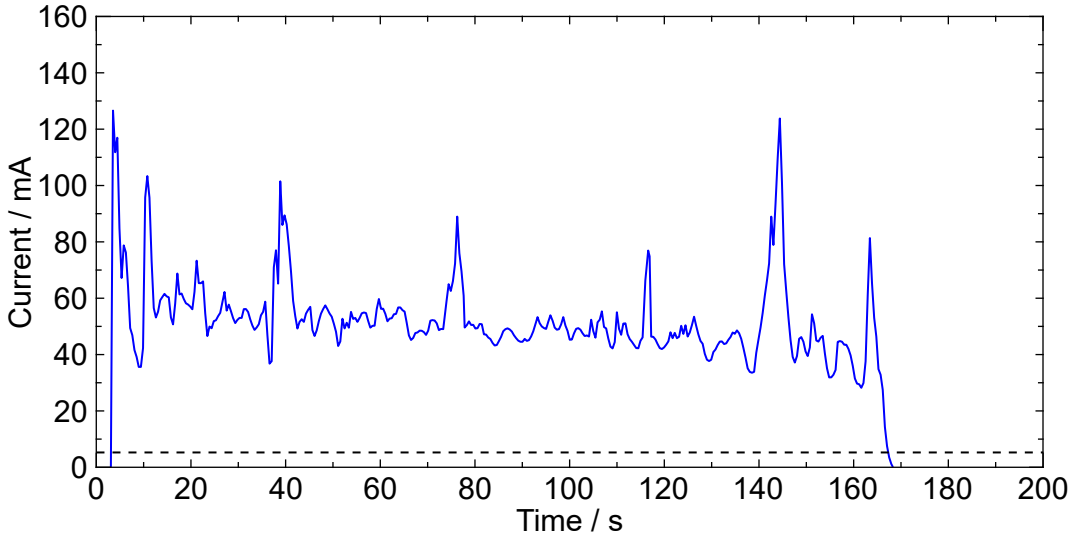

Figure 5-6: An example of the current through the tip during etching. The black dashed line corresponds to the cutoff current, indicating the current (here 4 mA) at which the etching process is automatically stopped.

etch it is lowered by 5 mm, whilst on the second etch it is lowered by 3 mm. Using a LabVIEW program control system, a bias of 9 V is then applied between the W rod and the Au ring, beginning the etching process. The current through the circuit is monitored and when it falls below a set threshold, initially 4 mA, the bias is turned off causing the etch to stop. If the drop-off did not occur, or occurred and the bias did not stop, the threshold current can be altered. After the first etch is complete, the tip is raised, rinsed in isopropanol, and re-submerged to the requisite depth and the second etch begins. After etching the aspect ratio of the tip is inspected using an optical microscope and visually-sharp tips are then stored tip-up in foam.

The resulting shape and quality of the tip is controlled by a number of factors; the rate of etching, the amount of submerged W, as well as the general conditions of the process will each affect the produced tips and so must be controlled. The rate of etching is clearly visible by the rate of H_2 bubbles released from the cathode, and can be controlled by adjusting the bias to the circuit. An etch that is too slow results in overly long tips, whilst a fast etch leads to short or irregularly shaped tips. The depth of the wire essentially controls the mass of the section beneath the resultant tip. The more wire submerged, the greater the mass and the earlier the neck will break. In this case break that is too slow will again lead to long tips, whilst a break that is too quick results in blunt tips as well as a large force on the apex during the drop-off, potentially damaging the apex. Finally, vibrations during etching can cause changes

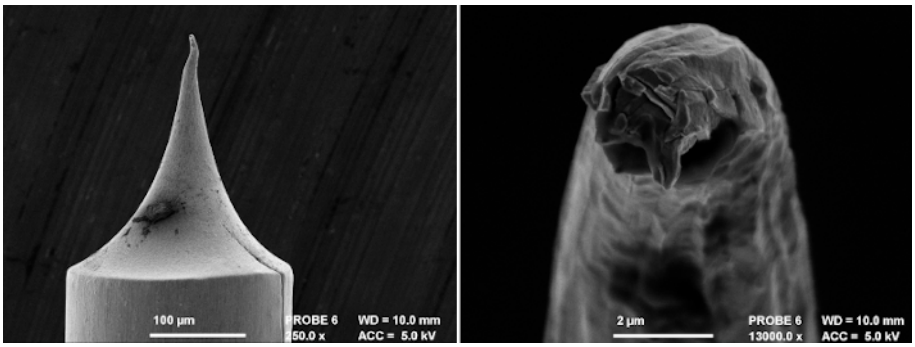

Figure 5-7: Scanning electron microscope images of a W tip manufactured using the drop-off method. In (left) the taper of the apex is clearly visible, showing a good aspect ratio. Images produced by Dr Rusimova.

in the position of the meniscus on the wire, which can result in stepped or otherwise uneven tips. This vibration is reduced by encasing the etching station in foam which acts to damp external mechanical vibrations.

Tips produced using this method have previously been imaged using a scanning electron microscope (SEM) in order to measure the aspect ratio of the apex as well as to check for any microscale faults. Examples of these images for one tip with a good macroscopic aspect ratio are shown in figure 5-7 . Additionally, by imaging the tip using transmission electron microscopy it has been shown that these tips usually have a tip-apex radius of the order of 10 nm [30], sufficient to achieve atomic scale resolution STM imaging.

While the above method produces high quality tips, several novel alterations have been documented. These novel techniques trade the relative speed and simplicity of the above method, either providing increased reliability or more control over the result. For example, Chang et al. [121] replace the constant etching bias with a pulsed DC bias. Between pulses the tungstate ions disperse, and so do not accumulate along the wire and the the protection of the lower section of the rod from etching is not observed. Beneath the meniscus etching occurs uniformly, and instead of the drop-off of the lower section the entire lower section is etched away. As a result the aspect ratio of the tip can be entirely controlled by the etching parameters. Alternatively, multi-step etching procedures have been suggested to offer unprecedented control over both the macroscopic and microscopic structure of the tips. Qin and Deng [122] use a method similar to the above drop-off process to produce tips to macroscopic aspect ratio specifications, however an additional lamellae drop-off etching process, in which the NaOH electrolyte is only a membrane within the cathode ring, provides additional control over the microscopic apex. In this second step, the length and therefore weight

of the lower section is minimal and so the drop off force is small. Additionally after drop-off the remaining tip will be electrically disconnected from the loop, and so etching will be automatically stopped. However, lamellae etching is an extremely challenging and previous in-house attempts were not successful.

5.2.2 Annealing

Immediately after etching, exposure of the bare W to air results in the formation of an insulating tungsten trioxide surface. This layer insulates the tip, inhibiting tunnelling and thereby STM images of the surface. Instead, prior to use, the oxide layer must be removed via sublimation of the surface layer. At high temperatures (approximately 1075°C), the WO_3 layer will react with the underlying W and sublimate as tungsten dioxide,

$$2\,WO_3(s) + W(s) \longrightarrow 3\,WO_2(g), \tag{5.4}$$

leaving a clean W surface. Additionally, heating the tip degasses it in addition to removing other surface contaminants.

To heat the tip and catalyse the above reaction the tip is connected to an electrical feedthrough as shown in figure 5-8. This feedthrough provides electrical connection to both the tip and a second pin, connected to a tungsten crossbar, which is in contact with the tip near the apex. This crossbar is much thicker than the tip, and so the resistance across it is lower. Upon passing a current across the feedthrough, the tip will be resistively heated. Prior to heating, the feedthrough is connected to the load-lock which is then pumped down to approximately $< 10^{-5}$ mbar. While the flashing process is automated using a LabVIEW program connected to the power supply, the exact temperatures reached are optically calibrated manually. To prevent overheating, the tip is initially heated in short (3 s) flashes at increasing currents and the temperature of the tip is estimated by observing the colour of the resulting incandescence. Once a moderately bright orange (at approximately 1200°C) is reached, the tip is flashed at that current 3 or 4 times to complete the sublimation of the oxide layer. The tip is then baked at a lower current, such that a dull red glow is observed (approximately 600°C), for 10 minutes to degas the tip and remove other contaminants.

At this point the load-lock is vented with N_2 to minimise oxidation and the tip is removed from the load-lock. With the tip once again exposed to the air, oxidation will begin anew, however the oxide layer forms slowly and so brief exposure will only result in an incomplete layer. The tip is then placed into a tip holder, the tube of which is crushed to hold the tip in place and provide a strong electrical contact with the STM

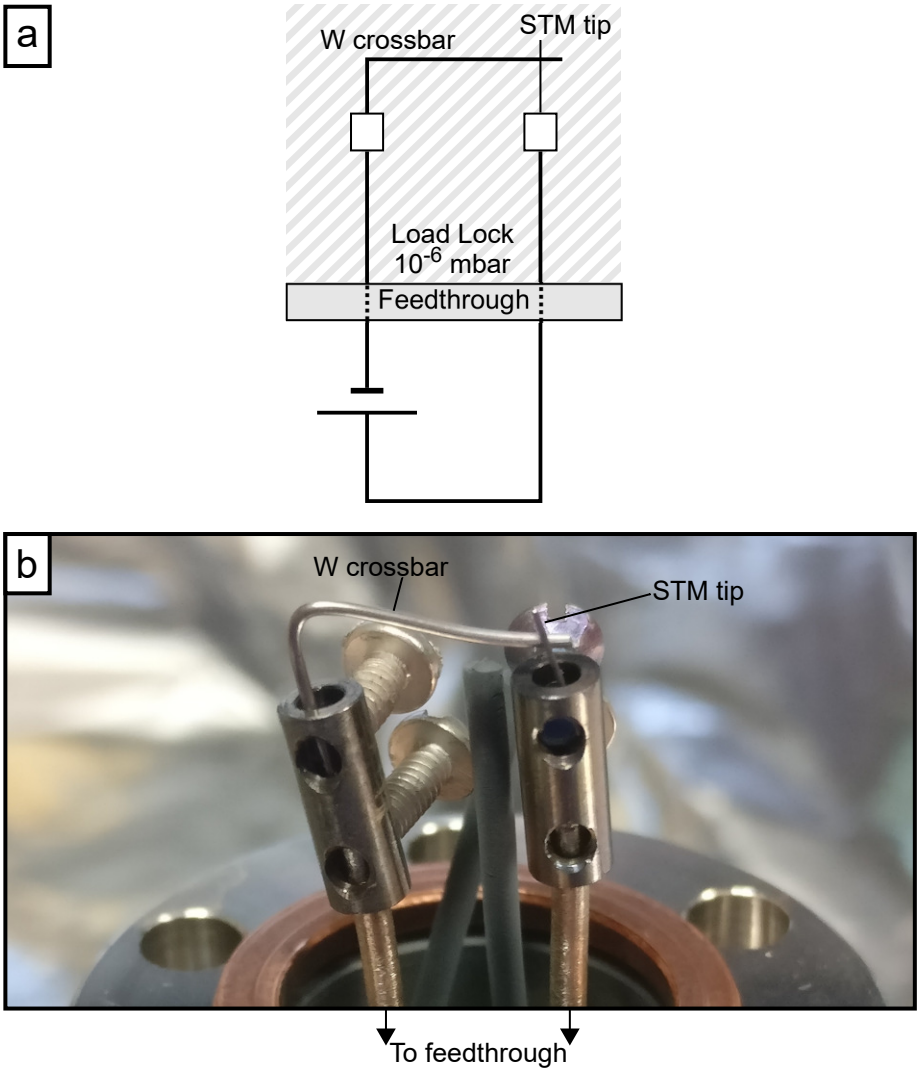

Figure 5-8: An STM tip in the load-lock flashing stage. The tip is in electrical contact with a thicker W crossbar, and connected via an electrical feedthrough to a power supply allowing a current to be passed through the tip. Prior to annealing, this stage is mounted in the load-lock, which can be pumped down to 1×10^{-6} mbar. (a) Diagram of the electrical circuit during flashing. (b) Photo of the flashing stage outside of the load-lock.

electronics. Finally, the tip holder is placed on a tip holder plate and transferred to the prep chamber of the STM in two stages, in the same manner as the Si sample discussed above.

To remove the small amount of oxide on the tip after the brief exposure, the tip is heated using the sample heating stage in the prep chamber. Unlike with sample heating or tip heating in the load-lock, the current is not passed directly through the tip. Instead, the plate behind the tip is resistively heated. The tip is heated only indirectly, and so cannot reach sufficiently high temperatures to chemically sublimate the oxide layer. This method can, however, act to degas the tip and plate, and reduces the quantity of contaminants dropped by the tip during scanning.

5.2.3 In vacuo tip fixing

While the initial etching stage is relatively quick, transferring tips into vacuum and the annealing processes are very time consuming. Tips are very fragile, which means that manually moving tips frequently results in a ruined apex. Additionally, achieving atomic-resolution can be difficult with new tips, as not all tips will have sufficient apex structure. For this reason, an important part of STM imaging involves in situ modifications of the tip structure via altering scan parameters to induce changes. A number of examples of STM images produced by bad tips are shown in figure 5-9. The main fixable categories of poor quality tips include unstable tips, tips with poor resolution, and "doubled" tips. Although tips with which no STM imaging is observed can potentially be fixed, it is unlikely, therefore more extreme measures will potentially be required.

Small changes to the tip apex structure can be induced to occur using short duration pulses at increased bias compared to the normal passive scan parameters of 1 V. Positive bias pulses, usually 3 to 4 V, are used in an attempt to remove W, Si or contaminants from the tip, dropping them on the surface or otherwise emitting them into the vacuum chamber. The presence of contaminants on the tip can either act as insulation, effectively blunting the tip and resulting in reduced resolution or otherwise incorrect imaging, or may drop off during scanning, resulting in an unstable tip as well as possibly imaged contaminants on the surface. In comparison, a negative bias pulse above the work function of Si, -3 to -4 V, attempts to rebuild the tip apex using surface Si atoms emitted from the surface due to the pulse. This can change the tunnelling site to a new apex, resulting in a new, potentially high resolution and stable tip. These small duration, low bias pulses generally only result in small changes in the apex structure. Longer duration pulses or pulses at increased bias can induce larger

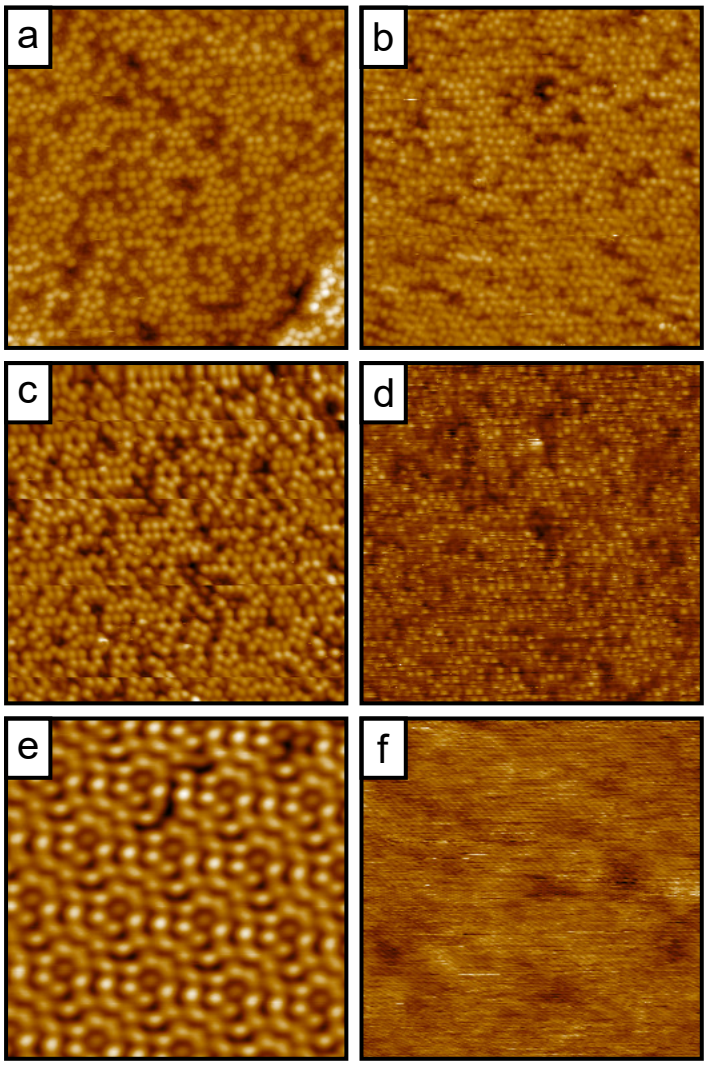

Figure 5-9: STM surface images (images a-d and f are 25 nm^2, e is 10 nm^2) taken with variable quality tips. (a) A good quality tip. (b) A doubled tip such that the tunnel current includes major contributions from multiple separate points on the tip apex. (c-d) An unstable tip. In (c) the tip state changes infrequently throughout the scan, whilst in (d) the tip state is changing rapidly resulting in a "scratchy" image. (e) A blunt tip resulting insufficient lateral resolution to clearly image individual atoms. (f) A poor tip such that the structure of the surface cannot be discerned.

changes, however these larger changes are more likely to lead to the loss of any previous resolution.

If a tip refuses to improve after some time spent pulsing, a final, extreme tip reconstruction attempt can be made by crashing the tip into the surface. This can be achieved either by changing the STM feedback loop to enter a "tapping" regime in which the tip will repeatedly contact the surface, reducing the STM bias through 0 V such that the tip will contact the surface in an attempt to achieve the requisite tunnel current, or by manually moving the tip towards the surface using the stepper motor. Each of these methods essentially culminates in the same result, albeit with increasing magnitude. In a successful tip-crash, upon retraction, surface atoms will be attached to the tip forming a new apex and thereby STM imaging. However, a crash will often result in a complete loss of the previous apex, and there is a good chance that the tip will be destroyed and must be replaced. Crashing the tip can also destroy a large area of the surface, which means that the scan area should be moved prior to further scanning to prevent contamination of the tip from the damaged area.

Tip fixing is not a deterministic process. Sometimes small changes in bias results in a complete change in the imaging characteristics of the tip, whereas on other occasions, long duration, high bias scans result in no change. Usually, it is best to start with small modifications and to slowly increase the intensity of the attempts. After each such attempt the tip quality is assessed by scanning at passive scanning parameters, and tip-fixing is repeated or escalated as deemed necessary. It is important to accept, however, when a tip is beyond fixing and must be replaced. In general, a good-quality STM tip is able to last for a long time. The majority of the data in this report was collected with a single tip, and previous tips on the same machine have lasted for several years. Anecdotally, the most common reason for the loss of a tip is human error, either via missetting scanning parameters or misjudging approach. In addition, high bias or otherwise more "extreme" experiments may also lead to the loss of the tip.

5.3 Tip-sample Approach

STM scanning requires a nanometre scale gap between the tip and the sample surface before a tunnel current can reasonably be measured. A mechanism by which the tunnel current can be established is therefore required prior to scanning. Initially, as in figure 5-10a, the tip and the sample are separated by approximately half a centimetre and a manual approach is performed where, using a coarse motor, the sample is moved towards the tip. This process is aided by a camera focused on the apex of the tip,

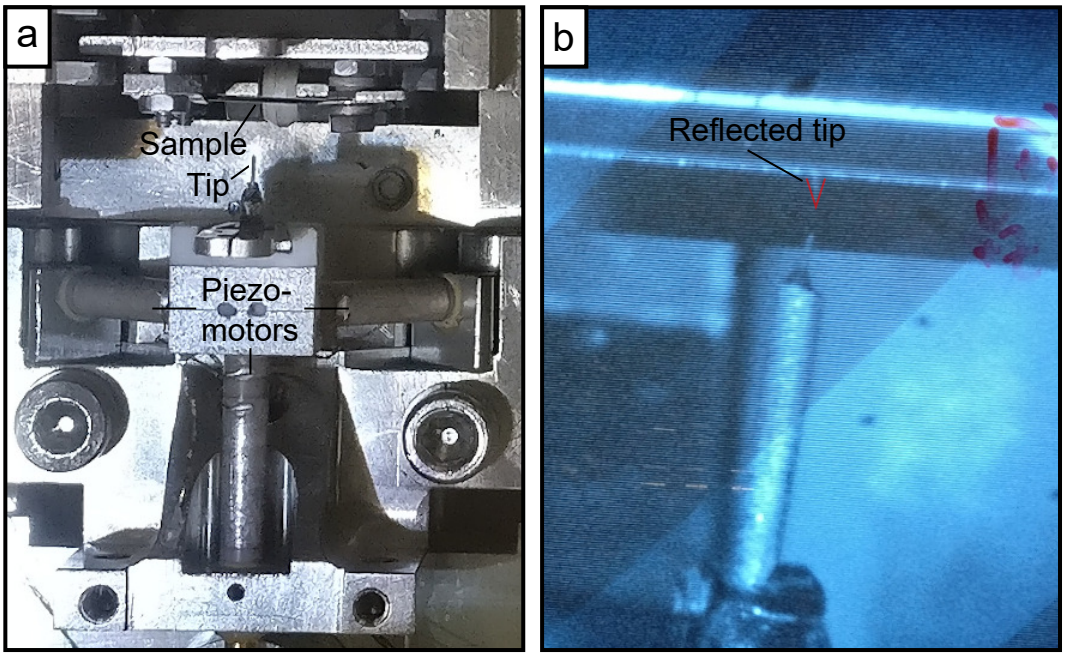

Figure 5-10: The tip-sample junction during the initial approach. (a) An image of the STM junction with the sample maximally retracted. At the bottom of the image the three piezo-motors are visible. (b) An image of the junction from the camera with the sample close to the tip. In the surface of the sample a reflection of the tip is visible. The separation of the tip and the surface can be estimated by the separation of the real tip and the reflected tip.

resulting in figure 5-10b. When the sample is close to the tip a reflection of the tip is visible on the surface of the sample, and this can be used to aid in estimating the tip-sample separation and when to cease the manual approach. However, the tip-sample separation will still be far greater than the required distance and so a further automated approach process is performed using the tip-positioning piezo-motors.

Piezo-motors only have a limited range of motion (in our case, $\approx 1\mu$m) due to the maximum expansion or contraction of the material. As a result, the automated approach process is separated into a fine approach using the piezo-motors and a coarse approach using the previous coarse motor. In the fine step, the piezo-motors are expanded from the fully contracted state, during which the tunnel current is measured and the approach is automatically stopped if a reasonable user-defined current is observed ($\approx$100 pA at a 3 V applied bias is generally used). Once the piezo is maximally expanded it is again fully retracted and the coarse motor completes one step towards the surface. The coarse motor has a step-size less than the range of the piezo-motor such that con-

tact with the surface will not occur. This process is then repeated until the set tunnel current is measured.

5.4 Noise

Both mechanical and electrical noise can influence the quality of STM imaging, either causing effects that are similar to an unstable tip shown in figure 5-9d, reducing resolution sufficiently to prevent imaging atoms at all, or even resulting in the tip contacting the surface. Mechanical noise results from the coupling of external vibrations to the Omicron STM1 STM head, leading to real oscillations in the displacement of the tip relative to the surface and thereby altering the tunnel current. Whereas for electrical noise, similar oscillations in the observed images are caused by capacitive coupling from electronics to the recorded signal prior to the preamplifier.

Mechanical noise is attenuated primarily by ensuring the isolation of the tip from external vibration sources. This is achieved in three different stages; isolation of the STM head itself, isolation of the whole STM body from the ground, and isolation of the ground from external effects. However each of these components interact to result in an improvement of the overall damping characteristics of the STM.

Our STM sits on a solid concrete surface on the lowest floor of the building, reducing any vibrations caused by building sway. Additionally, efforts are taken to prevent vibrations due to, for example, nearby water cooling systems or the movement of large items in the room whilst the STM is in operation. Isolation of the STM table from the ground is primarily achieved by supporting the six legs with elastomeric pads. The material used in these pads has a high damping coefficient, reducing mechanical vibrations via the dissipation of the energy to heat [123]. Finally, the isolation of the STM head whilst scanning is achieved primarily by suspending it on four springs, labelled in figure 5-11. Unlike the high resonant frequencies of the elastomeric pads under the STM and the metal components of the STM body, these springs have a low resonant frequency; which limits the efficiency of vibrational coupling between the body and the head. It should be noted that the metal springs have a low damping coefficient, acting only as a high-pass filter, and elastomeric damping cannot be used as the material is unable to withstand the increased temperatures during baking. For this reason a secondary eddy current damping system is used. This system consists of a ring of copper fins around the floating STM head, and a separate ring of permanent magnets attached to the STM body. When the head is suspended, the magnets and fins alternate such that the fins are themselves suspended within the resultant electric field. Movement of the

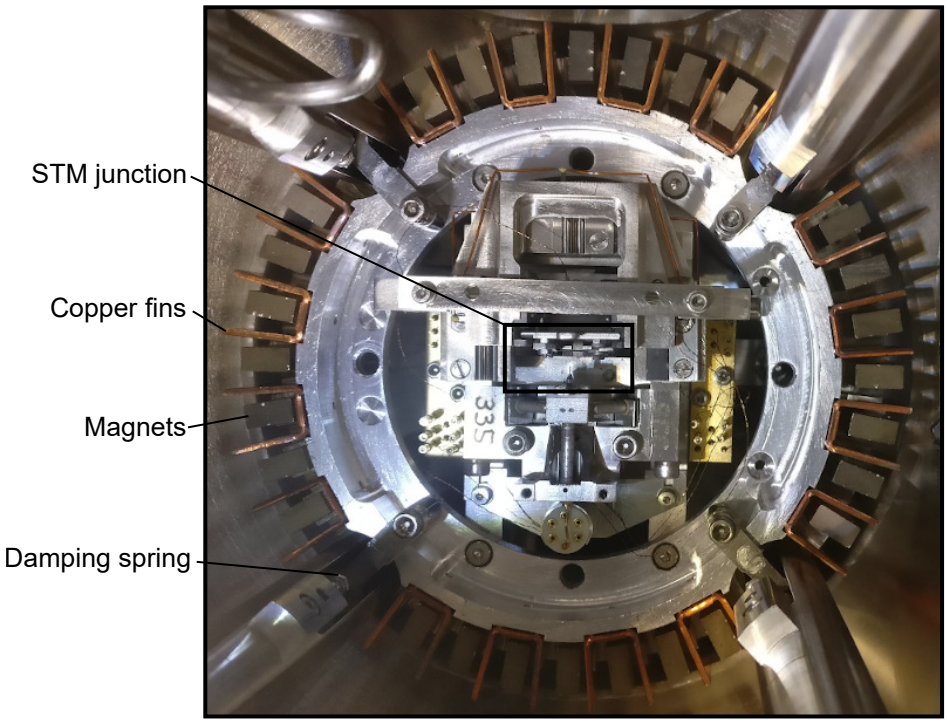

Figure 5-11: The Omicron STM 1 head during scanning, such that it is supported only by springs connected to the STM body. Copper fins attached to the head and permanent magnets attached to the frame provide additional eddy current damping.

head relative to the body results in the movement of the conducting fins relative to the magnetic field, and as a consequence the induction of a current in the fins. According to Lenz's law, this induction is associated with an electromotive force in the opposite direction to the initial motion, thereby counteracting the motion as a damping element.

As an important part of the mechanical vibration isolation occurs externally to the STM head, it is important that vibrations of the STM body itself are minimised. This essentially means that all efforts should be taken to ensure that the STM is not touched during operation. Even light taps of the frame can result in large movements of the STM head and can potentially result in crashing the tip. Additionally, it is important to ensure that any connected pumps are switched off, namely the roughing and turbomolecular pumps used to pump the load-lock, and the turbomolecular pump's water cooling is disconnected from the circulation.

The primary source of electrical noise is capacitive coupling from the standard 50 Hz mains supply. Even after reasonable attempts to reduce the magnitude of the electrical noise, characteristic peaks at multiples of 50 Hz can be observed in the spectrum in

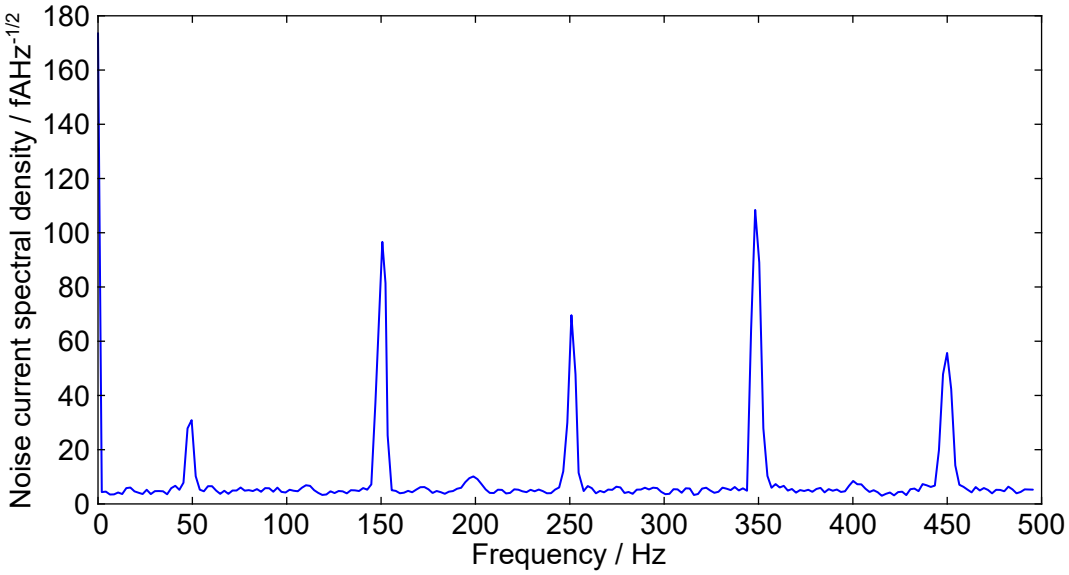

Figure 5-12: Noise spectral density of the grounded STM, with the tip retracted from the sample. Spectral peaks at multiples of 50 Hz indicate that the mains supply is the primary source of noise.

figure 5-12 whilst no other clear peaks are observed. As it is unlikely that mechanical vibrations result in peaks at exactly the same frequencies, this demonstrates that the dominant source of residual noise is electrical.

Electronic noise is reduced by ensuring that the system is fully grounded, with an isolated ground loop to prevent interference from other devices connected to the same ground. Prior to the preamplifier, the signal from the STM is extremely vulnerable to noise, with small noise signals equally being amplified. Care is, therefore, taken to minimise the opportunity for electrical signals to couple to the STM signal prior to the preamplifier by ensuring that the preamplifier is as close to the base of the STM as possible. After being amplified the signal is much less vulnerable to noise, however the cable from the preamplifier to the Nanonis SPM controller is shielded to reduce any interference. Finally, all electrical devices near or connected to the STM are turned off when not required during scanning.

5.5 Dosing

Experiments in this report study the distribution of toluene and bromobenzene (BrPh) molecules adsorped on the Si(111)-7×7 surface, however over time and during the daily flashing process these will be removed. For this reason, each day prior to scanning a

new layer of molecules must be produced. Furthermore, the surface density of these molecules must be relatively consistent and somewhat controlled. While small variation in the coverage is inevitable, too high coverage may result in the failure of the molecule-finding analysis software and too low coverage leads to insufficient statistics. Additionally, the effects of surface coverage on manipulation dynamics has not been fully investigated, and so should be controlled for.

To dose the surface, a valve between the prep chamber of the STM and a test tube containing liquid (e.g.) BrPh is opened. BrPh gas then flows down the connecting gas line into the prep chamber, where it is able to chemisorb onto the Si sample, dosing the surface. This process has been automated using a LabVIEW program, which controls the opening and shutting of a valve between the prep chamber and the gas line using a connected stepper motor, whilst measuring the pressure in the chamber. An example of the partial pressures of gases in the prep chamber during dosing, measured using a Hiden quadrupole mass spectrometer, is shown in figure 5-13. It should be noted, however, that during usual dosing, the total pressure within the prep chamber measured with an ion gauge is used as the relevant parameter. After the initial pressure spike caused by a release in gases from turning on the mass spectrometer, the pressures are initially constant until the motor opens the valve between the prep chamber and the gas line. Increases in the pressure then correspond to the BrPh gas entering the chamber, alongside other contaminant gases, and hence the exposure of the Si sample to the dosing gas can be estimated. Note that the log scale of the y-axis shows that the net increase in the pressure of BrPh in the chamber is much lower than the increase of the other gases.

The LabVIEW program minimises contamination of the chamber by limiting the maximum pressure in the chamber during the dosing process. When the pressure in the prep chamber increases above a set value (here set to 1×10^{-9} mbar) the stepper motor will begin to shut until the pressure decreases to below the threshold value at which point the valve is reopened. This feedback loop results in the oscillatory behaviour observed in figure 5-13. A relative measure of the total exposure can be measured and represented in Langmuirs, the product of the increase in total pressure within the prep chamber during dosing and the total exposure duration. For the nonlocal manipulation of chemisorbed bromobenzene experiments presented in this thesis, a dose of 2 L is used; this corresponds to a surface coverage of approximately 4 molecules per unit cell. Once the total measured exposure is greater than this value the valve will be shut, stopping further dosing.

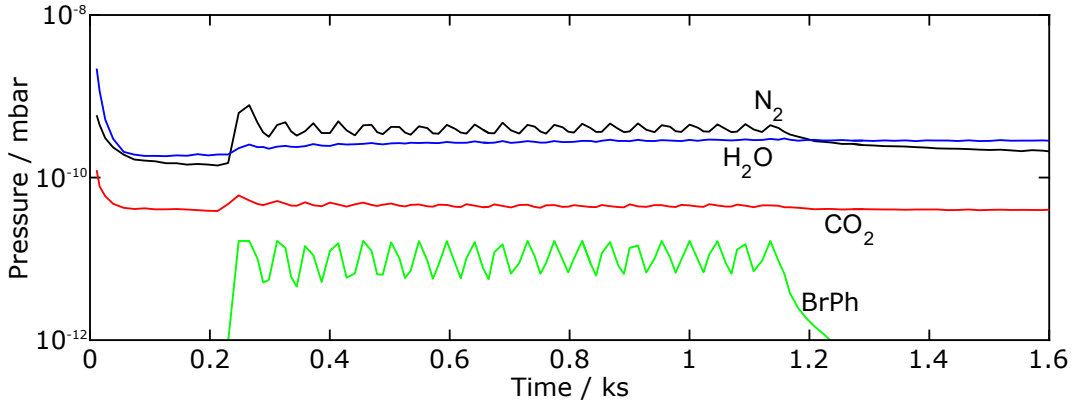

Figure 5-13: The Partial pressures of the characteristic mass to charge ratios of the main constituents of the gases in the prep chamber during a 3 L dose of BrPh, with a maximum set pressure of 1×10^{-9} mbar. The peak visible at the start of the trace is due to the emission of gases from the mass spectrometer upon the start of measurement. While the valve begins to open at 0 s, there is an initial period before gas from the test tube is able to enter the chamber, and hence the pressure does not begin increasing until some time afterwards. Similarly, while the requisite dose is achieved slightly before 1.2 ks, some time is required for the valve to fully shut.

5.5.1 Freeze-pump-thaw purification

In order to reduce the number of contaminants on the surface, the purity of the dosing gas is optimised prior to use. This is achieved by using a freeze-pump-thaw process shown in figure 5-14. High purity BrPh ($\geq$ 99.5% purity from Sigma Aldrich) in a test tube is connected to the gas line leading to the stepper motor-controlled value via a second valve, which is initially closed. The gas line is pumped down from atmospheric pressure using the same roughing pump backed turbomolecular pump used to pump the load-lock. This is able to reduce the pressure in the gas line to approximately 1×10^{-6} mbar. The freeze-pump-thaw method consists of the following procedure which is repeated until the requisite purity is achieved. Firstly, the test tube is submerged in liquid nitrogen to the level of the liquid BrPh, which causes it to freeze. Secondly, the valve between the test tube and the evacuated gas line is opened. The gas above the BrPh will be pumped out, whilst the frozen BrPh will not. However contaminants dissolved in the liquid will still be present after the liquid freezes, and as such will similarly not be pumped. Finally, the valve is closed and the frozen BrPh is melted by submerging it in lukewarm water.

Henry's law states that the amount of dissolved gas in a liquid is proportional to the partial pressure of that substance in the gas phase [124]. Initially the partial pressure of each contaminant in the test tube is the same as that in air at atmospheric pressure,

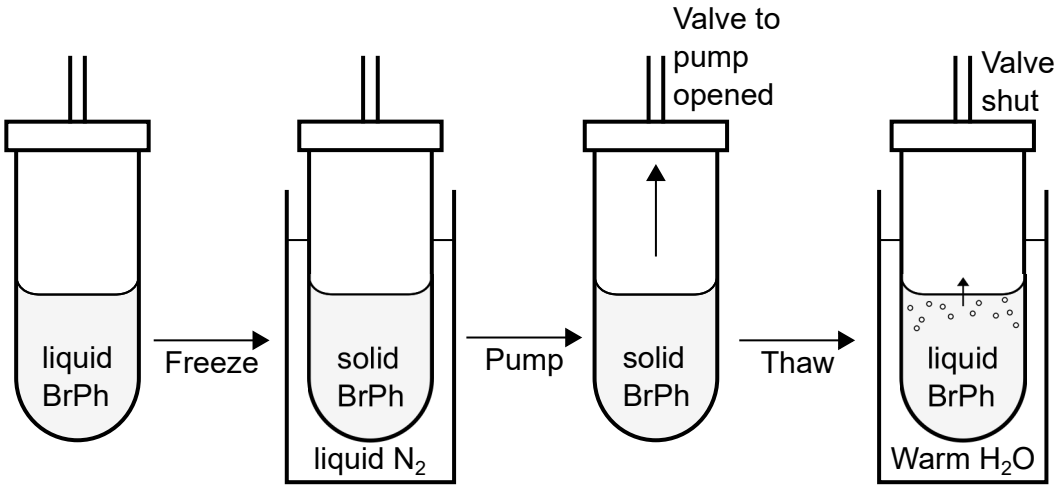

Figure 5-14: The freeze-pump-thaw process for purifying the dosing gas.

which means that the amount dissolved in the BrPh is relatively high. When the liquid is frozen, the quantity of each contaminant within does not change. However, during pumping the partial pressure of each contaminant in the gas of the test tube is lowered, and so when thawed, the amount dissolved in the BrPh will be proportionally reduced according to Henry's law. The contaminants will be released from the now-liquid BrPh as gas bubbles, increasing the pressure of the gas in the test tube whilst increasing the purity of the liquid BrPh. In the next freeze-pump-thaw cycle the newly released gas will be pumped off, and thus the partial pressures will be further reduced. The purity of the liquid can be roughly approximated by the amount of bubbles released during thawing, with a more pure liquid resulting in fewer bubbles as there are fewer contaminants.

The maximum purity of the liquid will be limited by the system's pumping speed for each contaminant. The partial pressures in the test tube will only be reduced so far during pumping, meaning that the quantity dissolved will reach a minimum plateau. With each freeze-pump-thaw cycle an amount of BrPh will be pumped, resulting in an additional limiting factor; this process can only be repeated so many times whilst maintaining a reasonable volume of BrPh. The amount of gaseous BrPh is defined by its vapour pressure, which is the pressure exerted by a vapour in contact with its liquid or solid phase. This value also determines the partial pressure of the gas above the liquid in the evacuated test tube after completion of the freeze-pump-thaw process, and therefore the theoretical maximum pressure during dosing.

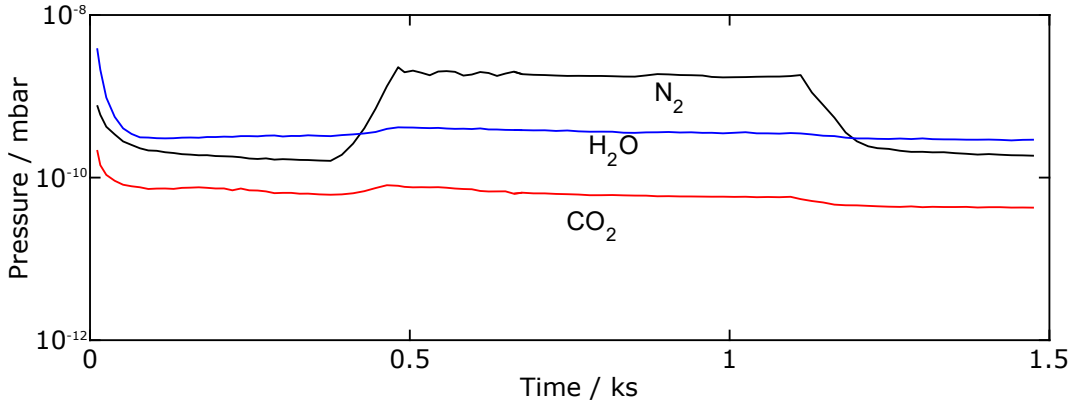

Figure 5-15: The Partial pressures of the characteristic mass to charge ratios of the main constituents of the gases in the prep chamber during dosing of 3 L through a second gas line open to the atmosphere.

5.5.2 Verifying the dosing gas

The purity of the BrPh in the test tube cannot be directly measured, instead it can be inferred by the change in the partial pressure of gases within the prep chamber upon opening the connected valve. A Hiden quadrupole mass spectrometer attached to the prep chamber allows the measurement of these partial pressures, and by comparing them before and during dosing, the make-up of the dosing gas can be estimated. While a complete mass sweep can be used to identify the main constituent components of the gas in the prep chamber, during the automated dosing procedure the pressure within the prep chamber fluctuates more quickly than the mass spectrometer is able to measure. Instead, by scanning only the characteristic mass to charge ratios of each of the main contaminants, reasonable time resolution during dosing can be achieved. The main components of the dosing gas are essentially air plus the BrPh; H_2O (m/z of 20), N_2 (28), CO_2 (44), and BrPh (77).

While figure 5-13 shows the change in partial pressures of the main constituent gases in the prep chamber during dosing, figure 5-15 shows the partial pressures of the dosing gases when not connected to the BrPh test tube. Instead, here the stepper motor opens a valve connected through the gas line to atmosphere. Additionally, the set max pressure in figure 5-15 is increased to 5×10^{-9} mbar compared to the 1×10^{-9} mbar for figure 5-13, and so a greater partial pressure of all constituent gases is expected. In this case no BrPh is measured without the connected test tube, with the increase in the pressure in the chamber entirely supplied by air.

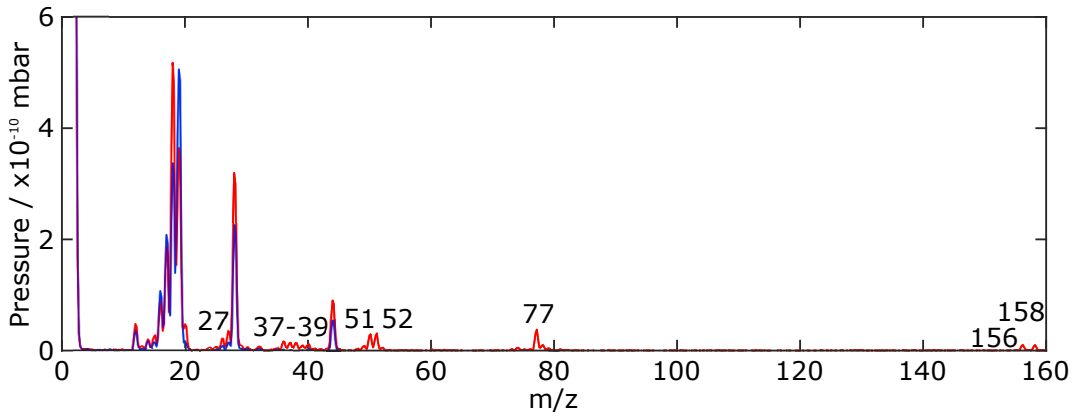

Figure 5-16: The mass-to-charge ratio of the prep chamber during dosing with bromobenzene (red) and prior to dosing (blue). The numbered peaks refer to characteristic m/z values for bromobenzene from NIST [125]. Due to the limited range of sensitivity of the mass spectrometer used, the peaks at m/z of 156 and 158 appear smaller than expected for BrPh.

Figure 5-16 shows a spectrum measured in the prep chamber during dosing across the m/z range of the mass spectrometer compared to a background scan of the chamber prior to dosing. As the partial pressure of BrPh will vary during measurement, the measured pressures across the m/z range should not be directly compared. Instead, only the presence or absence of peaks should be considered. As can be expected, strong peaks characteristic of H_2O (at m/z 20), N_2 (at 28) and CO_2 (at 44) are visible in both the before and during traces. However, in the during dosing trace, each additional peak can be correlated with an expected BrPh emission spectrum [125]. This suggests that there is only trace presence of other gases exposed to the sample during dosing.

Chapter 6

Automation of local and nonlocal injection procedures

One of the main advantages of the STM is the ability to directly and controllably inject hot carriers from the tip into the surface. As can be observed from the range of examples discussed previously, this greatly broadens the scope of available experimentation. The main results of this thesis use the STM tip as a local source of hot charge carriers with specific and controlled injection parameters, including injection bias, current, duration, and position on the surface.

The outcome of each STM charge injection experiment is probabilistic, so large volumes of data are required to reduce the experimental uncertainty and allow fine sweeps through the parameter space. See, for example, the desorption of H from a Si(100) surface due to STM charge injection by Soukiassian et al., in which the collection and analysis of a statistically large data set over a range of injection currents showed the desorption rate to be an order of magnitude lower than previous reports [56]. To achieve this we minimise the standard error of the experiment, $\sigma/\sqrt{n}$, via either reduction of the standard deviation σ or increase of the experimental sample size n.

Whilst each part of this process could be performed manually, the overall injection procedure has been automated to allow for the collection of large sets of data with minimal oversight, whilst limiting human error. As an example, over $34,000$ manipulation events were recorded during a part of the work comprising chapter 8 and published in reference [10]. This automation consists of a combination of LabVIEW and MATLAB programs, allowing for control over the Nanonis SPM controller as well as sufficient in situ image analysis for automated site-specific injection. In this chapter, the overall

injection process is described, with a focus on achieving high quality experiments with an automated system.

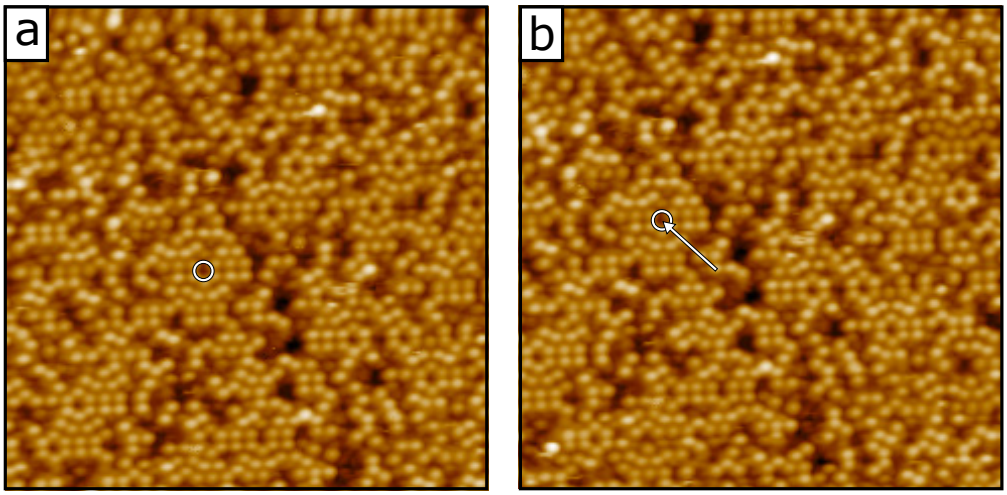

Figure 6-1: An example of the drift observed between successive 25 nm^2 STM scans, without compensation of thermal drift. The white circle in both (a) and (b) labels the same corner hole site, it is, however, observed at different positions within the image. The white arrow in (b) shows the apparent distance travelled during and between these images.

6.1 Drift correction

Drift during STM imaging refers to the relative movement of the imaged surface compared to the position of the scan window, an example of which can be seen in figure 6-1. Reducing the drift increases the ease of automated site-by-site analysis, lowering the probability of computational error (and thereby reducing σ), and maximises the amount of area common between the before injection and after injection images (increasing n). At its worst, this drift can result in an apparent movement rate sufficient to completely change the imaged area in consecutive scans; a reasonable drift, prior to correction, of 100 pm s^{-1} results in a movement of the tip relative to the surface of approximately 50 nm between consecutive 50×50 nm scans. However, even a relatively small drift rate will result in the position of the tip changing substantially whilst supposedly held still during an injection, thereby preventing site-specific or long-duration injections. As such, this must be ameliorated prior to any injection.

During room temperature experiments, as all experiments in this thesis are, the temperature of the STM head is not actively controlled. Fluctuations in the temperature of the STM result in the expansion or contraction of the various components of the STM head by differing amounts depending on the material [126, 127]. These small size changes lead to a movement in the position of the tip relative to the surface, causing the imaged movement of the surface between, and during, scan images. Whilst these

natural changes cannot be controlled entirely, several factors limit the rate and magnitude of thermal fluctuations. The microscope is held in a vacuum chamber, which is only connected to the external chamber by thin springs and wires. In addition, the room has some degree of thermal stability, with only one user at any time. Finally, although the sample is flashed to a high temperature each morning, it is left for at least 2 hours prior to transfer to the STM head. Thus any temperature changes, and hence the rate of thermal expansion, should be small and gradual. This is observed as a near-constant drift rate.

To counteract the effects of this drift, LabVIEW software has previously been written. This program correlates the central sections of two consecutive STM images taken at the same supposed location. By locating the maximally correlated position of the second image-section with respect to the first image, the displacement between the two images can be measured and the drift rate and direction calculated. Via Nanonis, a linear, time-varying voltage is then superimposed onto the piezo tip position voltages. The STM tip therefore "follows" the surface drift, such that when two consecutive images are taken they image the same surface area. This program is run repeatedly until the drift between consecutive scans is less than 0.5 pm s^{-1}. It should be noted, however, that the thermal fluctuations and therefore drift will change over time, and so the drift compensation must be periodically refreshed. We perform this prior to each series of injection experiments.

6.2 Piezo creep

In addition to thermal drift, piezo creep results in the translation of the scanned area over time after moving the tip. Examples of this are shown in figure 6-2. This is due to the well known nonlinear response of the piezo motors positioning the tip with respect to the applied electric field. That is, in positioning the tip an electric field is applied across the piezo motors resulting in the almost-instantaneous expansion (or contraction) of the piezo linearly with the applied field. However, after reaching the requisite position the piezo will continue to expand or contract. The length of the piezo, L, varying as

$$\Delta L(t) = \Delta L(t_0)\left[1 + \beta \ln\left(\frac{t}{t_0}\right)\right], \tag{6.1}$$

where t is the time since the field was applied, β is a variable dependent on several parameters including the temperature and the specific material and design of the piezo-motors, and $\Delta L_0(t_0)$ is the nominal displacement of the piezo at time t_0 shortly after the field is applied, subsequent to the supposed linear response [128]. For low temperature

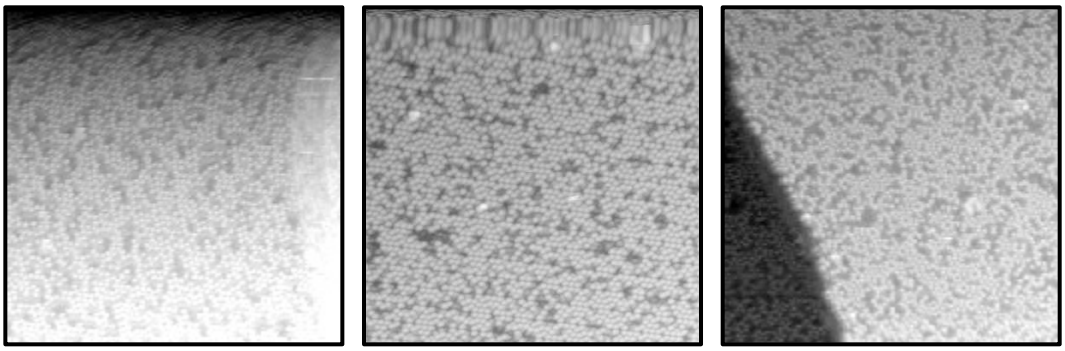

Figure 6-2: 40×40 nm STM images of the Si(111)-7 × 7 surface with visible creep, such that the top of each image appears distorted due to the continuation of movement of the tip between surface scans.

STM (e.g. 4 K) $\beta \approx 0$ and the nonlinear piezo creep response is minimal [129]. At room temperature, however, there is enough thermal energy for the dipole domains within the piezoelectric material to change orientation under the influence of the static electric field, increasing the polarisation [130, 131]. This changes the magnitude of the piezo response and, therefore, changes the position of the STM tip beyond the initial expansion or contraction.

From both figure 6-2 and the logarithmic term in the above equation, it is clear that the effects of creep decay over time, with the rate of change in the length of the piezo reducing $\propto 1/t$. As such, the effect of creep on the scanned area can be reduced by waiting after moving the tip but prior to scanning. Additionally, the value of β varies with the applied field, generally being greater for larger field. As such, moving the tip further (i.e. a greater contraction or expansion) will result in a larger observed creep movement. This means that creep can be further reduced by limiting the distance moved by the tip and performing any large movements across the surface by retracting the tip and using the coarse motors.

6.3 Injection overview

In this thesis, charge-injection experiments are separated into two categories, local and nonlocal. In local experiments, only manipulation of a molecule directly beneath the tip within the tunnel junction is generally considered, whereas nonlocal manipulation can occur many nanometres from the injection site. Whilst these different manipulation regimes have slightly different experimental procedures, the actual injection processes differ only slightly.

Single injection experiments, local or nonlocal, consist of three necessary parts from which data can be extracted; a scan of the surface prior to injection (figure 6-3a), the injection itself (figure 6-3c), and a scan after the injection has completed (figure 6-3e).

Automation during injection relies on a combination of a LabVIEW control program directly interacting with Nanonis and a MATLAB program used for real-time data analysis necessary for automatically determining the position of molecules on the surface from previous images. Interaction between LabVIEW and MATLAB occurs indirectly, via scan files being saved into a folder, with analysis occurring when MATLAB detects a correctly named file in the folder. The output of the analysis, usually containing the determined injection sites, is again saved in the folder, where it is detected by LabVIEW and tip positions for each of the injection sites are then used to control the injection. This process typically takes 5-10 seconds, during which the STM is paused at the end of the scan. In experiments where the injection positions are not at specific surface sites, however, the MATLAB program is not used and all positioning is performed by the LabVIEW program.

To minimise the required human oversight and maximise the amount of data collected, an additional LabVIEW program is used to repeat the injection procedure at different areas on the surface, shown in figure 6-4a. After moving to a new location this program waits for a user defined length of time prior to starting the large-before scan, which reduces the effects of creep when moving the tip large distances. For each new complete injection process, the injection parameters are randomly selected from a set list. This allows a range of parameters to be trialled, whilst minimising the opportunity for local effects to influence the same parameters multiple times. For example, the tip-state may change after several sets of injections, which may alter the desorption probability independently of the injection parameters.

6.4 Automated molecule finder

If the experiment requires site-specific injection, the large before-injection image, for example in figure 6-3a, is used with a "molecule-finder" program. The automated molecule finding program described here is the same as that used for the analysis of the images to extract experimental results, which is discussed in more detail in section 7.2.1. This software has been used in previous experiments [7,8,95,110]. The MATLAB program automatically identifies the positions of corner holes in the image by cross-correlating it with an array of template corner hole images. This results in a "best-fit" image with correlated maxima at each corner hole site, from which the orientation of the

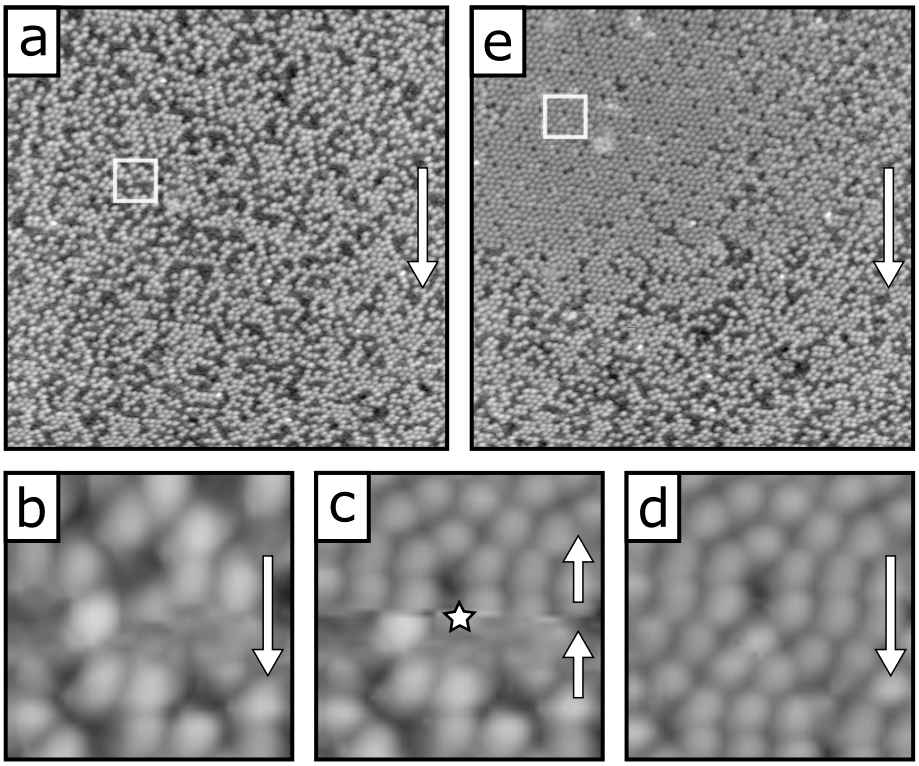

Figure 6-3: The main STM scans taken as a part of the injection process. The slow scan direction of each scan is indicated by the white arrow. (a) A large, here 50 nm^2, scan of the surface is taken prior to injection. This is used to identify an injection site, as well as locate the positions of molecules and clean sites prior to injection. (b) A small scan, here 5 nm^2 and located within the white square in (a), is taken of the area centred on the injection site. (c) A scan of the same area as in (b) is started, then paused at the injection site (labelled by the star) and injection parameters are applied for the requisite injection duration. To minimise unnecessary movement of the tip, and consequently piezo creep, in this scan the slow scan direction is reversed. After the injection, passive scan parameters are reapplied and the scan recommences, hence the clear change in molecular coverage at the middle of the scan image in (c). (d) A downwards scan around the tip site post-injection. (b) and (d) are used to identify the position of the injection site in the large scans. (e) Finally, a large 50 nm^2 post-injection scan is taken, which is used to identify the positions of molecules and clean sites after the injection. The white square in (e) indicates the scan area of (d).

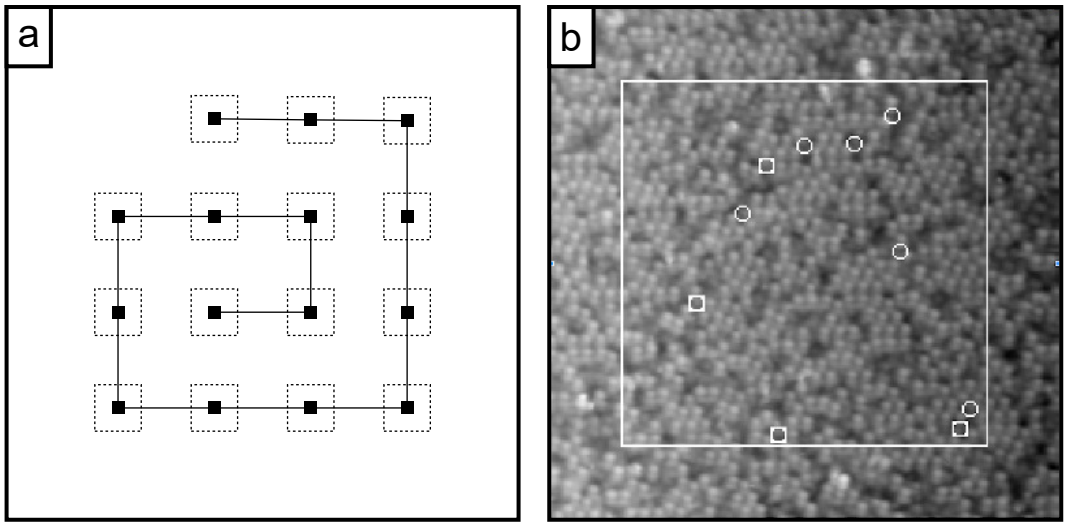

Figure 6-4: A LabVIEW program automates the position of the scan window for each series of injections and the position within the scan for each individual injection. (a) Between each injection scan, the scan window is moved by a user defined amount to the positions labelled by the black squares. The dashed lines indicate the size of the scan at each position. (b) For each injection position, after the initial pre-injection scan a MATLAB program determines the location of the injection sites. After each individual injection, the LabVIEW program determines whether the injection was successful (marked with a square), or unsuccessful (marked with a circle).

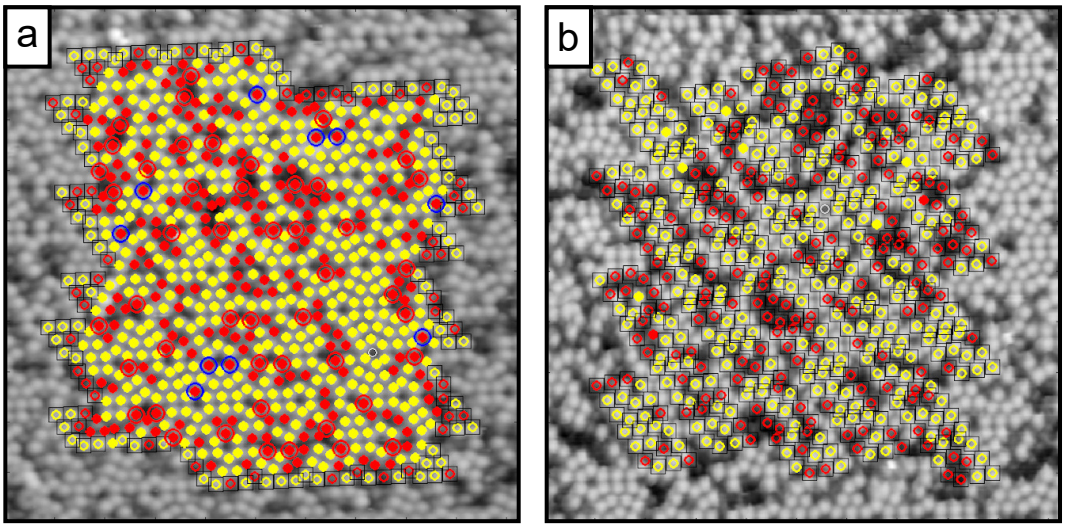

Figure 6-5: Output of the automated molecule finding MATLAB program for 25×25 nm STM images of a BrPh dosed Si(111)-7×7 surface. In (a) the adatom sites were correctly located, with occupied sites labelled red and unoccupied sites labelled yellow. From this injection locations were selected from potential sites, here labelled with a blue outline. In (b) adatom sites were not determined correctly and as such no reasonable injection sites could be located.

surface and the lattice vectors are estimated. The cross-correlation step allows for some flexibility in the structure of the imaged lattice, reducing the effects of, for example, residual creep or thermal drift. From the corner hole positions the positions of all of the adatoms within the scan are predicted. The sites are then labelled as molecules or clean adatoms, depending on the z-height of each, and numbered depending on the position within the unit cell (e.g. faulted middle, unfaulted corner, etc.). MATLAB then randomly selects injection sites from the occupied sites fulfilling the set criteria, including the number of injections per scan and specific position within the cell. The output of this is shown in figure 6-5a. The selected molecules are then converted to coordinates within the scan image, and the injection positions are fed back into LabVIEW, shown in figure 6-4b. For local injection, this is usually several injection sites per scan image (5-10 are commonly used here) however for nonlocal injections this is usually just one site.

Depending on the surface within the scan area and the tip state, the entirely automated molecule finding routine may either incorrectly locate adatoms, shown in figure 6-5b, or fail entirely, which may result in the program freezing. This can be, for example, due to the presence of a step in the scan image resulting in a large z-height discrepancy, a change in tip state during the scan, or the sample being too heavily dosed to identify

a corner hole. If the injection process continues with incorrect injection sites, this must be manually identified from the position of the injections in the pre- and post-injection scans and the data removed prior to analysis. If the program freezes, however, it must be restarted.

6.5 Injection

For each individual local or nonlocal injection, a small scan is taken, here usually 3×3 nm for local experiments and 5×5 nm for nonlocal to aid in tip location, centred on the injection site, as in figure 6-3b. However due to thermal drift, in the time between the large scan and this small scan, the small scan is likely to be not quite at the correct location and so the injection site is not centred. To ensure the specific location of the injection, a further cross-correlation is performed between this small scan and the expected injection location, cropped from the previous large scan. From this, an estimate of the drift between these scans is calculated and an additional small scan occurs in a newly estimated injection site-centred position. Further small scans are repeated until either the image is sufficiently similar to that cropped from the large scan, or 7 scans are completed at which point that injection is aborted. This may occur due to excessive thermal drift between images such that the correct site is never found, or surfaces changes for example contaminant adsorption or a large amount of diffusion or desorption of adsorped molecules between the pre-injection large and small scans.

Once the injection site is set, a final passive scan is taken (figure 6-3b) before the scan direction is reversed and a half-scan is performed until the tip reaches the centred injection site and the scan is paused (figure 6-3c). The scan direction is reversed here to minimise unnecessary movement of the tip and reduce the effects of piezo creep; the tip does not have to return to the top of the scan window prior to the upwards scan. The tip-height feedback loop is then turned off and the tip is retracted from passive scanning parameters (+1 V, 100 pA) by a set amount (1 nm for nonlocal injections, 0.4 nm for local injections). Next, the injection parameters are applied and the feedback loop is restarted, causing the tip to approach the surface. In nonlocal manipulation the approach is performed in two steps to minimise any spikes in current; a primary approach until the tunnel current = $20pA$, followed by a secondary approach to the requisite parameters. For local manipulation experiments the feedback loop is slowed, such that the tip approaches the surface more slowly and a current spike is not observed. During injection, the tip height, bias and tunnel current are recorded giving further insight into the tunnel junction during injection. After the injection is complete, either upon manipulation or reaching the specific injection duration, the tip is retracted from

the surface and passive scanning parameters are reapplied. The tip retraction step is critical to erase all sudden current pulses due to a change in the voltage, it also means that the current changes smoothly and therefore that we can accurately measure all the injection charge during an experiment.

Finally, after the injection itself is complete, the tip will finish the second half of the reversed-direction "during" scan (figure 6-3c), before a final scan of the post-injection region (figure 6-3d). For each identified injection site, this process is then repeated. Note that for nonlocal parameter injections, only one injection site per large scan is used to maintain a relatively constant adsorbed molecule distribution for each injection.

6.5.1 Local

The manipulation of a molecule in the tunnel junction results in the exposure of a clean adatom with a corresponding increase in the LDOS of the surface at the injection bias. Thereby, upon manipulation of the local molecule the tip will be automatically retracted by the feedback loop to reduce the current to the requisite parameters, resulting a clear step in the tip height trace. In local injections only manipulation of the local molecule is considered, and so this step can be taken as the time of manipulation. Further manipulation is suppressed by retracting the tip immediately after this point and reducing the tunnelling current to zero. There is a slight variation in the height of this step after manipulation due to the exact position of the tip on the surface and the LDOS of the tip state during injection. The vast majority of manipulation events result in a tip height change of greater than 30 pm away from the surface. As such, the tip is automatically retracted if a height change greater than 30 pm is observed during injection. Otherwise, if manipulation is not observed, the tip will be retracted after 8 s (an arbitrary upper limit on injection duration). An example of the tip height, current, and bias during a local injection is shown in figure 6-6.

6.5.2 Nonlocal

In a nonlocal manipulation injection, we observe the manipulation of many more molecules than the one within the tunnel junction. Furthermore, the majority of nonlocal manipulation experiments are performed with sufficiently high current and bias that the manipulation of a molecule within the tunnel junction has only a small affect on the tip height during the injection. Hence we continue an injection until a requisite duration has been completed, at which point the tip will again be retracted and passive scanning parameters reapplied. An example of the tip height during a nonlocal injection is shown in figure 6-7.

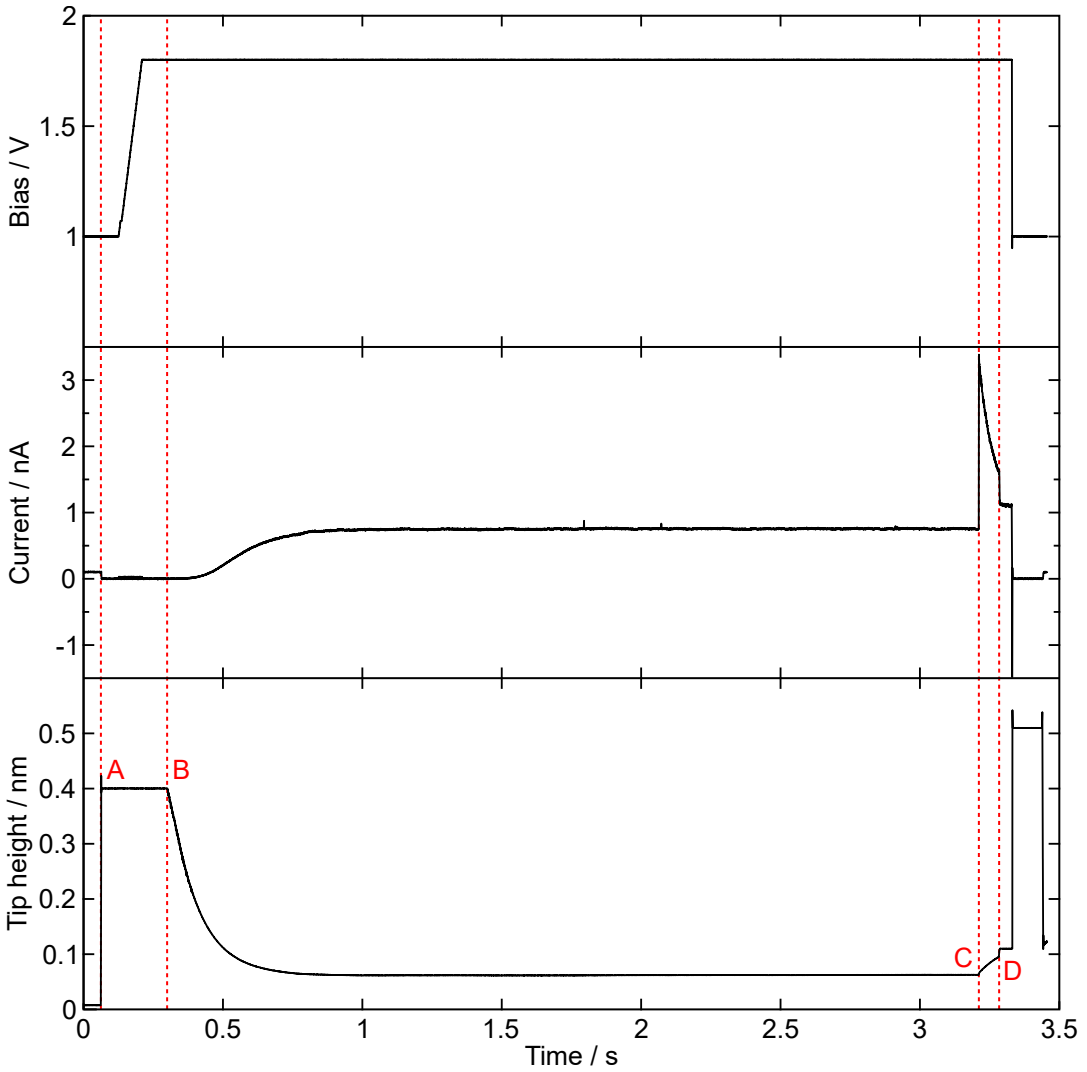

Figure 6-6: The bias, current and relative tip-sample separation during a local injection. At $t = 0$ s the STM is in passive scanning parameters (+1 V 100 pA). (A) The feedback loop is stopped and the tip is retracted from the surface by 0.4 nm. (B) The feedback loop is initiated with the injection parameters, here +1.8 V 750 pA. (C) The molecule beneath the tip is manipulated by the injected charge carriers, resulting in an increase in the available LDOS and the tip retracting to maintain the tunnel current. (D) This height change overcomes the 30 pm threshold for manipulation and the tip is automatically retracted by the LabVIEW program with the injection process concluded.

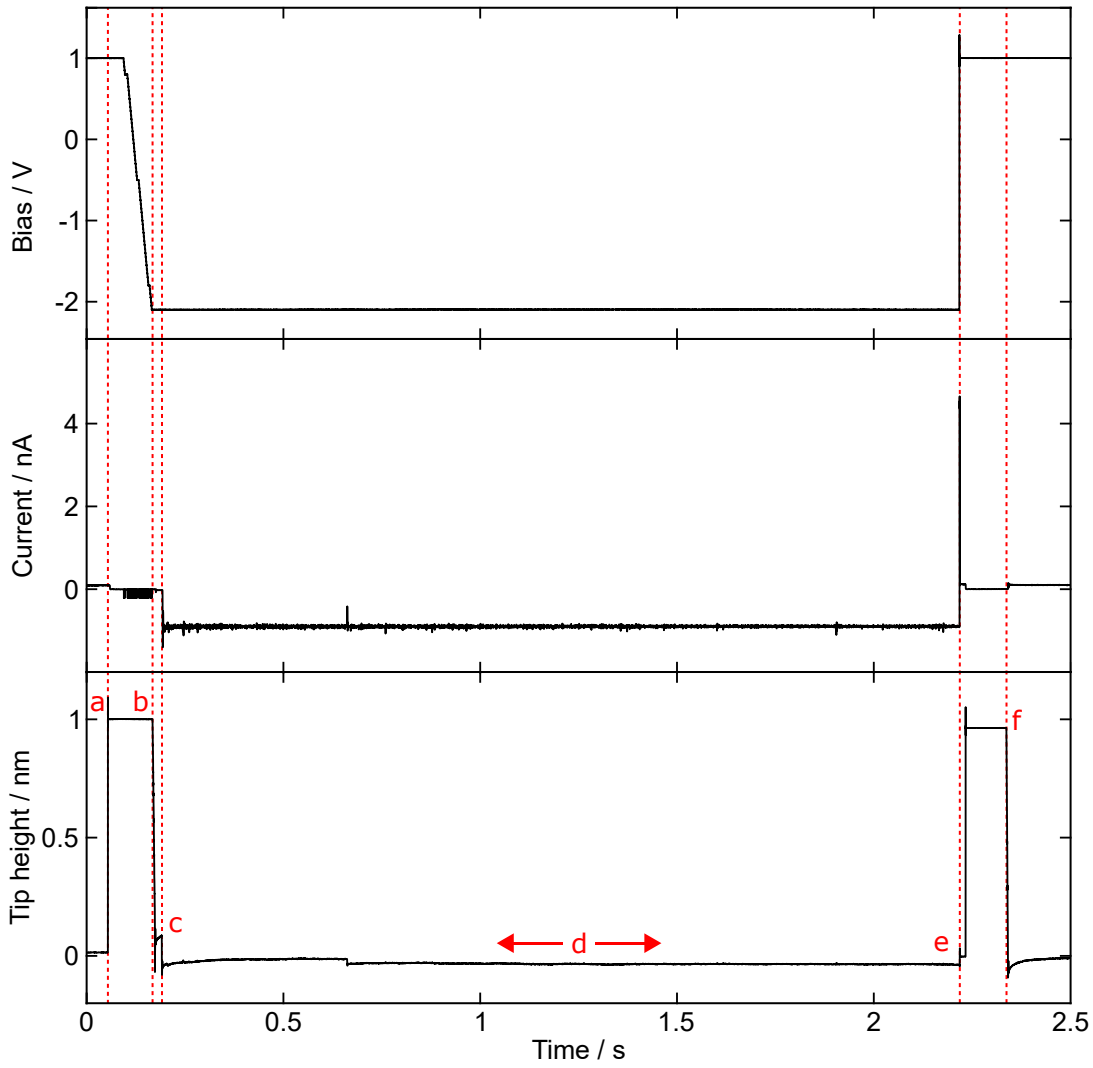

Figure 6-7: The bias, currant and relative tip-sample separation during a 2 s injection at nonlocal injection parameters (-2.1 V 900 pA). At $t = 0$ s the STM is in passive scanning parameters (+1 V 100 pA). (a) The feedback loop is stopped and the tip is retracted by 1 nm. (b) The injection bias is set and the feedback loop is reactivated, causing the tip to approach the surface. To prevent overshooting the injection current, the approach is paused at 20 pA. (c) The approach continues until the injection current is (here) 900 pA. (d) The tip then remains at the same position with the same parameters for the specified duration, here 2 s. (e) At the end of the injection time the bias is returned to +1 V and the tip is retracted. (f) Finally, passive scanning parameters are reapplied and scanning recommences.

6.5.3 Drift during injection

For site-specific injections, the stability of the tip over the injection site is paramount. If the tip moves by more than a fraction of a nanometre then the tip will essentially be injecting into multiple positions during the one experiment, which means that the injection will not be site-specific. The main source of tip movement is expected to be thermal drift, which is corrected prior to injection experiments as described in section 6.1. The rate of drift will change both in magnitude and direction over time, however, and so without repeated correction, injections cannot necessarily be assumed to be site-specific.

The amount of drift during an injection can be estimated by comparing the position of the surface scans immediately before (figure 6-3b) and after injection (figure 6-3d). In each of these images the injection site should be centred, and so any change in the position of the centre of the image will be due to drift. Each of these small images takes approximately 30 s (at 48 pixels per line and with 15 nms^{-1} scan speed), and so for sufficient injection duration (i.e. $\approx$ 100 s and greater) the majority of the time for the drift will be during the injection itself. To measure the drift during injection, the same site in the successive pre- and post- scan images has been manually located. While an automated molecule finding or image correlation process could be used, the often large changes in the surface coverage during scanning frequently results in incorrect estimates, whereas a manual process allows for straightforward removal of unclear results. An example of the drift during an injection is shown in figure 6-8, in which the surface has moved 0.6 nm between the before and after injection images. Whilst the occupancy of many sites on the surface has changed here, the local structure around the labelled sites has not, allowing for the same sites to be located in both the before and after injection images.

In the short term, thermal drift is expected to occur at a roughly linear rate. The total amount of time between these consecutive images will be two complete small scans ($\approx$ 30 s each), plus the injection time itself. For the shorter injections, such that the time for each injection is negligible compared to the constant scan duration, and assuming the majority of the drift is due to a linear thermal drift, the total drift between the two images should be approximately consistent. However, as can be seen in figure 6-9, this is not observed. Within the scope of large uncertainty, instead the magnitude of the drift appears to increase roughly logarithmically with the injection duration across the range. While this figure contains data for 78 injections, note that for a longer duration injection the probability of identifying any one site is reduced as the overall probability of manipulation in the scan image surrounding the injection

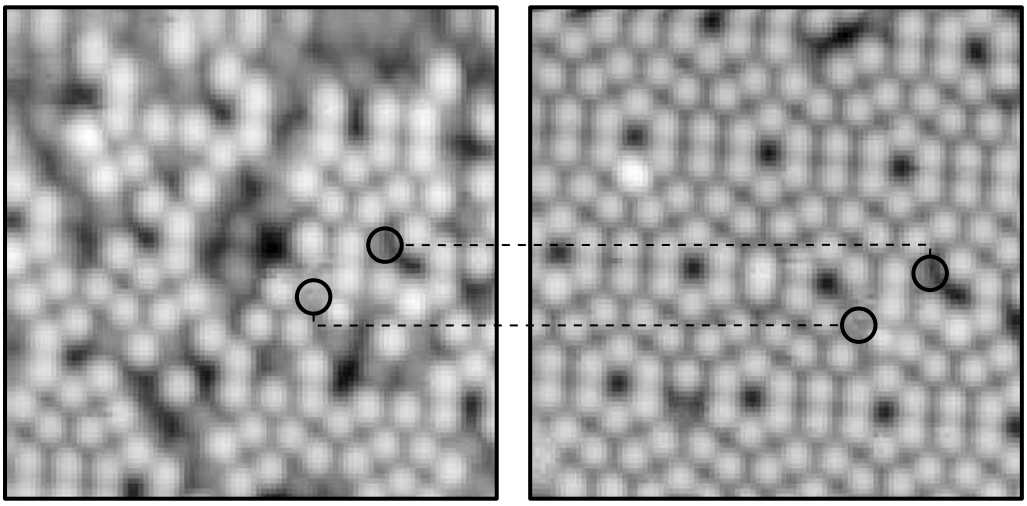

Figure 6-8: 10×10 nm STM images of a BrPh dosed Si(111)-7×7 surface before (left) and after (right) an injection (-2.1 V, 900 pA) for 100 s at the centre of the left image. The labelled circles show identifiable points common between the two images, such that the drift during the injection can be determined. Here these points, and thereby the surface, move by approximately 0.6 nm between these two scan images.

site is increased. This effect likely results in the anomalous data point at 500 s, as it comprises data from only 3 injections.

The logarithmic relationship of the position of the tip is similar to that for creep in equation (6.1), with displacement reducing over time during the injection. It is possible that instead of thermal drift, creep is the major source of movement of the tip during injection. However, in addition to the injection duration, there is approximately 30 s between the before and after injection images; one complete scan (figure 6-3c) and two partial scans (figures 6-3b and d). Hence for this effect to be creep driven, there should be a large initial drift observed that is independent of the injection duration and this is not observed here. It is possible, however, that this displacement is due to a small amount of creep accumulated due to the movement of the tip during the scanning process, which means that after the tip stops scanning across the surface it continues to drift slightly during the injection.

Across the Si(111)-7 × 7 reconstruction, each surface site covers an area of roughly 0.5 nm^2. Assuming perfect tip positioning, with the tip initially directly atop the requisite site, site-specific injections require the tip to drift by less than one site position. Hence, from figure 6-9 it is likely that the tip will drift over multiple sites during the longer duration experiments. This limits the reliability of site-specific injections at increased injection durations. As such, while local injection experiments are performed into

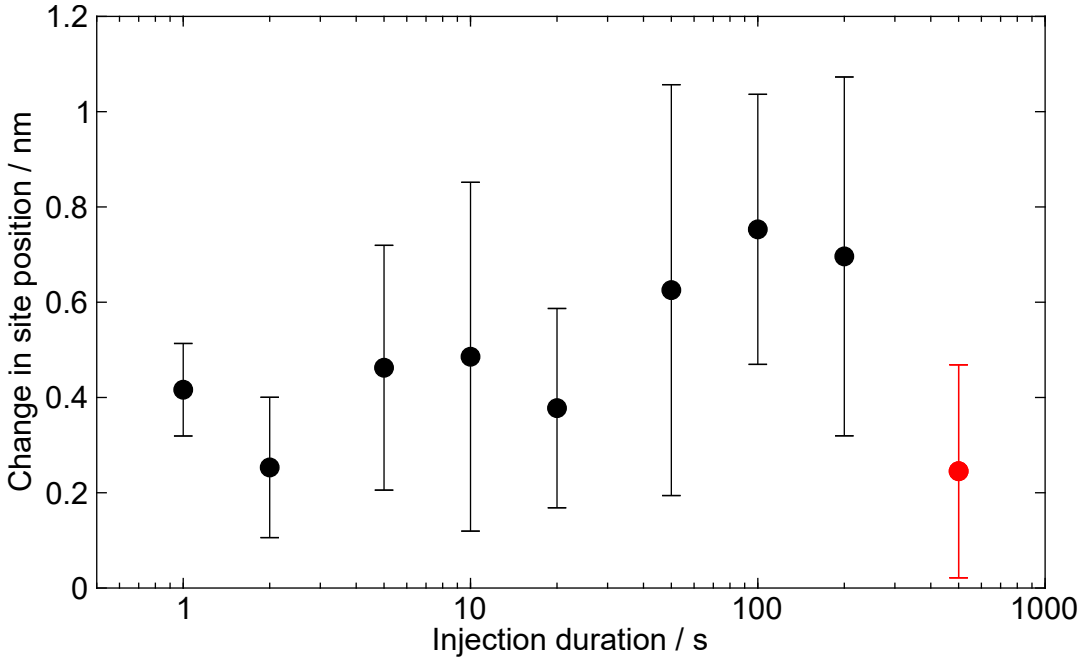

Figure 6-9: The average displacement of a specific site on the surface between the scan immediately before and immediately after an injection with duration between 1 and 500 s. Uncertainty is given by the standard deviation on the mean for each injection duration from 78 total individual injections.

specific surface sites, nonlocal injection experiments will be performed with the tip positioned above a specific position relative to the scan, say the centre of the scan window. This removes the requirement of the in situ MATLAB analysis, which for the large surfaces used in nonlocal experiments can take several seconds and often results in the experiments freezing.

Chapter 7

Data analysis

For local experiments, the small before and small after injection scans can be manually compared to identify whether the local molecule was manipulated and whether neighbouring sites become occupied; a process which takes several seconds. For nonlocal experiments every atom in a large radius must also be considered. The output of these manipulative-injection experiments is simply a set of images of the silicon surface before and after injection, examples are shown in figures 6-3a and 6-3e. Whilst these images clearly hold information about the state of the system, namely the position of clean and occupied adatom sites, this needs to be extracted. In the large scale nonlocal experiments the number of adatoms within each image is especially large; a 50×50 nm images will have well over 1000 individual sites. Whilst it would be possible to manual identify and characterise each individual site, as my supervisor Dr Peter Sloan did during his PhD, this would result in a significant time investment as well as the potential of substantial human error. As such this process has been previously automated using a combination of LabVIEW and MATLAB programs. In this chapter the data analysis processes for both local and nonlocal experiments will be presented.

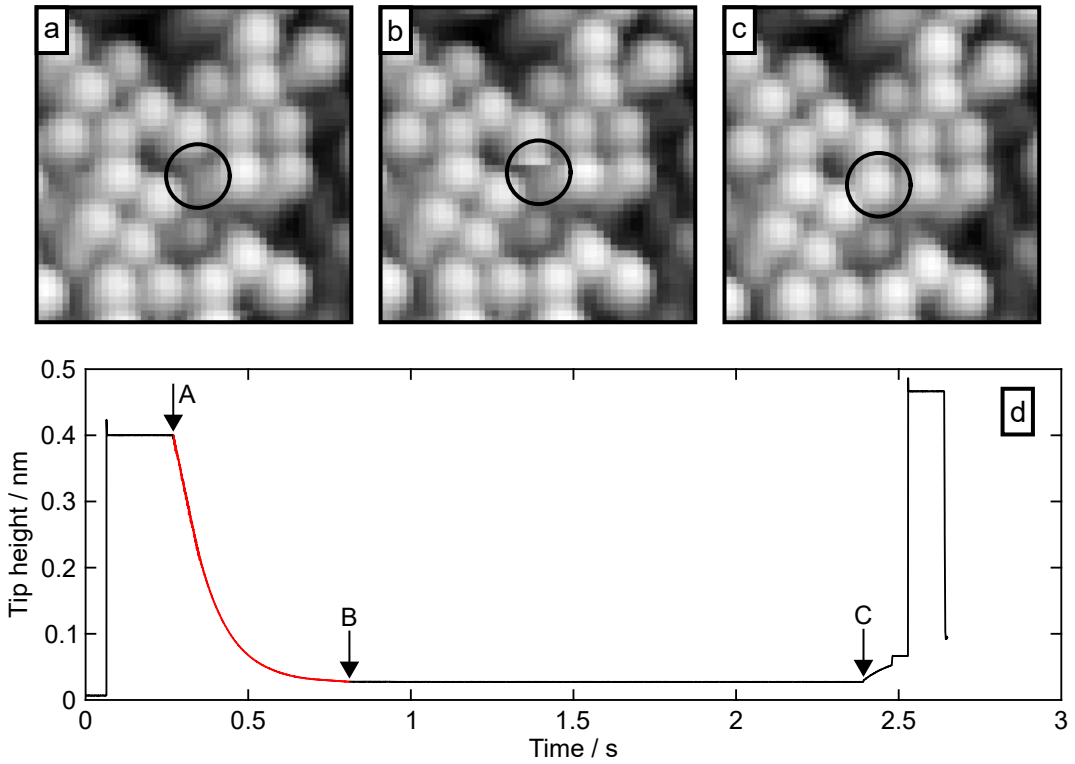

Figure 7-1: 5×5 nm STM images before (a), during (b) and after (c) local manipulation (-1.3 V, 5 pA) of a BrPh molecule within the black circle chemisorbed on a Si(111)-7 × 7 surface. (d) The relative height of the STM tip during the injection. At (A) the feedback loop is initiated with the injection parameters, which results in the tip approaching the surface to achieve the requisite tunnel current. This process is not instantaneous, resulting a finite approach time between (A) and approximately (B). At (C) the molecule beneath the tip is manipulated, and the injection is subsequently concluded with the tip retracted from the surface.

7.1 Local injection analysis

In local parameter injection experiments, only the molecule directly beneath the tip is expected to be manipulated. Determining whether the molecule beneath the tip was manipulated is simple, assuming manipulation only occurs once and no additional molecules chemisorb to the surface after injection. In this case, it can be determined by comparing the occupancy of the site in the centre of the before and after injection images, for example the clear change in occupancy between figures 7-1a and c, as well as the appearance of the newly unoccupied adatom site above the injection in figure 7-1b. Note that the small drift between images allows for site-specific local injection.

As the manipulation occurs directly within the tunnel junction, additional information about the manipulation can be extracted by considering the tip height trace during the injection. At the lower biases resulting in local manipulation, compared to the nonlocal bias resulting in figure 6-7, the tip will be closer to the surface and so any change in the tunnel junction, for example from the molecule leaving the junction, will result in an extremely fast increase in the tunnel current immediately after manipulation, followed by an automatic change in the tip-height due to the feedback loop. An example of the tip-height-step due to manipulation can be observed in figure 7-1d at point (C).

By considering the time to manipulation, a more precise measure of the number of injected carriers resulting in manipulation can be extracted. To achieve this, in addition to the time of the manipulation step, the time of the start of the injection must also be considered. After the initiation of the feedback loop at injection parameters (figure 7-1d point (A)), the tip will approach the surface at a finite rate determined by the feedback loop until the requisite tunnel current is reached. This results in a differing injection tip height and therefore approach time depending on the injection current and bias. At nonlocal parameters, for example -2.1 V 900 pA as shown in figure 6-7, the approach duration is short compared to the injection duration and the start of the injection is relatively well defined. However at local injection parameters, for example -1.3 V 5 pA in figure 7-1, this is not necessarily true. During the approach the tunnel current will steadily increase, and therefore the injection will not reach the set injection parameters until some time after the supposed initiation time. MATLAB code has been written to allow identification of the time taken to reach injection parameters, via the location of the start of the injection ((A) in figure 7-1) and the point at which injection parameters are actually reached ((B) in figure 7-1). Due to the nature of an exponential decay, and as each charge injection event is independent, starting the exponential counting from after the tip approach and looking at only those molecules who survive we will still recover the same exponential decay constant. From this, the total time to manipulation at injection parameters can be determined as the difference between the times of points (B) and (C) in figure 7-1.

7.2 Nonlocal injection analysis

7.2.1 Manual molecule Finder

To characterise the surface, the positions of molecules in consecutive STM images are compared. The positions within each image are found using a MATLAB program. This

program is similar in function to the entirely automated version discussed in section 6.4, although user interaction reduces the probability of missed or mislabelled sites.

In this program, the user identifies several adjacent corner holes around a single half unit cell (faulted or unfaulted) near the centre of the image, which are then used to calculate the lattice vectors of the reconstruction. By extrapolating these vectors across the image, the locations of each unit cell can be estimated. A cross-correlation routine is used to precisely locate each unit cell in order to reduce the effects of thermal drift or creep. The positions of adatoms within each unit cell can then be calculated from the known positions of adatoms relative to the corner holes. The MATLAB program then identifies whether there is a "light" adatom or a "dark" chemisorbed molecule on each of these sites by comparing the recorded z-height of the tip at that position with a boundary value relative to the image average. The user then identifies the faulted half of a unit cell known from previous negative bias images of the surface. The twelve sites in each unit cell are then numbered corresponding to the adatom location within the cell, along with the number of basis vectors from an arbitrary centre point such that each adatom has a unique coordinate set. Finally the locations of both the adatom and molecule sites on the surface are recorded. The result of this is shown in figure 7-2.

Areas in scan images in which the structure of the surface is irregular, for example due to step edges, grain boundaries or contaminants, can be excluded from the recorded data by manually deselecting these areas. The program can also be used to change or remove identified sites where the automatically calculated position or brightness of the site is deemed incorrect, for example a chemisorbed molecule is identified where there is a visible adatom or no expected site. This system works well in identifying sites near the user-selected corner holes, however further away, any irregularities in the surface or human error in the corner hole positions will be exaggerated, resulting in incorrectly estimated adatom locations and thereby incorrect molecule or adatom site identification. The effects of this can be limited by manually comparing the calculated positions and the image and either removing the incorrect sites, re-doing this analysis with newly selected corner hole positions or adjusting the z-height boundary. While these errors cannot be entirely removed without manual selection of each adatom and molecule location, the increase in error probability for sites far from the centre of the image is an accepted trade off for the increase in analysis speed; this step takes several minutes compared to the hours it would take to manually identify each site otherwise.

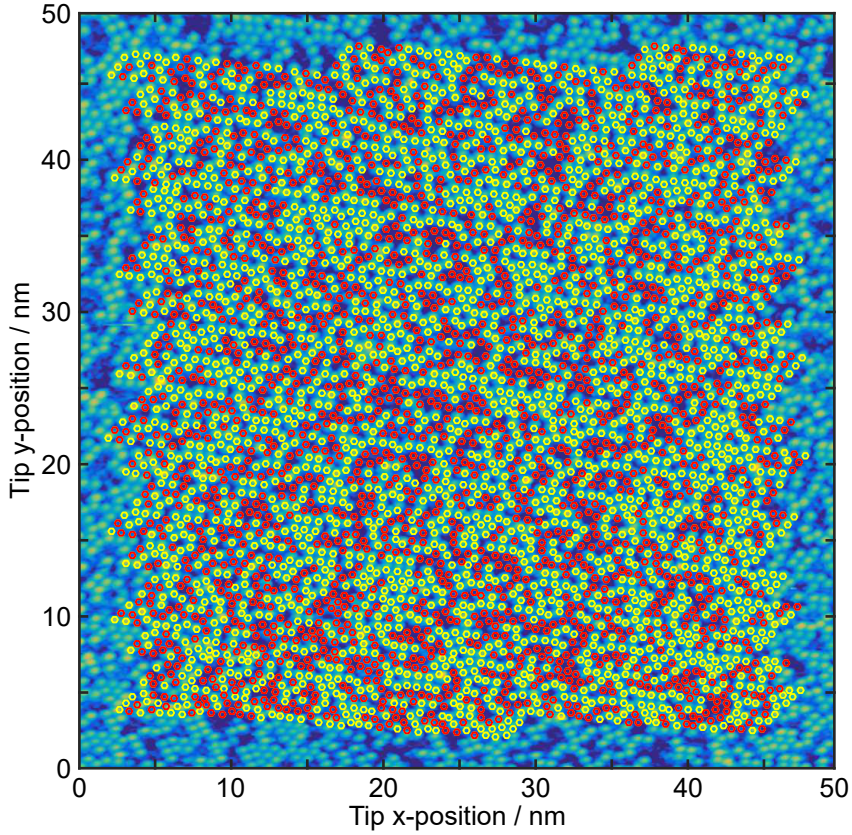

Figure 7-2: The output of the automated molecule finder MATLAB program after manual correction. Adatom sites across the surface are predicted and labelled as a molecule (red) or a clean adatom (yellow). Manual adjustments have been made to incorrect sites, by either changing the occupancy or removing automatically identified sites from the analysis entirely.

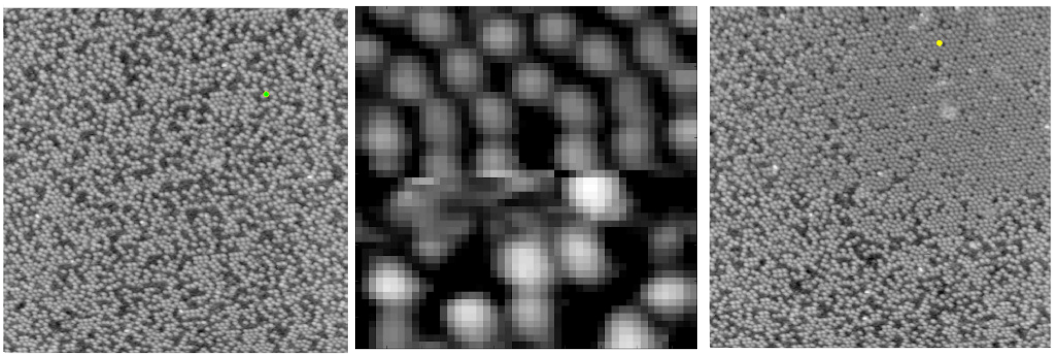

Figure 7-3: The tip position finding LabVIEW program. The position of the tip (green circle) in the 50×50 nm pre-injection image (left) is manually located by comparing the adatom sites with the small 5×5 nm scan surrounding the injection (centre). From this, the position of the tip (yellow circle) is automatically located in the 50×50 nm after injection scan (right).

7.2.2 Tip Position

Knowing the positions of adatoms and molecules within an STM image is not sufficient, however, to obtain information about the occupancy of specific sites in two separate images of the same surface area. A relative point on both images is additionally required to compare them. Here we use the tip site as the common point, such that the position of each site is calculated relative to the injection site. This site also needs to be identified because the manipulation will be centred around the injection site. Using a LabVIEW program, the output of which shown in figure 7-3, the tip site is manually located in the large before-injection image, figure 6-3a, by visually comparing the positions of molecules within the image to those in the small during-injection image, figure 6-3c, of which the injection site is in the centre. Note that random movement of chemisorbed molecules can occur between the large and small scans, which means that the surface around the tip location is not necessarily identical. This can result in difficulty locating the tip position, however due to the stability of chemisorbed aromatic molecules on the Si(111)-7 × 7 surface they are usually not too dissimilar, assuming no adsorption of contaminant molecules near the injection site.

Once the injection site in the before-injection image is located, the LabVIEW program uses an automated cross-correlation routine, similar to that discussed in section 6.1, comparing the area around the manually selected tip site with the after injection image to estimate the maximally correlated region. From this the injection site in the after-injection image is located and marked. Note, however, that if the drift between the two images is large or the surface contains a large number of dark sites, this cross correlation

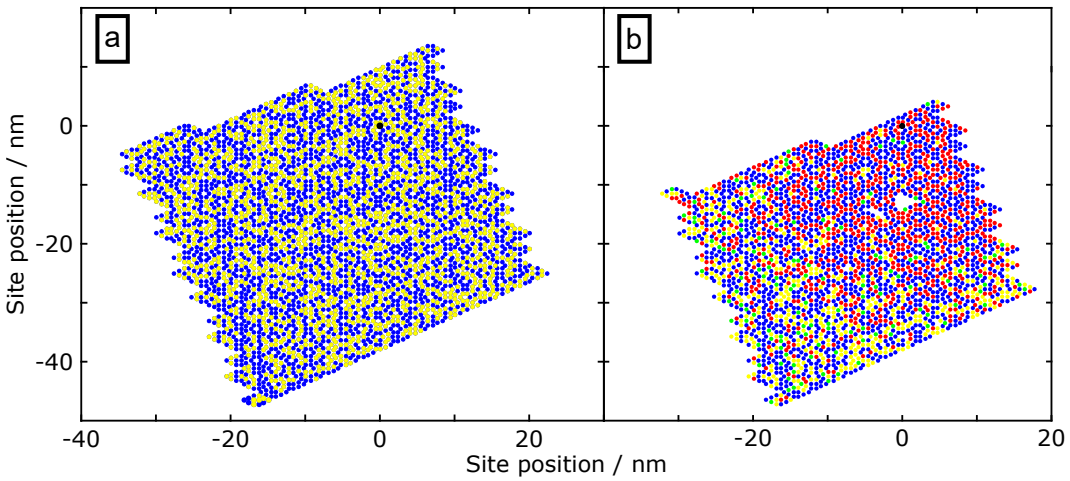

Figure 7-4: The position and occupancy of adatom sites relative to the injection site (black circle at the origin) from the arrangement of a perfect Si(111)-7×7 lattice, determined from STM images. (a) The surface prior to injection, with a yellow circle labelling an occupied site and a blue circle a clean adatom. (b) The change in occupancy of sites between (a) and the same area after a -2.1 V, 50 s, 900 pA injection at the black circle. The colour of the label at each adatom indicates the occupancy before and after injection; yellow, occupied in both images; red, from occupied to unoccupied; green, unoccupied to occupied; blue, unoccupied in both images. Only sites in both the before and after injection are included, with contaminated and unclear sites excluded.

routine may incorrectly estimate the tip position, in which case small changes in the selected before-injection tip site may result in a large change in the given after-injection tip position.

7.2.3 Radial analysis

The position of the tip in each image is then used as a relative zero point in the location of adatoms, such that both the before and after images have the same origin and, as the surface does not rotate, therefore the same adatom sites at each location. Due to image aberrations such as thermal drift, the position of each adatom site within the STM images is not necessarily identical to that expected for a perfect lattice. This means a "true" array is formed from the expected vector coordinates for the Si reconstruction, with each site occupied or unoccupied depending on the output of the molecule finding program. An example of this is shown in figure 7-4a. The before and after injection state of each individual site can then be compared and separated into four categories depending on whether it was or was not initially occupied, and whether the occupancy changes between the images. These can be seen in figure 7-4b.

After injection of charge carriers with energy above the nonlocal manipulation threshold, the distribution of molecules around the tip is expected to vary with radial distance from the injection site. To characterise this distribution, surface sites are separated into annular bins during analysis. It is assumed that each manipulated site (previously occupied site that became unoccupied) observed results in a molecule entering the physisorbed state, which have then either diffused to a neighbouring site or desorbed from the surface. While desorption results in fewer dark sites in the scan area, diffusion occurs when a molecule reabsorbs onto a nearby site and so the total number remains constant. Therefore as a simple approximation, within each radial bin the number of desorbed molecules is the overall change in the number of occupied sites, the number of diffused molecules is the number of previously unoccupied sites that become occupied, and the number of molecules that weren't manipulated is the number of occupied sites that remain occupied in the post-injection image. While here we assume that molecules will only diffuse to neighbouring sites, it is acknowledged that molecules will be able to diffuse between annuli, such that a molecule diffusing to a neighbouring annulus will cause an underestimate in the number of diffused molecules in the initial annulus, and an overestimate in the final annulus. This effect limits the minimum width of each annulus.

7.3 Thermal manipulation of benzene derivatives

The injection process in this report is the main method by which molecules on the surface are manipulated, however, even without the presence of hot carriers, the molecules are not entirely immobile at room temperature. Instead, the chemisorbed molecules have temperature dependent thermal energy, which results in a finite probability of transition from the chemisorbed to the physisorbed state and thereby undergoing desorption or diffusion and changing the specific positions as well as the total number of occupied sites on the surface. Additionally, molecules or other contaminants in the gas phase are able to adsorb to surface, increasing the number of occupied sites. The rate of desorption on the surface has been observed to be equivalent whether the STM is scanning with passive parameters or not scanning, so the process is independent of the position of the tip and is dominated by thermal manipulation effects [89].

Using a similar adsorbate-location system to that discussed here, Lock et al. tracked the location of chemisorbed molecules on an area of the surface between consecutive STM scans, counting the number of molecules that retain their initial site (i.e. do not desorb or diffuse) [108]. For each of the tested molecules, benzene, toluene and chlorobenzene, the site-specific (i.e. x = FC, FM, UC, or UM) rate of change was

Table 7.1: The site-specific rate of thermal manipulation, α^x, for chlorobenzene, benzene and toluene on a Si(111)-7×7 surface. Data from [108].

	α^x (10^{-4})		
Site, x	Chlorobenzene	Benzene	Toluene
FC	1.64 ± 0.07	10.32 ± 0.25	5.55 ± 0.37
FM	3.49 ± 0.19	8.98 ± 0.20	8.41 ± 0.50
UC	0.29 ± 0.12	2.09 ± 0.15	1.39 ± 0.08
UM	0.41 ± 0.02	1.53 ± 0.12	0.75 ± 0.04

observed to follow a first order rate equation,

$$\frac{dN_c^x}{dt} = -\alpha^x N_c^x, \tag{7.1}$$

which can be integrated to show that the number of chemisorbed molecules N_c at a surface site x (e.g. UM, FC, etc.) decays exponentially over time t with a rate constant α,

$$N_c^x(t) = N_c^x(0)\exp(-\alpha^x t). \tag{7.2}$$

Values of the site-specific rate constant α^x from reference [108] are displayed in table 7.1. Within the range of these molecules, it was observed that the benzene has the highest rate of thermal desorption, followed by toluene then chlorobenzene. This decreasing rate follows the increasing molecular mass of the molecules (benzene = 78 Da, toluene = 92 Da, chlorobenzene = 113 Da), which suggests that the total thermal manipulation rate of bromobenzene (157 Da) should be further reduced.

7.3.1 Correction for the thermal manipulation of toluene

The population of each site on the imaged surface is known at two points during the injection process; in the large before and large after injection images, separated by the injection itself. In the time between the injection and the before injection image as well as the injection and the after injection image, thermal manipulation will affect the surface coverage. Assuming a negligible duration injection, the number of molecules retaining the same position as the original image will vary as shown in figure 7-5.

Prior to injection, for each specific site within a unit cell the surface coverage can be assumed to be homogeneous, with an even distribution of molecules at all points on the surface. Whereas after injection, the distribution will vary radially from the injection site. Hence all thermal corrections are applied to each annulus independently based on the number of molecules at each site within. Note however, that observed

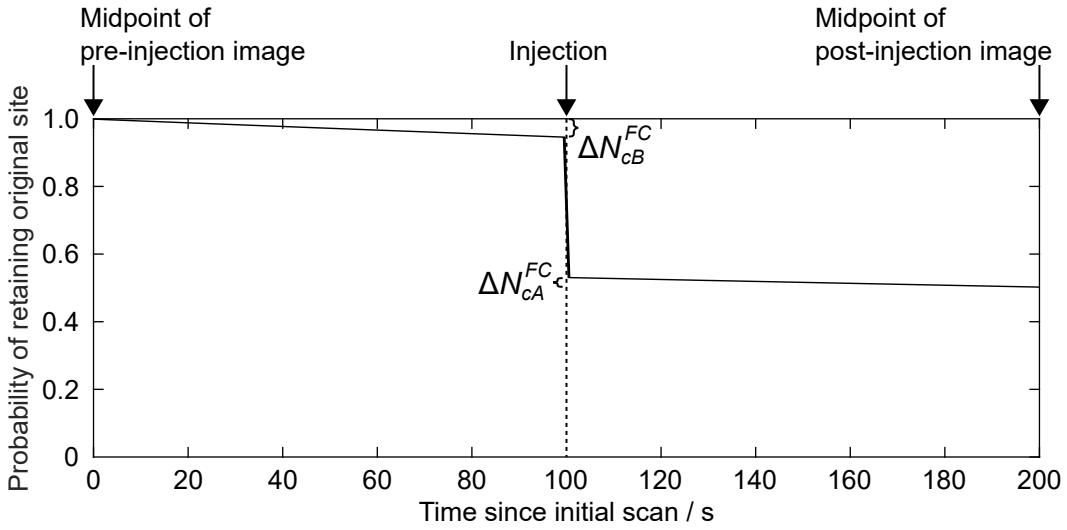

Figure 7-5: The probability of a toluene molecule initially chemisorbed at a faulted corner (FC) site of retaining its original position throughout the injection process, assuming the duration of the injection and small scans are negligible compared to the large scans of, here, duration 200 s. In this case, the overall manipulation probability is 0.50, however using equation (7.10) the probability of the injection inducing manipulation can be calculated as 0.52.

contaminants may affect the local population and such sites are removed from the analysis where possible. Assuming that the duration of the small images and the injection are negligible compared to the large scans, the average time between the initial scan and the injection, and the injection and the final scan are each equal to half of the large scan duration. This is approximately half of the difference between the time of the injection t_I and the time of the onset of the before injection scan t_0,

$$\Delta t \approx (t_I - t_0)/2. \tag{7.3}$$

By using the time of the onset of the scan as opposed to the duration of the scan, the duration of the small scans before, during and after the injection are implicitly included in the correction. This will result, however, in the midpoint of the images not quite aligning with the actual time of the midpoint. With this approximation, in the period before the injection the expected site-specific number of thermally manipulated molecules ΔN_c^x can be estimated using equation (7.2),

$$\Delta N_{cB}^x = N_c^x(t_0) - N_c^x(t_0 + \Delta t) \tag{7.4}$$

$$= N_c^x(t_0)\left(1 - \exp\left(-\alpha^x \Delta t\right)\right). \tag{7.5}$$

Similarly, the expected number of thermally manipulated molecules between the injection at $t_0 + \Delta t$ and the post-injection STM image at $t_0 + 2\Delta t$

$$\Delta N_{cA}^{x} = N_c^x\left(t_0 + \Delta t\right) - N_c^x\left(t_0 + 2\Delta t\right) \tag{7.6}$$

$$= N_c^x\left(t_0 + 2\Delta t\right)\left(\exp\left(\alpha^x \Delta t\right) - 1\right). \tag{7.7}$$

An estimate of the total number of thermally manipulated molecules is then simply the sum of equations (7.5) and (7.7). Assuming thermal manipulation is negligible, the probability of manipulation P due to the charge injection is simply one minus the proportion of molecules retaining their original position within an annulus,

$$P = 1 - \frac{N_c^x(t_0 + 2\Delta t)}{N_c^x(t_0)}. \tag{7.8}$$

From this, an estimate of the "true" probability of a molecule being manipulated during the charge injection pulse can be calculated by considering the population immediately before and after the injection. This results in the site-specific thermally corrected probability of manipulation

$$P' = 1 - \frac{N_c^x(t_0 + 2\Delta t) + \Delta N_{cA}^x}{N_c^x(t_0) - \Delta N_{cB}^x} \tag{7.9}$$

$$= 1 - \exp\left(2\alpha^x \Delta t\right) \frac{N_c^x(t_0 + 2\Delta t)}{N_c^x(t_0)}. \tag{7.10}$$

In the following chapters we primarily consider the total probability of a molecule being manipulated across all surface sites within an annulus between radius r and $r + \Delta r$, with Δr defined in the analysis with a usual value of 1 nm. In this case, the thermal correction is applied independently to each surface site within each annulus before averaging,

$$P'(r) = 1 - \frac{1}{N_c(r, t_0)} \sum_x \exp\left(2\alpha^x \Delta t\right) N_c^x(r, t_0 + 2\Delta t), \tag{7.11}$$

resulting the annulus-wide thermally corrected probability of manipulation due to charge injection. Examples of this are shown in figure 7-6

There are, however, two situations when the above equation will erroneously estimate the probability of thermal correction. Firstly, at distances far from the injection site or for low bias, duration or current injections, the probability of manipulation due to charge injection approaches zero, and so any manipulation must be due to thermal effects. As the rate coefficients are averages, in annuli or situations where little to no manipulation is observed, the thermal correction may estimate a negative number

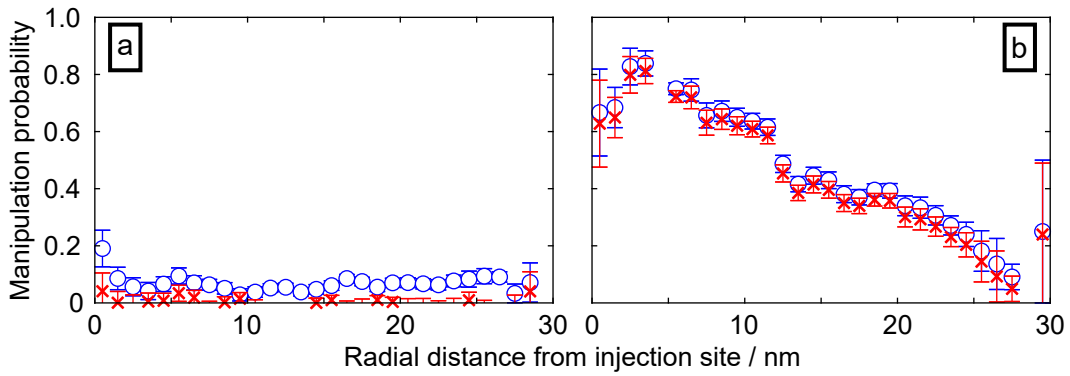

Figure 7-6: The radial distribution of the probability of manipulation of toluene chemisorbed on Si(111)-7 × 7 due to STM charge injection at (a) below (-0.7 V, 250 pA, 20 s) and (b) above (-1.6 V, 250 pA, 20 s) the nonlocal manipulation threshold. Blue circles show data prior to thermal corrections, while red crosses indicate the adjusted manipulation probability after applying thermal corrections. In (a), a number of the thermally corrected probabilities are calculated as negative but within uncertainty of zero due to the small probability of movement between the scans.

of manipulation events, for example the points below the axis in figure 7-6a. This is clearly unphysical, and, as such, is removed and replaced with zero manipulation due to the injection in later analysis. To prevent this affecting the shape of any overall fit, all points with a probability of manipulation below 0.05 are removed from the analysis prior to fitting. Secondly, in opposite situations, where all or nearly all remaining molecules are manipulated during the charge injection, the thermal correction will still have been applied between the injection and the after injection image. In this case we expect the "true" manipulation probability to approach unity, limited by contaminants on the surface, however, the thermal correction will calculate a greater theoretical unmanipulated population by overrepresenting the contaminant population. When averaging across a sufficient number of individual injections we expect a homogeneous distribution of contaminants, and so while this effect reduces the maximum calculated probability of manipulation it does not affect the overall shape of the distribution.

7.3.2 Thermal manipulation of bromobenzene

To measure the thermal manipulation rate of bromobenzene dosed Si(111)-7 × 7, the site-specific surface coverage has been measured. By comparing consecutive scans, the rate of non-injection related manipulation can be estimated. Figure 7-7 shows the sites that changed in occupancy between a pair of consecutive scans. Across eight pairs of 25 × 25 nm images, the probability of any occupied site becoming unoccupied during scanning was found to be (0.6 ± 0.1)%, whilst the probability of an unoccupied site

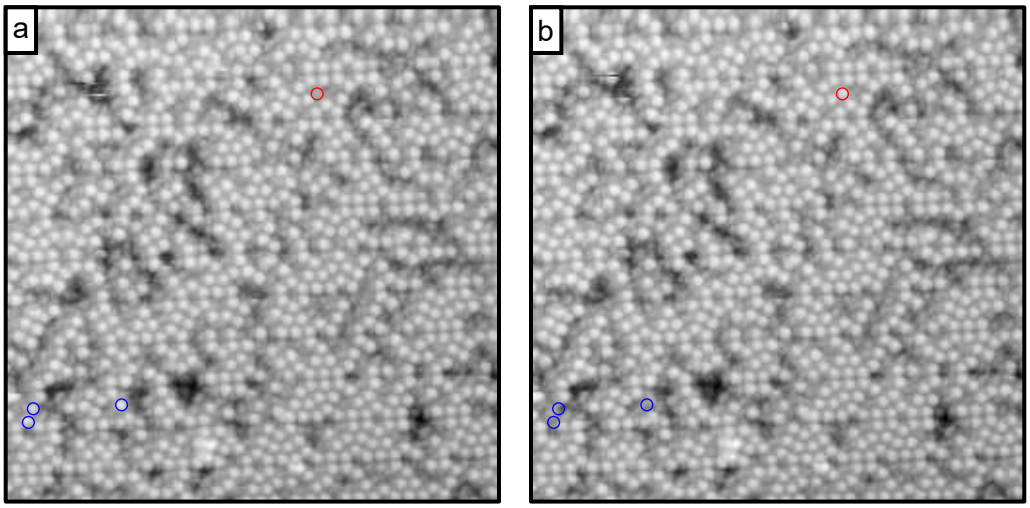

Figure 7-7: An example of the change in adatom occupancy for two consecutive 25×25 nm STM images of a BrPh dosed Si(111)-7 $\times$ 7 surface. Blue circles indicate sites that became occupied (i.e. light to dark in STM images) between the first (a) and the second (b) image, whilst the red circle indicates the one site that became unoccupied in the same period (dark to light).

becoming occupied was $(0.9 \pm 0.2)\%$. With uncertainty here from the standard error on the mean of a normal approximation with a 95% (2σ) binomial confidence interval. Note, however, that the manual molecule finding process is not 100% accurate, which means the number of changed sites is likely to be somewhat overestimated. Instead of the expected first order decay in the total number of occupied sites, here more sites become occupied than unoccupied. This difference cannot be explained by diffusion and desorption alone, instead, an additional source of adsorbates must contribute to the newly occupied sites.

Over a longer time period and averaged across a range of different surface positions, the total change in BrPh surface coverage at specific surface sites is shown in figure 7-8. Here, instead of following the same surface area over a number of STM scans, each image has been taken at a different location on the surface to reduce the effects of tip-influenced manipulation. In this figure, the occupancy of each site within each STM image is normalised compared to the surface coverage shortly after initial dosing, with uncertainty again given by a 2σ standard error. Hence while long term occupancy trends can be clearly observed for the total population, the specific change of individual sites is not tracked. The most important observation is that the overall surface coverage (figure 7-8a) does not dramatically change over the course of 7 hours, remaining within uncertainty of the initial coverage. Other trends appear to be in line with that observed

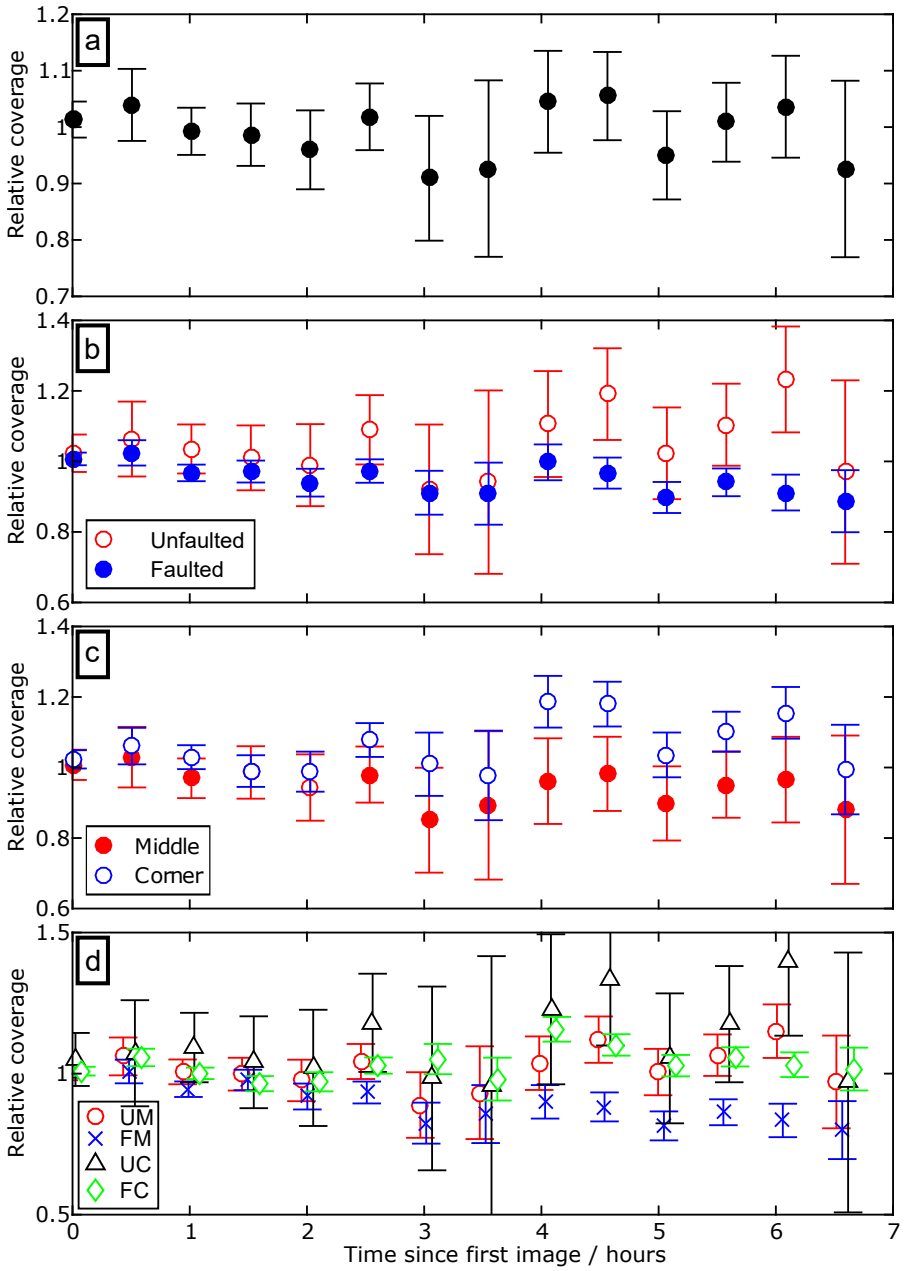

Figure 7-8: The change in surface coverage of BrPh dosed Si(111)-7 × 7 over 7 hours, relative to the coverage of an image shortly after initial dosing. Each data point is the average over all sites of the specified type across several individual surface images each taken at a new surface site, and uncertainty given by the standard error on the mean. In (d) points have been horizontally offset for clarity.

for the smaller benzene derivatives [108], with an increase in the occupancy of the unfaulted half of the unit cell compared to the faulted half (figure 7-8b) and a greater reduction (or lesser increase for faulted corner sites in figure 7-8d) in the number of occupied middle sites than corner sites (figure 7-8c).

In previous nonlocal analysis, a correction has been applied to the calculated probabilities of manipulation to control for the effects of thermal manipulation based on the rates calculated in reference [95]. However, in the case of bromobenzene dosed Si(111)-7 $\times$ 7, we do not observe a clear decay in the surface coverage due to thermally induced desorption and so a decay rate cannot be calculated. Instead, due to the nearly invariant coverage observed in figure 7-8a, we assume that the rate of thermal manipulation is negligible compared to the change in surface occupancy due to IET induced manipulation during the injection, and so thermal corrections are not applied in bromobenzene dosed experiments.

Chapter 8

Models of nonlocal manipulation

This chapter aims to provide more support for the nonlocal charge mediated manipulation and the associated hot charge transport models developed previously within the atomic manipulation group at the University of Bath in, for example, references [95] and [8]. Here we expand the measured parameter space beyond the experiments detailed in those references to show that instead of merely explaining the previously observed results, the model can be used to predict additional information from the system. This is primarily achieved by measuring the radius of nonlocal manipulation whilst varying the number of injected charge carriers and the injection bias, comparing the observed results with those predicted by the charge transport models. Although such an analysis is implicit in the prior reports, here I will make it explicit and show that the model fits the data well, thereby giving extra confidence in the model.

This work also explains more simply the shape and size of the nonlocal effect and therefore how it could be controlled. We attempt to mathematically separate the overall charge injection mediated nonlocal manipulation into the constituent parts of the process;

- the molecules manipulation properties,
- the experiment specific conditions including the injection parameters,
- the surface mediated hot charge transport dynamics,

in order to demonstrate the ability of nonlocal manipulation experiments to directly measure properties of the system and lead to a greater understanding of the hot charge transport that drives the observed manipulation.

We also consider the possibility of a different process driving the nonlocal manipulation, localised surface plasmons (LSP). In this case, charge injection results in the excitation of plasmons centred at the tip site, the decay of which may induce manipulation alongside light emission. LSPs are known to drive light emission from an STM junction in certain systems, and experimental work within the atomic manipulation group at the University of Bath demonstrates identical bias thresholds for both light emission and nonlocal manipulation in our system [11]. While this model shows strong agreement with the manipulation distribution for an individual injection, the determined constant prefactor term is not observed over varying injection times and the plasmon distribution requires a tip radius or tip-sample separation several orders of magnitude greater than experimentally used. Additionally, an LSP model fails to predict the observed nonlocal manipulation close to the tip injection site.

Hence, we instead propose that light emission is, here, mediated by the same charge transport as nonlocal manipulation; in which the final relaxation step may result in either manipulation of a molecule or photon emission. This is supported by both the identical bias thresholds for the onset of nonlocal manipulation or light emission, as well as an invariance of the ratio between these two outcomes per injected charge carrier with varying injection bias for injection into a single surface state.

This chapter contains experimental work mainly performed by the author using the injection process described in chapter 6.5 with nonlocal manipulation of bromobenzene dosed Si(111)-7 $\times$ 7. However in addition data has been provided by Dr Kristina Rusimova, comprising nonlocal manipulation data for toluene dosed Si(111)-7 $\times$ 7 gathered during her time as a PhD with Dr Peter Sloan. Where not otherwise credited, the additional data was provided as before-and-after injection STM images of the surface and all further analysis was performed by myself as described in chapter 7 and within this chapter.

The experimental results and analysis presented in parts of this chapter have been published in "The nanometer limits of ballistic and diffusive hot-hole mediated nonlocal molecular manipulation", by H.G. Etheridge, K. R. Rusimova and P. A. Sloan [10]. This publication primarily consists of the bromobenzene dosed Si(111)-7 $\times$ 7 nonlocal manipulation experimental work in section 8.2.5, and the analysis of sections 8.3 and 8.4. This paper is presented in full in appendix A.

Additionally, the conversion in section 8.6.1 between the probability of manipulation per charge-molecule interaction and the probability of manipulation per injected charge carrier has been published as a part of "Common source of light emission and nonlocal

molecular manipulation on the Si(111)-7×7 surface" by R. M. Purkiss, H. G. Etheridge, P. A. Sloan and K. R. Rusimova. This paper is presented in full in appendix B.

8.1 Introduction and experimental methodology

Nonlocal manipulation experiments of benzene derivatives on Si(111)-7 × 7 have previously suggested that the final manipulation step is a one electron or one hole process [8], identical to that observed in local manipulation [6]. By varying the injection current I, the time between charge injection can be controlled with $\delta t = e/I$. However within the attainable range of injection currents (no greater than 1 nA is used in this thesis) the lifetime of a charge carrier in the excited state, $\sim$ 200 fs [95, 113], is far less than the time between charge injection, $>\sim$ 100 ps. Thereby we expect only one hot charge carrier to be within the transport state at any one time during injection, and that each individual charge injection event occurs independently and statistically identically throughout the injection pulse. As such the distribution of the manipulation, for example those given in figure 8-1b [7], is consistent across experiments with different injection biases but constant total number of injected charge carriers.

In previous manipulation experiments within the atomic manipulation group at the University of Bath, the injection current I and injection duration t have generally been inversely varied to maintain the total number of injected charge carriers as $n_e = It/e$. This method was chosen to maximise the useful nonlocal effect; not so small that few manipulation events were observed, not so large that all molecules in the image were driven to desorp. Here, instead we maintain a constant injection bias and injection current whilst varying the total injection duration, and thereby the number of injected charge carriers, in order to directly observe the effect on the distribution and absolute extent of the manipulation region itself.

In this section, both the bromobenzene and toluene dosed experiments are performed as discussed in section 6.5; with the large before and large after injection images used for the data analysis process from section 7. The real-time electron dynamics can only be inferred, not directly observed, however the discrete manipulation events occur probabilistically with a rate determined partially by the nature of the charge carrier injection and subsequent transport. That is, all that can be observed is the locations of occupied and unoccupied sites and thereby the change in both the total occupation and, by comparing the sites directly, the change in the occupation of individual sites. Thereby we can determine the radial probability of manipulation $P(r) = N(r)/N_0(r)$, which is the ratio of the number of manipulated molecules $N(r)$ to the number of molecules in the original image $N_0(r)$ within an annulus at radius r. While in chapter 9 we consider the specific outcome of manipulation, here we only consider whether an occupied site becomes unoccupied during the current pulse. That is, both diffusion and desorption

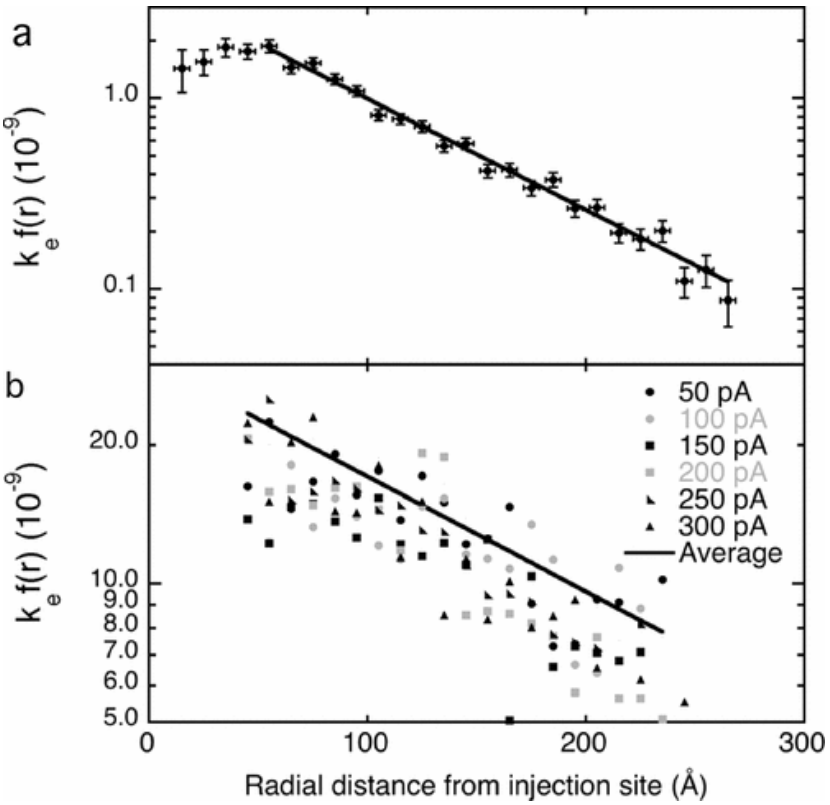

Figure 8-1: (a) Nonlocal desorption probability of ClPh dosed Si(111)-7×7 as a function of the radial distance from the injection site, here expressed as $K_e f(r)$, at an injection bias of + 2.7 V. Error bars reflect the 10 Å width of the annulus used in the analysis and the standard deviation on the mean assuming a Poisson distribution for the number of molecules before and after injection. The fit shows a single exponential decay, with points closer than 50 Å from the injection site omitted. (b) As for (a) but for six different tunnelling currents and an injection bias of + 3.6 V. The total charge dose was kept approximately constant by varying the duration of the injection pulse: 50 pA = 37.8 s, 100 pA = 18.9 s, 150 pA = 12.8 s, 200 pA = 10 s, 250 pA = 7.5 s, 300 pA = 6.3 s. Figure from [7].

events are considered and counted towards the overall number of manipulation events, while initially unoccupied sites becoming occupied are ignored.

While the bromobenzene data collected by myself and the toluene data collected by Dr Rusimova follow the same overall process, specific experimental parameters differ. More detailed description of the methodology behind the toluene-dosed data is provided by Dr Rusimova in reference [132], however critical differences are discussed here. In the collection of toluene data, the surfaces were dosed with near-saturation coverage corresponding to over 1000 molecules per 50×50 nm image and a dosing amount of $\sim$ 4 L. The bromobenzene surface was instead dosed with a lower amount, $\sim$ 2 L, which results in a somewhat lower surface coverage with an approximate occupancy of 4 molecules per unit cell. The reduction in the amount of dosing was used to aid in the manual location of the injection site within the large scale images. However note that the applied dose to surface coverage relationship is not linear, and despite the different molecules having different vapour pressure (which will affect the dosing as discussed in section 5.5) and dosing exposure the pre-injection surfaces are similarly covered. Additionally, previous measurement of the length scale of nonlocal manipulation of benzene dosed Si(111)-7×7 found it to be invariant for surfaces with coverage between 2 and 5 molecules per unit cell [133].

More importantly, injection on the toluene dosed surfaces is deliberately positioned into specific surface sites, generally undosed unfaulted middle (UM) sites near the centre of the large before injection scan for the data presented here, whereas this was not controlled for the bromobenzene data in which injections were performed at an arbitrary location towards the top left corner of the large scan. There are several reasons for this alteration in the methodology. Firstly, while it is known that the probability of manipulation per injected charge carrier for electron injection is strongly affected by the injection site [7], with the rate enhanced by injections into the faulted half of the unit cell and at corner holes into which electrons couple more efficiently, this effect has not been observed for hole injections [132]. Secondly, as shown in section 6.5.3, at room temperature the position of the tip relative to the surface is not entirely stationary. Hence, especially for longer duration injections, the position of the injection itself is limited by the apparatus and site-specific long duration injections are not possible here. While we go to great lengths to maximise the stability of the injection experiments, this additionally results in an upper limit on the duration of the injections; injections in this thesis are performed up to a maximum of 500 s at room temperature. Thirdly, by positioning the injection towards the top left of the image we maximise the observed radial distance from the injection site.

8.2 Radial distribution of desorption

The structure of the analysis in this section is based on prior work within the atomic manipulation group at the University of Bath performed by Dr Lock et al. [95], however note that in comparison to the earlier work here we introduce an additional τ_s term relating to the lifetime of a hot charge carrier within the surface transport state. This addition allows the probability of manipulation to be expressed per injected charge, removing the time dependence.

It is initially considered that charge carriers are injected from a point source, at a rate determined by the injection current I. Assuming that the injected charge carriers will then disperse radially symmetrically, the normalised "total interaction probability" ξ across all space for a single hot charge injection can be described as

$$\xi = 1 = \xi_0 \int_0^\infty \int_0^\infty 2\pi r \rho_d \left(r, t'\right) dt' dr, \tag{8.1}$$

where ξ_0 is a normalisation constant, r is the radial distance from the injection site, t' is the time since the injection of the charge carrier, and $\rho_d(r, t')$ is, essentially, the probability of finding the charge carrier at a given position at a particular time relating to the hot charge transport mechanism. This time dependence additionally includes the decay of the injected charge carrier via any molecule-charge interaction that leads to the decay of the charge without leading to manipulation of the molecule, be it via phonon scattering, photon emission or non-manipulative excitation, which is here described as a first order decay process with time constant τ_s defined by the lifetime of the transport state such that

$$\rho_d \left(r, t'\right) = \rho \left(r, t'\right) \exp\left(\frac{-t'}{\tau_s}\right), \tag{8.2}$$

with ρ purely describing the dynamics of a charge carrier in the surface transport state. The total interaction can therefore be expressed

$$\xi = \xi_0 \int_0^\infty \exp\left(\frac{-t'}{\tau_s}\right) \int_0^\infty 2\pi r \rho \left(r, t'\right) dr dt', \tag{8.3}$$

and so, as $\rho(r, t')$ must itself be normalised across all space,

$$\int_0^\infty 2\pi r \rho \left(r, t'\right) dr = 1, \tag{8.4}$$

$$\xi_0 = \frac{1}{\tau_s}. \tag{8.5}$$

Consider however that the manipulation events occur not at infinitesimal points, but at molecules with cross-sectional area σ which is taken here to be (1.5 Å)^2 [50]. Then, assuming a constant interaction probability across the molecule, the proportion of the total interaction that interacts with a specific molecule at radius r, $\xi_{m(r)}$, will be

$$\xi_{m(r)} = \frac{1}{\tau_s} \int_0^\infty \sigma\rho\left(r, t'\right) \exp\left(\frac{-t'}{\tau_s}\right) dt'. \tag{8.6}$$

This interaction probability can be considered as a number of manipulation "attempts", with each "attempt" resulting in a probability κ_e of manipulation. The previous normalisation results in each electron having a single total "attempt" across all space, and so this probability results in being per injected charge carrier. For each molecule, a first order rate equation can be used to calculate the probability P_{nm} of (for mathematical simplicity) not resulting in manipulation per injected hot charge carrier,

$$\frac{dP_{nm}}{dn_e} = -\kappa_e \xi_{m(r)} P_{nm} \tag{8.7}$$

$$P_{nm}(n_e, r) = \exp\left(-\kappa_e n_e \xi_{m(r)}\right). \tag{8.8}$$

This can then be related to the outcome of our nonlocal manipulation experiments in which the change in the number of molecules in an annulus centred at radius r is measured,

$$P_{nm} = \frac{N(r, n_e)}{N_0(r, n_e)}, \tag{8.9}$$

where $N(r)$ molecules remain of the initial $N_0(r)$ within the annulus after injection of n_e charge carriers. Thus the probability of manipulation

$$P(n_e, r) = 1 - \exp\left(-\kappa_e n_e \xi_{m(r)}\right) \tag{8.10}$$

$$= 1 - \frac{N(r, n_e)}{N_0(r, n_e)}. \tag{8.11}$$

This equation can be reframed to expose key parameters of the injection process. The number of charge carriers injected into the transport state is dependent on the injection current and pulse duration as

$$n_e = \frac{sIt}{e}, \tag{8.12}$$

with the additional factor s describing the fraction of the injected charge captured by the surface-resonance that mediates the nonlocal spread of the injected charge carrier; the value of s has previously been taken as unity [95]. Furthermore, the interaction probability can be further separated into the charge transport and surface-molecule manipulation dependent components, resulting

$$\xi_{m(r)} = \frac{\sigma}{\tau_s} C(r), \tag{8.13}$$

such that $C(r)$ is the time-integrated charge density for a single carrier across all space. This allows the overall manipulation probability to be expressed

$$P(r) = 1 - \exp\left[- \left(\frac{\sigma \kappa_e}{\tau_s} \right) \times \left(\frac{sIt}{e} \right) \times C(r) \right]. \tag{8.14}$$

The above expression highlights the three factors that control the measured distribution of the nonlocal manipulation;

- the fixed molecular manipulation properties through κ_e, σ, and τ_s,
- the experimental parameters that determine the number of hot charge carriers entering the surface transport state during the injection,
- the hot charge carrier dynamics themselves that drive the distribution of the nonlocal manipulation.

8.2.1 Dealing with contamination

This above analysis assumes that for each injection the probability of manipulation for a site directly beneath the injection site can be driven to unity, however this is not observed in actual experiments. Figure 8-2 shows that for sufficient injections (i.e. bias above the manipulation threshold, large number of injected charge carriers, etc.) the maximum probability of manipulation is instead observed to plateau at an approximately consistent value of roughly 0.75 for the apparatus and parameters used here. This upper boundary is due to the presence of contaminants on the surface which will not be manipulated by the injection, but are however imaged by the STM as immovable dark sites identical to chemisorbed benzene derivatives. As such, individual contaminant sites cannot be removed from the analysis and instead can only reasonably be observed statistically. Additionally for short duration injections the probability of manipulation is below one even for sites near the injection site, with not all molecules driven to desorb. The probability of manipulation for a site near the injection location over the range of injection durations used within this section are shown in figure 8-2.

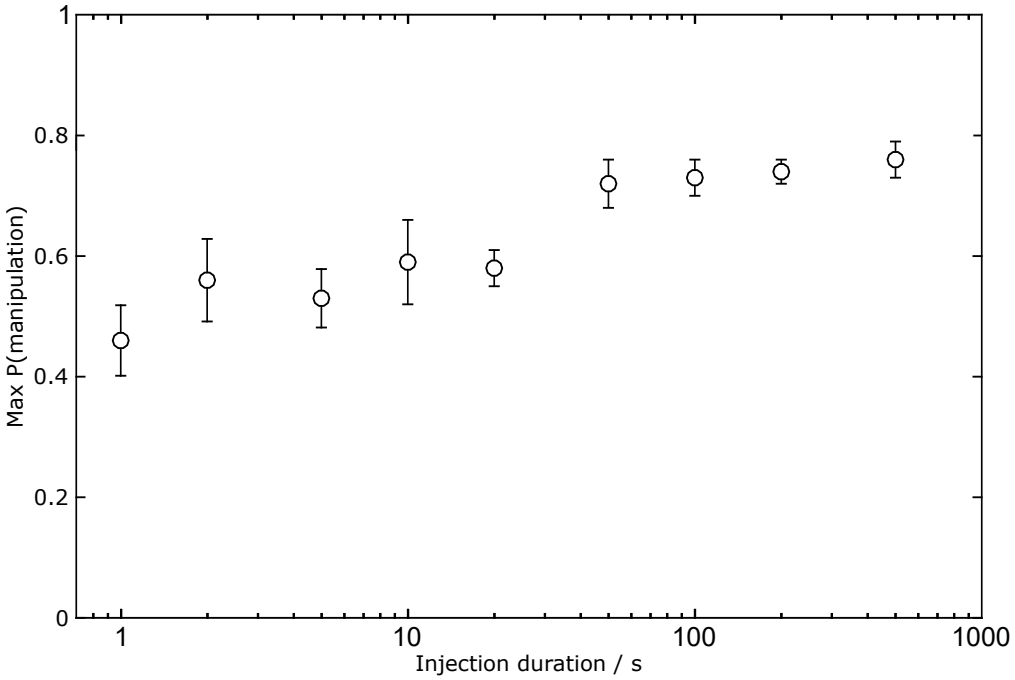

Figure 8-2: The probability of manipulation of chemisorbed bromobenzene for a site within a region of radius 2 nm surrounding the injection site averaged across a minimum of 5 injections at -2.1 V, 900 pA for each injection duration. Error bars show binomial uncertainty due to the finite number of observed sites.

To correct for these effects, a simple additional multiplicative term C is used within the fitting process such that the corrected probability of manipulation $P_c(r) = CP(r)$. From here on, all manipulation probabilities, $P(r)$, refers to a corrected manipulation probability.

8.2.2 Nonlocal manipulation half radius

We assume that the rate of charge decay due to interaction between hot charges within the surface transport state and chemisorbed molecules is negligible compared to other decay pathways, and hence that the charge lifetime is independent of the surface coverage. Thus for each individual injected charge carrier, the transport dynamics are independent of the injection duration. As such, the distribution of the manipulation should not be affected by varying the injection duration. Instead by varying the injection duration the footprint of the manipulation can be observed and extracted from the other parameters.

In this section the effective radius of manipulation is characterised by the half radius $r_{1/2}$; the radius at which the probability of manipulation due to the nonlocal charge

injection is one half of the probability of manipulation in the annulus closest to the injection site. Using this measure has several advantages. Primarily, it is a robust measure that is simple to extract from data, with changes in the fitting model generally only slightly affecting the value. In the following section we extract $r_{1/2}$ by fitting a 2 dimensional diffusive transport model to the probability distribution curves, however when fitting a Gaussian charge transport model as in section 8.5 the extracted half radii differ only slightly from the full coherent expansion-diffusion model. Secondly, it is a measure that combines several individual parameters that describe the distribution into a single measure, allowing for a simple comparison across a data set and thereby proves apt for further analysis.

An example of the manipulation probability distribution is shown in figure 8-3a for a 50 s injection on bromobenzene dosed Si(111)-7 $\times$ 7. This includes an example of the fit as well as the half radius and associated uncertainty. The uncertainty of the probability of manipulation within each individual annulus is given by 95 % standard error using a normal approximation such that the uncertainty

$$\sigma_P = 1.96\sqrt{\frac{P(1-P)}{N}}, \tag{8.15}$$

where P is the probability of manipulation and N is the total number of observed molecules within the annulus prior to the injection. Hence we calculate far greater uncertainty at radii at which few manipulation events or chemisorbed molecules are observed. Due to the radial dependence on the number of sites within an annulus (i.e. for infinitesimal width the number of sites $N \propto 2\pi r$), few sites are observed close to the injection site. Hence at short radii we observe an approximately linear increase of the number of sites within each annulus close to the injection site in figure 8-3b. However few sites are also observed at the greatest distances from the injection, which can also be seen in figure 8-3b, both due to the fact that little surface is imaged far away as well as the increased probability of these sites being removed during the molecule finding process. This uncertainty is used as a weighting on the fit, with the weight $w = 1/\sigma^2$, hence points with larger uncertainty will have a reduced impact on the fit and therefore other measured quantities such as the half radius.

8.2.3 Tunnelling current dependence

Figure 8-4 shows the radial distribution of the probability of manipulation of chemisorbed toluene for several injections at (a) -1.6 V and (b) -2.0 V with fixed total charge, but varying current and time. For each injection the injection duration was varied inversely

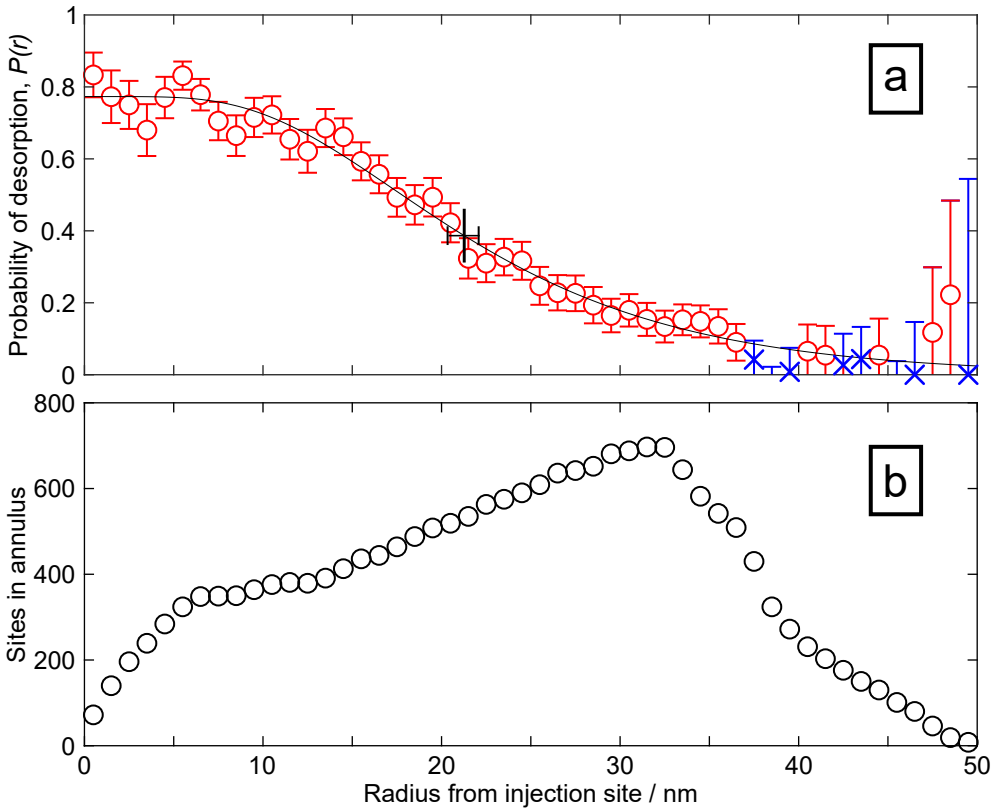

Figure 8-3: (a) The radial distribution of the probability of manipulation after a 50 s injection of -2.1 V, 900 pA at the origin for bromobenzene on Si(111)-7 × 7, with uncertainty given by the 95 % standard error. The black curve shows a fit based on the 2D diffusive transport model, with the marker at the half maximum probability displaying the half radius with uncertainty given by the 95 % uncertainty from the fit. Note that the blue crosses marks points with manipulation probability less than 0.05 which have not been included in the fit. (b) The total number of sites, occupied or unoccupied, found in both the before- and the after-injection molecule finding routines within an annulus of width 1 nm at a given radius from the injection, sum across three individual injections at different surface locations. For each injection, a surface area of 50×50 nm is scanned and the injection is performed towards the top left corner of the image.

with the current, such that the total number of injected charge carriers is constant at each bias, with $n_e = It/e = 3.12 \times 10^{10}$; resulting in injections with a duration of 7.14 s at 700 pA, 9.09 s at 550 pA, 12.50 s at 400 pA, 20.00 s at 250 pA and 50.00 s at 100 pA. This number of charge carriers was selected such that approximately half of the initially occupied sites were manipulated within the central half of the image, surrounding the injection site, for each injection. This is, in essence, a reproduction with new data and updated analysis, theory, and programs of the original report on nonlocal manipulation presented in figure 8-1b [7].

From this figure, fits to the data at each current were estimated and values of the half radius at each current were found. Figure 8-4c shows the relationship between the injection current and the half radius for the two series of injections, figure 8-4a at -1.6 V and figure 8-4b at -2.0 V, with all injections into clean UM sites. These biases are both above the nonlocal manipulation threshold, and were selected to be at the peak (-1.6 V) of the nonlocal transport surface state (i.e. S_3 in figure 4-2) and well above the manipulation onset (-2.0 V) attempting to maximise the observed range of ballistic transport as measured in reference [8] and discussed in section 8.4 below. The total number of injected charge carriers, and hence the duration of each injection, is the same at each injection current for either bias. Each data point in this figure is the weighted mean across a minimum of five individual injections, with the error bars here displaying the 95 % standard error on the half radius fit. As can be expected from the similarity of the probability distributions displayed in figure 8-4a, the measured half radii are approximately consistent across the range of injection currents. This results in mean half radii of 10.7 ± 0.3 nm at -1.6 V and 13.9 ± 0.3 nm at -2.1 V.

Discussion

Prior work, such as that discussed in section 4.3 [6, 12, 52], has shown that the final manipulation step is a one charge carrier DIET process when injecting either holes or electrons such that the rate of charge carrier injection is expected to have no effect on the overall manipulation dynamics or characteristics. Furthermore, as the rate of charge injection is several orders of magnitude below the lifetime of the charge carrier within the surface transport state even at the highest currents here, only one charge carrier will exist within the transport state at any one time. Hence multiple injected charge carriers will not interact, and the dynamics should again be charge injection rate independent. Figure 8-4 shows no clear variation in the half radii with respect to the injection current, suggesting that we again observe a one hole process.

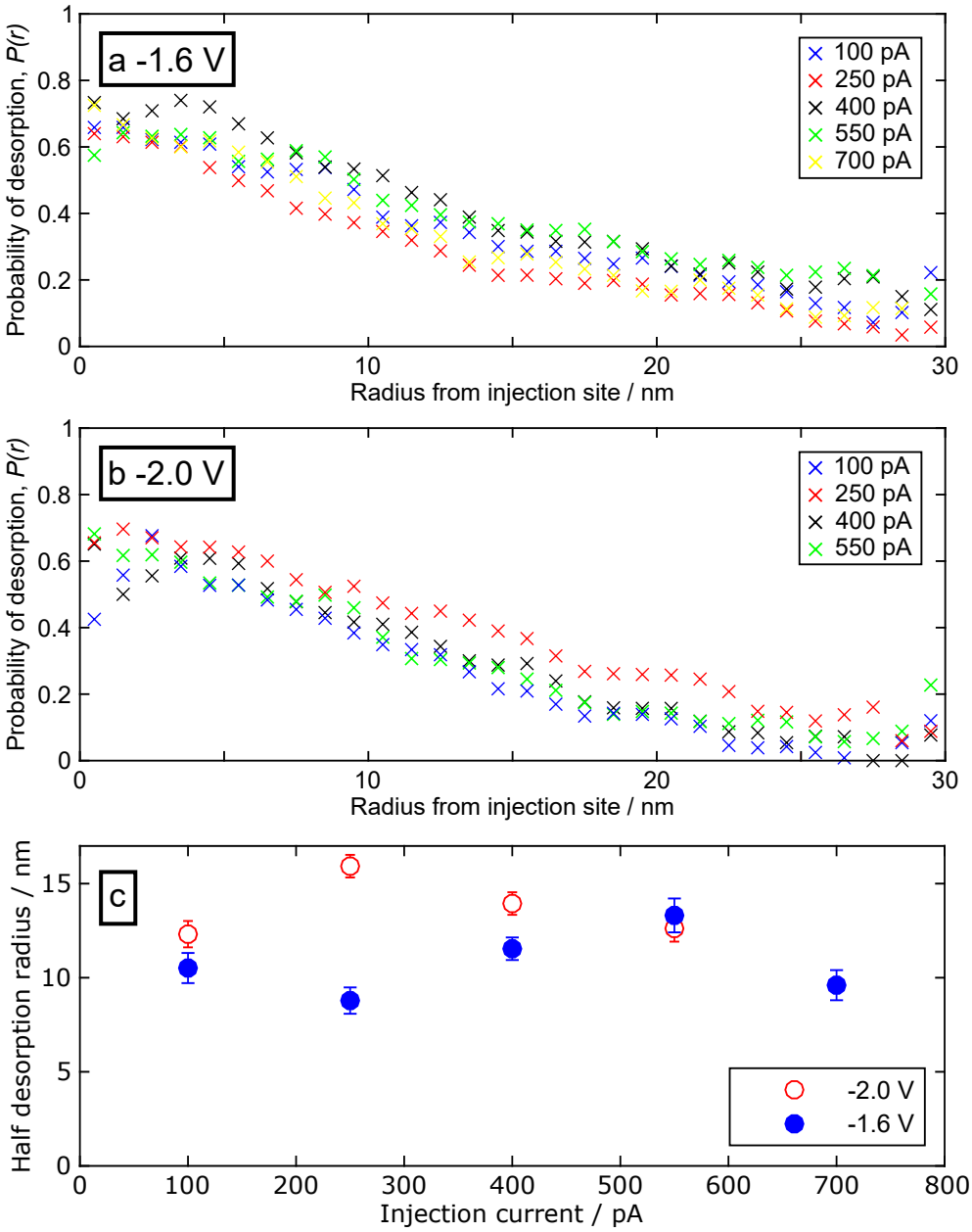

Figure 8-4: (a-b) The radial distribution of the probability of manipulation of chemisorbed toluene after an injection of (a) -1.6 V or (b) -2.0 V with a constant number of injected charge carriers, but varying current; for each injection $n_e = 3.12 \times 10^{10}$. Each data set is averaged across a minimum of five individual injections. Error bars are excluded to aid visual clarity, however the magnitude and distribution of the uncertainty is similar to that observed in figure 8-3a at all currents and biases. (b) The half manipulation radius as a function of the injection current at both -1.6 V (filled blue, data from (a)) and -2.0 V (unfilled red, data from (b)). The average half desorption radii are calculated to be 10.7 ± 0.3 nm for -1.6 V and 13.9 ± 0.3 nm for -2.0 V across the range of injection currents.

This relationship can be more clearly displayed by considering the total number of manipulated molecules across the surface as a function of the injection current, similar to that performed by Maksymovych et al. in reference [59]. Considering briefly that the order of the reaction n is unknown, such that the local rate of manipulation will vary as $r \propto (I/e)^n$, then the probability of manipulation at any one point on the surface will vary not only with the injection current, but also the local charge density at that point. Therefore in nonlocal manipulation the overall manipulation rate will scale as

$$R \propto \left[\frac{I}{e}C(r)\right]^n, \tag{8.16}$$

in which $C(r)$ is the time-integrated charge density for a single injected carrier from equation (8.13). From this, the distribution of the probability of manipulation in equation (8.14) can be re-expressed, showing that

$$P(r) = 1 - \exp\left(-\frac{\sigma\kappa_e s}{\tau_s}t\left[\frac{I}{e}C(r)\right]^n\right). \tag{8.17}$$

Considering all manipulation events across the surface by summing across each annulus,

$$-\sum_r \ln\left(1 - P(r)\right) = \frac{\sigma\kappa_e s}{\tau_s e^n}tI^n\sum_r C(r)^n. \tag{8.18}$$

Therefore the total (contaminant corrected) rate of change of the surface coverage

$$-\frac{1}{t}\sum_r \ln\left(\frac{N(r)}{N_0(r)}\right) = \frac{\sigma\kappa_e s}{\tau_s e^n}I^n\sum_r C(r)^n \tag{8.19}$$

$$\propto I^n. \tag{8.20}$$

While the radial summation could be expressed in integral form, to aid comparison with the data analysis we consider each radius as a discrete value over which the probability of manipulation is summed. The result of this analysis applied to the data of figure 8-4c is shown in figure 8-5. At both biases the order of the manipulation process is shown to be within uncertainty of unity, with $n = 1.1 \pm 0.3$ for -1.6 V holes and $n = 1.0 \pm 0.4$ for -2.0 V holes. This result further implies a one hole DIET process in agreement with the half radius analysis within this range of injection biases and currents.

8.2.4 Bias dependence

In figure 8-6, the half radius for a toluene dosed surface is shown for the injection of both holes between -1.2 V and -2.2 V at 900 pA and electrons between +2.0 V and

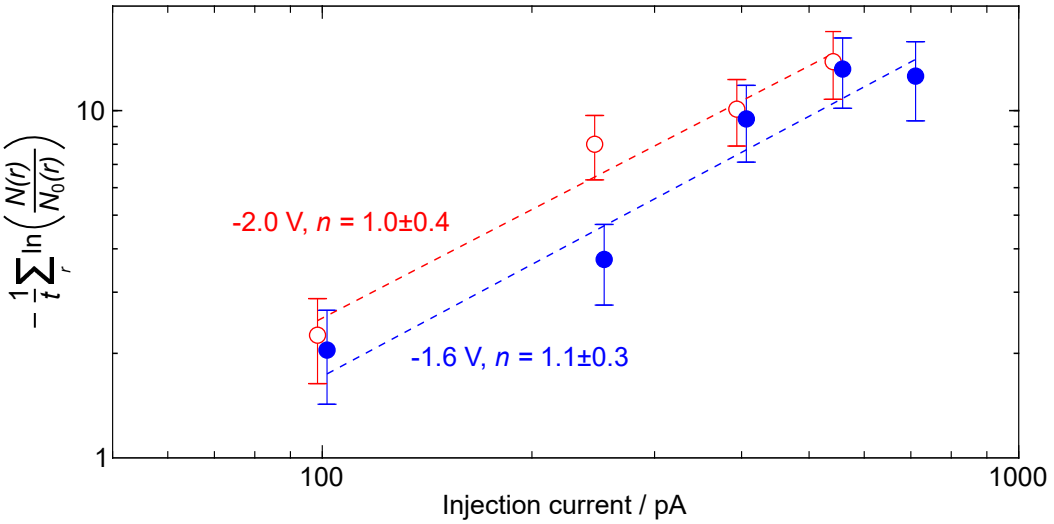

Figure 8-5: Current dependence of the rate of nonlocal manipulation of toluene for the injection of holes at -1.6 V (blue, filled) and -2.0 V (red, unfilled). At each current, the total injection duration is varied to maintain a constant total number of injected charge carriers, with $n_e = 3.12 \times 10^{10}$. At either bias a weighted linear least squares fit to equation (8.20) is shown, with the slope n indicating the order of the underlying manipulation process. Data points have been horizontally offset to aid clarity.

+3.6 V at 750 pA. The negative bias hole injections were all performed for 20 s, and hence have a constant number of injected charge carriers. Conversely, the positive bias electron injections occurred with varying injection durations; 30 s for +2.0 V and +2.2 V, 15 s for +2.4 V and +2.6 V, 10 s for +2.8 V, 5 s for +3.0 V, 2 s for +3.2 V, and 1 s for +3.4 V and +3.6 V. For both positive and negative bias injections, the bias range begins slightly above the onset of nonlocal manipulation; which is -1.2 V for hole mediated and +2 V for electron mediated. While additional data was collected at lower negative biases, between -0.7 V and -1.1 V, too little manipulation was observed to extract a value for the half radius and it has therefore been removed from this analysis. Even so, any manipulation occurring at biases below the nonlocal manipulation threshold is likely due to effects other than the nonlocal charge injection induced manipulation. The upper bounds of the biases selected correspond to the onset of higher lying bands within the surface or bulk structure. For the positive electron injection, the +3.6 V limit corresponds with an unoccupied band within the underlying bulk Si at +3.5 V [112]. Whereas the -2.2 V bias lies slightly below the -2.4 V onset of the S_4 surface state [8].

Within reasonable uncertainty, for negative bias hole injection above the nonlocal threshold, the radius of manipulation appears to have an approximately linear de-

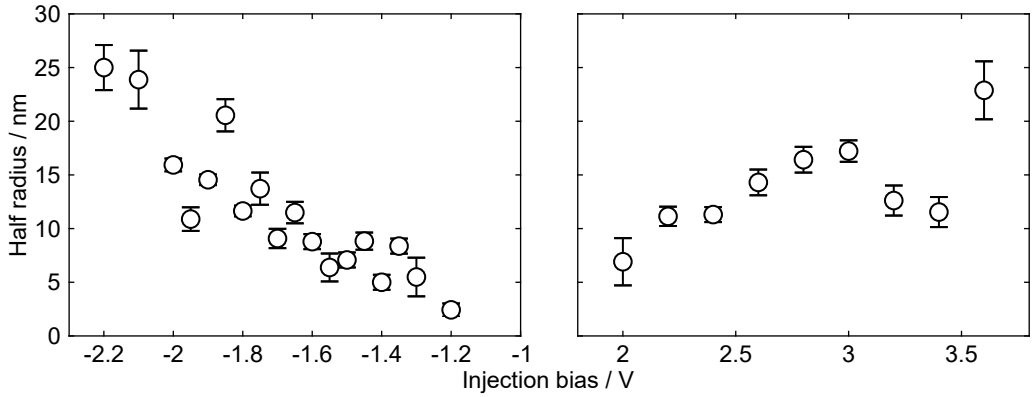

Figure 8-6: The half manipulation radius as a function of the injection bias for both hole at 900 pA (left, negative) and electron at 750 pA (right, positive) injection. While hole injections were performed for 20 s, the electron injections have a varying injection duration; 30 s for +2.0 V and +2.2 V, 15 s for +2.4 V and +2.6 V, 10 s for +2.8 V, 5 s for +3.0 V, 2 s for +3.2 V, and 1 s for +3.4 V and +3.6 V. Each data point is calculated from a minimum of four individual injections. Error bars show the 95 % standard error from the half radius fit to the manipulation probability distributions.

pendence on the injection bias. As the varying injection duration will affect the half radius, only broad trends can be considered from the bias-varying electron injection data. In section 8.2.5, dependence of the injection duration on the half radius is considered with the injection bias held constant. However, several trends can be identified from this data. Between +2.0 V and +3.0 V the half radius monotonically increases, which is similar to that observed for hole injection, with reductions in the number of injected charge carriers only reducing the rate of increase. This trend is not observed at higher biases; the half radius decreases between +3.0 V and +3.2 V (injection duration 5 s and 2 s respectively), then sharply increases between the two highest biases (+3.4 V to +3.6 V) despite the unchanging (1 s) injection duration.

Discussion

Within a specific transport state, the charge transport process should not be dependent on the injection bias. After injection into the surface transport state, charge carriers undergo an ultrafast decay process ($\sim$ 10 fs) relaxing into a common energy level at the bottom of the surface state [113]. Hence further transport will occur identically for all charge carriers injected into a specific band, regardless of the initial injection bias. This is in agreement with the characteristic and voltage invariant wavelength of light emitted during STM charge tunnelling above the nonlocal manipulation threshold [11]. However, here we observe that the radius of the manipulation is strongly affected by

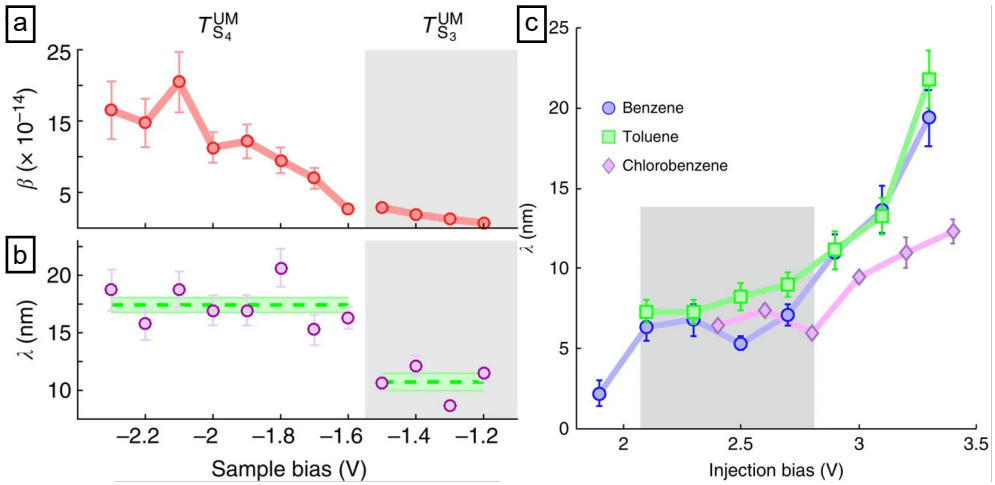

Figure 8-7: (a-b) Injection bias dependence for injection into UM adatoms site on the nonlocal manipulation of UM toluene molecules for negative bias hole injection on; (a) the probability of manipulation per injected hole β, and (b) the diffusion length scale λ. Note that in comparison to the λ used elsewhere in this thesis, λ here does not follow the standard form for 2D diffusion and is instead greater by a factor 2. Figures from [8]. (c) Injection bias dependence on the length scale of nonlocal manipulation of benzene, toluene and chlorobenzene for positive bias electron injection. Figure from [95].

the injection bias both for positive and negative injection biases. The hole injection results are in agreement with previous observations shown in figure 8-7a-b [8], where, while the length scale of the nonlocal effect plateaus between -1.6 V and -2.2 V, the probability of manipulation per injected charge carrier increases relatively linearly with increasing bias across the range. The increase in the probability of manipulation leads to an increase in the total amount of manipulation at distances far from the injection site as the injection bias is increased, and hence we observe an increase in the half manipulation radius.

For electron injection, threshold biases have previously been observed at approximately +2.0 V and +2.8 V, for example characterised by the plateau region of the diffusion length scale in figure 8-7c [8, 95]. These biases correspond with the onset of nonlocal manipulation within the antibonding state of the Si-Si bond beneath the adatom, and a higher energy surface resonance through the opening of a new diffusive pathway into the underlying +3.4 V bulk state respectively [95]. In STM the total tunnelling current is formed of contributions by charge carriers tunnelling into any available surface state. In this case, the LDOS of the surface can be considered as multiple distinct states each with different distributions. Depending on the various LDOS and the factors discussed in chapter 2, at certain injection biases transition from the tip into one specific state

may dominate the tunnelling current. As the bias is varied, tunnelling into other surface states may effectively reduce the number of charge carriers tunnelling into the former state even if the LDOS is increased at the new bias. Here for example, manipulation can only occur for charge carriers tunnelling into the manipulative surface transport state, however the onset of tunnelling into the higher lying bulk state reduces the number of charge carriers able to induce manipulation. Hence, this latter pathway may itself reduce the radius of the nonlocal manipulation in concert with the previously observed increase in the diffusive length scale by suppressing the probability s of an injected charge carrier entering the surface transport state. While previously s has been set to unity, the value is clearly affected by the injection bias and results in the observed change in the half radius across the range of injection biases for both hole and electron injection in figure 8-6.

Exact measurement or calculation of the voltage dependence of s is beyond the scope of this thesis, however here we consider a simple model in which all injected charge enters a single surface state. In this model, a charge carrier in the tip at a specific bias may tunnel from the tip to the surface with a probability dependent on the LDOS of the surface state at that bias. The tunnelling current, through s, is proportional to the total probability of a charge carrier tunnelling from the tip to the surface at biases between the onset of the surface state and the injection bias. Hence, by integrating across all biases between these two points, we obtain a value proportional to s at that injection bias. Using scanning tunnelling spectroscopy, the peak position and distribution of surface states in Si(111)-7×7 have been observed to be well approximated by Gaussian distributions [8]. At a specific injection bias V_{tip} and with the onset of the surface state at 0 V,

$$s = A \int_0^{V_{tip}} \exp\left(\frac{-(V - V_0)^2}{\sigma^2}\right) dV, \tag{8.21}$$

in which V_0 and σ are, respectively, the peak position and the FWHM of the Gaussian surface state, and A is an unknown constant of proportionality. The LDOS is site-specific, with both the width and peak bias varying slightly across surface sites [8]. Considering a single available surface state into which charge carriers are injected, say the S_4 surface state measured at an FC site at which $V_0 = -2.4$ eV and $\sigma = 0.5$ eV [8] shown in figure 8-8a, s can be plot as a function of the injection bias, as in figure 8-8b.

s cannot be directly related to the half manipulation radii presented in figure 8-6, instead we compare the general trends. Increasing the injection bias results in both an increase in $r_{1/2}$ as well as an increase in s. Qualitatively, in the hole injection bias range of figure 8-6 (-1.2 to -2.2 V), the form of both $s(V)$ and $r_{1/2}(V)$ are similar;

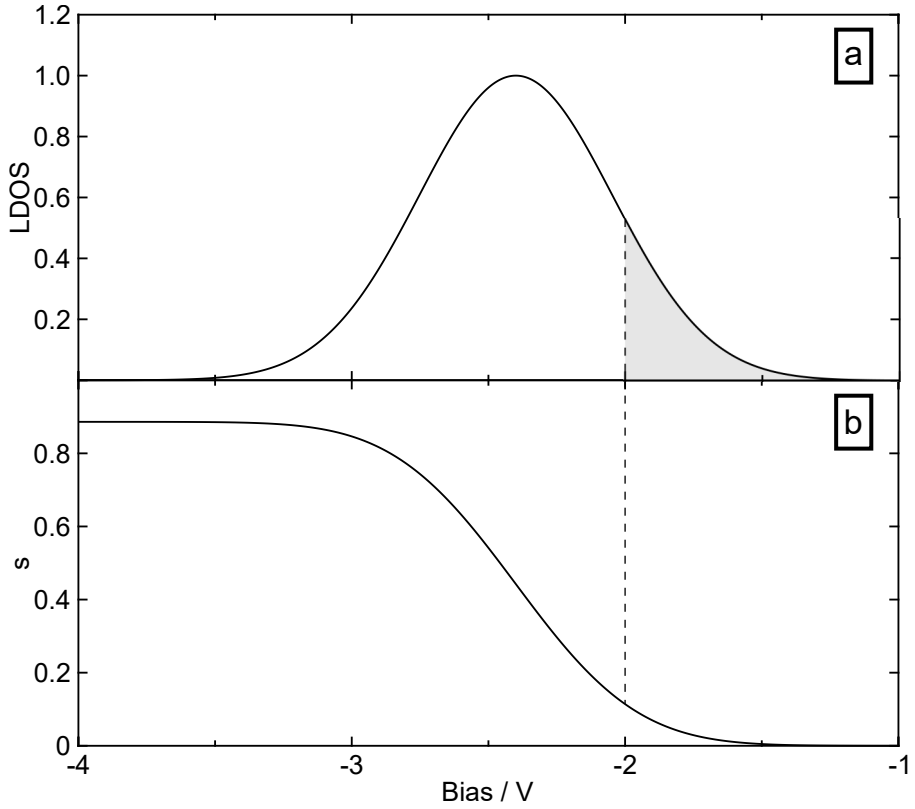

Figure 8-8: (a) A normalised Gaussian approximation of the LDOS of the S_4 surface state of Si(111)-7 $\times$ 7 above FC adatoms, with the peak position (-2.3 V) and FWHM (0.5 V) from STS measurements [8]. (b) The integral of (a) between 0 V and the tip bias as a proportional estimate of the probability s of a tunnelling charge carrier entering the transport state. The dashed line and shaded region denote the available LDOS and corresponding value of s for a -2.0 V injection.

in either case monotonically increasing and relatively linear with increasingly negative biases. Hence this model, in a simple approximation with only injection into a single surface state at a specific surface site, can explain the voltage dependence of s. A more detailed analysis of the injection bias dependence of s is to be the focus of future work. Here, for consistency with prior work, the value of s is taken as unity within the remainder of this chapter.

Electric field

The radial extent of the depopulated region after nonlocal manipulation has been shown to be invariant to the presence of up to four steps within the region [102]. Assuming a tunnel gap of ~ 10 Å and a step height of 3.14 Å, there would be significant variation in the strength of the tip-surface electric field at the top of a step or the bottom of multiple steps. Yet no change in the nonlocal manipulation spot-size was observed. Similarly, within the range of injection biases in figure 8-6 the tip-sample separation has been measured to only vary by ~ 2 Å [132]. This is far less than the change observed over several steps, and results in a nonlinear variation of the electric field across the surface with varying bias. Therefore we can rule out any active role for the tip-sample electric field in the manipulation process.

8.2.5 Charge carrier dependence

Toluene

Previously, the total number of charge carriers has been maintained throughout each injection series by inversely varying the injection current and duration such that the number of charge carriers is constant in equation (8.12). Here however, the number of injected charge carriers is effectively varied by sequentially injecting into the same site. In this case, the injection procedure occurs identically to that used for the data presented above and discussed in chapter 6.5. However after each injection, rather than moving to a new site and repeating the process, after the large after injection image the injection process is repeated at the same location. Each individual injection consists of a 15 s injection at -1.6 V and 900 pA. An image of the surface prior to any injection, as well as after each injection in the series, is displayed in figure 8-9.

From the radial distribution after each injection we compare the distribution of molecules not before and after each injection individually, instead considering the total change across every injection by comparing the surface coverage between the initial pre-injection scan (figure 8-9 0 s, top left) to each after-injection image individually. From this, the half radius for each total injection duration is calculated across a minimum of three

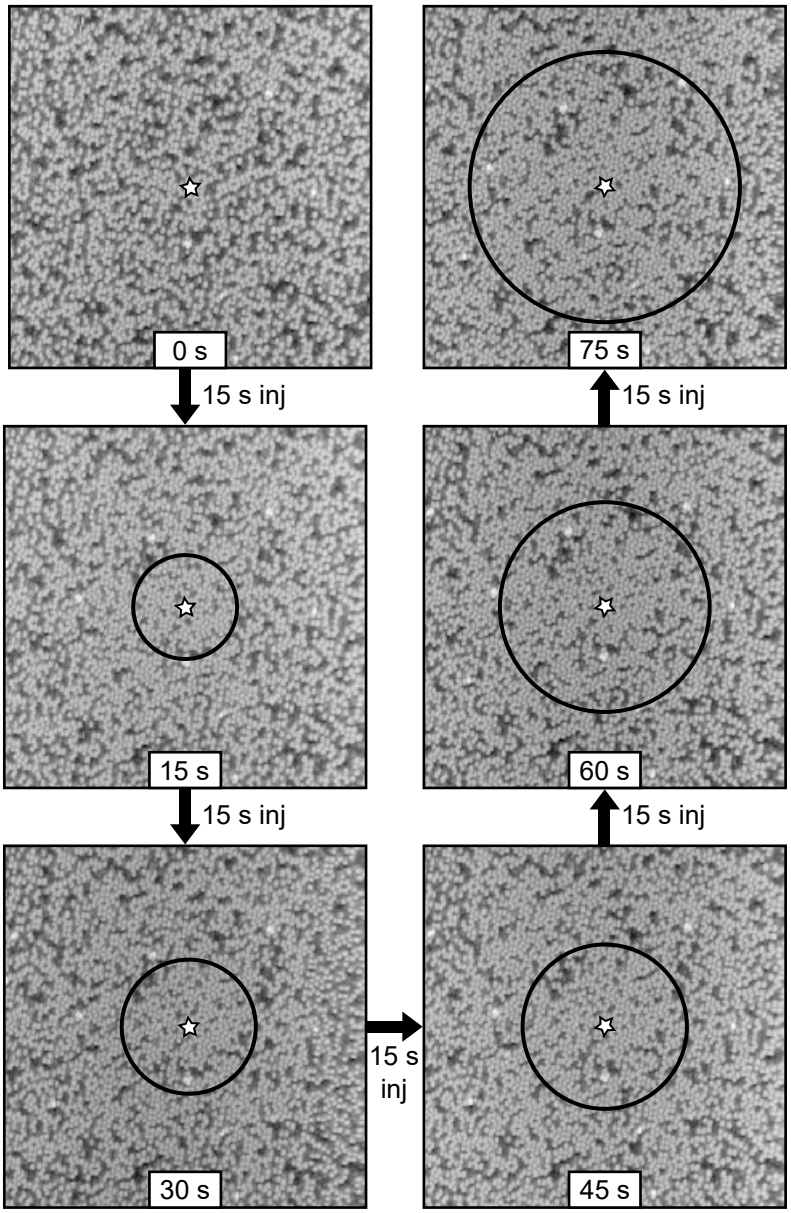

Figure 8-9: 50 × 50 nm STM images of the same toluene dosed Si(111)-7 × 7 surface area at passive scanning parameters over a series of 5 consecutive 15 s injections (-1.6 V, 900 pA) into the same site, centred at the star. The first image (top left) precedes the first injection, the second image (middle left) displays the surface after a single 15 s injection, and the third image (bottom left) displays the same surface after a second 15 s injection. This pattern continues for a total of 5 injections. Each image is labelled with the total injection duration prior to that image, as well as a circle indicating the half manipulation radius compared to the surface prior to any injection.

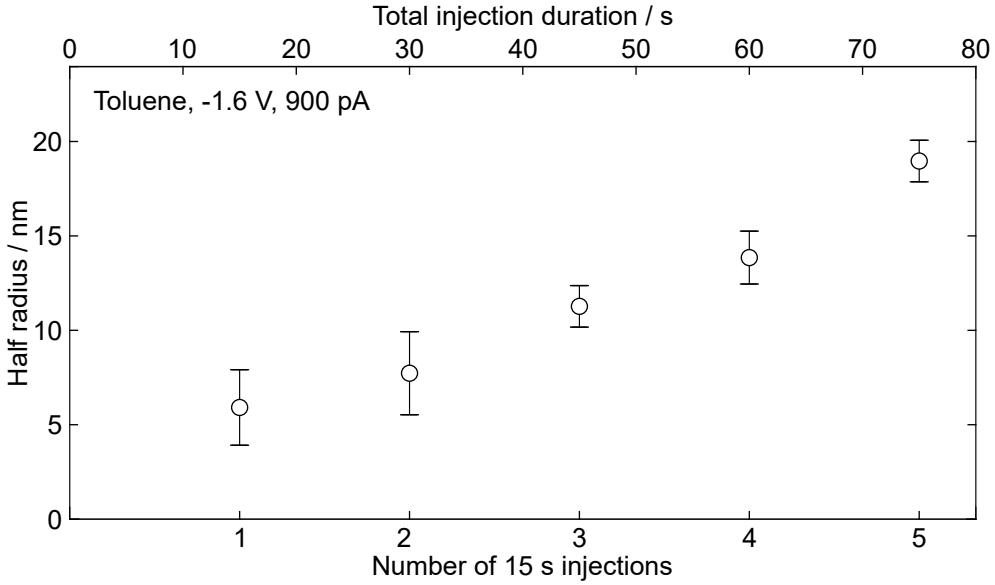

Figure 8-10: The half manipulation radius as a function of the total injection duration for a series of injections at -1.6 V and 900 pA averaged over several injections for toluene dosed Si(111)-7 × 7. Each individual injection has a duration of 15 s, after which subsequent injections are repeated at the same site. For more detail, see main text.

injections, which is displayed in figure 8-10. Here we observe a strong relationship between these parameters, with an approximately linear increase in the half radius across the range of injection times up to a maximum here of 19 ± 1 nm for a total injection of 75 s. However note that within this range the total number of injected charge carriers varies by less than an order of magnitude; between approximately 1×10^{11} electrons for a 15 s injection and 4×10^{11} electrons for a 75 s are injected.

In this injection process the amount of time spent scanning the surface is dramatically increased for longer duration injections, especially compared to the previous individual location injections. As such, the time for thermal manipulation or additional surface changes is equally increased. Attempts to correct for this as discussed in section 7.3.1 have been made, however the injection process cannot be simply considered as two thermally varying populations with a step change between as in figure 7-5. Alternatively, calculating the change in surface coverage for each injection (i.e. before and after injection images) separately and then summing the probability distributions often resulted in extreme over correction with the probability of manipulation commonly negative. Additionally, this process results in the surface area being scanned many times over the course of the longer duration injections. Whilst at passive scan parameters changes in

the surface are not expected to result from scanning, some tip-sample interactions are likely to occur. Hence for the longer duration injections, an increased rate of observed manipulation will be observed. Finally for the longest injection times, the observed probability distribution commonly remains substantially above zero even at the edges of the scan image. This results in an increased uncertainty on the resultant fitting parameters. While this doesn't correlate to a large uncertainty in the half radius, this effect does limit the ability to further extract information from this experiment.

Bromobenzene

Here we consider the charge carrier dependence on the half manipulation radius for bromobenzene dosed Si(111)-7 × 7 for injections at 900 pA and two different injection biases; -1.6 V and -2.1 V, comprising a total of greater than 34,000 manipulation events. In this case each injection is performed separately, at a new position on the surface, such that for each injection duration the injection process varies only by the length of the injection itself. As such, in contrast to the prior toluene charge carrier dependence, the surface is not re-scanned part way through. Furthermore, here injections are performed into an arbitrary location towards the top left of the scan area in order to maximise the possible observed radial distance from the injection site. STM images of the surface before and after -2.1 V injection can be seen in figure 8-11, as well as the location of the injection and resultant half manipulation radii. While the -1.6 V data was taken over a series of several tips, the -2.1 V data was all taken with a single tip.

The resultant half manipulation radii for bromobenzene dosed Si(111)-7 × 7 at both -1.6 V and -2.1 V for injections between 1 s and 500 s, alongside the toluene dosed injections from figure 8-10, are shown in figure 8-12. Note that here, unlike with figure 8-10, the x-axis is on a logarithmic scale to reflect the exponentially increasing nature of the duration of the injections used. The data for both toluene and bromobenzene dosed surfaces show approximately the same trends, however the increased range of injection times within the latter reveals additional information. In this case, across the range of injections with duration below 20 s the half radius only slightly increased with increasing number of injected carriers; $r_{1/2} = (9 \pm 2)$ nm for -2.1 V injections and $r_{1/2} = (7 \pm 3)$ nm for -1.6 V injections within this range. While injections with fewer injected charge carriers were attempted, on average too few molecules were manipulated to allow for the fitting process to measure a half radius. At greater injection durations the size of the nonlocal effect increased with a corresponding increase in the half radius, in a manner similar to that observed within the range of the toluene data. For 500 s injections $r_{1/2} = (33 \pm 2)$ nm for -2.1 V and $r_{1/2} = (18 \pm 1)$ nm for -1.6 V, the

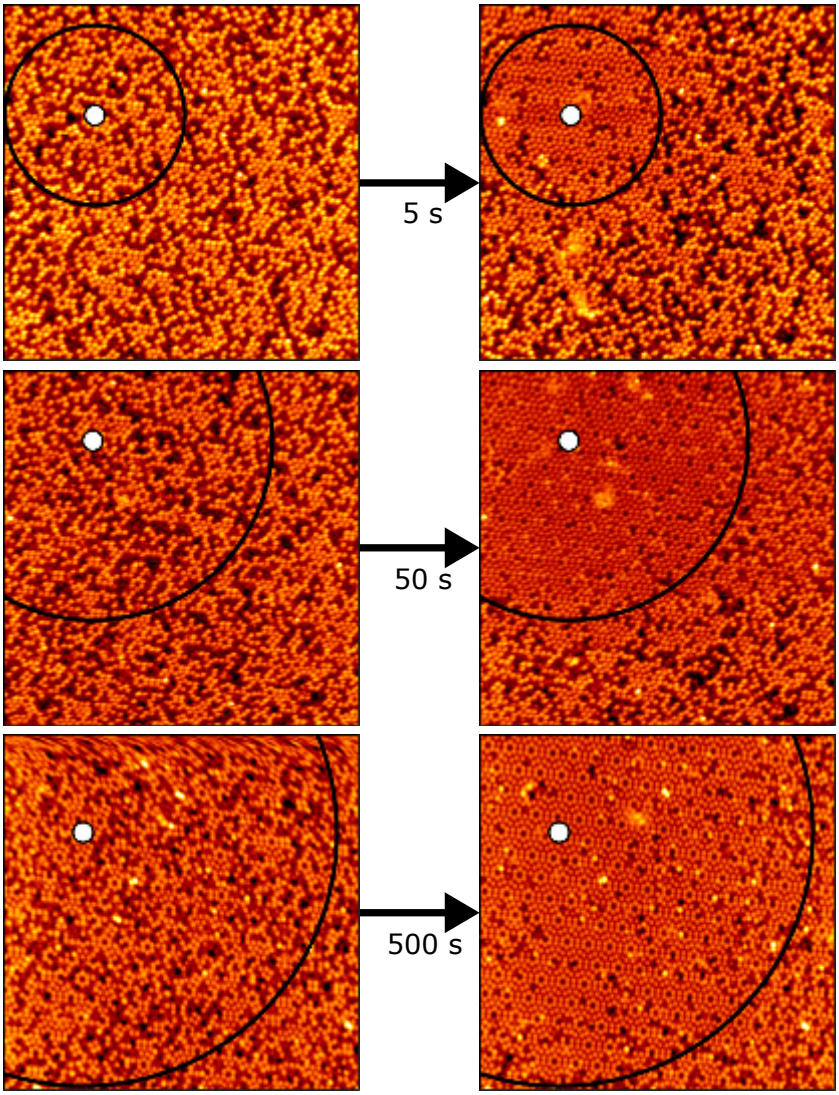

Figure 8-11: 50×50 nm STM images of Si(111)-7×7 dosed with bromobenzene at passive scanning parameters (+1 V, 100 pA) before (left) and after (right) a −2.1 V 900 pA injection of duration 5 s (top), 50 s (middle) and 500 s (bottom) located at the white circle. The black circles indicate the radius at which the probability of manipulation in the after image is half that in the annulus nearest the injection site. To allow easy visual comparison the circle is also superimposed on the before images. Figure and caption adapted from [10]

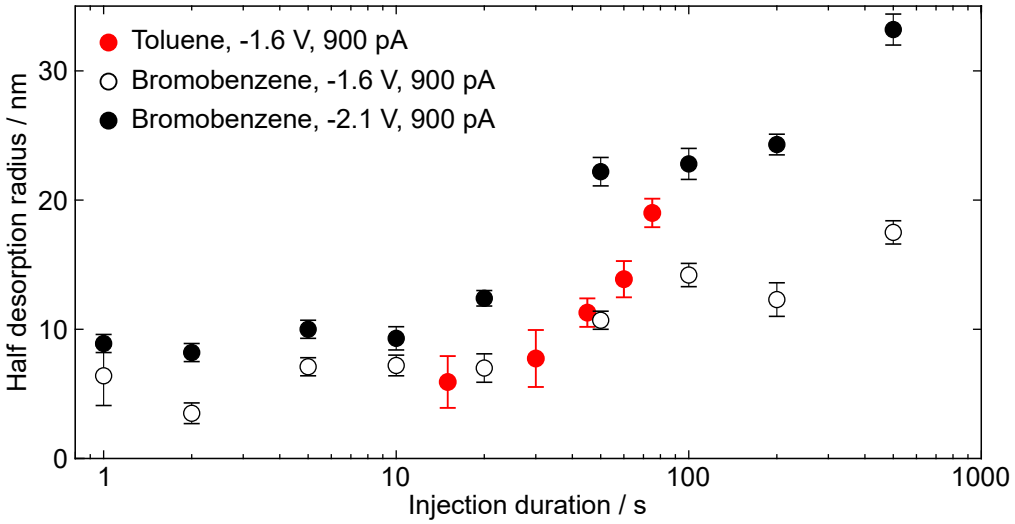

Figure 8-12: The half manipulation radius as a function of the injection duration for injection into both a toluene (-1.6 V, filled red, from figure 8-10) or bromobenzene (-1.6 V, unfilled black, and -2.1 V, filled black) dosed Si(111)-7 × 7 surface averaged across a minimum of 2 individual injections. Error bars show the 95 % standard error of the half radius fit at each injection duration, however in many cases the uncertainty is smaller than the marker size.

longest injections and the largest half radii at each bias. Overall, unlike with the aforementioned toluene dosed experiment, while the increase in the half radius with injection duration is monotonic, it is not linear. Instead for both voltages, although much clearer in the -2.1 V data, below approximately 10 s there is an initial region with a roughly consistent minimum half radius followed by a logarithmic increase.

Discussion

During injection molecules will desorb from the surface at a rate inversely proportional to their distance from the injection site, with the proportion of remaining molecules given by equation (8.14). For sufficient duration injections all molecules immediately surrounding the injection site will be manipulated, hence the probability of manipulation will saturate at a maximum value and further injection is unable to induce manipulation close to the injection site. As the length scale of the manipulation has previous been shown to be independent of the surface coverage, the probability of manipulation for each molecule is independent of the injection duration and so the completely manipulated region will expand at a rate determined by the distribution of the injected charge, $C(r)$.

In the following sections we link the results of these charge carrier dependent experiments to the charge transport models developed in references [95] and [8].

8.3 Diffusion from an instantaneous point source

The probability of finding a charge carrier at a position on the surface $\rho_d(r, t')$ from equation (8.6) will depend on the transport dynamics of the injected charge. Here we initially consider a purely diffusive model from a point source, as in reference [8], in which the injection of charge carriers from the tip of the STM immediately results in the charges at the bottom of the surface transport state localised entirely and directly beneath the tip. After the injection, each hot charge is then free to randomly diffuse across the surface within the surface state resulting in the transfer of charge from regions of high concentration (i.e. beneath the tip) to low concentration. In this case the motion of each charge carrier is not affected by an external force, for example an electric field, and after the initial injection no further charges are injected on the timescale of the lifetime of a hot charge within the diffusive state. Furthermore as in section 8.2, we initially deconvolve the charge transport itself from the decay of the charge carriers, instead focusing purely on the dynamics of the charge carriers within the surface state; $\rho(r, t')$.

The two dimensional diffusion equation is applicable, such that

$$\frac{\partial \rho}{\partial t'} = D_x \frac{\partial^2 \rho}{\partial x^2} + D_y \frac{\partial^2 \rho}{\partial y^2}, \tag{8.22}$$

in which D_x and D_y are the coefficients of diffusion in the x and y-axes respectively [134]. At $t' = 0$, all injected charge is located beneath the tip, which is here defined as the origin and so

$$\rho(x, y, t' = 0) = \delta(x)\delta(y), \tag{8.23}$$

with δ as the Dirac delta function. Note that here the total charge dose is normalised, such that each charge injection results in a probability unity of finding the charge carrier across all space. In equation (8.22) the x and y terms on the right hand side are uncoupled, such that diffusion along the x-axis is only dependent on x (i.e. first term on the right hand side) and diffusion along the y-axis is only dependent of y (i.e. second term on the right hand side). As such, the solution must itself be the product of two uncoupled solutions describing the independent distributions in x and y;

$$\rho(x, y, t') = \rho_x(x, t')\rho_y(y, t'). \tag{8.24}$$

Using equation (8.24) as a trial solution for equation (8.22) results

$$\frac{\partial \rho}{\partial t'} = \frac{\partial \left(\rho_x \rho_y\right)}{\partial t'} \tag{8.25}$$

$$= \rho_x \frac{\partial \rho_y}{\partial t'} + \rho_y \frac{\partial \rho_x}{\partial t'}, \tag{8.26}$$

and hence

$$\rho_x \frac{\partial \rho_y}{\partial t'} + \rho_y \frac{\partial \rho_x}{\partial t'} = D_x \frac{\partial^2 \rho}{\partial x^2} + D_y \frac{\partial^2 \rho}{\partial y^2}. \tag{8.27}$$

This above equation can be rearranged to show that

$$\rho_y \left(\frac{\partial \rho_x}{\partial t'} - D_x \frac{\partial^2 \rho_x}{\partial t^2} \right) + \rho_x \left(\frac{\partial \rho_y}{\partial t'} - D_y \frac{\partial^2 \rho_y}{\partial t^2} \right) = 0, \tag{8.28}$$

and thereby a non-trivial solution to equation (8.22) exists in which each of the two sets of brackets in equation (8.28) is equal to zero, such that

$$\frac{\partial \rho_x}{\partial t'} = D_x \frac{\partial^2 \rho_x}{\partial t^2} \tag{8.29}$$

and

$$\frac{\partial \rho_y}{\partial t'} = D_y \frac{\partial^2 \rho_y}{\partial t^2}. \tag{8.30}$$

Both equations (8.29) and (8.30) are themselves in the form of the one dimensional diffusion equation, hence we can consider the standard form of the solution [134], in which

$$\rho_x(x, t') = \frac{A_x}{\sqrt{4\pi D_x t'}} \exp\left(\frac{-x^2}{4 D_x t'} \right) \tag{8.31}$$

alongside the equivalent for ρ_y with constant A_x replaced with A_y, where A_x and A_y are arbitrary normalisation constants. Thus the full solution will have the form

$$\rho(x, y, t') = \rho_x \rho_y = \frac{A_x A_y}{4\pi t' \sqrt{D_x D_y}} \exp\left(-\frac{x^2}{4 D_x t'} - \frac{y^2}{4 D_y t'} \right). \tag{8.32}$$

Across all space the probability of finding the charge carrier must be unity for all t', and so we apply the normalisation condition

$$\int_{x=-\infty}^{\infty} \int_{y=-\infty}^{\infty} \rho dy dx = A_x A_y = 1. \tag{8.33}$$

Previous charge injection experiments on Si(111)-7 $\times$ 7 have shown that the charge transport process is isotropic [7], with the probability of manipulation equivalent in

any direction from the injection site, hence $D_x = D_y = D$ and

$$\rho(x, y, t') = \frac{1}{4\pi D t'} \exp\left(\frac{-x^2 - y^2}{4Dt'}\right). \tag{8.34}$$

This can be reframed in terms of cylindrical polar coordinates, such that

$$\rho(r, t') = \frac{1}{4\pi D t'} \exp\left(\frac{-r^2}{4Dt'}\right). \tag{8.35}$$

To obtain the probability of finding the charge at any point in space at any time after injection, here we reintroduce the exponential decay term describing the rate of thermalisation of the injected charge. Applying the above solution to equations (8.6) and (8.13) results the time integrated charge density for a single carrier across all space, in which

$$C(r) = \frac{1}{4\pi D} \int_0^\infty \frac{1}{t'} \exp\left(\frac{-t'}{\tau_s}\right) \exp\left(\frac{-r^2}{4Dt'}\right) dt', \tag{8.36}$$

the solution to which has be found using Maple to be

$$C(r) = \frac{1}{2\pi D} \mathrm{K}_0\left(\frac{r}{\sqrt{D\tau_s}}\right), \tag{8.37}$$

in which K_0 is a modified Bessel function of the second kind. Furthermore, considering the diffusion length λ, which is related as usual for 2D diffusion through $\lambda = \sqrt{4D\tau_s}$,

$$C(r) = \frac{2\tau_s}{\pi\lambda^2} \mathrm{K}_0\left(\frac{2r}{\lambda}\right). \tag{8.38}$$

Thus, by inserting the above form into equation (8.14), the total probability of manipulation due to the injection of n_e charge carriers as a function of the radial distance from the injection site

$$P(r) = 1 - \exp\left(-\frac{sIt}{e} \frac{2\kappa_e \sigma}{\pi\lambda^2} K_0\left(\frac{2r}{\lambda}\right)\right). \tag{8.39}$$

The above equation has shown excellent agreement with the distribution of manipulation for the injection of both holes and electrons across a range of injection biases above the nonlocal manipulation thresholds. To aid in simplicity for fitting to experimental

data letting

$$t_0 = \frac{\pi e \lambda^2}{2\sigma\kappa_e Is}, \tag{8.40}$$

in which all parameters other than λ and κ_e are taken as known constants or controlled experimental variables, allows the total manipulation probability P to be expressed in terms of the characteristic time-scale of the manipulation t_0;

$$P(r) = 1 - \exp\left(-\frac{t}{t_0} K_0\left(\frac{2r}{\lambda}\right)\right). \tag{8.41}$$

In this case, fitting can proceed with only two unknown terms; the diffusion length λ, and the characteristic time-scale t_0. In the above sections, for example sections 8.2.3 to 8.2.5, the half radii were extracted by fitting a curve with the form of equation (8.41) and calculating the point at which the probability of manipulation is equal to half of the maximum value; as shown in figure 8-3. In the prior fitting processes the value of these variables was neither initially set nor constrained. Clearly however, especially as the value of t_0 is dependent on the square of λ, each of the fit-estimated variables are strongly correlated; with slight changes in the value of one variable resulting in a large change in the other. However when varying only the injection duration, it is expected that time-scale and the length-scale of the manipulation should be invariant. By considering the form of the half radius itself, we can obtain further information of the value of these constants.

8.3.1 Derivation of the half radius

For observed values of λ, t_0 and κ_e the proportion of manipulated molecules undergoes a relatively sharp step at some radius from the injection site; close to the injection site nearly all molecules have been manipulated, far from the injection site nearly all molecules remain. Only in a relatively small band are both states observed with comparable probability. Furthermore, the manipulation probability described by equation (8.41) is a single exponential function dependent on r, and so for each non-zero injection duration, $t > 0$, there exists a single value of r such that $P(r) = \frac{1}{2}$. This radius is defined as the half radius, $r_{1/2}$. Using the half radius offers two key benefits. Firstly, it is a value combining each of the several variable terms into a single value, simplifying analysis. And secondly, it is extremely simple to extract from data and is relatively robust with slight changes to the fitting parameters only slightly changing its value. In this section, an analytical expression for the half radius is derived. Furthermore, a simplified approximation for the half desorption radius is defined. This simplified ap-

proximation allows ease of fitting, as well the ability to simply extract approximations of several key fitting parameters.

In an annulus at $r_{1/2}$, such that half of all molecules have been manipulated,

$$P(r = r_{1/2}) = \frac{1}{2} = \exp\left(-\frac{t}{t_0} K_0\left(\frac{2r_{1/2}}{\lambda}\right)\right). \tag{8.42}$$

Thus,

$$t(r = r_{1/2}) = \frac{\ln(2) t_0}{K_0\left(\frac{2r_{1/2}}{\lambda}\right)}. \tag{8.43}$$

The above equation is not analytically solvable for $r_{1/2}$, hence we consider an approximation for the zeroth order modified Bessel function of the second kind in which, for sufficiently large argument A [135],

$$K_0(A) \approx \sqrt{\frac{\pi}{2}} \frac{e^{-A}}{\sqrt{A}}. \tag{8.44}$$

Therefore in cases such that $r_{1/2} \gg \lambda$, equation (8.43) can be approximated

$$\frac{2r_{1/2}}{\lambda} + \frac{1}{2}\log\left(\frac{2r_{1/2}}{\lambda}\right) \approx \log\left(\frac{t}{t_0}\right) - \log\left(\sqrt{\frac{2}{\pi}}\log(2)\right). \tag{8.45}$$

For a sufficiently large injection duration, such that

$$t \gg t_0 \sqrt{\frac{2}{\pi}}\log(2), \tag{8.46}$$

and away from the injection site, where

$$\frac{2r_{1/2}}{\lambda} \gg \frac{1}{2}\log\left(\frac{2r_{1/2}}{\lambda}\right), \tag{8.47}$$

equation (8.45) can be further approximated

$$r_{1/2} \approx \frac{\lambda}{2}\log\left(\frac{t}{t_0}\right). \tag{8.48}$$

Thus an approximation of the effective manipulation radius of nonlocal STM is bounded by a $\log(t)$ dependence for sufficiently long duration injections; a linear increase in the radius requires an exponential increase in the injection time. This equation allows the

extraction of both λ, simply the gradient, and t_0 averaged across injection durations, requiring only measurements of the half radii instead of complete fits.

8.3.2 Discussion

A comparison between the full expression given in equation (8.43), the Bessel approximation from equation (8.45) and the complete logarithmic approximation in equation (8.48) is given in figure 8-13. At short injection duration, here below approximately $t = 10$ s, divergence is seen between the log approximation and the other two equations, with the log approximation dropping non-physically to negative half radii at $t = 2$ s while the other two tend to zero. At even shorter injection duration the Bessel approximation and the complete equation begin to diverge, however only slightly. Extremely short injections are not considered in detail in this section due to the extremely limited number of manipulated molecules in such experiments. Conversely at large injection duration the form of all three equations are similar, although the logarithmic equation results a slightly increased gradient. This will manifest as a slight increase in the extracted value of λ in comparison to the less approximate forms of the model, or measurement of λ from the distribution of manipulation using equation (8.41).

To determine robust values for λ and κ_e we perform an iterative fitting routine, using determined values of λ from equation (8.48) to feedback into the initial curve fitting process. We initially find these parameters, as well as the contaminant scaling factor, by fitting the model given by equation (8.41) to the data; as shown in figure 8-14 for -2.1 V injections into a bromobenzene-dosed surface. Each injection duration thereby generates unique values for the three fitting parameters. From these fitted curves we determine values of the half radius for each injection duration and hence plot the injection duration dependence of the half radius as presented previously in figures 8-10 and 8-12. Here, however, we now then fit the logarithmic dependence given by equation (8.48) and so extract another measure of λ, with the value here additionally fit across the range of injection times for each voltage. This results in the dashed lines displayed on figures 8-15 for toluene dosed surfaces and 8-16 for bromobenzene dosed surfaces, showing the excellent fit of this logarithmic model to the experimental results. Here, we only fit to the half radii from injection times greater than or equal to 10 s; below which a plateau is observed in contrast to figure 8-13. For the toluene dosed surface in figure 8-15 this analysis results $\lambda = 9 \pm 7$ nm, with the large uncertainty indicative of the limited range of injection times within this data set. In the case of the bromobenzene dosed surfaces resulting in figure 8-16, $\lambda = 7 \pm 2$ nm for -1.6 V and $\lambda = 11 \pm 3$ nm for -2.1 V. Each of these values of λ is in agreement with previous measurements based on

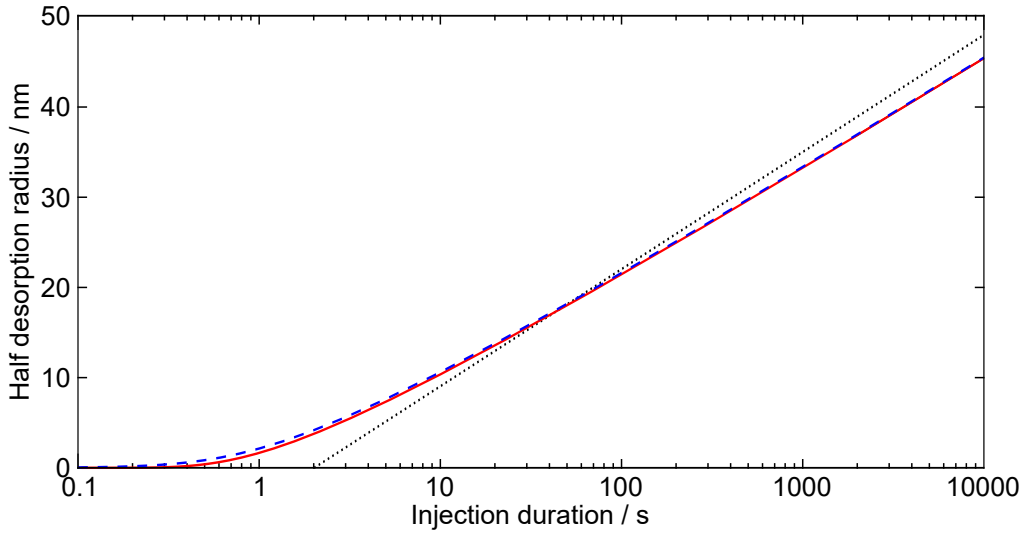

Figure 8-13: The radius $r_{1/2}$ at which half of the molecules initially adsorped onto a surface have not yet been manipulated during nonlocal STM as a function of the injection time. (Solid red) the calculated value from equation (8.43). (Dashed blue) an approximation from equation (8.45), using an approximation for the Bessel function given in equation (8.44). (Dotted black) a further approximation given in equation (8.48) in which only the terms dominant for large injection duration are regarded. The parameters t_0 and λ for each of the equations are set to reasonable values for a -2.1 V injection into a bromobenzene dosed surface.

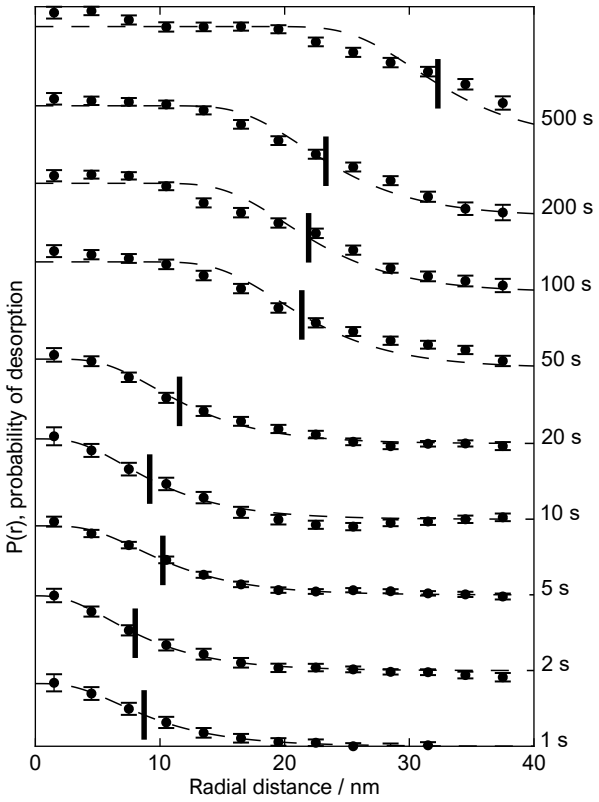

Figure 8-14: $P(r)$ as function of radius from tip site after an injection of -2.1 V and 900 pA. Circles mark experimental data points, see main text for fitted curve. Each set of data-points/curve-fit has been offset vertically for ease of viewing - labels on right-hand side indicate the monotonically increasing injection time. Vertical black markers indicate the radius $r_{1/2}$ at which the probability of desorption is half the maximum probability.

direct fitting to equation (8.41) [8], in which λ was determined to be 9.0 ± 0.2 nm for all injections with biases between -1.6 V and -2.3 V corresponding to injections into a common surface state. Due to larger uncertainty of the measured λ from the toluene-dosed surface data, further analysis is to focus on the bromobenzene-dosed surface data exclusively.

After this initial fitting process, these values of λ are then used to refit the data of figure 8-14, however now with the value of λ set and only κ_e and the contaminant scaling factor as fitting parameters. Through this route we aim to minimise the effect of the inherent statistical variation we have in our experimental results and extract the best values for hot charge carrier dynamics. The half radii extracted from the second fitting pass of figure 8-14 change only slightly with the variations in λ compared to the initial results due to the inherent stability of the half radius as a measure. Hence in this

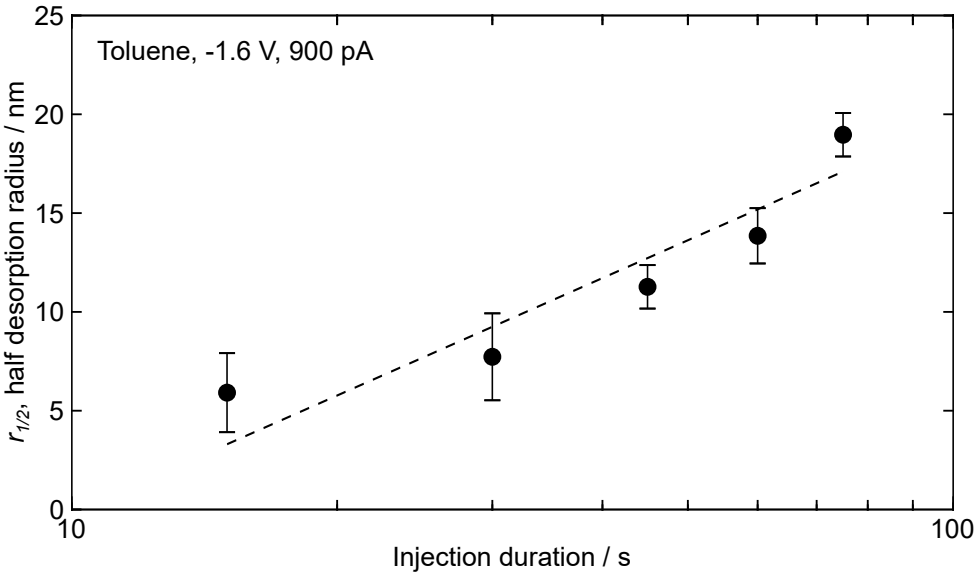

Figure 8-15: The half desorption radius as a function of the total injection duration for an injection of -1.6 V and 900 pA on a toluene dosed surface. Each individual injection has a duration of 15 s, after which subsequent injections are repeated at the same site. The dashed line is a fit from equation (8.48) to all data points. Error bars show standard deviation of the mean for each injection time.

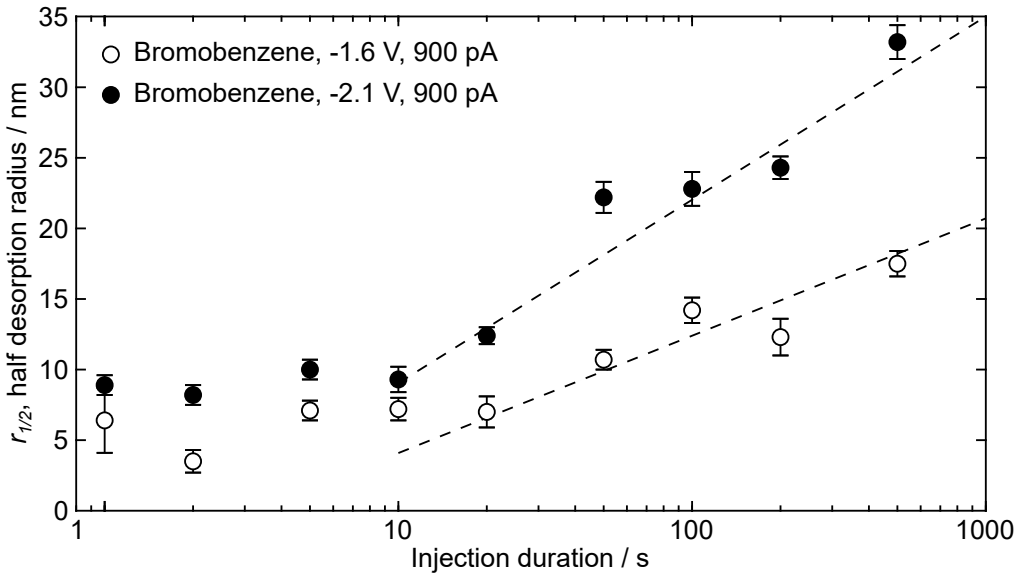

Figure 8-16: Half-desorption radius as a function of the injection duration for -2.1 V (filled) and -1.6 V (unfilled) injections at 900 pA on a bromobenzene dosed surface. Dashed lines are logarithmic fits to $r_{1/2}$ for injection duration greater than or equal to 10 s, with all fit parameters presented in the main text. Error bars show standard deviation of the mean for each injection time.

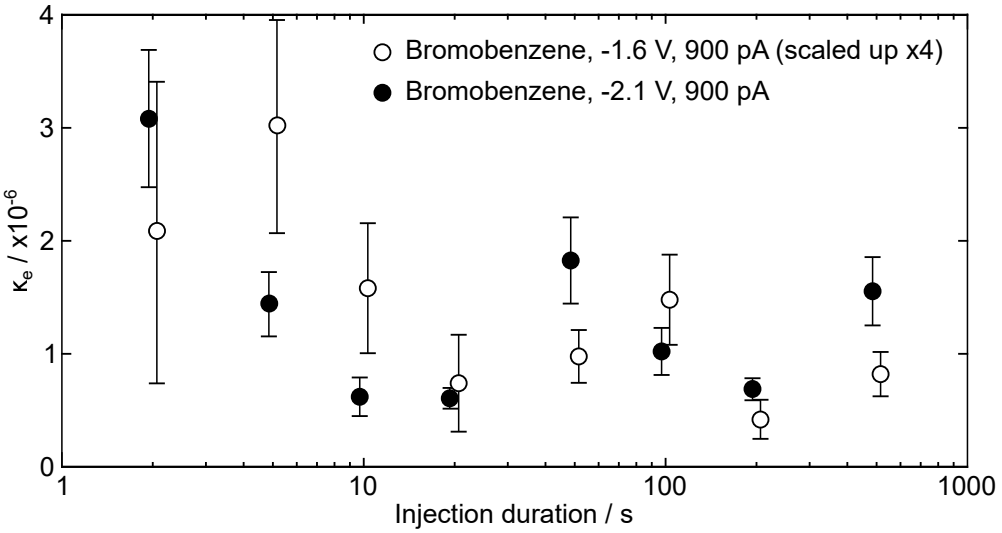

Figure 8-17: Nonlocal probability of manipulation per injected charge carrier κ_e across a range of injection durations between 2 s and 500 s at both -1.6 V (unfilled, each data point scaled up by a factor 4 to aid clarity) and -2.1 V (filled). Each data point has been horizontally offset. This results in a weighted average of $\kappa_e = (2 \pm 2) \times 10^{-7}$ and $(8 \pm 5) \times 10^{-7}$ for -1.6 V and -2.1 V respectively. At both biases a value of κ_e for 1 s injections has been excluded; $(3 \pm 2) \times 10^{-6}$ for -1.6 V and $(6 \pm 1) \times 10^{-6}$ for -2.1 V, with the low number of manipulated molecules and relatively poor fit at the lowest injection duration leading to a large uncertainty in both cases.

case, further iterative fitting does not significantly affect the resultant values. Using a weighted average across all injection times gives the probability of manipulation per hot charge carrier injection $\kappa_e = (2 \pm 2) \times 10^{-7}$ at -1.6 V and $\kappa_e = (8 \pm 5) \times 10^{-7}$ at -2.1 V; shown for each injection duration in figure 8-17.

In comparison, the probability of manipulation per injected charge carrier for the local manipulation of toluene molecules with -1.3 V holes on the same surface is remarkably similar at $k_e = 3 \times 10^{-7}$ [12]. Due to the similarity of bromobezene and toluene, and the near identical structures of the molecules bonded to the Si(111)-7 $\times$ 7 surface, it is reasonable to expect similar molecular manipulation properties. We further suggest that the final step in the charge injection mediated manipulation process is common between these two regimes, and thereby that the probability of manipulation per charge carrier-adsorbate molecule interaction should be identical. In the nonlocal manipulation regime, each injected charge is distributed probabilistically around the injection site, with no one adsorbate molecule experiencing the entire interaction. Hence κ_e is normalised as per injected charge, with surface coverage determining the interaction rate and overall manipulation probability. Conversely, during local manipulation ex-

periments the charge carrier does not enter the surface transport state after injection. Instead the charge is localised to the molecule directly beneath the tip, which experiences the entirety of the interaction. Thus to relate the local k_e and nonlocal κ_e manipulation probabilities, we consider the geometric fraction of the surface initially covered with molecules; which for an adsorbate occupancy of 4 molecules per unit cell is ≈ 0.4. However additionally, in local manipulation the injected charge carrier does not enter the surface transport state, and hence the lifetime of the process, relating to the lifetime of a hot carrier in the transport state $\tau_s \approx 200$ fs in nonlocal manipulation, is now considered to be the lifetime of the excited state of the molecule τ_m. For the similar system of benzene on Si(100), $\tau_m \approx 10$ fs for the hole excited state [50]. We assume a linear increase in the probability of manipulation with the increase in the carrier lifetime. This results in an approximate relation such that

$$k_e \approx 0.4 \times \frac{\tau_s}{\tau_m} \kappa_e \tag{8.49}$$

$$\approx 0.9 \kappa_e. \tag{8.50}$$

It is therefore reasonable for the nonlocal manipulation probability per injected charge carrier to be of the same order as its local counterpart for a common manipulation process.

Due to the logarithmic relationship between the size of the manipulated region and the number of injected charge carriers, attaining a spot size far greater than those observed in this thesis would require unfeasibly long duration injections. In addition, the instability of room temperature STM leads to the maximum injection duration itself being further limited by the mechanical stability of the microscope. At cryogenic temperatures STM are more stable, and thereby longer duration, position-specific injections are possible. However, the thermally driven diffusive charge transport is slowed at such temperatures, with the diffusion length λ and hence ultimately the size of the manipulation region reduced [95].

While the purely logarithmic model in figure 8-16 appears to fit the experimental data well for injection times greater than 10 s, at the lower injection times this model does not fit. This is partially due to the approximations taken in the derivation of equation (8.48), which suggests that the predicted half radius becomes non-physically negative for low t, however even the full diffusive expression is not sufficient to explain the observed plateau in the half radius. The full diffusive equation, equation (8.43) shown in figure 8-13, instead tends to zero at low t.

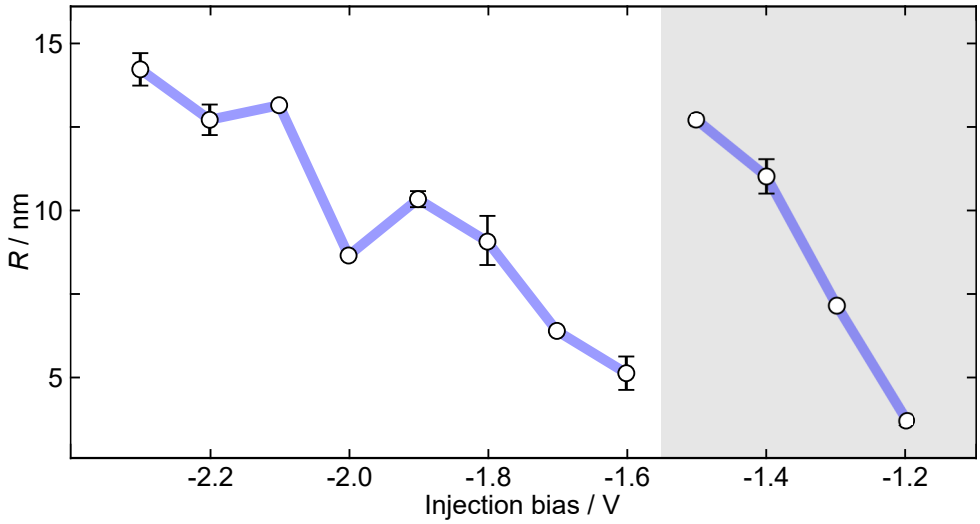

Figure 8-18: Injection bias dependence of the range of the suppression region R for the nonlocal manipulation of toluene molecules located at UM adatom sites on the Si(111)-7×7 surface. STM injection is performed into UM sites. The shaded (unshaded) region relates to injection leading to manipulation due to transport primarily within the S_3 (S_4) surface transport state. Data from [8].

8.4 Ballistic-diffusive transport

The above approximation that an injected charge carrier diffusively decays from a point source was the first model proposed within our group [8]. However, at short radii from the injection site, less than between 5 and 15 nm depending on the injection parameters, the rate of manipulation was observed to be greatly reduced compared to the full diffusive model described by equation (8.14), even when considering the presence of contaminants on the surface. The radius of this reduced manipulation effect was observed to be strongly voltage dependent, see figure 8-18, with minima associated with the onset bias of the surface transport states. The injection biases used here correspond to the onset, -1.6 V, and far above the onset, -2.1 V, of the S_4 surface transport state, and hence relate to a minimum radius and a much larger radius of the suppression region respectively. In reference [8] this effect was considered to be due to an initial ballistic transport regime, in which injected charge carriers travel without interacting with adsorbed molecules for some time before intra-band thermalisation and subsequently undergoing the aforementioned diffusive transport. That is, manipulation will only occur after the charge has already travelled for some distance from the injection site.

Consequently, the initial spatial distribution of charge density before diffusion is not, as is assumed in the purely diffusive case, a Dirac delta function at the injection site. Rusimova et al. model the distribution of charge carriers after the ballistic expansion by considering the evolution of a wavepacket initially located at the injection site until reaching the radius of the experimentally measured suppression region [8]. Using a 2D cylindrical Schrödinger model with an equivalent tight-binding model, see figure 8-19 and reference [8] for detail, a nearly constant charge carrier density was predicted immediately after the ballistic transport regime across a cylindrical region surrounding the injection site, as can be seen in figure 8-19**e**. The radius of this region is governed by the physical properties of the surface electronic state and the ballistic transport lifetime. Using experimentally determined values for properties of both the S_3 and S_4 surface states, the initial ballistic transport is propagated for 10 fs prior to alignment with the measured radii of the suppression region and onset of diffusive transport for injections between -1.2 and -2.3 V. The lifetime prior to relaxation into the manipulative transport state is somewhat less, although comparable, to the $\sim$ 40 fs relaxation time for electrons in the U_1 surface state observed by time-resolved two-photon photoemission spectroscopy [81, 113]. The additional pre-relaxation transport leads to an initial distribution of the diffusive regime, and intuitively sets a lower limit on the half manipulation radius at the radius of the suppression region. We observe this in the plateaus of the half radii at short injection duration in figure 8-16.

To expand the one-step diffusive model to include the initial ballistic transport and the resultant effects on the radius and distribution of nonlocal manipulation, we here consider diffusive transport not from a point source, as in equation (8.37), but, to mimic the ballistic expansion, instead from a disc of constant charge density surrounding the injection site. The radius R of this region will be defined by the extent of the ballistic transport, which is expected to be equivalent to previous measurements of the suppression region. As the 2D diffusion equation is linear and separable, the superposition principle can be used such that the total charge per unit area at a distance r from the injection site is the sum of the charge per unit area from each initial position. Thereby the total charge density, which can be fed into equation (8.14),

$$C(r) = C_0 \int_R \frac{2\tau_s}{\pi\lambda^2} K_0\left(\frac{2r'}{\lambda}\right) dA, \tag{8.51}$$

in which $C_0 = 1/\pi R^2$ and is a normalisation constant defining the initial charge concentration within the top hat maintaining the one interaction per injected charge carrier, and r' is the distance between a point on the initial disc and the radial distance from the injection site r; a diagram outlining this model is presented in figure 8-20. Thus,

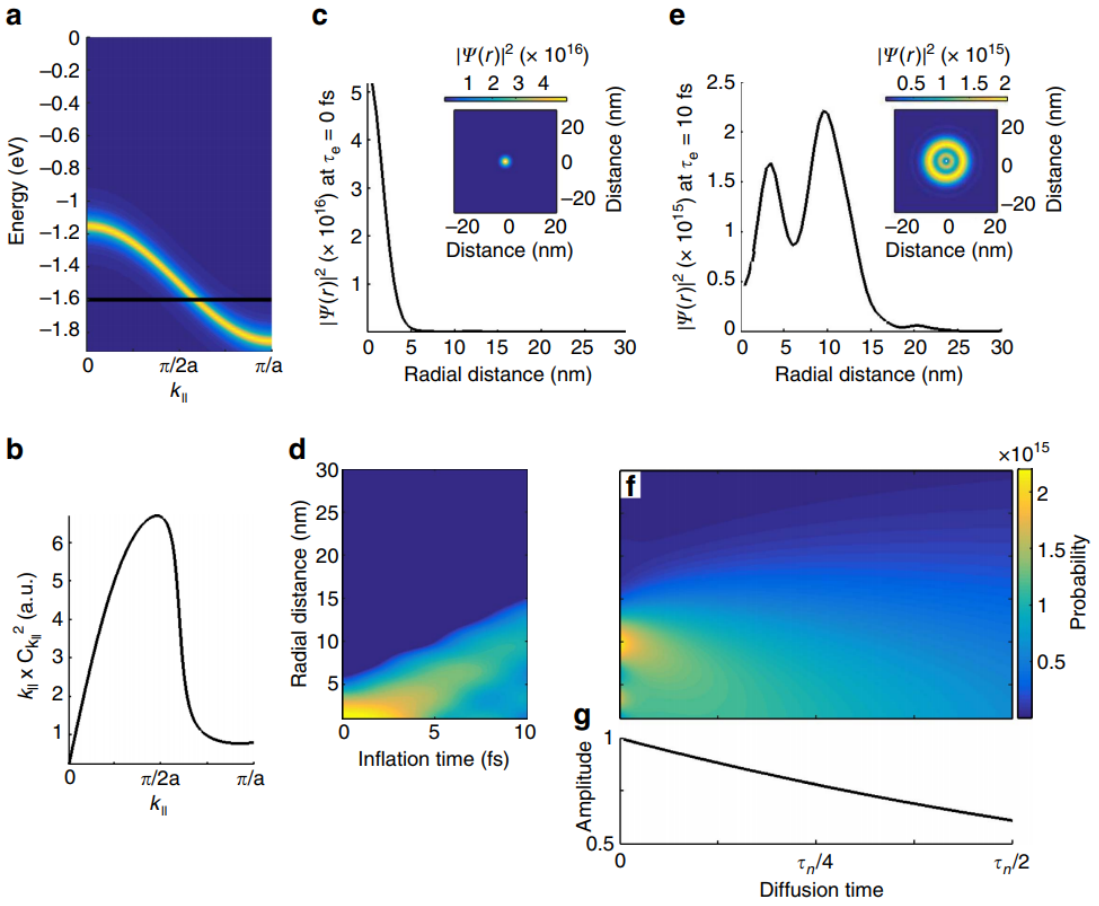

Figure 8-19: Initial coherent inflation (**a**-**e**) followed by the 2D diffusion (**f**-**g**) of a wave packet injected at -1.6 V. (**a**) Energy band diagram of the S_3 back-bond state of the Si(111)-7×7 surface. The black line indicates the injection voltage. (**b**) Tunnelling probability of populating $k_{||}$ values. (**c**) Radial probability distribution of the initial pre-inflation wave packet. (**d**) Time evolution of the wave packet during inflation, the intensity colour map is on a log scale for clarity. (**e**) Radial probability distribution of the inflated wave packet at t = 10 fs. (**f**) Time evolution of the radial probability distribution during the diffusive post-inflation period. (**g**) Time evolution of the total charge in the wave packet, demonstrating the exponential decay. Figure from [8].

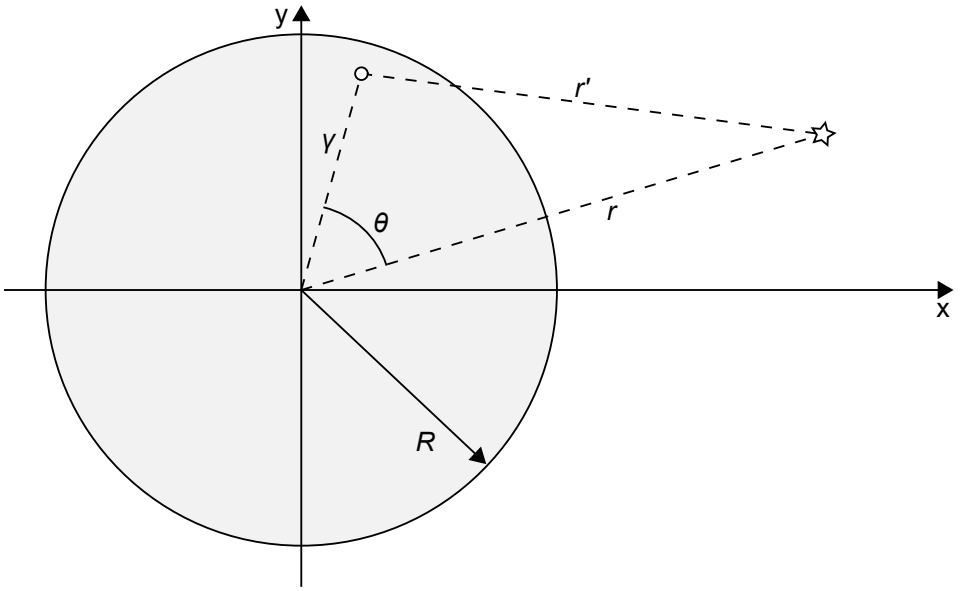

Figure 8-20: A model of diffusive charge transport after an initial, short duration ballistic expansion of charge injected at the origin. The ballistic expansion results in a homogeneous disc of radius R with constant charge density. Any single point within the disc, at distance γ from the origin and angle θ from r, contributes to the total charge per unit area experienced by a point at radius r dependent on the distance r' between the two points. The total charge at r is determined by the sum of charge transport from all points within the disc.

considering γ as the distance to the origin and θ the angle with respect to a vector between the origin and r for each point within the circular region,

$$C(r) = \frac{4\tau_s}{\pi R^2 \lambda^2} \int_0^{2\pi} \int_0^R r K_0 \left(\frac{2}{\lambda} \sqrt{r^2 + \gamma^2 - 2r\gamma\cos(\theta)} \right) d\gamma d\theta. \tag{8.52}$$

To fit this equation we perform a repeated fitting to the half radius data presented in figure 8-16 using the same values of κ_e and λ determined in section 8.3, however varying the value of R and calculating the goodness-of-fit parameter R^2 across the entire range of injection times as demonstrated in figure 8-21. In figure 8-22 the best-fit curves are presented, from which we determine the radius of the suppression region. We observe excellent fits by this ballistic-diffusive model to all of the data, resulting in $R = (5 \pm 1)$ nm for -1.6 V injections and $R = (8 \pm 1)$ nm for -2.1 V injections. Uncertainty here is estimated from the range of "acceptable" fits whilst varying R. These values are in good agreement with those calculated from direct fits to the manipulation probability distributions presented in figure 8-18 [8].

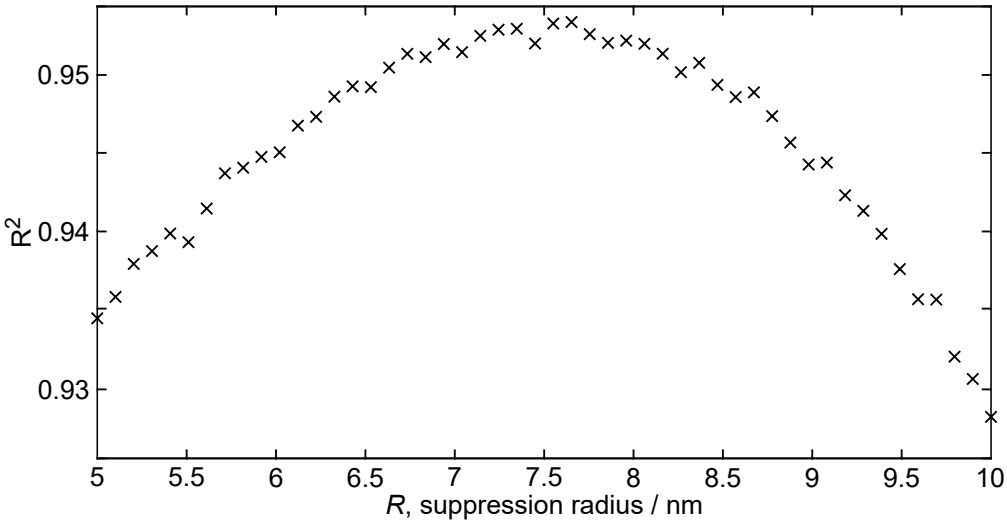

Figure 8-21: Goodness-of-fit parameter R^2 calculated from the ballistic-diffusive model compared to the -2.1 V, 900 pA half radius data across the entire range of injection times. κ_e and λ have been set to the values estimated in section 8.3, whilst the suppression radius R is varied.

In addition to the ballistic-diffusive curves, figure 8-22 displays the fits to the purely diffusive logarithmic model from figure 8-16. As can be expected the broadening of the initial pre-diffusion distribution has little effect on distant adsorbate sites, such that for the longer injection times $r_{1/2}$ is similar within both models. In effect the probability of desorption for the non-point source model can be separated into two distinct regions, with a continuous transition between. From this, the upper and lower bounds of the size of the nonlocal manipulation effect are set; with a maximum radius limited by the logarithmic dependence of the diffusive transport on the number of injected carriers, and a minimum radius determined by the radius of the initial ballistic transport regime.

8.5 Localised surface plasmon induced manipulation

Experimental work by Dr Rebecca Purkiss, within the atomic manipulation group at the University of Bath, reveals an identical bias threshold for both light emission and nonlocal manipulation on the Si(111)-7×7 surface due to the injection of electrons from the tip of an STM [11]. This is discussed in more detail in section 8.6. Taking into consideration the ballistic-diffusive model discussed above, the bias threshold suggests that in both mechanisms the injected charge follows the same overall process; ultrafast relaxation to the bottom of the same surface transport state, diffusive transport within

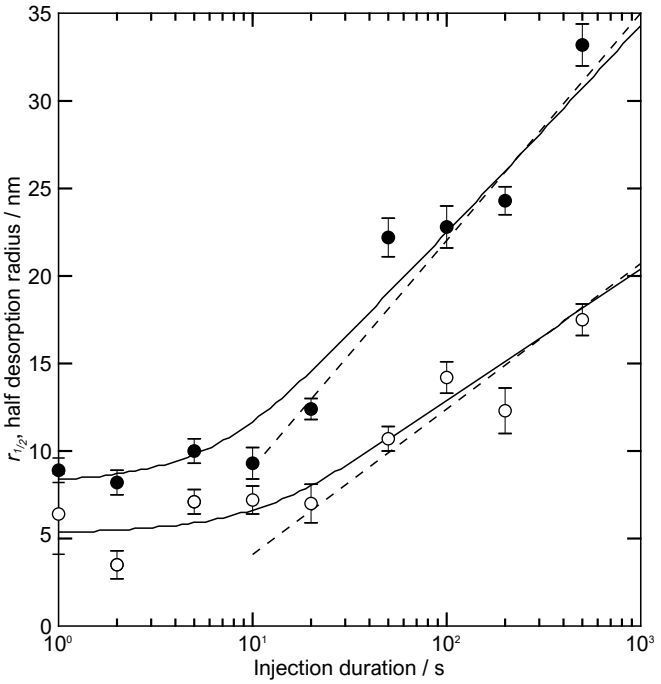

Figure 8-22: Half-desorption radius as function of injection duration for −2.1 V (filled) and −1.6 V (unfilled) injections at 900 pA. Dashed lines are logarithmic fits to $r_{1/2}$ for injection duration greater than 10 s. Solid lines are fits to all data points to a ballistic-diffusive model with an initial disc of charge density. All fit parameters presented in the main text. Error bars show standard deviation of the mean for each injection time. Figure and caption from [10].

this state, and, finally, an electronic transition out of the state which potentially results in either molecular manipulation or light emission.

It is, however, possible that both light emission and nonlocal manipulation are mediated by an alternative process. There are three main mechanisms by which light is emitted from an STM junction; electron-hole recombination [136, 137], electronic transitions [138, 139], or through the relaxation of a localised surface plasmon (LSP) [140–142]. In an indirect semiconductor, such as silicon, photon emission due to electron-hole recombination is forbidden, therefore it cannot be the source of light emission in this case. Here we consider the other option; nonlocal manipulation (and simultaneous light emission) mediated by LSPs.

8.5.1 Localised surface plasmons

A tunnelling electron may interact with the background electron field, inelastically exciting a quantised oscillation in the surface electron layer, known as a surface plasmon [140]. Surface plasmons can be derived as a nontrivial solution to the electromagnetic wave equation by considering a stable, propagating wave localised at the interface between two materials. This requires a real wavevector parallel to the interface as well as imaginary wavevectors perpendicular to the interface in both media in order to obtain a bound solution, with the electric field decaying exponentially perpendicular to the surface. It can be shown that at the boundary between a metal, especially a noble metal such as Ag or Au, and a dielectric, a localised electromagnetic mode can exist. Due to the coupling between the electron oscillations and electromagnetic waves, surface plasmons are commonly known as surface plasmon polaritons (SPPs).

SPPs are known to radiatively decay; they are a primary mechanism of light emission from metal-insulator-metal junctions. However, as the phase velocity of an SPP is always lower than that of free-space light [143], SPPs on metal or metal-like surfaces cannot directly couple to free photons and, conversely, cannot be created by a free photon. SPPs therefore cannot directly radiate. Several different mechanisms have been proposed to explain the light emission, these include surface roughness [144, 145] and small metal particles on the surface [146], in which the SPP wavevector is increased due to variation in the surface symmetry allowing it to couple to a free photon and the system to emit light [147]. Generally, however, a very small proportion of SPPs decay into photons. Instead, it is much more likely for an SPP to couple to a phonon mode in the surface, thereby dissipating into surface vibrations [148, 149].

Early studies of photon emission from noble metal surfaces using the STM by Berndt et al. [140, 150] revealed strong dependence of the spectra of the emitted radiation on the size of the STM junction itself. This suggests that rather than being entirely defined by the surface medium, in this system, the light emitting plasmon modes were primarily localised to the tip-sample junction. The presence of an atomically sharp metallic or dielectric tip close to a metal-like surface leads to interaction between the SPPs of the surface and localised electromagnetic modes of the tip. This coupling results in localised surface plasmon (LSP) modes, which are able to couple with photon modes and thereby able to radiatively decay without need of surface aberrations [151]. Note that the intensity of an LSP in an STM is strongly dependent on the material of the tip, with a silver tip resulting in an intensity several orders of magnitude greater than for, e.g., a molybdenum or tungsten (as in this thesis) tip [138].

Here we consider that, in addition to light emission, the excitation and subsequent decay of LSPs leads to molecular manipulation for adsorbed molecules distant to the tip-sample junction. In this model, rather than the hot charge transport discussed previously, the distribution of the observed manipulation could be determined by the distribution of the LSPs. In this case, the adsorbed molecules act as scattering sites, such that the plasmon modes decay inelastically, but not necessarily radiatively, potentially exciting an electron-hole pair close to the adsorbed molecule [152]. The final manipulation step will then be functionally identical to that for local manipulation; with the local excitation resulting in a DIET process which may result in observable manipulation.

Due to the metal-like surface layer, the structure and formation of an LSP on Si(111)-7×7 is identical to that for a metal; with an almost Gaussian distribution across the surface, calculated by solving Laplace's equation for a sphere above a plane [153]. From this, the solutions are well approximated as

$$\Psi \sim \exp\left(-\frac{r^2}{2h^2}\right) \tag{8.53}$$

laterally, in which r is the lateral distance from the plasmon centre and $h = \sqrt{Rz}$, with R the mean tip radius and z the tip-surface separation. Similarly to hot charge induced manipulation, we consider that each excited LSP has one "interaction attempt" between excitation and decay. In analogy with ξ for charge transport mediated manipulation, the "total interaction probability" will be determined by the normalised probability density (i.e., the probability per unit area of "finding" the plasmon) of the wavefunction;

thus, as

$$\Psi \approx \frac{1}{\sqrt{2\pi}h} \exp\left(-\frac{r^2}{2h^2}\right), \tag{8.54}$$

$$\Psi^2 \approx \frac{1}{2\pi h^2} \exp\left(-\frac{r^2}{h^2}\right). \tag{8.55}$$

The lifetime of a plasmon on a perfect lossless surface, for example a noble metal-air interface, is of the order of ps and is reduced by several orders of magnitude for a lossy interface (e.g. Ti-air interface) [154]. At 900 pA, the maximum current used in this report, the injection frequency is approximately one injected charge carrier per 100 ps. Therefore, even for a lossless interface, only one plasmon is likely to exist in the surface at any time and interaction between multiple plasmons or between plasmons and subsequent injected charge carriers can be neglected.

Assuming immediate formation and decay, we are, thereby, able to further assume that the distribution of each LSP is static; Ψ is not a function of the time since the injection of the charge carrier. As discussed previously for a diffusing hot charge carrier, multiple events can result in the decay of a localised plasmon without leading to manipulation. However, as Ψ^2 is normalised across all space, the addition of a normalised decay term will only ensure that manipulation occurs shortly after plasmon excitation with no effect on the distribution of manipulation events. For example, consider, as in equation (8.2), that the lifetime of the plasmon is limited by a normalised first order decay process with time constant τ_p, such that

$$\Psi^2(r, t'_p) \approx \frac{1}{2\pi h^2} \exp\left(-\frac{r^2}{h^2}\right) \cdot \frac{1}{\tau_P} \exp\left(-\frac{t'_p}{\tau_p}\right), \tag{8.56}$$

where t'_p is the time since plasmon formation. The total probability density of "finding" the plasmon at a specific position across all time after injection

$$\Psi^2(r) \approx \int_0^\infty \Psi^2(r, t'_p) dt'_p \tag{8.57}$$

$$\approx \int_0^\infty \frac{1}{2\pi h^2 \tau_p} \exp\left(-\frac{r^2}{h^2}\right) \exp\left(-\frac{t'_p}{\tau_p}\right) dt'_p \tag{8.58}$$

$$\approx \frac{1}{2\pi h^2} \exp\left(-\frac{r^2}{h^2}\right), \tag{8.59}$$

which is equivalent to equation (8.55), prior to the addition of the first order decay term.

Considering that a tunnelling charge carrier has a probability α of exciting an LSP, then the total number of LSPs will depend on the injection duration t and injection current I such that

$$N_p = \frac{It}{e}\alpha. \tag{8.60}$$

Therefore, the total number of plasmons interacting with a given molecule centred at a radius r from the injection site

$$n_p(r) = \frac{It}{e}\alpha\sigma\Psi^2 \tag{8.61}$$

$$= \frac{It}{e}\alpha\sigma\frac{1}{2\pi h^2}\exp\left(-\frac{r^2}{h^2}\right). \tag{8.62}$$

Further considering that the LSP will induce manipulation in a similar manner to hot charge carrier transport; manipulation will occur with a probability κ_p upon interaction between a plasmon and a surface molecule of cross-section σ. In this case the proportion of molecules retaining their original site as a function of the radial distance from the injection site,

$$P(r) = 1 - \exp\left[-\sigma\kappa_p \times \frac{\alpha It}{e} \times \frac{1}{2\pi h^2}\exp\left(-\frac{r^2}{h^2}\right)\right]. \tag{8.63}$$

In analogy with equation (8.14), the expression above presents the three main factors determining the distribution of manipulation; the molecule-specific manipulation properties though σ and κ_p, the experimental parameters determining the total number of excited LSPs, and the distribution of the resultant interactions that lead to nonlocal manipulation.

8.5.2 Results and discussion

Figure 8-23 shows examples of fitting equation (8.63) to the -2.1 V time varying data presented in section 8.2.5. In this figure both h and a prefactor term,

$$a_p = \frac{\sigma\alpha I\kappa_p}{2\pi e}, \tag{8.64}$$

as well as a contaminant scaling factor are independently fit for each injection duration data set. It is clear that this equation fits the data well in each case, which can be expected as $K_0(x) \approx \exp(-x)$ for sufficient argument. This is one of the reasons why an SPP should be considered as the underlying physics mediating the nonlocal manipulation.

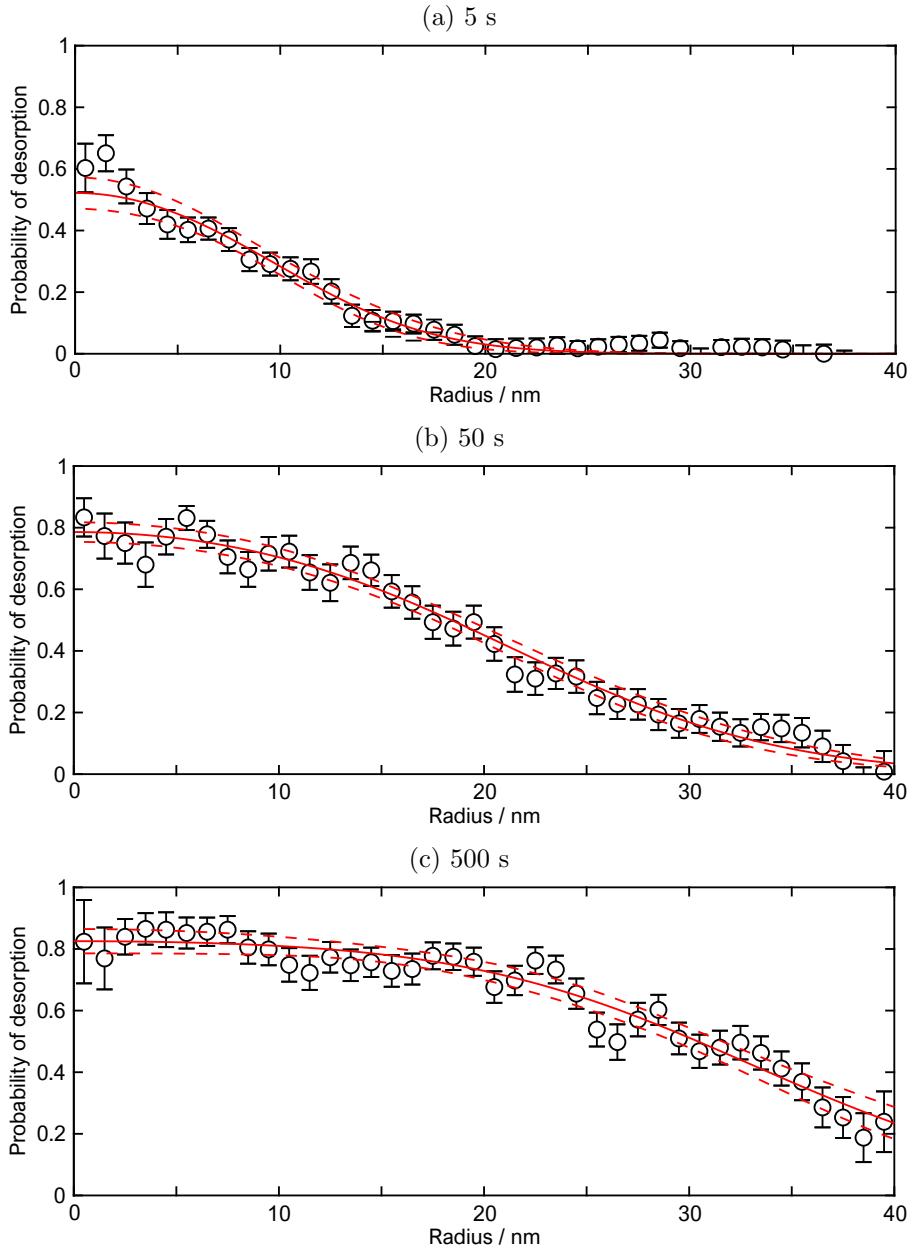

Figure 8-23: The probability of manipulation, averaged across a minimum of 5 separate injections, as a function of the distance from the injection site after an injection of -2.1 V at 900 pA with duration (a) 5 s, (b) 50 s and (c) 500 s. Fitted curves are based on a purely Gaussian manipulation distribution, assuming LSP mediated manipulation, with both the prefactor term and h, alongside a contaminant scaling factor, used as fitting parameters. Dashed red lines show 95 % confidence intervals on the fit curve.

Only the -2.1 V data has been presented here. This was selected as it was collected with a single STM tip, and thereby the tip radius R is expected to be constant. Furthermore, as all injections here occurred with the same injection parameters, -2.1 V and 900 pA with only the injection time varying, the tip-surface separation z should also be constant. As a result, the overall h parameter, which effectively determines the width of each individual plasmon, should not vary with injection duration and should be constant here. Figure 8-24 shows fitted values of h remain relatively consistent with a weighted mean of 140 ± 20 nm. However, each component of a_p should be consistent with varying injection times, but values of the prefactor term vary exponentially across the range of the injection times, inconsistent with an SPP process.

An estimate of h can be calculated from known values of the tip-sample separation during injection and the tip radius. Using simultaneous non-contact atomic force microscopy and STM, Majzik et al. measured the height of the tip relative to a chemisorbed benzene molecule on Si(111)-7×7 [32], resulting in a maximum repulsive force at approximately 0.6 nm from the molecule. The force-maximum can then be correlated to the onset of mechanically-induced manipulation of toluene [12]. This provides a useful reference height for the tip. By comparing the z-piezo extension during an injection and during tip-induced mechanical manipulation, the tip-surface separation during the injection can be determined. In [12], the height of the tip across local injection parameters (either -1.3 V or +1.6 V, between 2 pA and 1000 pA) was observed to vary between 0.9 nm and slightly above the 0.6 nm threshold, logarithmically decreasing for increased current as can be expected from Fermi's golden rule. At each current the higher magnitude bias resulted a slightly increased tip height, albeit with less than 0.1 nm difference. It is expected that the greater magnitude bias for nonlocal injections will result in a further increased tip height, however it is unlikely that this increase will be orders of magnitude and hence the tip height z can be approximated to be of the order of 1 nm. As discussed in section 5.2.1, tips used in this thesis have an apex radius of the order of 10 nm, and hence $h \approx 3$ nm. This result is nearly two orders of magnitude lower than that suggested by figure 8-24b.

Plasmon mediated half manipulation radius

As discussed previously, the half desorption radius $r_{1/2}$ is considered here an approximation of the radius of manipulation. Note, however, that the maximum probability of manipulation is expected to be below unity for short duration injections, as the charge distribution is continuous and finite at all radii, unlike in the diffusive hot charge model. As such, the following should only be reasonable for long duration injections, and the

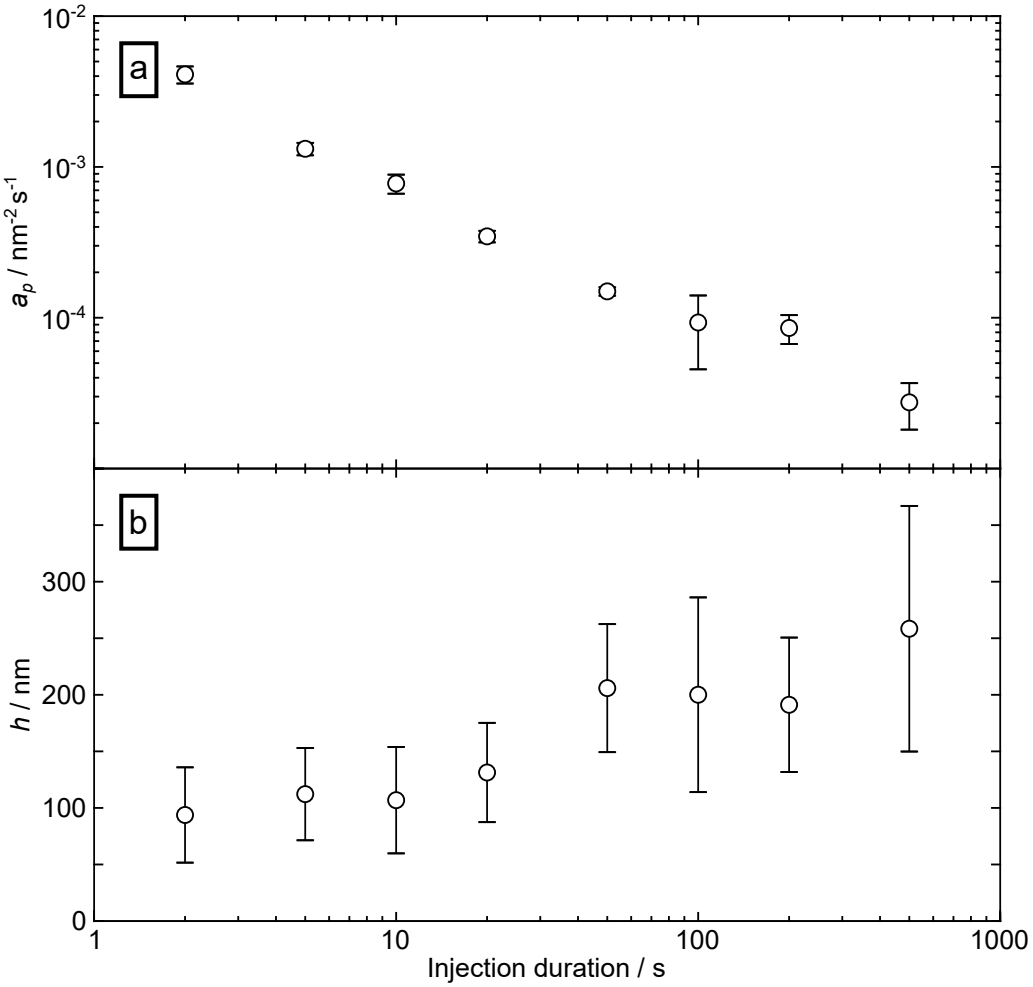

Figure 8-24: Values of (a) a_p and (b) h from the fits to varying injection duration data, for example shown in figure 8-23. For each injection duration, both a_p and h are fit to the data using a MATLAB least squares fitting function. Note the log-log scale on the top a_p graph. Error bars show 95 % uncertainties of the fit. While data is available for 1 s duration injections, MATLAB was unable to fit equation (8.63) to this data and so it is excluded from this figure.

full form of equation (8.63) will be required for short durations. At the radius at which

$$P(r) = \frac{1}{2} = 1 - \exp\left[-\frac{a_p}{h^2} t \exp\left(-\frac{r_{1/2}^2}{h^2}\right)\right], \tag{8.65}$$

$$r_{1/2} = h\sqrt{\ln\left(\frac{a_p t}{h^2 \ln(2)}\right)}. \tag{8.66}$$

Therefore in the long injection time regime and assuming plasmon mediated manipulation, the half radius is expected to scale proportionally with the square root of the log of the injection duration, in comparison to just the log of the injection duration predicted for hot charge mediated manipulation.

Fits for both equation (8.63) and equation (8.66) to the half desorption radius data from section 8.2.5 are shown in figure 8-25. These fits were produced by varying across a wide range of both h and a_p whilst aiming to maximise R^2, with the initial values determined by figure 8-24. Depending on the fitting equation, R^2 is considered only for a section of the data. The full range is used when fitting to the full equation, equation (8.63), however only injection times greater than 10 s are used in the fit to equation (8.66). This 10 s threshold is used as it corresponds to the end of the plateau region and the beginning of the logarithmic fit from section 8.3. Whilst new values of $r_{1/2}$ could be measured using the plasmon-mediated fits shown in figure 8-23, due to the robust nature of the half radius, such values vary only slightly from those used here. Additionally, by using the same values we can more easily compare the resultant fits with those produced by the hot charge transport models. To aid in such comparison, both the full ballistic-diffusive model and the 2D diffusion approximation are also presented. Both of the plasmon fits have a lower R^2 value than the hot carrier model, 0.85 and 0.90 for the > 1 s and > 10 s fits respectively, compared to 0.95 for the ballistic-diffusive fit. It is notable that in the full plasmon fit, the half radius for short injections times is consistently greater than the measured values; tending towards 11 nm compared to the 8 nm observed both in the data and the ballistic-diffusive fit.

Between the two plasmon fits the values of a_p and h are remarkably similar, being only slightly outside uncertainty despite the different fitting ranges. The value of a_p here coincides with those determined from fits to the data independent of the half radius in figure 8-24 at an injection duration of approximately 10 s. Due to the monotonically decreasing value of a_p in figure 8-24, however little can be discerned about an actual value. In contrast, the values of h are again an order of magnitude lower than those in figure 8-24b. This is much more in-line with the calculated value of 3 nm.

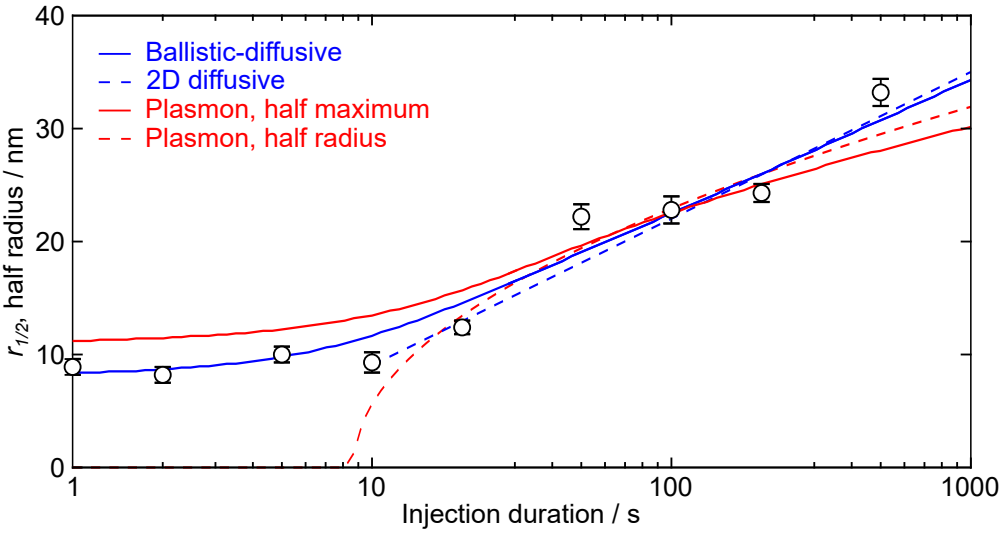

Figure 8-25: The half manipulation radius as a function of the injection duration for -2.1 V, 900 pA injections. Blue lines show fits to the (dashed) 2D diffusive and (solid) ballistic-diffusive hot charge mediated model described in sections 8.3 and 8.4 respectively, and presented in figure 8-16. Red lines show fits to the plasmon mediated manipulation model, see text for more detail on the fitting process. (Dashed red) Fit using the calculated half radius from equation (8.66) for between 10 and 500 s injections, resulting $a_p = (4.0 \pm 0.4) \times 10^{-4}$ nm^{-2} s^{-1} and $h = 15 \pm 3$ nm. (Solid red) Fit to full model of equation (8.63), such that the probability of manipulation is half the maximum probability, across the entire range of data. In this case, $a_p = (7.7 \pm 2.4) \times 10^{-4}$ nm^{-2} s^{-1} whilst $h = 13 \pm 2$ nm.

From the initial wavefunction of a localised surface plasmon, the expected distribution of manipulation has been developed as a function of the duration of the injections from which the plasmons form. This model provides a good fit to each individual injection. Unlike the ballistic-diffusive model, however, the prefactor term varies unexpectedly with the injection duration. Additionally, whilst fit values of the h parameter are consistent across the data, they are much greater than the calculated value. Fits to the half radius are reasonable, although this model overestimates the manipulation radius for short duration injections. In this case the h parameter is more in line with the calculated value, but differs from that calculated in the fits to each individual injection. Conversely in the ballistic-diffusive model, fit values of λ are approximately the same across a range of different measurements, as expected for a correct model.

8.6 Linking nonlocal manipulation and light emission

As discussed in section 8.5, in addition to nonlocal manipulation, charge injection results in the emission of photons. As we have ruled out plasmon mediated manipulation, here we consider light emission to occur during the final inelastic decay of the injected charge from the higher-lying transport state into a lower-lying state. The only difference between this and nonlocal manipulation is the outcome of the final step, hence (assuming, e.g., a reasonable, dosed surface) both manipulation and light emission can be measured with the same STM used elsewhere in this thesis. This section includes a brief overview of the experimental methods, performed by Dr Rebecca Purkiss, and key results, but primarily focuses on my contributions to reference [11]; namely, mathematically linking the expected probability per injected charge carrier of both nonlocal manipulation and photon emission.

Experimental methods

Measurement of light emission from the STM junction during charge injection is fundamentally identical in form to nonlocal manipulation, albeit with the addition of a light detection mechanism. Light detection was achieved using an Andor Luca R camera focused on the tip-sample junction. This is an electron multiplying CCD camera with a wavelength range of 400 nm to 900 nm (3.10 eV to 1.38 eV) and near-single photon sensitivity. The camera was mounted outside the vacuum chamber at the same position as the tip-approach camera discussed in section 5.3, with a direct view of the tunnel junction through a viewport. To minimise contamination due to external light sources, the camera and viewport were covered with blackout material and any lights (internal or external) were switched off prior to use. In this setup the camera was approximately

20 cm from the junction, resulting in a solid angle of ∼0.024 sr, at an angle of 80° to the surface normal, away from the maximal emission angle of 60° [155]. The optical system here is similar in form to early scanning tunnelling microscope light emission (STML) experiments performed by Gimzewski et al. [156], and the solid angle achieved is orders of magnitude lower than designs utilising optical equipment within the vacuum chamber [157–159]. Despite this, the sensitivity of the camera, in conjunction with a 40 s exposure time and up to 833 times gain, resulted in a sufficient STML signal without saturating the camera.

During injection, a single 8×8 μm^2 camera pixel is illuminated; observed as an increase in the average photon count during the 40 s injection compared to a similar 40 s "dark" period without injection. This can be observed in figure 8-26, in which the mean count rate increases from 642 ± 48 with the tip retracted 5 nm away from the surface and, thereby, no tunnelling (+3 V, 0 nA, 40s) to 1435 ± 98 during an injection (+3 V, 1 nA, 40 s) for the junction pixel [11]. The uncertainty in the count number is given by a 1σ standard error across 11 individual injections. A similar increase in the count rate for background (i.e. away from the tunnel junction) pixels was not observed, remaining within uncertainty both during and without an injection (606 ± 46 and 660 ± 73 counts respectively during the same 11 injections).

Bias dependence of photon emission

Using the same injection process whilst varying the injection bias, the bias dependence of light emission for electron injection between +1.5 V and +3.0 V was measured, this is displayed in figure 8-27 summed across 11 injections at each injection bias. Below approximately +2 V no clear light emission during tunnelling is visible, with the camera counts approximately equivalent both during STML and during the dark, no tunnelling measurements. Above the +2 V threshold, however, a near-monotonic increase in the count number with the injection bias is observed during tunnelling. This threshold is identical to the onset of nonlocal manipulation due to electron injection, itself at +2.0 V [8].

The identical bias thresholds for light emission and nonlocal manipulation suggest that the two outcomes follow the same overall electron dynamics. That is, in either nonlocal manipulation or STML, an injected charge carrier initially relaxes to the bottom of the U_3 (for injection between +2 V and +3 V) or the U_4 state (for injection greater than +3 V) without emission of a photon. Instead, photon emission or molecular manipulation is the final step of the process, and after diffusion the charge carrier inelastically decays to a lower lying state, potentially resulting in the observed dynamics.

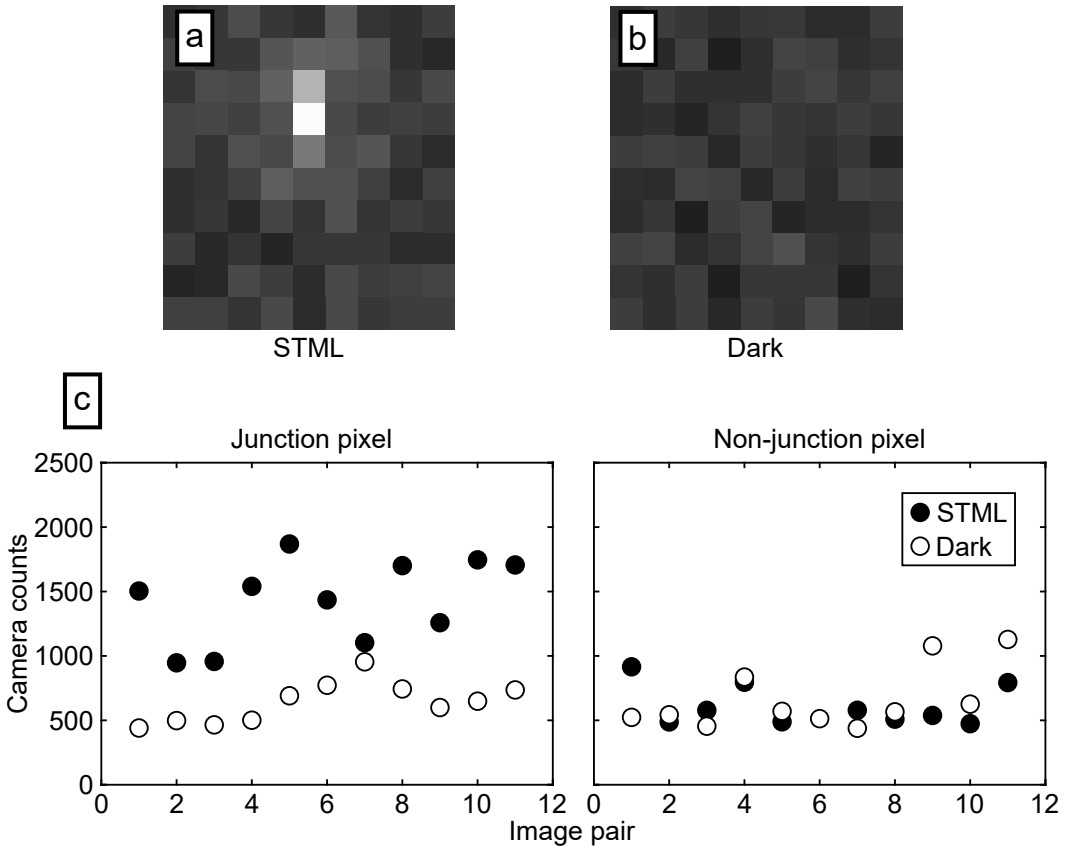

Figure 8-26: (a-b) Photographs of light emission from an STM junction, both (a) during an injection (+3 V, 1 nA, 40 s) and (b) with no tunnelling (+3 V, 0 nA, 40 s). The brightness of each pixel is proportional to the photon count. (a) and (b) show the same region, directly surrounding the tunnel junction. During injection the pixel associated with the tunnel junction measures far more photons than surrounding pixels. (c) Camera counts during an injection for (left) the tunnel junction pixel and (right) a pixel some distance from the tunnel junction. Each image pair refers to an STML measurement during injection followed by a measurement with no tunnelling at the same surface location. Camera gain ×333. Data from [11].

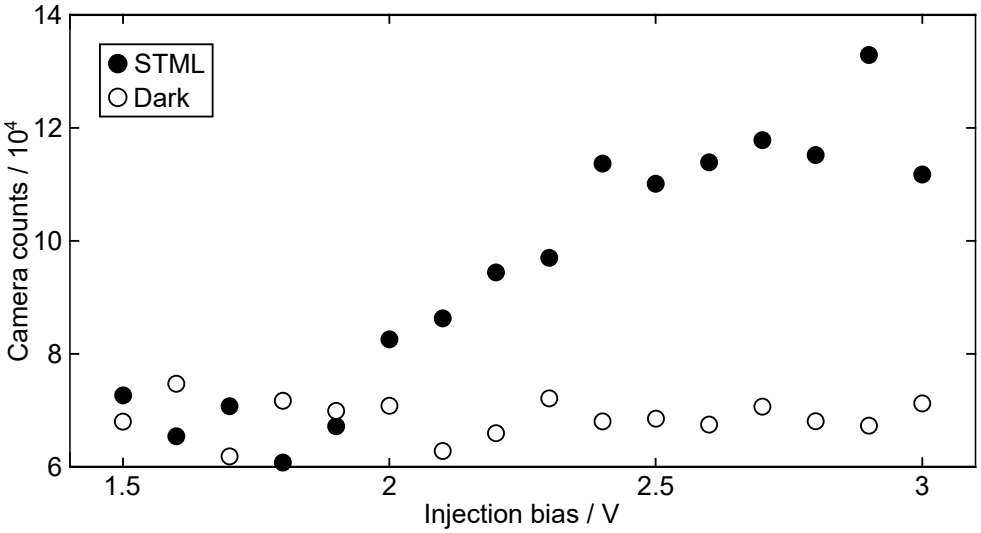

Figure 8-27: Bias dependence of STML, measured as the total number of camera counts for the tunnel junction pixel across 11 injections (40 s, 1 nA) at each bias. Camera counts are also given at each bias with the tip retracted from the surface such that no tunnel current is measured (40 s, 0 nA), again summed across 11 "injections". Camera gain ×833. Data from [11].

Within any specific surface transport state, the energy of a hot charge carrier will be injection bias invariant at the bottom of the state. The energy of emitted photons will be constrained by the energy of available transitions to lower-lying states, and should be equivalently bias invariant. This is in agreement with measurements of the energy of emitted photons by Imada et al. [138], in which several clear peaks were observed. Electron injection at +2.0 V, into the U_3 surface state, resulted in photon energy peaks at 1.4 eV and 1.85 eV. Injection at a higher +3 V bias, into the U_4 surface state, resulted in a peak at 2.4 eV in addition to peaks at 1.4 eV and 1.85 eV. The bias invariance of these latter two peaks is in agreement with the bias invariance of the nonlocal length scale, with emitted photons at the same energy corresponding to an identical electron transition which is only possible with a common initial energy level. By considering the energy of lower-lying states, this allows the final state of injected charge carriers, after the inelastic relaxation, to be determined [11].

8.6.1 Relative probability per injected electron

A comparison between the relative probabilities of nonlocal manipulation and light emission is not immediately obvious. What we measure in each of the two processes is different; in nonlocal manipulation the probability of manipulation κ_e is determined for a single interaction between an injected electron and a molecule, whereas the light

emission measurements are dependent on the total number of photons emitted during an injection. To qualitatively compare the probability of each of the two outcomes, here we recast both processes in terms of the probability of light emission or manipulation per injected charge across the entire surface.

This analysis contributes towards the discussion of reference [11]. Whilst the notation in [11] differs from that presented here, the only important difference is in the definition of the variables relating to the probability of manipulation; κ_e and β. κ_e (used in this chapter) is time independent whilst β (in reference [11]) is the probability of manipulation per unit time [95], a change that results in a different prefactor structure. Mathematically, there is no difference between the two analyses, and so the calculated manipulation probabilities per injected charge are the same.

Conversion from the measured camera count to the probability of photon emission per injected charge carrier was performed by Dr Peter Sloan, however, for completeness an overview is provided here. Noting, as before, that the total number of charge carriers during injection $n_e = It/e$, the camera count can simply be converted to a count rate per injected charge. Again we assume that all injected charge enters a manipulative surface state, i.e. $s = 1$. The value of s will affect both light emission and nonlocal manipulation equivalently and effectively not alter the relative probabilities of the two outcomes. The measured camera count signal cannot be directly considered to be the total number of photons emitted due to tunnelling electrons, instead we apply a correction to account for experimental limitations; see reference [11] for more detail. Primarily, we must consider the quantum efficiency as well as the gain and positioning of the camera, including the angle of the camera away from the maximal emission angle and transmission factor of the viewport. Additional factors such as the tip material are known to affect the photon emission intensity [138], this will not alter the injection process and must instead relate to the probability of photon emission. Finally, only photon emission due to the injection must be counted, hence the background count rate, measured as the count rate during the "dark" measurements, is subtracted from the STML count rate.

The probability of nonlocal manipulation κ_e in both the diffusive and ballistic-diffusive models has been determined for a single molecule-charge carrier interaction. Here, instead, we reframe the perspective of the experiment and consider the outcome for the injected charge carrier, such that each charge either does or does not result in manipulation of any molecule on the surface. In this case, the target molecule is not important, and so we consider the total probability of interaction with any molecule by integrating the probability across each molecule. For simplicity, we consider a purely

diffusive model, with the probability of manipulation for a single molecule at radius r given by equation (8.39). For a single electron the exponential can be expanded about zero, so the probability of manipulation of a specific molecule due to the injection of one electron

$$P_m = \kappa_e \cdot \frac{2s\sigma}{\pi\lambda^2} K_0\left(\frac{2r}{\lambda}\right). \tag{8.67}$$

For more direct comparison with STML, in which the presence of a molecule is not necessary for the measured outcome, we assume that each adatom site is occupied by a molecule and hence interaction between any one adatom site and the one injected charge carrier may result in manipulation. The number of sites within an annulus at radius r of width Δr

$$N_0(r) = \rho \cdot 2\pi r \Delta r, \tag{8.68}$$

in which $\rho = 1.92 \times 10^{18}$ m^{-2} is the number density of adatom sites. The total probability of manipulation across all molecules will be dependent on the probability of interaction between the charge and each molecule at each radius, with

$$P_e = \int_0^\infty \kappa_e \cdot \frac{2\sigma}{\pi\lambda^2} K_0\left(\frac{2r}{\lambda}\right) \rho 2\pi r dr. \tag{8.69}$$

In the limit of $r \to \infty$ the integral $\int r\mathrm{K}_0\left(2r/\lambda\right) dr \to \lambda^2/4$, and so

$$P_e = \rho\sigma\kappa_e. \tag{8.70}$$

Thus, as $\rho \cdot \sigma$ is simply the area of the surface covered by molecules, the probability of nonlocal manipulation per injected charge carrier is independent of the the charge transport dynamics. Hence we can apply a simple multiplicative factor to κ_e to calculate the probability of nonlocal manipulation per injected charge carrier.

In figure 8-28 the bias dependence of both the probability of nonlocal manipulation and photon emission per injected charge carrier are presented. In either case, a clear threshold at +2 V followed by an approximately exponential increase can be observed. Within this bias range, the ratio of the probability of these two decay outcomes varies only slightly, suggesting that within a transport regime the state of the charge carrier prior to molecular manipulation or light emission is the same, independent of the injection bias. The variation in the probabilities can be explained by the voltage dependence of the probability of an injected charge carrier entering the transport state (through $s(V)$). This proposal provides additional evidence towards the identical charge carrier dynamics leading to the possible outcome of molecular manipulation or light emission, as well as the hot charge transport model presented in this chapter.

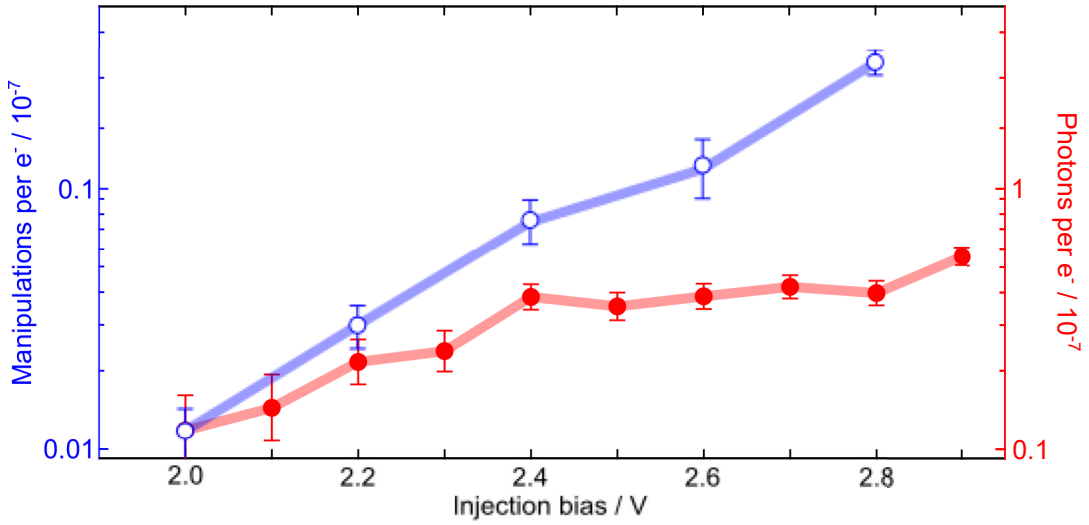

Figure 8-28: Probability per injected charge carrier of either molecular manipulation (unfilled blue, left y-axis) or photon emission (filled red, right y-axis) as a function of the injection bias. Data from [11].

8.7 Conclusions

Measurement of the distribution of nonlocal manipulation within this chapter supports a two-step ballistic-diffusive charge transport model. From this, physical limits on both the minimum and maximum radii of such manipulation can be discerned; with a lower limit set by the initial, purely ballistic transport, and an upper limit determined by the length scale of hot charge diffusion as well as feasible injection parameters. It is clear that the surface itself plays a key role in the manipulation, with the upper limit on the radius bound by a dependence on the charge diffusion length λ. By engineering the diffusive properties of the surface, for example altering the doping level, this analysis provides a route to control the hot charge carrier dynamics and hence enhance or suppress the nonlocal manipulation itself.

Similarities between light emission and nonlocal manipulation suggest a common mechanism for both processes. While a plasmon mediated nonlocal manipulation process provides a good fit to the manipulation distribution for an individual injection, this model overestimates the manipulation radius for short injections and several parameters unphysically vary across different injection durations. In addition, when considering the diffusive charge transport model, we observe a similar relationship between the probability of manipulation and the number of emitted photons per injected charge carrier. In either case, an approximately exponential increase can be observed with increasing injection bias between +2.0 V and +2.7 V. This suggests that the initial charge

injection step is the same, and hence provides further evidence towards a ballistic-diffusive model mediating both processes, with the relaxation of the injected charge after nonlocal transport resulting in (among other possible outcomes) either molecular manipulation or light emission.

Chapter 9

Measuring the outcome of local and nonlocal manipulation

Through observation of the outcome of nonlocal manipulation, be it molecular desorption or diffusion, rather than simply the radial distribution of the raw manipulation as in the previous chapter, here we aim to isolate the final manipulation step in nonlocal manipulation. We aim to show that the manipulation in both local and nonlocal manipulation occurs identically, with the injected charge relaxing into the bottom of a common surface state prior to inducing the final manipulation step. This means that the manipulation occurs identically for each injected charge, invariant to the energy of the charge upon injection. Our premise is that a change in the final manipulation process would result in different surface-molecule dynamics, leading to a change in the overall probability of manipulation alongside some change in the relative probability of the various outcomes as evidenced by the branching ratio.

Local charge injection can result in two observable manipulation results; desorption or diffusion of the local molecule to a neighbouring site. Prior measurement of the ratio of these two outcomes resulted in a value that is invariant across a range of experimental parameters, including the injection bias, current, and tip height [9,12,160]. This suggests that the final step of the injection-manipulation process is identical, independent of, for example, the energy of the injected charge, with the conclusion that the charge carrier non-radiatively relaxes to the bottom of an electronic band prior to the manipulation step.

Nonlocal and local manipulation are expected to differ by only the addition of a charge transport step in the former process. Prior to a nonlocal manipulation event, we expect

the charge carrier within the transport state to decay to a common manipulative energy level at the bottom of the local manipulation state, just as in local manipulation, so that the final step would itself be invariant across local and nonlocal injections. In that case, the nonlocally induced branching ratio will be the same as the locally induced branching ratio.

Previous work on the outcome of local manipulation has been performed using toluene dosed Si(111)-7×7, and this found a strong preference for desorption over diffusion [12]. Here we use a heavier benzene derivative, bromobenzene, as the adsorbate molecule in an attempt to reduce the desorption probability and make our system more sensitive to changes in the ratio of the two outcomes. We also compare the branching ratio across two molecule species; the previous results of toluene dosed local and nonlocal charge injection, as well as bromobenzene dosed charge injection including that performed in chapter 8.

9.1 Local toluene branching ratio

In our system, two different manipulation outcomes can be perceived. These are defined as desorption or diffusion based on the observed change in occupancy of the binding sites neighbouring the injection. In all of our local and nonlocal experiments, we operate well below the high energies required for C-Cl or C-Br bond breaking [161, 162]. Here, a desorbed molecule is defined as a molecule that breaks all bonds with the surface and either enters the gas phase or otherwise leaves the scan area. Diffusion is usually defined as molecules entering the physisorbed state, translating across the surface, and then re-chemisorbing elsewhere on the surface. Here, however, we limit our definition of a diffused molecule to those only breaking a single σ bond between the phenyl ring and the surface adatom before re-bonding with a neighbouring adatom. This single break results in an apparent translation of only a single adatom atomic binding site, which means that the molecule can be tracked between images. The possible outcomes of diffusion are displayed in figure 9-1. We are not probing the actual diffusion process, instead, we are comparing the relative probability of this "diffused" outcome to the total desorption probability, such that we can qualitatively evaluate the energy of the adsorbate molecule immediately prior to manipulation.

This definition of diffusion dramatically limits the range of the effect. Wolkow and Moffatt, for example, found thermally activated diffusion of benzene on Si(111)-7×7 to occur with a mean translation of 2.3 nm [89], far larger than the spacing between neighbouring sites ($<$ 1 nm). They observed only 24% of new adsorbates adjacent to newly unoccupied sites between successive images. In contrast, our definition results in two outcomes that are clearly distinguishable within the small scans surrounding a local manipulation parameter injection, as shown in figure 9-2; either a new dark site is observed neighbouring the injection site (i.e. diffusion, figure 9-2c→d), or not (i.e. desorption, figure 9-2a→b).

By considering the ratio of the two outcomes, i.e. the ratio of the number of observed diffusion events to desorption events, the final step in the manipulation process can be indirectly measured. We could expect that the branching ratio could be altered by varying the injection parameters; for example, higher energy charge carriers being more likely to provide sufficient energy to induce desorption, or that with certain injection parameters diffusion would become the dominant outcome [160]. Instead, in line with the prior work and hypothesis, we find the branching ratio to be invariant across a range of parameters, including the current [12] and bias [9] of the injection. The bias dependence of both the branching ratio and the probability of local manipulation are

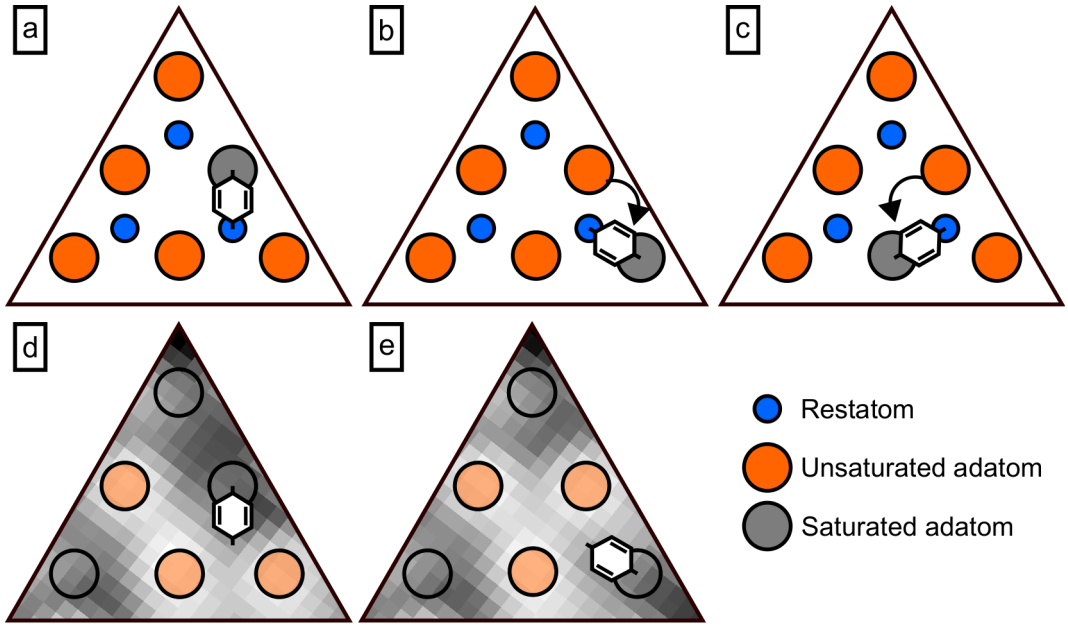

Figure 9-1: (a-c) Schematic diagrams and (d,e) STM images of possible diffusion results for a molecule initially bonded to a middle adatom site in (a) and (d). During diffusion the σ bond between the molecule and the adatom breaks while maintaining a bond with a restatom, before the molecule re-bonds to one of two neighbouring adatoms resulting in either a bond with a corner site (b,e) or another middle site (c).

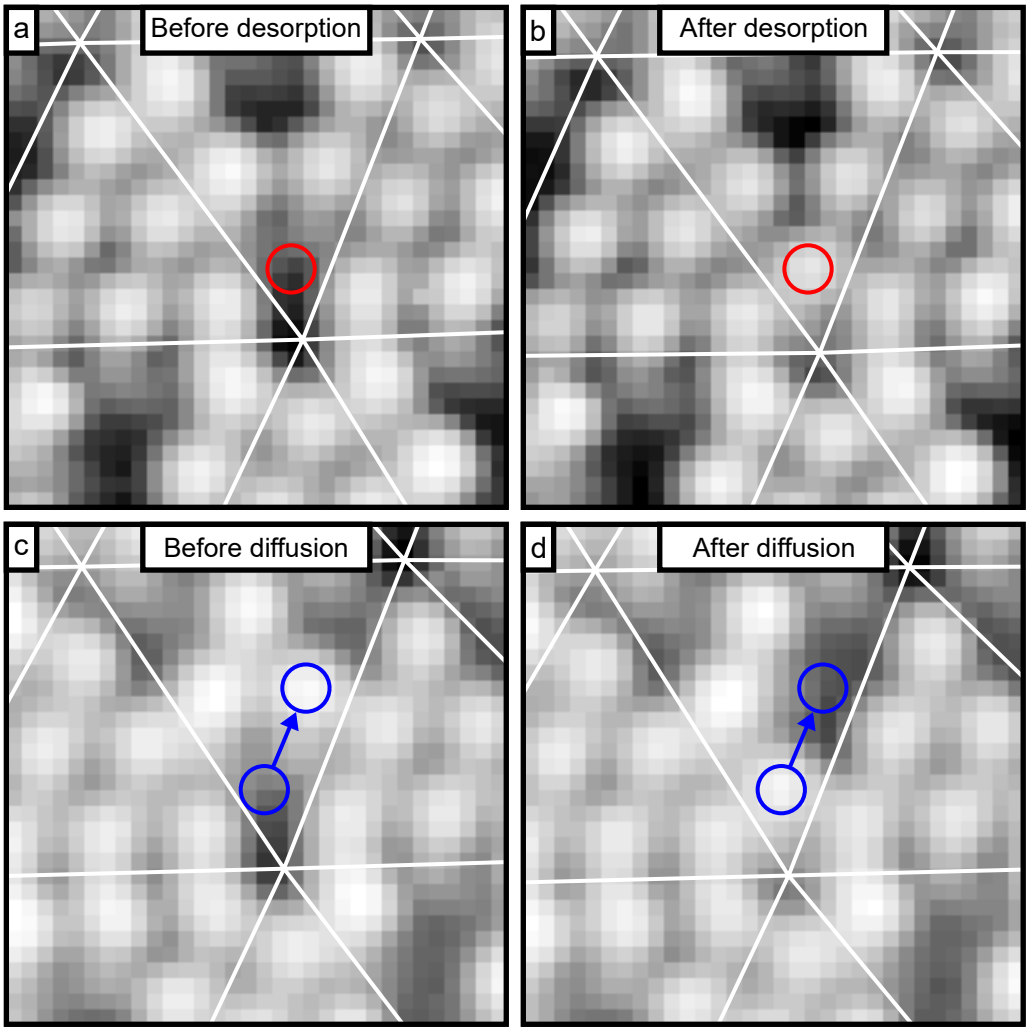

Figure 9-2: 3×3 nm STM images of a BrPh dosed Si(111)-7 × 7 surface before (a,c) and after (b,d) charge injection (750 pA, 1.6 V) into an adsorbate at the centre of the image. The white lines in each image mark the edges of the half unit cells. (a→b) After injection the target molecule has desorbed from the surface, such that no dark site is observed either at the red labelled site or neighbouring sites. (c→d) The target molecule has diffused, apparently resulting in the dark site transferring to a neighbouring site.

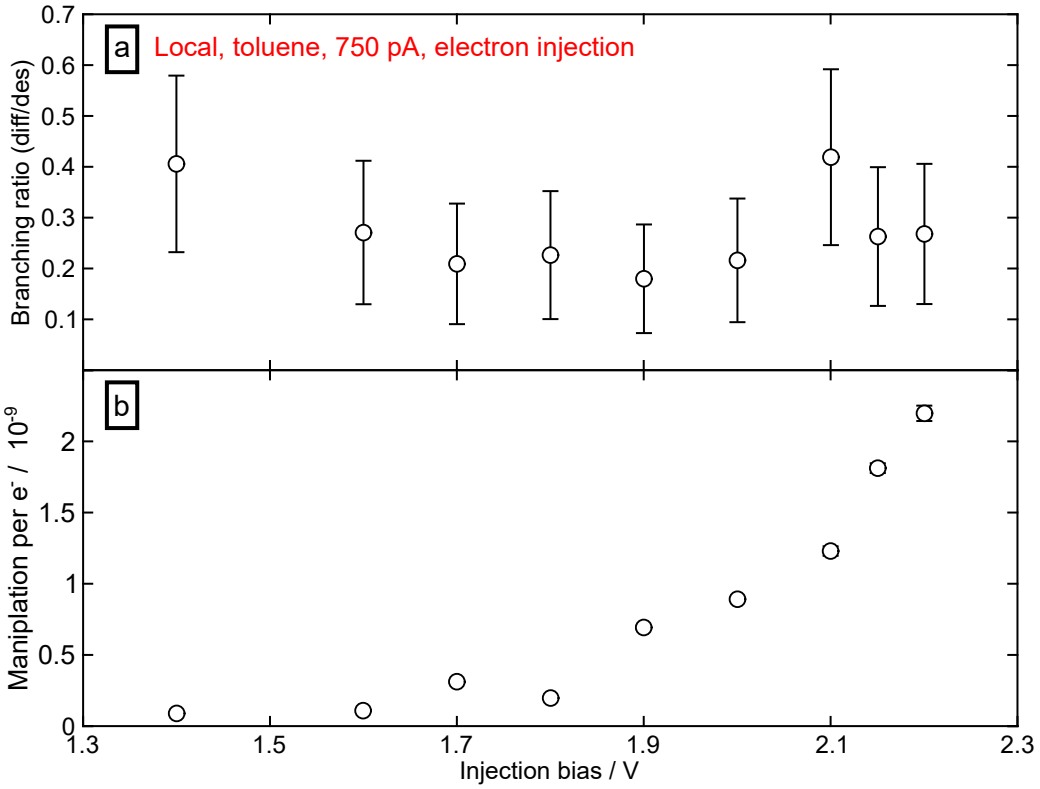

Figure 9-3: (a) The ratio of diffusion to desorption events and (b) the probability of local manipulation per injected electron as a function of the injection bias for 750 pA local injections into a toluene dosed Si(111)-7×7 surface. For electron injection between +1.4 and +2.2 V the branching ratio is shown to be invariant, with a value of 0.24 ± 0.03, while the probability of manipulation increases exponentially. Data from [160].

shown in figure 9-3. Whereas the branching ratio remains consistent with increasing bias, the probability increases exponentially across the same range, in agreement with figure 8-8. The branching ratio was, however, observed to vary between injection of either holes or electrons, with a value of 0.037 ± 0.004 for hole injection and 0.24 ± 0.03 for electron injection [12]; in both regimes favouring desorption.

The uniformity of the final outcome suggests that the manipulation step is itself constant for each carrier type and, thereby, that the excited state of the molecule pre-manipulation is the same. Much like the surface transport step in nonlocal manipulation [8], the injected charge carriers must undergo ultrafast relaxation within an electronic state through a non-radiative decay mechanism prior to manipulation (e.g. via phonon emission or electron scattering [113]). This means that carriers injected within a range of energies into a broad electronic state ultimately induce manipulation

with the same energy. In this case, local manipulation due to electron injection is observed with a minimum bias threshold of +1.4 V [9], at this bias the tunnel current is unable to populate the broad +2 V adatom backbond state associated with nonlocal charge transport. Very few local manipulation events were observed within an 8 s injection period at +1.3 V, and even fewer at +1.2 V [160]. This threshold suggests that each injected carrier relaxes towards +1.4 V prior to manipulation, and greater injection biases only serve to enhance the probability of an injected charge carrier entering the relevant surface state.

9.2 New adsorbate molecule selection

Previous experiments varied the injection bias and injection current. Here we additionally vary the manipulated molecule. When varying only the functional group attached to the benzene ring, different adsorbate molecules will bind to the surface with a near-identical structure and similar binding energy [99]. As the surface itself is unchanged, the underlying surface states will be unaffected. This means that when varying the adsorbate molecule, the distribution of manipulation in nonlocal charge injection experiments should only be altered by the change in manipulation probability, likely experienced as a multiplicative offset without affecting the overall distribution. To measure the branching ratio more easily, we aim to vary the adsorbate molecule such that the probability of the two manipulative outcomes are more even and we observe an increase in the branching ratio.

After excitation by an injected charge carrier, a benzene-derivative adsorbate molecule will enter an excited state with a repulsive potential with respect to the ground state [97]; see figures 3-1a and 4-5. The optimised geometry of the excited state is similar across a range of benzene derivatives [97], and hence we consider the potential energy surface of the excited state to also be similar. The force F on the molecule upon excitation will be determined entirely by the shape of the excited state potential,

$$F = -\frac{\mathrm{d}E}{\mathrm{d}z}, \tag{9.1}$$

with E the potential of the excited state at distance z from the surface. However, as force is equal to mass times acceleration, the acceleration a of the molecule will be reduced with increased mass m. Assuming an equivalent excited state lifetime τ, a heavier benzene derivative will be displaced less from the neutral state equilibrium

position than a lighter benzene derivative [48]; with displacement

$$s = \frac{1}{2}a\tau^2, \tag{9.2}$$

$$= \frac{-\tau^2}{2m}\frac{\mathrm{d}E}{\mathrm{d}z}, \tag{9.3}$$

$$\propto \frac{1}{m}. \tag{9.4}$$

Whilst this will have no effect on the amount of kinetic energy gained during the excitation-relaxation process, reducing the displacement will reduce the probability of the molecule fully overcoming the desorption barrier. The molecule may instead diffuse to a neighbouring site, breaking a single bond with the surface rather than desorbing entirely. As a result, in this simple model we expect that increasing the mass of the adsorbate molecule will increase the branching ratio.

In order to measure an increased branching ratio, the adsorbate molecule is required to have several properties akin to previously used molecules. Namely, the molecule must adsorb in a similar manner to the aforementioned small benzene derivatives, with similar electronic properties and geometric structure, whilst also being heavier than previously studied molecules. In addition, the molecule must work within the experimental process set up in chapter 5. The STM and dosing system used within this thesis, discussed in more detail in section 5.5, requires a gaseous adsorbate that is able to dose the surface within a reasonable timescale. For this, we require a molecule that is liquid at room temperature and that has sufficient vapour pressure.

Likely candidates are expected to be similar in structure to the previously used benzene derivatives, maintaining the phenyl ring and the resultant strained $\sim$1 eV di-σ bonds between opposing carbon atoms in the phenyl ring and the silicon adatom and restatom resulting in a stable chemisorbed state [89]. As such, the initial candidate molecules are phenyl group molecules, as with chlorobenzene and toluene, however substituting the functional group with an equivalent but larger group, e.g. chlorine for a larger halogen, or adding additional functional groups, e.g. chlorobenzene to dichlorobenzene. The additional functional groups should have similar electronic effects on the phenyl structure to maintain the strong di-σ bonding and must be bound sufficiently to minimise dissociation during adsorption, due to injection, or due to thermal effects. Relevant properties of candidate molecules are presented in table 9.1, and experimental or theoretical properties of the same molecules adsorbed on a Si(111)-7 $\times$ 7 surface are presented in table 9.2.

Table 9.1: Molecules known or expected to have similar characteristics to benzene when adsorbed onto Si(111)-7×7 for use in IET induced nonlocal manipulation experiments. Acceptable replacement molecules are required to be liquid at room temperature [163] and have a reasonably high vapour pressure to allow surface dosing in vacuum [164]. The values for vapour pressure are provided at 300 K or the lowest available temperature, however no values were available for several potential adsorbates.

Molecule		Mass / Da	Melting point / K [163]	Vapour pressure / mbar (at / K) [164]
Benzene	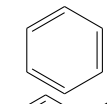	78	278	125 (300)
Toluene	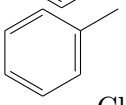	92	178	41 (300)
Chlorobenzene	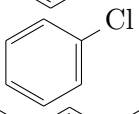	113	228	97 (315)
Mesitylene	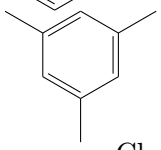	120	225	64 (355)
1,2-Dichlorobenzene	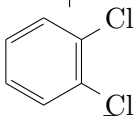	147	256	2 (300)
Bromobenzene	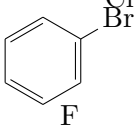	157	242	31 (330)
Hexafluorobenzene	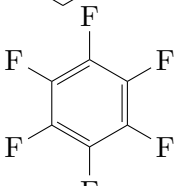	186	278	N/A
Iodobenzene	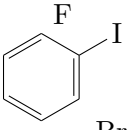	204	242	N/A
1,2-Dibromobenzene	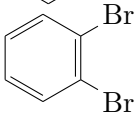	236	278	N/A

Table 9.2: Properties of the molecules in table 9.1 adsorbed on a Si(111)-7 × 7 surface. This includes the structure of the bonded system, whether the molecule adsorbs molecularly (i.e., without dissociation) and whether STM induced manipulation (local or nonlocal) has been observed. *Note that the iodobenzene data is from a density functional theory model, rather than experimental results.

Molecule		Binding configuration	Molecular adsorption	STM manipulation
Benzene		di-σ [165]	Yes [165]	Yes [95]
Toluene	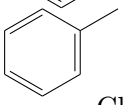	di-σ [100]	Yes [100]	Yes [9]
Chlorobenzene	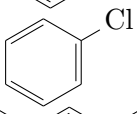	di-σ [90]	Yes [90]	Yes [6]
Mesitylene	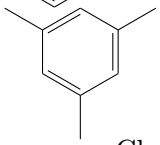	di-σ [166]	Yes [166]	N/A
1,2-Dichlorobenzene	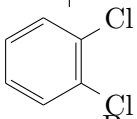	di-σ [167]	Mostly [167]	N/A
Bromobenzene	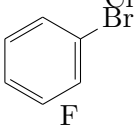	di-σ [168]	Yes [168]	N/A
Hexafluorobenzene	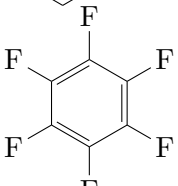	N/A	N/A	N/A
Iodobenzene	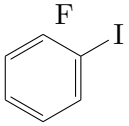	di-σ* [99]	Yes* [99]	N/A
1,4-Dibromobenzene	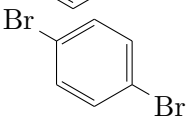	di-σ [169]	$\sim$ 45% [107]	N/A

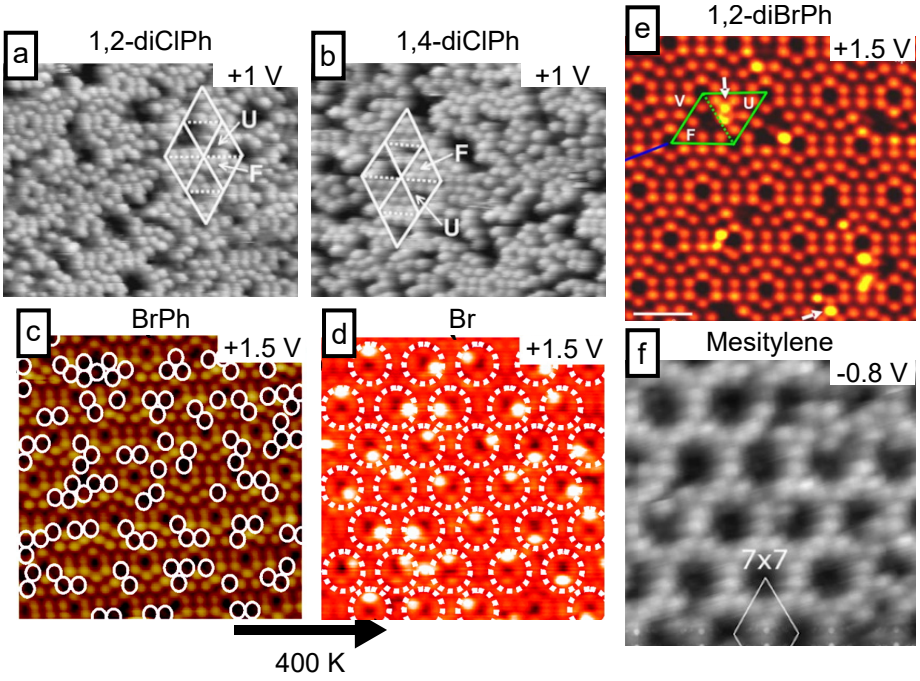

Figure 9-4: STM images of a Si(111)-7×7 surface dosed with (a,b) dichlorobenzene [167], (c) bromobenzene [168], (d) bromine [168], (e) dibromobenzene [107], or (f) mesitylene [166]. Between (a) and (b) the surface is annealed to 400 K, dissociating the BrPh into bromine ions. At low biases (a,b) halogen-Si bonds appear as "missing" adatom sites, identical to chemisorbed benzene derivatives. However, at higher biases (c-e) bright spots, characteristic of a halogen-Si bond, are observed.

9.2.1 Larger benzene-like adsorbates on Si(111)-7×7

Photoinduced dissociation of dichlorobenzene

An investigation by Lu et al. into photoinduced local atomic reactions of 1,2- and 1,4-dichlorobenzene adsorbed on a Si(111)-7×7 surface shows that 193 nm (6.42 eV) photons induced dissociation of the adsorbed molecules [167]. Prior to dissociation empty-looking dark sites are observed in STM images at +1 V (-1 V in the setup of the reference) equivalent to other benzene derivatives, as shown in figures 9-4a and b. However in these low bias images some of the dark sites are chemisorbed chlorine ions, which when imaged at a bias above +2 V appear instead as bright spots due to an available Cl-Si anti-bonding state [170].

Shortly after exposure to a dose of 0.9 L (0.5 L), the surface coverage of 1,2- (1,4-) dichlorobenzene was observed to decrease from approximately 40% (44%) to 33% (37%) over the course of 182 minutes (247 minutes). Over this period the site adsorption

preference changed from slightly favouring the faulted half, 53% (51%) initially in faulted half, to favouring the unfaulted half, 43% (42%) in faulted half.

Long range repulsion of bromine and brominated hydrocarbons

Ebrahimi et al. reported long range repulsive interactions between physisorbed brominated hydrocarbons and also between chemisorbed bromine atoms on a Si(111)-7 $\times$ 7 surface, resulting in the self-assembly of a one-per-corner-hole pattern [168]. Unlike the other brominated hydrocarbon, for bromobenzene, neither a physisorbed state nor the one-per-corner-hole structure were directly observed at 300 K. Instead, a random distribution of chemisorbed molecules is seen, as in figure 9-4c. This is attributed to the di-σ bonding of the phenyl group on Si(111) not seen in the non-aromatic brominated hydrocarbons; the high reactivity of the BrPh molecules with the surface limiting the lifetime of the precursor physisorbed state. After annealing at 400 K, figure 9-4d, the BrPh adsorbates are observed to have dissociated, leaving a one-per-corner-hole brominated surface with no evidence of reattachment of the phenyl radical. Due to the existence of an available back-bond state at about 1.5 eV above the Fermi level, the Br-Si bond is clearly visible as a bright spot in an STM image at biases above +1.5 V [171].

Local atomic reactions of adsorbed dibromobenzene

Upon dosing a Si(111)-7 $\times$ 7 surface with 1,2- or 1,4-dibromobenzene, Dobrin et al. reported observing several different adsorbed products as can be seen in figure 9-4e [107]. At room temperature the chemisorption process was often sufficient to induce dissociation, which, when imaged at +1.5 V, were observed either as dark spots, characteristic of chemisorbed benzene derivatives, or as bright features here corresponding to a Br-Si bond.

Immediately after dosing, adsorbed products were observed in five different states; isolated dark features (mainly undissociated dibromobenzene molecules), single bright spots (a single Br-Si with no adjacent adsorbed bromobenzene), single bright spots with an adjacent dark feature (singly-dissociated bromobenzene with adjacent Br-Si bond), pairs of bright spots (two Br-Si bonds), and pairs of bright spots with an adjacent dark site (doubly-dissociated benzene with two adjacent Br-Si bonds). By counting the number of observations in each category, it was calculated that for 1,2- (1,4-) dibromobenzene, approximately 81% (55%) of the adsorbed molecules undergo dissociation at room temperature resulting in single or double adjacent bright features. For both

precursor molecules, the observed number of single dissociation events outnumbered the number of double dissociation events by 2-3 times.

Theoretical study of halogen-substituted benzene on Si(111)-7×7

In a density functional theory study on the absorption of singly halogen-substituted benzene (fluoro-, chloro-, bromo- and iodobenzene) on Si(111)-7×7 by Petsalakis and Theodorakopoulos [99], it was calculated that there should be minimal transfer of the halogen atom to the surface accompanying room temperature chemisorption. For the undissociated molecules, surface binding energy was found to increase with the size of the halogen atom. Further stabilisation was calculated for Br or I substituted benzene, with the increased halogen-C bond length resulting in an additional interaction between the halogen and a surface adatom in certain orientations. As a result, the transfer of Br or I atoms to the surface results in a higher energy structure than chemisorbed bromo- or iodobenzene. Conversely, the barrier to the transition, primarily governed by the halogen-carbon bond strength, decreases with increasing halogen size. Thus, although the transition of F or Cl atoms to the surface results in an overall lower energy structure, the initial barrier to dissociation is too large to commonly occur thermally at room temperature.

The formation of a well ordered array on Si(111)-7×7 due to saturation coverage mesitylene

McLean et al. used saturation-level dosing of mesitylene (1,3,5-trimethylbenzene) to form a translationally-ordered array on Si(111)-7 × 7 [166]. At low surface coverage the mesitylene molecules were observed to marginally favour chemisorption to middle adatom sites, however at increased adsorbate coverage the preference switched to corner sites. This preference is maintained up to saturation coverage, at which point the corner sites were measured to have approximately 92% occupancy, compared to the 8% average occupancy of middle sites. This results in a well-ordered structure, with only centre adatom sites being unoccupied. This effect is shown in figure 9-4f.

Interaction between hydrogen atoms in the methyl groups of neighbouring toluene molecules, for example, results in a repulsive steric interaction between the toluene molecules themselves. Tomimoto et al. show that a half-unit cell with two toluene molecules adsorbed to centre sites prevented the adsorption of toluene to the third centre site; a third molecule was observed to always adsorb to a corner adatom [100]. Compared to toluene, mesitylene has additional methyl groups distributed evenly around the central phenyl ring. This additional rotational symmetry limits the sites at which

minimal intermolecular steric forces are felt between the mesitylene molecules, as all neighbouring sites in the half unit cell will result in steric hindrance from hydrogen atoms in close proximity. The maximum number of molecules per half unit cell, 3, has the lowest energy configuration when no molecules are chemisorbed on neighbouring sites, which is only possible with all 3 in the more-separated corner positions.

9.2.2 Discussion and conclusions

A key requirement for the adsorbate molecules is that they chemisorb onto the Si(111)-7 × 7 surface without dissociating, this is displayed in table 9.2. This clearly removes dibromobenzene and, although only few Cl-Si sites were observed after exposure, dichlorobenzene, as well as likely other larger benzene derivatives (e.g. tribromo- or trichlorobenzene). From table 9.1 it is clear that each of the listed molecules has a sufficiently low melting point to be liquid at room temperature. However, the vapour pressure of the listed molecules is observed to roughly decrease with increasing molecular mass. Although vapour pressures are unknown for the largest derivatives here, this suggests that the vapour pressure of both hexafluorobenzene and iodobenzene may be insufficient to allow for dosing, and as such should also be discounted.

This leaves two potential candidates; mesitylene and bromobenzene. Both of these are able to be dosed at room temperature, and have been experimentally observed to chemisorb without dissociation. Whilst there is no available information about the desorption characteristics of either molecule, both molecules are likely to undergo a DIET process upon IET above a threshold bias similar to the smaller benzene-like molecules. At higher surface coverage, the increased steric hindrance of mesitylene compared with other benzene derivatives may affect the adsorption characteristics as well as hinder diffusion across the surface. In addition, bromobenzene has the higher mass of the remaining potential molecules, and, due to it having a similar structure to the halogen-substituted benzene molecules, is more likely to interact in a manner that is equivalent to the other singly halogen-substituted benzene derivatives than mesitylene. As a result, bromobenzene is selected as the adsorbate molecule.

9.3 Local manipulation of bromobenzene

During local injection experiments, with the bias set below the nonlocal threshold, the injected charge carriers are unable to enter a surface transport state with energy sufficient to induce manipulation. This means no nonlocal manipulation will occur. Instead, any manipulation is limited to charge carriers exciting the local molecule. As

with the prior nonlocal analysis in chapter 8, we can reflect this localisation by altering the probability distribution ρ_d of finding an injected charge carrier (which is able to induce manipulation) at a given radius r. In this case, ρ_d will only be non-zero at the origin,

$$\sigma\rho_d(r,t') = \begin{cases} 1, & \text{for } r = 0 \\ 0, & \text{otherwise,} \end{cases} \tag{9.5}$$

and so a molecule at the origin (i.e. the injection site) will experience the entire charge "interaction". This allows us to simplify 8.6 and remove the radial dependence of the manipulation probability as, here,

$$\xi_m = \frac{1}{\tau_m}\int_0^\infty \exp\left(\frac{-t'}{\tau_m}\right) dt' = 1. \tag{9.6}$$

Note that for local injections we consider the lifetime of the manipulation not to be dependent on the lifetime of the hot carrier within the surface transport state, $\tau_s \approx 200$ fs, but instead, the lifetime of the excited state of the molecule, $\tau_m \approx 10$ fs [50]. The probability of the local molecule not undergoing manipulation can therefore be described by a first order rate equation,

$$\frac{dP_{nm}}{dn_e} = -k_e P_{nm}, \tag{9.7}$$

in which k_e is the probability of local manipulation per injected charge carrier. With no injected charge carriers $P_{nm} = 1$ and so

$$P_{nm} = \exp\left(-k_e n_e\right). \tag{9.8}$$

Thus the probability of manipulation,

$$P = 1 - \exp\left(-k_e n_e\right), \tag{9.9}$$

is dependent only on the total number of injected charge carriers and the probability of manipulation per injected charge carrier. This relation is shown in figure 9-5.

9.3.1 Binding site dependence: middle versus corner

The above analysis considers a uniform manipulation probability, however, the probability of manipulation per injected charge carrier varies depending on the injection position compared to the local molecule binding site [9]. Due to the di-σ bonding

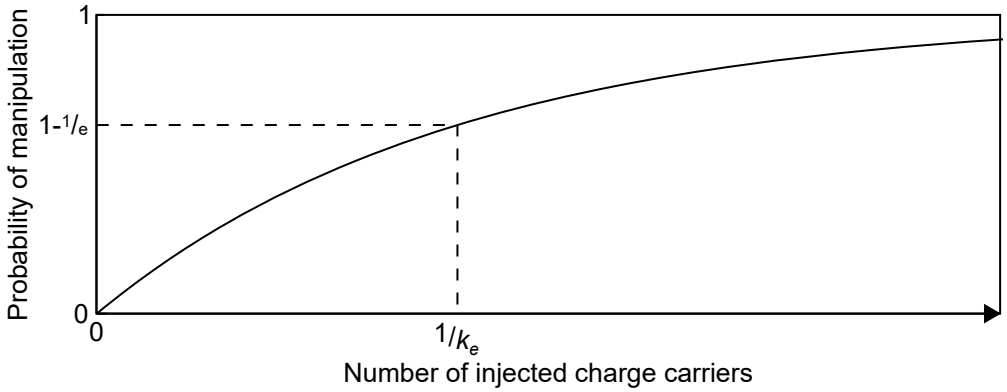

Figure 9-5: Schematic sketch of equation (9.9). When $1/k_e$ charge carriers have been injected, the probability of the local molecule being manipulated is $1 - 1/e$.

structure, there are two crystallographically equivalent binding orientations available for benzene-derivative molecules chemisorbed to middle adatom sites, these are shown in figure 9-6(a,b). In passive STM images these orientations appear to be identical, but each local manipulation injection experiment is performed into a near-identical position above the adatom which may either correspond to injection into the chemisorbed molecule or to the exposed adatom to which the molecule is bonded. This results in two apparent populations with differing manipulation characteristics and, as a result, decay constants. For local injections involving exclusively middle adatom sites, instead of a single exponential decay, the dual populations result in a double exponential decay with the overall rate equation equivalent to the sum of the individual manipulation rate for each of the two populations,

$$P_{nm} = \frac{N_0^A}{N_0} \exp\left(-k_e^A n_e\right) + \frac{N_0^B}{N_0} \exp\left(-k_e^B n_e\right), \tag{9.10}$$

where N_0^A and N_0^B are the initial number of molecules in each of the two populations, compared to the total number of molecules $N_0 = N_0^A + N_0^B$, with manipulation probability per injected charge carrier k_e^A and k_e^B respectively [9]. Here, we instead inject exclusively into corner sites. In this case there is only one possible binding orientation, shown in figure 9-6(c), and hence single exponential behaviour is predicted and found.

9.3.2 Results

The injection procedure from chapter 6.5 was repeated for a number of different injection biases. For each individual injection, the before and after injection images of the area around the injection site as well as the tip height trace during injection, an example

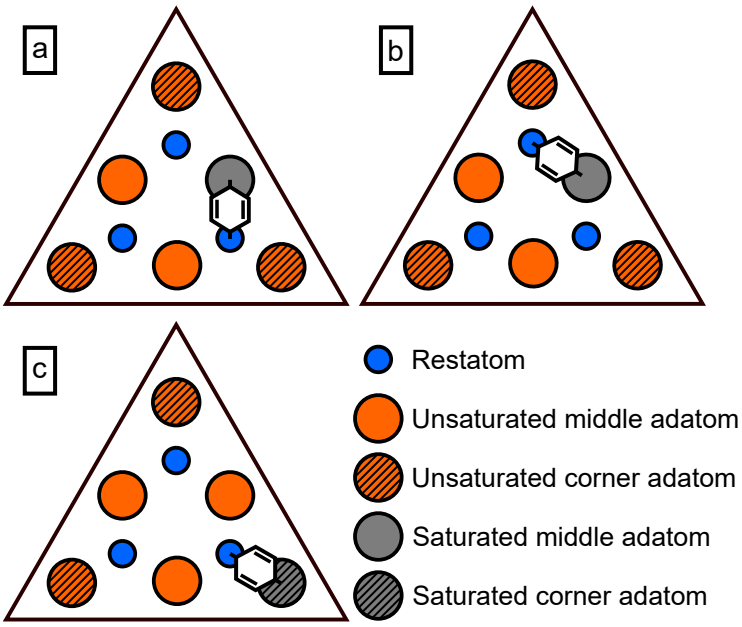

Figure 9-6: (a,b) A molecule bonded to a middle site has two possible orientations that appear identical in an STM image. For injection into a consistent surface position, this results in two distinct populations with slightly different manipulation probabilities [9]. (c) A molecule bonded to a corner adatom site in the only available orientation.

of which are shown in figure 7-1, were then used to identify; whether the local molecule was successfully manipulated, how many charge carriers had been injected when this occurred, and whether the manipulation resulted in diffusion to a neighbouring site or desorption (both of which result in the molecule leaving the tunnel junction). To minimise the effects of contaminants or multiple manipulations, the injection process was limited to a maximum duration of 8 s. If no manipulation occurs prior to the end of the 8 s injection or multiple potential manipulation steps can be identified on the tip height trace, the injection is discounted whether or nor a manipulation event is observed across the surrounding STM images.

Local manipulation below the nonlocal threshold

In figure 9-7 time-to-manipulation curves are shown for both -1.3 V hole injection and +1.8 V electron injection; both biases are above the local manipulation threshold but below the nonlocal threshold. In either case a single exponential fit shows good agreement with the data. From the single exponential fit and equation (9.8) the probability of manipulation per injected charge carrier has been determined. For injection into FC sites we observe $k_e = (2.1 \pm 0.1) \times 10^{-8}$ for 5 pA -1.3 V hole injections and $(6.7 \pm 0.2) \times 10^{-11}$ for 750 pA +1.8 V electron injections.

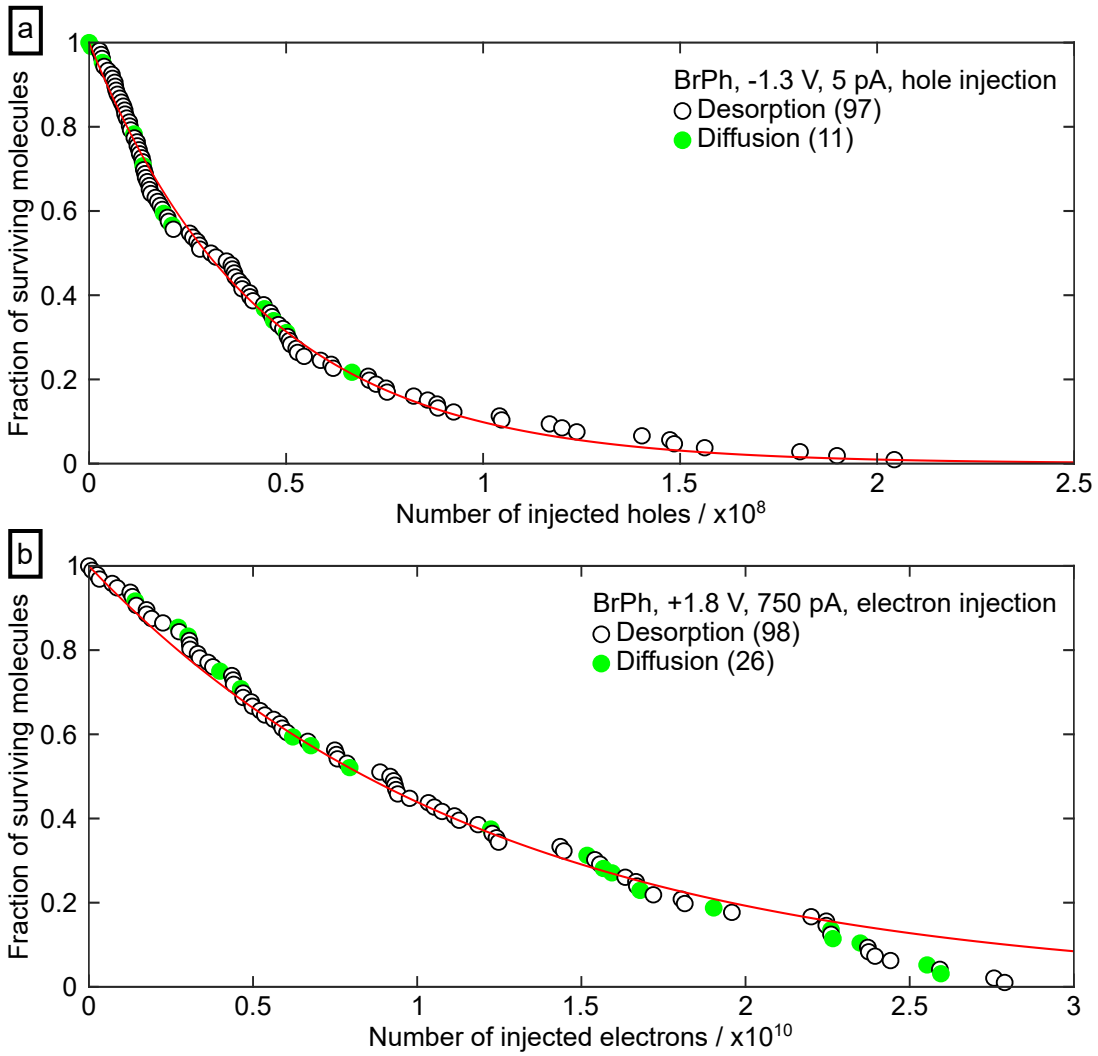

Figure 9-7: The probability of a molecule not being manipulated as a function of the total number of injected charge carriers for both hole (a) and electron (b) injection at local manipulation parameters. Each local manipulation event is coloured based on whether it resulted in desorption (black) or diffusion to a neighbouring site (green). The red lines show fits to a first order exponential decay from equation (9.8).

In addition, figure 9-7 displays whether each observed manipulation event resulted in diffusion or desorption of the local molecule. These two outcomes appear to be approximately evenly distributed along the injection process, with neither a quick nor slow manipulation more likely to result in (e.g.) desorption. The branching ratio (the number of diffusion events divided by the number of desorption events) was measured to be 0.11 ± 0.06 (11 diff / 97 des) for -1.3 V hole injection and 0.27 ± 0.09 (26 diff / 98 des) for +1.8 V electron injection, with uncertainty determined from the 2σ standard error of a binomial distribution.

Local manipulation above the nonlocal threshold

To aid in comparison with the nonlocal injection data in section 8, "local" injections were also attempted at injection biases above the nonlocal threshold. In this case, we expect to induce both local and nonlocal manipulation, although here, only the result of the local molecule is measured. Due to the short-range ballistic transport regime, the probability of "nonlocal" manipulation of molecules immediately surrounding the tip site does not approach unity. Local manipulation should, therefore, remain the dominant mechanism, with few nearby manipulations observed in the timescale of the single local manipulation event. Therefore, we should be able to determine the final outcome of local manipulation.

Time-to-manipulation curves for the high bias local manipulation injections are shown in figure 9-8 for -1.6 V and -2.1 V injections. At these higher biases and, correspondingly, higher manipulation probabilities, the probability of a manipulation occurring during the tip approach is extremely high and so a large proportion of the total manipulation experiments were removed prior to this analysis. As discussed in section 7.1, starting the exponential fit after the tip approach and including only molecules that have not yet been manipulated does not affect the exponential decay constant. This does, however, limit the observed number of manipulations at the set injection parameters.

For both voltages, manipulations were observed and every successful manipulation resulted in desorption of the local molecule; no molecules were observed to diffuse over 130 individual manipulations (0 diff / 71 des for -1.6 V, 0 diff / 59 des for -2.1 V). From the single exponential fits the probability of manipulation per injected charge carrier has again been determined, with $k_e = (2.8 \pm 0.2) \times 10^{-6}$ for 5 pA -1.6 V injections and $(5.7 \pm 0.7) \times 10^{-6}$ for 5 pA -2.1 V injections. Note that the limited time-resolution of the analysis used results in discrete time steps at which manipulation was determined

Table 9.3: Local manipulation probability and local branching ratio for injection at different biases into either an adsorbed toluene or bromobenzene molecule. While the toluene-dosed data consists of injections entirely below the nonlocal manipulation thresholds, for bromobenzene the data has been separated into biases below the nonlocal threshold (+1.8 V, -1.3 V) and above the -1.6 V threshold (-1.6 V, -2.1 V).

Adsorbate molecule	Injection bias / V	Manipulation probability per charge, k_e	Branching ratio (diff/des)
Toluene	+1.8	1×10^{-10} [9]	0.24 ± 0.03 [12]
	-1.3	3×10^{-7} [12]	0.037 ± 0.004 [12]
Bromobenzene	+1.8	$(6.7 \pm 0.2) \times 10^{-11}$	0.27 ± 0.09
	-1.3	$(2.1 \pm 0.1) \times 10^{-8}$	0.11 ± 0.06
	-1.6	$(2.8 \pm 0.2) \times 10^{-6}$	0
	-2.1	$(5.7 \pm 0.7) \times 10^{-6}$	0

to occur. While this affects the quality of the fit, it should have little effect on the overall distribution or magnitude of the resulting manipulation probability.

9.3.3 Discussion and conclusions

Altering the adsorbate molecule

Comparing the values of the local branching ratio for BrPh at local injection parameters with those for toluene (0.037 ± 0.004 for hole injection and 0.24 ± 0.03 for electron injection [12], see table 9.3) suggests that while the final manipulation step due to electron injection is relatively molecule-independent, manipulation due to hole injection is strongly dependent on the adsorbate molecule; with the branching ratio increased significantly for BrPh compared to the smaller toluene. We can additionally compare the probability of manipulation per injected charge carrier with prior measurements of toluene dosed surfaces ($k_e = 3 \times 10^{-7}$ for -1.3 V injections [12] and $k_e = 1 \times 10^{-10}$ for +1.8 V injections [9], see table 9.3). Again, we observe that the manipulation due to electron injection is relatively independent of the adsorbate species, whilst changing the adsorbate molecule changes the manipulation probability due to hole injection by an order of magnitude between these two molecules.

The manipulation process differs between electron and hole injection. After electron injection the negative charge is primarily localised in the surface, not on the molecule, and manipulation is mediated via the adatom hopping process, which pushes part of the adsorbate away from the surface [9, 94]. Alternatively, after hole injection the

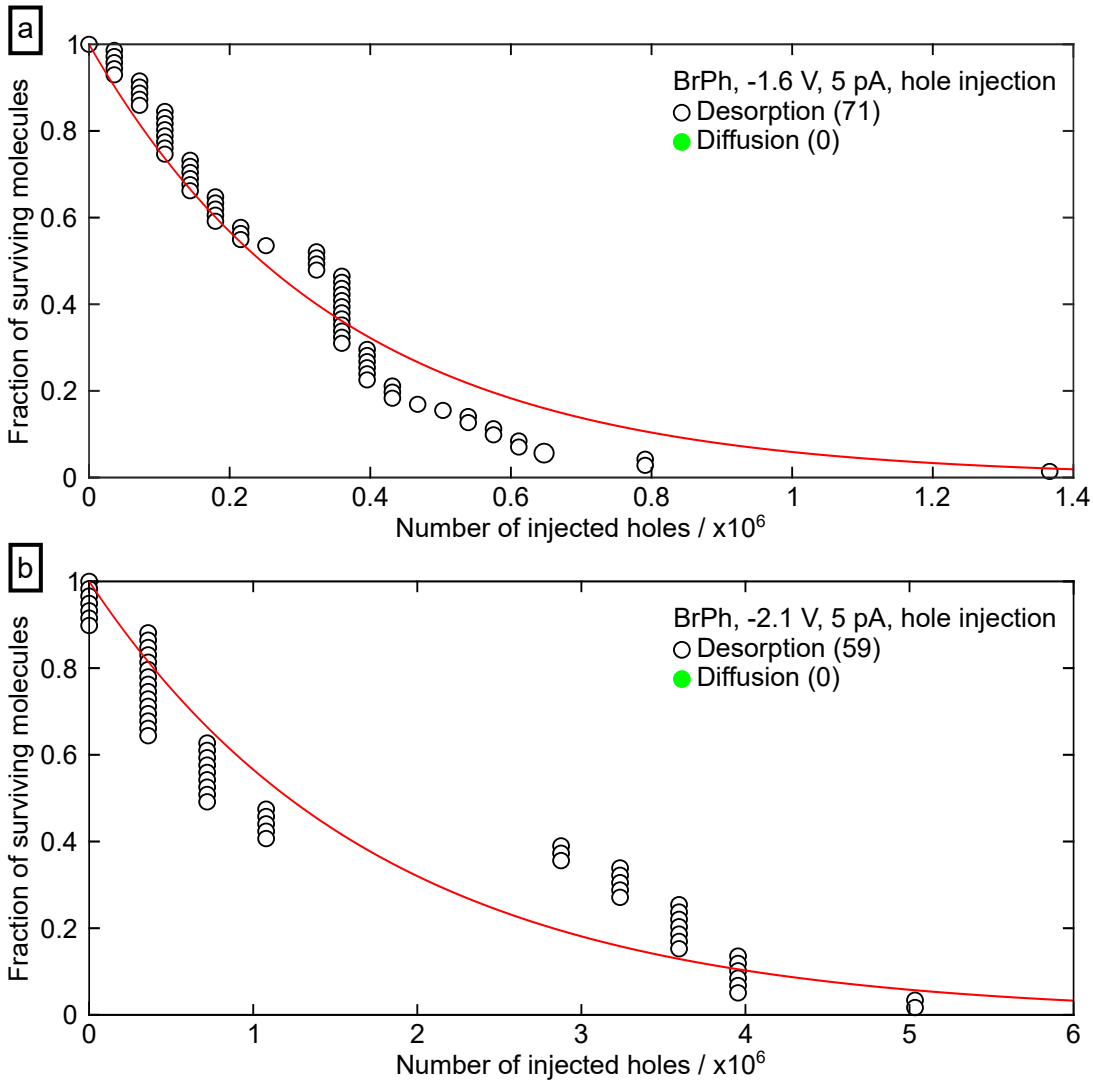

Figure 9-8: The probability of the local molecule not being manipulated as a function of the total number of injected charge carriers injections at biases above the nonlocal manipulation threshold; at -1.6 V in (a) and -2.1 V in (b). The red lines show fits to a first order exponential decay from equation (9.8).

positive charge is additionally located on the molecule and manipulation occurs through molecular excitation and vibrational adatom-molecule bond breaking [12, 94].

The differing benzene derivatives have little affect on the local structure of the surface, with near-identical adsorped structures [99], and so the adatom hopping process is likely to be identical for both a toluene or bromobenzene adsorbate. It is reasonable to assume, therefore, that the surface-mediated desorption process is minimally affected by changing the adsorbate molecule; with both the manipulation probability and branching ratio relatively invariant across these two species for the positive bias electron injection. Conversely, altering the mass of the adsorbate molecule will alter the desorption (or diffusion) probability after entering the excited state, which is observed as both a change in the manipulation probability and the branching ratio between the two molecules for hole injection.

Comparing local and nonlocal manipulation

As in figure 9-3, between the onset of local manipulation and the nonlocal threshold the manipulation probability increases dramatically [160], but the branching ratio is relatively invariant [160]. At the nonlocal biases here, it is likely that rather than the increased bias altering the branching ratio, the greater manipulation probability leads to multiple manipulation events occurring within the timescale of the manipulation. That is, after an initial manipulation resulting in diffusion of the local molecule and corresponding increase in the tunnel current, subsequent nonlocal manipulation with the molecule now at the neighbouring site leads to a dramatic overestimation in the proportion of desorbed molecules. This suggests that the local manipulation probability at the nonlocal biases determined from figure 9-8 (i.e. calculated from measuring the number of charge carriers injected prior to the first manipulation event) are reasonable, however the branching ratio is unable to be determined from this data. Instead, a measurement of the branching ratio at increased bias would require a more controlled and quicker method of preventing further manipulation, limiting the magnitude of the current pulse after the local manipulation.

In section 8.3 the probability of nonlocal and local manipulation is determined to be of the same order of magnitude due to the relative effects of the differing lifetimes of the excited states and probability of interaction with a molecule. However, that analysis is comparing local manipulation of toluene at a local bias with nonlocal manipulation of BrPh at nonlocal biases. Here, however, we are able to more directly compare the manipulation probabilities to determine whether there is a fundamental difference between the manipulation step itself for local and nonlocal manipulation at the same

bias. Comparing the purely local manipulation probabilities of BrPh in table 9.3 with the nonlocal manipulation probabilities at the same biases in chapter 8 ($\kappa_e = (2 \pm 2) \times 10^{-7}$ at -1.6 V and $\kappa_e = (8 \pm 5) \times 10^{-7}$ at -2.1 V) suggests that the probability of any one injected charge carrier resulting in local manipulation is approximately an order of magnitude greater than that charge carrier manipulating any one nonlocal molecule.

However, as discussed in section 8.6.1, κ_e and k_e are, effectively, not measuring the same thing; with the nonlocal probability κ_e a measure of the manipulation probability per injected charge carrier for a single molecule, rather than per charge carrier-molecule interaction. To more reasonably compare the probability of manipulation between local and nonlocal manipulation, we reframe the nonlocal manipulation probability for a single molecule per injected charge κ_e in terms of the total nonlocal manipulation probability for all molecules across the surface per injected charge, following the analysis of section 8.6.1. The probability of an injected charge interacting with a molecule at radius r, $P_m(r)$, depends on both the distribution of the injected charge at r, $\xi_m(r)$, as well as the area covered with molecules at r,

$$P_m(r) = \xi_m(r) \cdot \rho \cdot 2\pi r \Delta r \cdot \sigma, \tag{9.11}$$

where $\rho(r)$ is the number density of molecules on the surface, each of which cover an area σ. Thus, noting the result of equation (8.38), the total probability of an injected charge carrier interacting with a molecule across the surface

$$P_{mi} = \frac{4\rho}{\lambda^2} \int_0^\infty r \mathrm{K}_0 \left(\frac{2r}{\lambda} \right) dr. \tag{9.12}$$

In the limit of $r \to \infty$ the integral $\int r \mathrm{K}_0 \left(2r/\lambda\right) dr \to \lambda^2/4$, hence

$$P_{mi} = \rho\sigma, \tag{9.13}$$

which is simply the area of the surface covered by molecules, entirely independent of the charge transport process. Assuming that, prior to injection, each adatom has a probability 0.4 of being occupied by an adsorbate molecule and noting that the number of adatoms per m^2 on the Si(111)-7×7 surface is equal to 1.92×10^{18} [11], $P_{mi} = 0.017$. The lifetime of the charge carrier excited state in nonlocal manipulation is far longer than for local manipulation, $\tau_s \approx 200$ fs compared to $\tau_m \approx 10$ fs. Assuming (as in chapter 8) that an increase in the carrier lifetime results in a linear increase in the probability of manipulation, we expect the nonlocal probability of manipulation, κ_e, to

relate to the local probability of manipulation, k_e, through

$$\kappa_e \approx \rho\sigma\frac{\tau_s}{\tau_m}k_e \tag{9.14}$$

$$\approx 0.34k_e; \tag{9.15}$$

far lower than that determined in equation (8.50).

We thereby expect, for identical dynamics in the final manipulation step, the probability of nonlocal manipulation per injected charge carrier to be of a similar order of magnitude, perhaps slightly smaller, than for local manipulation at the same bias. From the results of figure 9-8 and the data from chapter 8, we observe $\kappa_e = (0.11 \pm 0.07)k_e$ (with the constant equal to 0.07 ± 0.10 at -1.6 V and 0.14 ± 0.09 at -2.1 V). This is in good agreement given the assumptions made. The evidence thus points to common final manipulation dynamics for both local and nonlocal manipulation. This suggest that, for example, a -1.7 eV electron, after nonlocal transport and upon localisation at a molecule, must undergo a rapid energy loss to attain the energy found for local manipulation.

9.4 Further linking local and nonlocal manipulation

The only fundamental difference between the two injection regimes is the addition of the transport step in nonlocal manipulation, and the additional threshold bias this introduces. In this section, further published experimental results linking the final manipulation steps of local and nonlocal manipulation to a common mechanism are given.

The excitation and subsequent emission of surface adatoms from the Si(111)-7×7 surface due to laser fluence shows key similarities with both local and nonlocal STM charge injection manipulation of adsorbate molecules. Laser-induced excitation of Si(111)-7×7 adatoms has been observed to be a two photon process with a minimum photon energy of $\sim$2 eV required to induce manipulation [172], see figure 9-9(left), this is in line with the +2 V threshold for nonlocal STM manipulation. Additionally, the kinetic energy of adatoms emitted by this process shows a consistent distribution independent of the energy of the incident photons [173], shown in figure 9-9(right), much like the voltage invariance of the final manipulation step of local STM manipulation.

Kanasaki et al. suggest that the adatom emission is mediated by two-hole localisation on the adatom site followed by a phonon-kick mechanism across the range of probed energies [173, 174]. Comparison of the desorption yield for both nanosecond

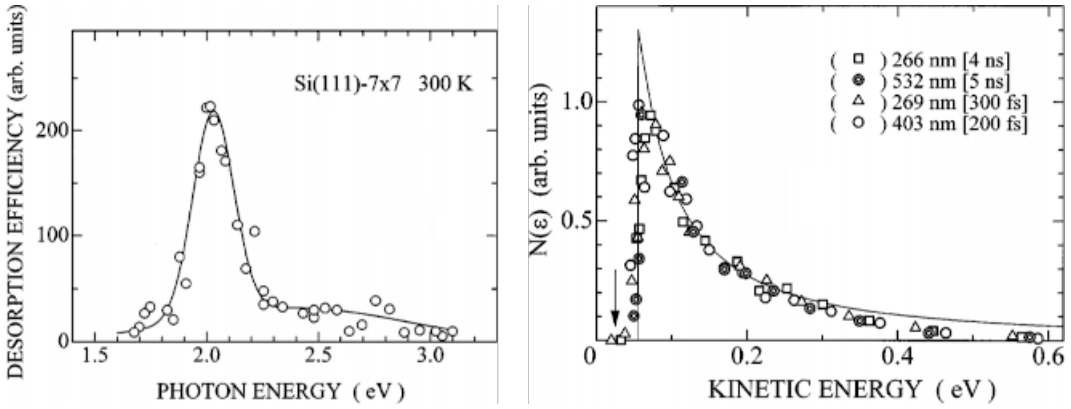

Figure 9-9: Laser-induced desorption of Si adatoms from the Si(111)-7 × 7 surface. (Left) Photon-energy dependence of the desorption efficiency for a fluence of 150 mJ/cm^2. From [172]. (Right) Translational energy distribution of Si atoms desorbed. Surface excitation was made at 300 K with laser pulses of different characteristics in wavelengths, fluences, and temporal widths. Data for different types of laser light are normalized to the same peak height. From [173].

and femtosecond-duration laser pulses in this model, such that the duration of each laser pulse is far longer or far shorter than the expected effective lifetime of a charge carrier in the excited surface state respectively, results in an estimate of the charge lifetime of the order of 100 ps [175]. However, time resolved 2-photon photoemission spectroscopy shows ultrafast decay of hot charge carriers in Si(111)-7 × 7 surface bands within several 100 fs of excitation [81, 113]. This mismatched timescale means that it is unlikely for the excited adatom state to remain for the 100 ps calculated for the phonon-kick, and thereby the mechanism is unfavourable.

Rusimova and Sloan proposed an alternate intermediary step, in which the adatom manipulation is not mediated by two-hole localisation, but instead by a two-step process, similar in form to the nonlocal manipulation of adsorbate molecules [9]. In this model, the first photon excites an electron-hole pair, which is able to explore the surrounding surface (as we observe in the nonlocal transport step of STM induced manipulation) prior to inducing an adatom into a metastable "hopped" state atop a neighbouring adatom site via excitation of the Si backbond. The hopped state can be observed in low temperature STM images as an adatom vacancy with a neighbouring bright protrusion, as seen in figure 9-10. At room temperature the hopped state has been observed to relax, with the adatom returning to the original site, within $\sim$ 600 ps [54] (far faster than an STM can resolve); comparable to the estimated two-hole localisation lifetime of $\sim$ 100 ps. Whilst this adatom hopping step may be sufficient to break a covalant bond between an adsorbate molecule and the surface, potentially resulting in the observed

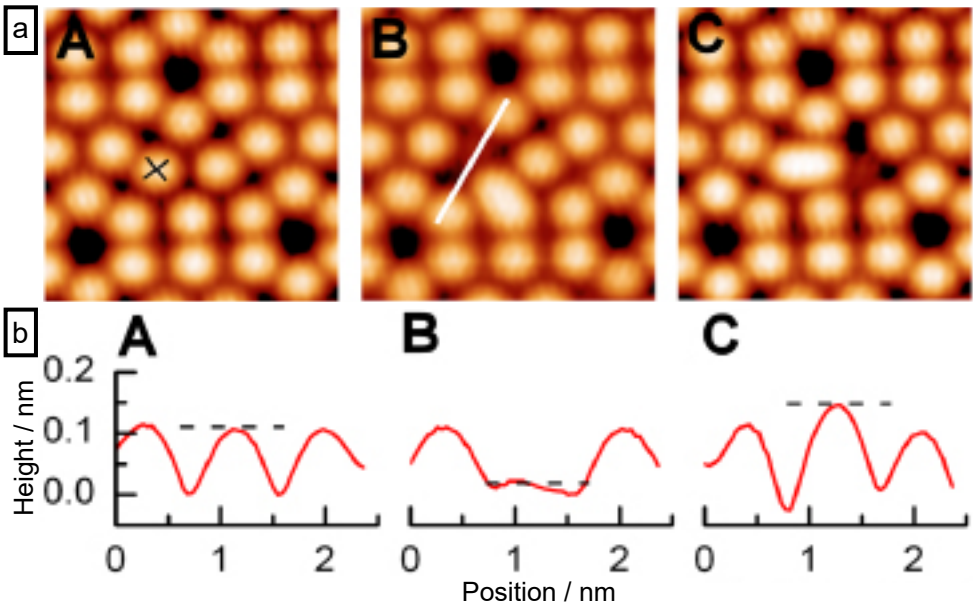

Figure 9-10: (a) Low temperature (77 K) STM images (+1 V, 100 pA) of an Si(111)-7×7 surface. (b) Tip height for each image in (a), with the profile for each image taken along the white line in B. Between each image the tip is positioned at the cross in (a) and the bias is increased to +1.8 V until a discrete change in the tip height is observed. These tip height changes are due to displacement of a middle adatom ("hopping"); the injected charge inducing movement of an adatom on top of a neighbouring site. An adatom has moved away from the injection site in B, whereas a neighbouring adatom has moved towards it in C. From [176].

manipulation of our STM experiments [9], a second photoelectron is required to desorb the hopped adatom; hence we recover the superlinear quadratic relation between desorption yield and laser fluence.

The key difference between the laser-induced desorption and local STM manipulation experiments is the localised nature of the latter, in which many charge carriers are able to be controllably injected into the same surface site. While the adatom hopping motion itself precludes two-electron desorption of the hopped adatom in local manipulation (i.e. the adatom leaves the tip-sample junction after manipulation, which prevents further local injection into the molecule), both models demonstrate charge relaxation to a common energy state prior to manipulation as elucidated by a consistent branching ratio (STM manipulation) or kinetic energy distribution (laser manipulation). Although we expect the hopped adatom mediated manipulation step to have a common minimum energy threshold, the threshold can be directly measured in local manipulation experiments but not in nonlocal or laser-induced manipulation. Instead, prior to this hopping step, the injected charges relax to the bottom of the +2 V surface state, within

which they are able to explore the surrounding surface prior to eventual thermalisation or manipulation local to the position of the charge relaxation. Overall, it is therefore likely that while the nonlocal and local manipulation processes are superficially different, the nonlocal process only adds one additional step and is otherwise identical to local manipulation. The higher barrier to nonlocal manipulation corresponds to injection of the charge into a surface transport state and, prior to manipulation, the charge carrier relaxes into the bottom of the same surface state as local manipulation.

9.5 Measuring the branching ratio in nonlocal manipulation

If the final manipulation step is consistent in local and nonlocal manipulation, then the branching ratio should be the same for both. In this section we expand the previously measured ratio of diffusion to desorption events during STM induced IET manipulation from purely local manipulation to nonlocal manipulation, and thereby more directly probe the final step for nonlocal manipulation. In nonlocal manipulation experiments far more molecules than just the one directly within the tip-sample junction are manipulated, and the movement of each individual molecule cannot be tracked. As a result, the identification of manipulated molecules can only be inferred by the change in the distribution of molecules before and after an injection. Note that here, for simplicity, we consider one-step diffusion from a point source described in section 8.3 as a reasonable model for the nonlocal charge transport, and so expect the results of this section only to be accurate for injection parameters at which this model is reasonable.

Here we define three outcomes of hot charge-molecule interaction; no-manipulation, such that the molecule retains its initial position; desorption, such that the molecule enters the gas-phase and can no longer be observed; and diffusion, such that a molecule moves to a neighbouring site on the surface. It is assumed that once a molecule has desorbed it will not be re-adsorped elsewhere on the surface. Similarly, it is assumed that a diffused molecule will not diffuse back to its initial site in subsequent charge carrier interaction, and so the number of molecules in each of the three possible states

can be described as a series of differential equations

$$\frac{dN_g(r,t)}{dN_e(r,t)} = \kappa_g N_0(r,t) + \kappa_g N_d(r,t) \tag{9.16}$$

$$\frac{dN_d(r,t)}{dN_e(r,t)} = \kappa_d N_0(r,t) - \kappa_g N_d(r,t) \tag{9.17}$$

$$\frac{dN_0(r,t)}{dN_e(r,t)} = -\kappa_d N_0(r,t) - \kappa_g N_0(r,t), \tag{9.18}$$

in which N_e is the number of electrons interacting with a molecule at distance r from the injection site for an injection of duration t, N_g, N_d and N_0 refer to the number of molecules desorbed, diffused or maintaining their original position respectively and κ_g and κ_d are the probabilities of a molecule desorbing or diffusing upon interaction with a charge carrier. Here N_g, N_d and N_0 are normalised such that $N_g + N_d + N_0 = 1$; the total number of molecules does not change during injection. Noting that N_e is equal to the total number of injected charge carriers n_e times the probability of a charge carrier at a given position r, $N_e = n_e \cdot \xi_{m(r)}$, and using equation (8.6), the solutions to these differential equations are

$$N_g = 1 - \exp\left(-\kappa_g \frac{t}{t_\kappa} \mathrm{K}_0\left(\frac{2r}{\lambda}\right)\right), \tag{9.19}$$

$$N_d = \exp\left(-\kappa_g \frac{t}{t_\kappa} \mathrm{K}_0\left(\frac{2r}{\lambda}\right)\right) - \exp\left(-\left(\kappa_g + \kappa_d\right) \frac{t}{t_\kappa} \mathrm{K}_0\left(\frac{2r}{\lambda}\right)\right), \tag{9.20}$$

and

$$N_0 = \exp\left(-\left(\kappa_g + \kappa_d\right) \frac{t}{t_\kappa} \mathrm{K}_0\left(\frac{2r}{\lambda}\right)\right), \tag{9.21}$$

in which t_κ is the characteristic time-scale of manipulation attempts, in analogy with t_0 the characteristic time-scale of the manipulation used in chapter 8,

$$t_\kappa = \frac{\pi e \lambda^2}{2\sigma I s}. \tag{9.22}$$

An example of the resultant proportion of molecules within each of the three states as a function of both injection duration and distance from the injection site for a -2.1 V, 900 pA injection using equations (9.19-9.21) can be seen in figures 9-11 and 9-12. Initially at $t = 0$, such that no charge carriers have been injected, all molecules retain their original site. As t increases, the radius at which an appreciable number of

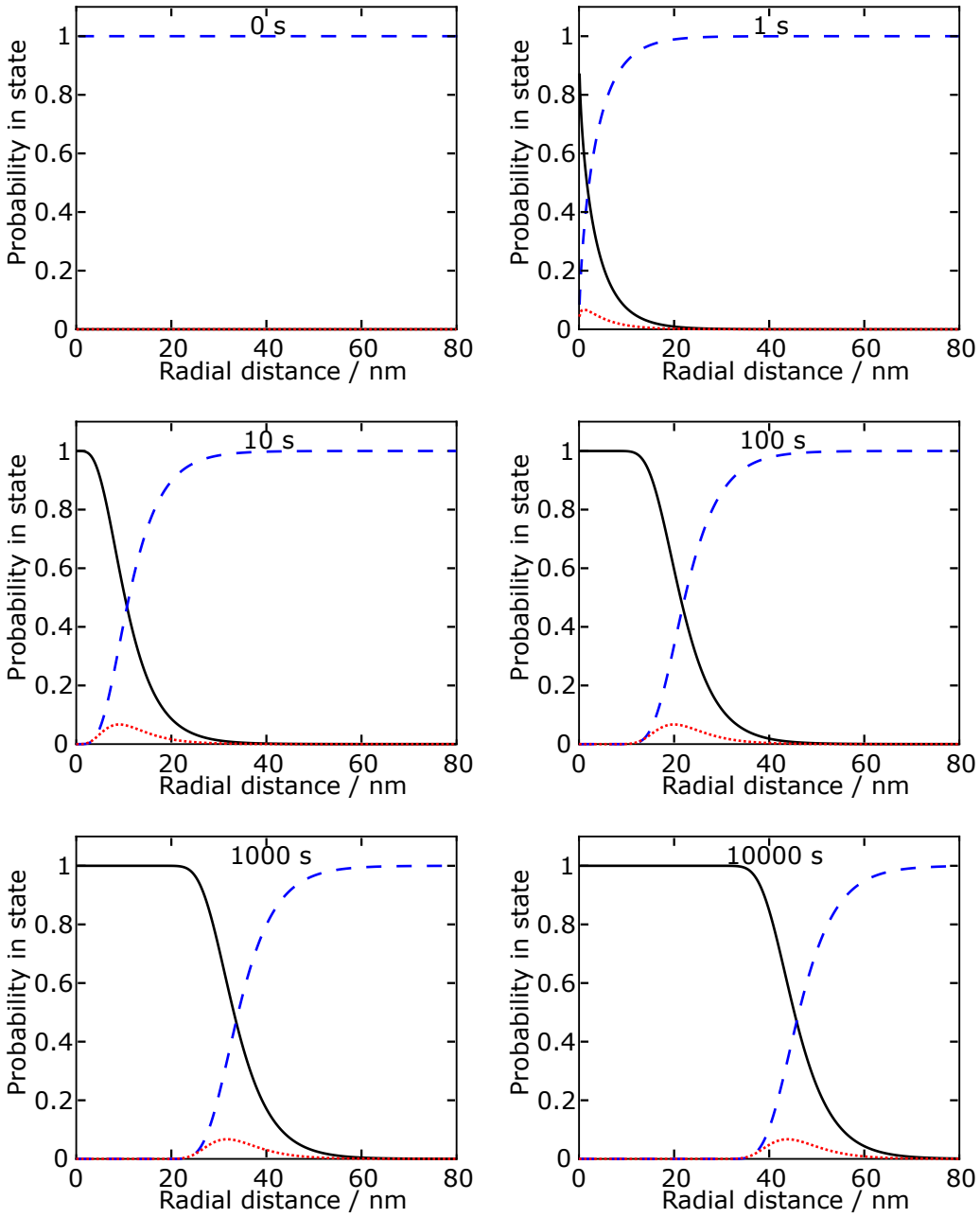

Figure 9-11: The proportion of molecules not manipulated N_0 (dashed blue), desorbed N_g (solid black) and diffused N_d (dotted red) in an annulus at radius r after a hot charge carrier injection at $r = 0$ as a function of the injection duration, t, between 0 and 10 ks. At $t = 0$, no electrons have been injected into the surface, and so no manipulation has occurred. The branching ratio ε has been set as 0.2. Other parameters have been set to reasonable values for a -2.1 V, 900 pA injection ($\kappa_g = 8 \times 10^{-7}$, $\lambda = 11$ nm).

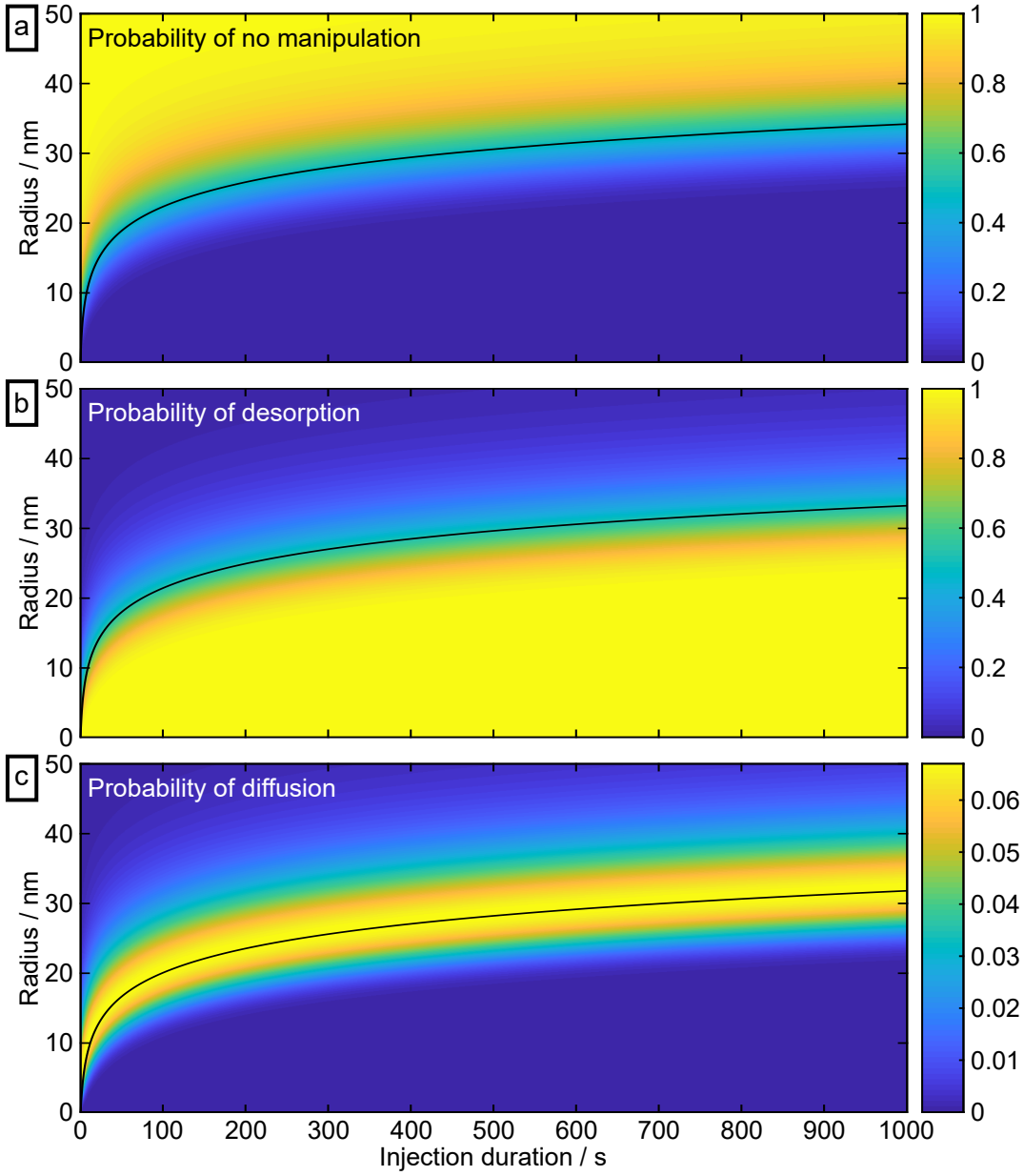

Figure 9-12: The proportion of molecules in each of the three possible states, (a) not manipulated, (b) desorbed or (c) diffused, in an annulus at radius r after a charge carrier injection as a function of both r and the injection duration t. The black lines in (a) and (b) show the half radii derived in sections 9.5.1 and 9.5.1 respectively, while the line in (c) shows the N_d peak with $N_d = 0.067$ here, derived in section 9.5.2. The branching ratio ε has been set as 0.2, while other parameters have been set to reasonable values for a -2.1 V injection ($\kappa_g = 8 \times 10^{-7}$, $\lambda = 11$ nm).

manipulated molecules increases, with the maximum proportion of diffused molecules remaining slightly greater. The maximum proportion of diffused molecules remains constant for all $t > 0$; with a value of 0.067 for the parameters defined in figure 9-12.

As in chapter 8, a portion of dark sites in STM images are not chemisorbed molecules able to be desorbed by charge injection, but instead, immovable contaminants. As such, the maximum probability of manipulation is limited by the probability of a site being an adsorbate. To correct for these effects, an additional multiplicative term C is used within the fitting process, such that the corrected probability of desorption $P_c^g(r) = C \cdot P^g(r)$. This effect conversely sets a lower limit on the proportion of not manipulated molecules at $1 - C$. Hence a similar correction is used, applying a multiplicative factor as with the corrected probability of manipulation, but also an offset; such that the probability of a molecule not being manipulated $P_c^{nm}(r) = C + (1 - C) \cdot P^{nm}(r)$.

9.5.1 Diffusion and no-manipulation half radii

Here again we use the half radius as a measure of the extent of manipulation, from which the branching ratio can be determined. While equations (9.19) and (9.21) for N_g and N_0 respectively are monotonic function and for all $t > 0$ have a single solution equal to 0.5, equation (9.20) for N_d is not and must be considered separately.

No-manipulation; $N_0 = \frac{1}{2}$

In an annulus at $r_{1/2}^0$, such that half of all molecules have not been manipulated,

$$N_0(r = r_{1/2}^0) = \frac{1}{2} = \exp\left(- \left(\kappa_g + \kappa_d\right) \frac{t}{t_\kappa} \mathrm{K}_0 \left(\frac{2r_{1/2}^0}{\lambda} \right) \right). \tag{9.23}$$

Thus,

$$t(r = r_{1/2}^0) = \frac{\ln(2) t_\kappa}{\left(\kappa_g + \kappa_d\right) \mathrm{K}_0 \left(\frac{2r_{1/2}^0}{\lambda} \right)} \tag{9.24}$$

and

$$\kappa_d = \frac{\ln(2)}{\frac{t}{t_\kappa} \mathrm{K}_0 \left(\frac{2r_{1/2}^0}{\lambda} \right)} - k_g. \tag{9.25}$$

Desorption; $N_g = \frac{1}{2}$

Equivalently, in an annulus at $r^g_{1/2}$, such that half of all molecules have desorbed,

$$N_g(r = r^g_{1/2}) = \frac{1}{2} = 1 - \exp\left(-\kappa_g \frac{t}{t_\kappa} \mathrm{K}_0\left(\frac{2r^g_{1/2}}{\lambda}\right)\right) \tag{9.26}$$

$$t(r = r^g_{1/2}) = \frac{\ln(2) t_\kappa}{k_g \mathrm{K}_0\left(\frac{2r^g_{1/2}}{\lambda}\right)} \tag{9.27}$$

$$\kappa_g = \frac{\ln(2)}{\frac{t}{t_\kappa}\mathrm{K}_0\left(\frac{2r^g_{1/2}}{\lambda}\right)}. \tag{9.28}$$

The probability of a molecule being desorbed or being diffused follows the same form in both equation (9.25) and (9.28), with, effectively, only an additional constant (and differing half radii) between the two equations. However, note that whilst κ_g can be determined from measurement of only the desorption half radius, κ_d requires measurement of both $r^g_{1/2}$ and $r^0_{1/2}$.

Branching ratio

The branching ratio ε is the ratio between the probability that a molecule is desorbed and the probability that it diffuses when interacted with by an injected electron,

$$\varepsilon = \frac{\kappa_d}{\kappa_g}. \tag{9.29}$$

By measuring both $r^g_{1/2}$ and $r^0_{1/2}$, the branching ratio can be calculated from equations (9.25) and (9.28) with

$$\varepsilon = \frac{\mathrm{K}_0\left(\frac{2r^g_{1/2}}{\lambda}\right)}{\mathrm{K}_0\left(\frac{2r^0_{1/2}}{\lambda}\right)} - 1. \tag{9.30}$$

For a non-linear function, an approximation of the uncertainty can be estimated using a first order Taylor expansion. Thus an estimate of the standard deviation in ε, σ_ε,

$$\sigma_\varepsilon^2 \approx \left(\frac{\partial \varepsilon}{\partial r_{1/2}^0}\right)^2 \sigma_{r_{1/2}^0}^2 + \left(\frac{\partial \varepsilon}{\partial r_{1/2}^g}\right)^2 \sigma_{r_{1/2}^g}^2 \tag{9.31}$$

$$\sigma_\varepsilon^2 \approx \left(\frac{2}{\lambda}\frac{\mathrm{K}_0\left(\frac{2r_{1/2}^g}{\lambda}\right) K_1\left(\frac{2r_{1/2}^0}{\lambda}\right)}{\mathrm{K}_0\left(\frac{2r_{1/2}^0}{\lambda}\right)^2}\right)^2 \sigma_{r_{1/2}^0}^2 + \left(-\frac{2}{\lambda}\frac{K_1\left(\frac{2r_{1/2}^g}{\lambda}\right)}{\mathrm{K}_0\left(\frac{2r_{1/2}^0}{\lambda}\right)}\right)^2 \sigma_{r_{1/2}^g}^2 \tag{9.32}$$

in which $\sigma_{r_{1/2}^0}$ and $\sigma_{r_{1/2}^g}$ are the standard deviations of $r_{1/2}^0$ and $r_{1/2}^g$ respectively, and K_1 is a modified Bessel function of the second kind of order 1. Assuming that $\sigma_{r_{1/2}^0} = \sigma_{r_{1/2}^g} = \sigma_r$, then

$$\sigma_\varepsilon \approx \frac{2}{\lambda}\left(\frac{\mathrm{K}_0\left(\frac{2r_{1/2}^g}{\lambda}\right) K_1\left(\frac{2r_{1/2}^0}{\lambda}\right) + K_1\left(\frac{2r_{1/2}^g}{\lambda}\right) \mathrm{K}_0\left(\frac{2r_{1/2}^0}{\lambda}\right)}{\mathrm{K}_0\left(\frac{2r_{1/2}^0}{\lambda}\right)^2}\right)\sigma_r. \tag{9.33}$$

9.5.2 Maximum diffusion probability

While the proportion of desorbed molecules in figure 9-11 tends towards unity at small radii, the proportion of diffused molecules has a constant peak at $N_d = 0.067$ for all $t > 0$ with $\varepsilon = 0.2$. By measuring the maximum proportion of molecules that have diffused at a given injection duration t, ε can be calculated. At the radius with the maximum proportion of diffused molecules, r^d,

$$\frac{\partial N_d}{\partial r} = 0. \tag{9.34}$$

As

$$\frac{\partial \mathrm{K}_0(x)}{\partial x} = -K_1(x), \tag{9.35}$$

$$\frac{\partial N_d(r,t)}{\partial r} = -\frac{2}{\lambda}\frac{t}{t_\kappa} K_1\left(\frac{2r}{\lambda}\right) \exp\left[-\kappa_g \frac{t}{t_\kappa}\mathrm{K}_0\left(\frac{2r}{\lambda}\right)\right] \cdot \left(\kappa_g - (\kappa_g + \kappa_d)\exp\left[-\kappa_d \frac{t}{t_\kappa}\mathrm{K}_0\left(\frac{2r}{\lambda}\right)\right]\right). \tag{9.36}$$

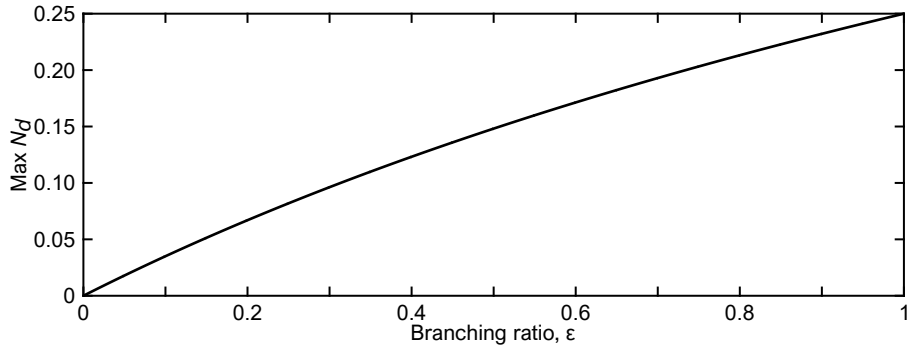

Figure 9-13: The maximum proportion of diffused molecules as a function of the branching ratio ε during nonlocal STM with a pulse duration $t > 0$ from equation 9.40.

For values of r such that $0 < r < \infty$, both $0 < \mathrm{K}_0(2r/\lambda) < \infty$ and $0 < K_1(2r/\lambda) < \infty$. Therefore, for non-zero t the above equation will only equal zero when

$$0 = \kappa_g - (\kappa_g + \kappa_d) \exp\left(-\kappa_d \frac{t}{t_\kappa} \mathrm{K}_0\left(\frac{2r^d}{\lambda}\right)\right), \tag{9.37}$$

and hence

$$t = \frac{\ln(\kappa_g + \kappa_d) - \ln(\kappa_g)}{\frac{\kappa_d}{t_\kappa} \mathrm{K}_0\left(\frac{2r^d}{\lambda}\right)}. \tag{9.38}$$

Substituting equation (9.38) into equation (9.20),

$$N_d = \left(\frac{\kappa_g}{\kappa_g + \kappa_d}\right)^{\frac{\kappa_g}{\kappa_d}} - \left(\frac{\kappa_g}{\kappa_g + \kappa_d}\right)^{\frac{\kappa_g}{\kappa_d}+1}, \tag{9.39}$$

and thus from equation (9.29),

$$N_d = (1+\varepsilon)^{-\frac{1}{\varepsilon}} - (1+\varepsilon)^{-\frac{(1+\varepsilon)}{\varepsilon}}. \tag{9.40}$$

Both the dependence of N_d on r and t have been eliminated, and so this predicts that the maximum proportion of the number of diffused molecules is radially and temporally invariant for $t > 0$; only dependent on ε. A plot of equation (9.40) can be observed in figure 9-13.

The uncertainty in ε, $\Delta\varepsilon$, as a function of N_d can be estimated by differentiating equation (9.40) with respect to the branching ratio,

$$\frac{dN_d}{d\varepsilon} = \frac{\ln(1+\varepsilon)}{\varepsilon(1+\varepsilon)^{-\frac{(1+\varepsilon)}{\varepsilon}}}. \tag{9.41}$$

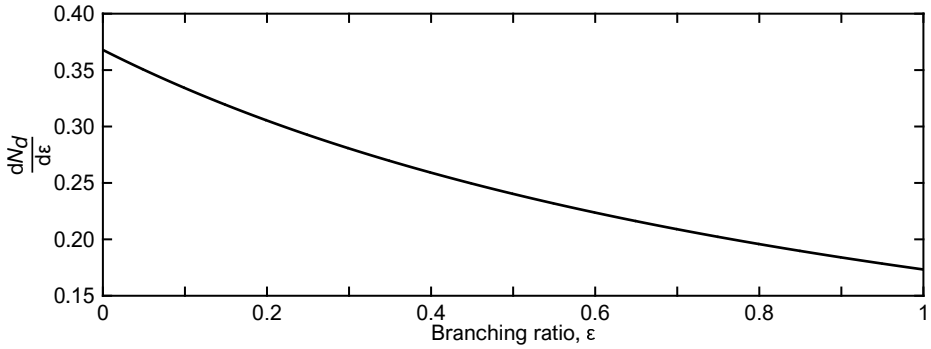

Figure 9-14: The differential of the branching ratio ε as a function of the maximum proportion of diffused molecules N_d against the branching ratio ε as an estimate of the uncertainty in the calculated value of the branching ratio.

and thus

$$\Delta\varepsilon \approx \frac{\varepsilon(1+\varepsilon)^{\frac{1+\varepsilon}{\varepsilon}}}{\ln(1+\varepsilon)}\Delta N_d, \tag{9.42}$$

in which ΔN_d is the uncertainty in the proportion of molecules that have diffused. Figure 9-14 shows a graph of equation (9.41). In this figure it is clear that for reasonably physical errors (ΔN_d of order 0.1) $\Delta\varepsilon$ will be small only for large ε.

9.5.3 Conclusions

Here we observe two different routes to extract the branching ratio from the probability of desorption, desorption and no-manipulation distributions; either measurement of both the half desorption and half no-manipulation radii, or measurement of the maximum probability of desorption. Through either method, an estimate of the uncertainty on the branching ratio can be determined. However, the uncertainty is determined to be strongly dependent on the size of the branching ratio itself, with smaller branching ratios corresponding to a larger uncertainty.

9.5.4 Results

Here we reanalyse the nonlocal charge injection data presented in chapter 8 in order to determine the nonlocal branching ratio. The output of the data analysis software described in chapter 7 includes the number of molecules in each annuli at increasing radius centred on the injection site, and whether they diffused, desorbed or were not manipulated by the injection. In the previous chapter all manipulated molecules were considered as one overall population, however, here we separately consider diffused and desorbed molecules and additionally fit curves to the radial probability distribution

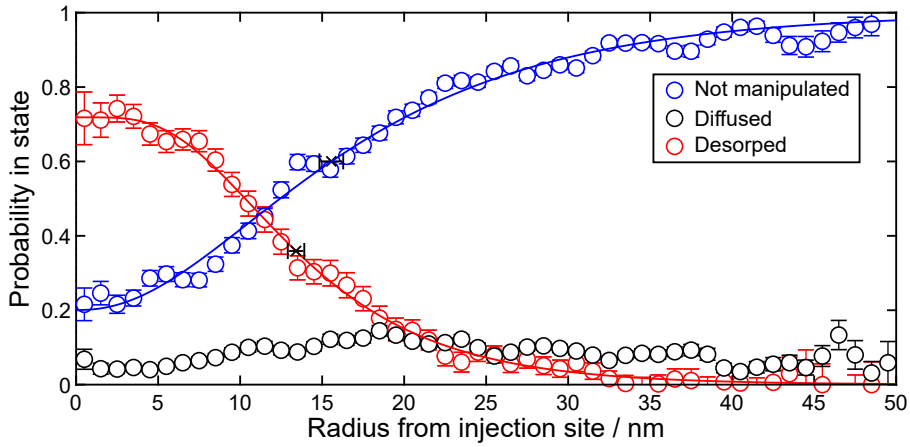

Figure 9-15: The radial distribution of the probability of a BrPh molecule chemisorbed on a Si(111)-7 × 7 surface being desorbed (red), diffused (black) or not manipulated (blue) after a -1.6 V, 900 pA injection for 100 s at the origin, averaged across 10 injections. The red and blue curves are fits to the data based on a 2D ballistic transport model, described by equations (9.19) and (9.21) respectively. The black crosses indicate the radii at which the probability of a molecule being desorbed or not manipulated is one half.

of non-manipulated molecules; for example shown in figure 9-15 for a -1.6 V, 900 pA injection for 100 s into a BrPh dosed surface.

It is clear from figure 9-15 that the probability distribution of diffused molecules does not follow a distribution as expected from equation (9.20) or displayed in figure 9-11. Instead, across both BrPh and toluene dosed surfaces, the probability of diffusion is approximately consistent, generally increasing at the largest radii but otherwise not showing a clear peak. This is most likely due to slightly incorrect systematic corrections to thermal manipulation and the uncertainty inherent in low number statistics. In this section, we therefore focus on determination of the branching ratio from measurement of $r^g_{1/2}$ and $r^0_{1/2}$ using equation (9.30). As $N_g + N_0 + N_d = 1$, any irregularities in the proportion of diffused molecules will affect the distribution of the other possible states, however here we assume that this effect will be minimal.

The analysis process used here closely follows that described in section 8.2, albeit with an additional fit to the distribution of non-manipulated molecules. For each injection we independently fit for λ, a prefactor term defined by the manipulation probability (κ_g/t_κ for desorption and $(\kappa_g + \kappa_d)/t_\kappa$ for non-manipulation), as well as the contaminant scaling factor C for both the desorption and non-manipulation curves. Data points with probability of desorption less than 0.05 or probability of non-manipulated greater

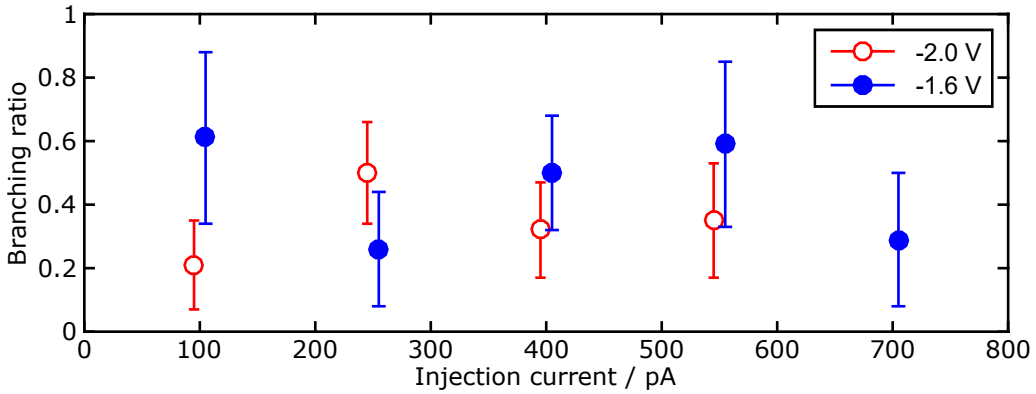

Figure 9-16: Calculation of the nonlocal branching ratio ε for toluene as a function of the injection current for holes at both -1.6 V (filled blue) and -2.0 V (unfilled red). The total number of injected charge carriers is held constant by varying the injection duration such that $n_e = It/e = 3.12 \times 10^{10}$. The average value of ε across the range of injection currents is 0.42 ± 0.09 for -1.6 V and 0.33 ± 0.08 for -2.0 V.

than 0.95 are excluded from the fitting process to minimise the impact of unphysical results, for example due to thermal manipulation, far from the injection site. The half radii are extracted, with uncertainty determined by the 95 % confidence intervals of the desorption and non-manipulation radial probability distribution curves. Hence, using equation (9.30) the branching ratio is determined with uncertainty given by equation (9.33).

9.5.5 Nonlocal toluene branching ratio

Current dependence

Figure 9-16 displays the calculated branching ratios for -1.6 V and -2.0 V injections into a toluene dosed Si(111)-7×7 surface across a range of injection currents between 100 pA and 700 pA, from reanalysis of data previously presented in section 8.2.3. The duration of each injection has been varied to maintain a constant total number of injected charge carriers, with $n_e = 3.12 \times 10^{10}$. Each data point consists of an average over a minimum of five individual injections into UM sites. Across the range of injection currents the branching ratio does not show a clear trend, neither increasing nor decreasing within the, albeit large, uncertainty. The average branching ratio $\varepsilon = 0.42 \pm 0.09$ for -1.6 V and 0.33 ± 0.08 for -2.0 V injections; approximately the same at both injection biases. This current independence is entirely consistent with a one hole manipulation process.

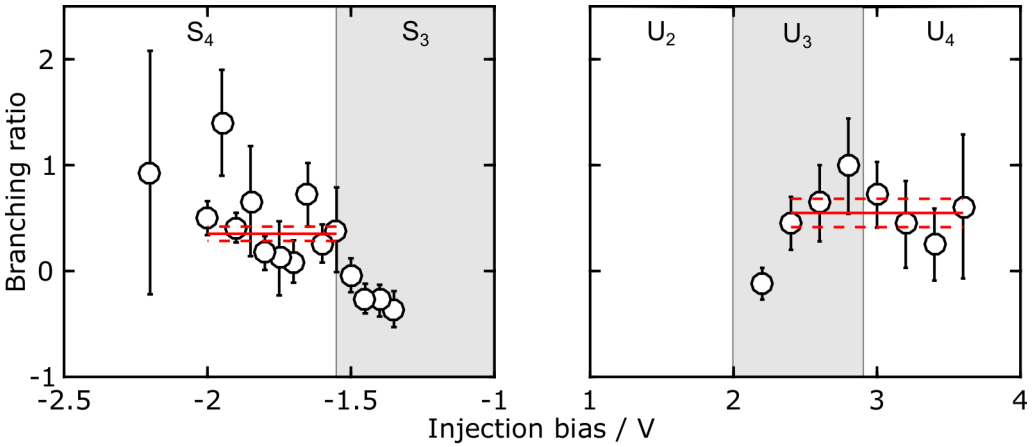

Figure 9-17: Calculation of the nonlocal branching ratio ε for toluene as a function of the injection bias for both injected holes (left, negative bias) and injected electrons (right, positive bias). For hole injection into the S_4 surface state with injection bias more negative than -1.55 V, $\varepsilon = 0.35 \pm 0.07$. For electron injection between +2.4 V and +3.6 V, at which ε is not unphysically negative, $\varepsilon = 0.55 \pm 0.13$. At both positive and negative biases, injections were performed into clean, unfaulted, middle adatom sites at 250 pA for hole injections and 750 pA for electron injection. The bias regimes for the transport surface states are indicated.

Bias dependence

Figure 9-17 shows a similar reanalysis of data from the nonlocal manipulation of a toluene dosed Si(111)-7×7 surface, here displaying the relationship between the branching ratio and the bias of the injected charge using the data from section 8.2.4. For holes, experimental data included injections at biases between -0.7 V and -2.2 V. Below the nonlocal manipulation threshold at -1.2 V very few molecules were manipulated, and so the half radii could not be reasonably fit and the branching ratio could not be defined. Furthermore, at the highest (i.e. most negative) hole injection biases, the scan-centred injections resulted in poor fits; with a large number of manipulated molecules occurring outside of the 50 nm image, leading to the branching ratio either being undefined or having large uncertainty.

The branching ratio determined during hole injection appears to increase with increasing (negative) bias; with the lowest biases resulting in an unphysically negative branching ratio. However, when considering only injection into the S_4 surface state with injection bias between -1.55 and -2.2 V [8], the branching ratio can be considered to be relatively consistent. The branching ratio averaged for injections between the lower limit for this state and the highest bias at which a reasonable fit was achieved at -2.0 V results $\varepsilon = 0.35 \pm 0.07$. The branching ratio for electron injection between

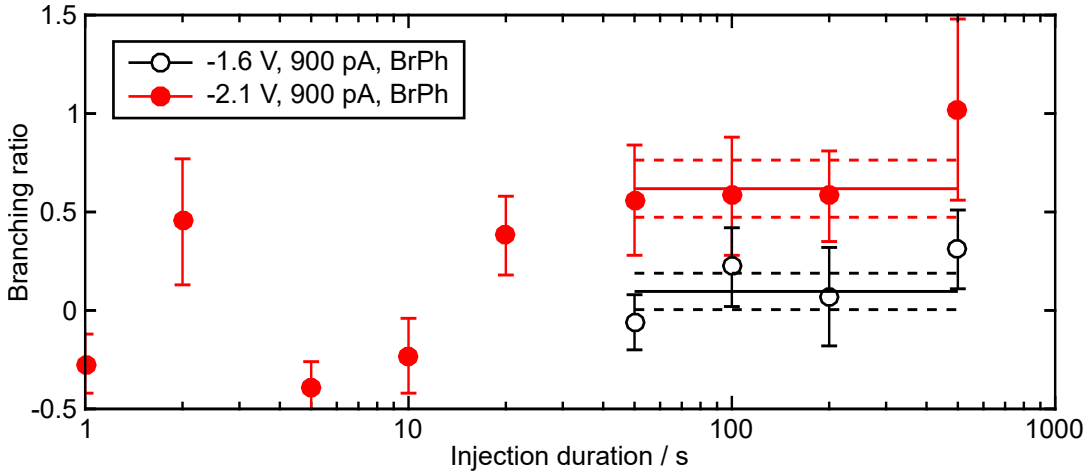

Figure 9-18: The nonlocal branching ratio ε for bromobenzene as a function of the duration of a 900 pA injection at both -1.6 V (unfilled black) and -2.1 V (filled red). At short injection duration, issues in fitting to the non-manipulated molecules resulted an undefined branching ratio for -1.6 V injections below 50 s. For the highest duration injections, between 50 and 500 s, ε is calculated to be 0.10 ± 0.09 for -1.6 V and 0.62 ± 0.15 for -2.1 V.

+2.4 V and +3.6 V, removing the unphysically negative branching ratio for +2.2 V injection, $\varepsilon = 0.55 \pm 0.13$,

9.5.6 Nonlocal BrPh branching ratio

In a similar manner to the reanalysis of the toluene-dosed nonlocal manipulation data, the BrPh-dosed injection duration dependent data collected in section 8.2.5 has been reanalysed to determine the nonlocal branching ratio. The results of this are displayed in figure 9-18 for both hole injection at -1.6 V and -2.1 V with injections between 1 s and 500 s. For each -1.6 V injection with duration shorter than 50 s, the non-manipulation curve could not be correctly fit and so the branching ratio is undefined. Additionally, several low duration -2.1 V injections result in unphysically negative values for the branching ratio. However, here we fit the manipulation probability distribution to a purely diffusive model, and so expect the results to diverge where this model diverges from the data (i.e., where the ballistic-diffusive transport model is required to accurately fit the half radius in figure 8-22). Considering only the longest duration injections, between 50 s and 500 s, the branching ratio is measured to be 0.10 ± 0.09 for -1.6 V injections and 0.62 ± 0.15 for -2.1 V injections.

Table 9.4: The toluene branching ratio for local and nonlocal bias injections of either holes or electrons. The nonlocal hole injection branching ratio has been determined from the mean value of both the current varying (from figure 9-16) and bias varying (from figure 9-17) data, while the nonlocal electron injection branching ratio is averaged across the bias varying data above +2.4 V (from figure 9-17).

Manipulation type	Branching ratio, ε	
	e^-	h^+
Local [12]	0.24 ± 0.03	0.037 ± 0.004
Nonlocal	0.55 ± 0.13	0.37 ± 0.14

9.5.7 Discussion

Initially considering the toluene dosed data, displayed in table 9.4, the nonlocal branching ratio is observed to be voltage and current invariant for hole injection into the S_4 surface state or electron injection above +2.4 V. This is in agreement with the invariance of the local branching ratio, as discussed in section 9.1. For electron injection, the branching ratio is observed to be a similar order of magnitude for both local and nonlocal injections, albeit with the nonlocal branching ratio two times higher than the local branching ratio. For hole injections, the local branching ratio was instead observed to be an order of magnitude lower than the nonlocal branching ratio; with the nonlocal branching ratio comparable to the (local or nonlocal) branching ratio for electron injection.

In local injections the tip is positioned directly above the manipulated molecule and will exert some unknown force (e.g. mechanical or electrical) on the molecule. While no current (and, thereby, tip-height) dependence on the local branching ratio has been observed for either hole or electron injection [12], it is likely that the presence of the tip has some effect on the manipulation and will skew the post-manipulation outcome. In local injections the presence of the tip is known to strongly influence the manipulation process for hole injection, which is molecule-mediated [94], while having less effect on electron injection, which is surface-mediated [12, 94]. During a nonlocal injection, the tip is (relatively) far from the majority of manipulated molecules, therefore any tip interaction effects will be minimal for either hole or electron injection. This will result in a larger change on hole injection induced manipulation, while the surface-mediated electron injection induced manipulation will remain largely unchanged; as we see in the data of table 9.4.

The nonlocal branching ratios for a bromobenzene dosed surface, displayed in figure 9-18, instead show a bias dependence for the longer duration injections; with -2.1 V

injections resulting in a branching ratio approximately six times greater than for a -1.6 V injection (0.62 ± 0.15 compared to 0.10 ± 0.09). The nonlocal -2.1 V branching ratio is higher than the local -1.3 V branching ratio (0.11 ± 0.06), in agreement with the toluene data and reduced tip-influence for nonlocal injections. However, the nonlocal -1.6 V branching ratio is remarkably similar to the local value, albeit with a large uncertainty. In each case, the nonlocal branching ratio is similar, with changes to the bias or adsorbate molecule only altering it by less than an order of magnitude. Hence, it is likely that the underlying manipulation process does not dramatically vary with the changing experimental parameters.

It is likely that the difficulty in determining the nonlocal branching ratio originates from the difficulty in determining whether a molecule has diffused or desorbed. This is characterised by the difference between the expected distribution of diffusion events in figure 9-11 and the measured distribution, for example that displayed in figure 9-15. Here, we naively treat the system as though molecules are only able to diffuse once, and that any new molecules observed on the surface after an injection are due to diffusion from a neighbouring site.

As shown in section 7.3.2, without injection the surface-molecule system is very stable, so it is unlikely that the molecular distribution is being affected by spontaneous manipulation or new adsorbates. Instead, it is possible that a large proportion of molecules determined to have "diffused" in the above analysis are actually molecules that have undergone a more traditional diffusion process; breaking both bonds with the surface and entering the physisorbed state. In this case, the diffusing molecules are able to translate larger distances across the surface and will likely diffuse to a position outside of the annulus within which they were initially positioned. In the above analysis, this would result in an underestimate in the number of diffused molecules within regions where most diffusion is expected to occur, and an overestimate elsewhere; essentially spreading out the radii at which diffusion is observed, which is observed in figure 9-15.

9.6 Conclusions

In this chapter, the final step of the manipulation process has been studied for both local and nonlocal manipulation. Two factors have been considered; the manipulation probability per charge-adsorbate interaction, and the outcome of a successful manipulation as characterised by the branching ratio.

For both local and nonlocal manipulation, the manipulation probability is observed to increase exponentially with increasing injection bias whilst the branching ratio is some-

what bias invariant. However, at a set bias above the nonlocal manipulation threshold, the probability of manipulation upon charge-adsorbate interaction is of a similar order of magnitude across these two regimes. Similarly, when considering electron injection, the branching ratio is observed to be comparable for both local and nonlocal manipulation. This suggests identical final manipulation dynamics across both local and nonlocal manipulation, independent of the injection bias. In this case, nonlocal manipulation cannot occur during the decay from the transport state, but instead from the same energy level as local manipulation. Hence, the nonlocal manipulation itself is a two-step process, with an ultrafast relaxation from the transport state to the local manipulation state preceding dynamics identical to local manipulation. The observed bias dependence must occur prior to the manipulation step, and is likely governed by the probability of an injected charge to be captured by a manipulative surface state (i.e., through $s(V)$) for both a local or nonlocal injection.

The dynamics of the manipulation process itself are observed to have a strong effect on the branching ratio. Due to the surface-mediated manipulation following electron injection, the adsorbate molecule is observed to have little affect on the local branching ratio during electron injection. Conversely for hole injection, (molecule-mediated) manipulation of a bromobenzene molecule results in a higher probability of diffusion events per desorption, and thereby a larger branching ratio, than a lighter toluene molecule. For a similar reason, the nonlocal branching ratio during hole injection is observed to be greater than the local branching ratio; with the tip likely influencing the outcome of local manipulation, but exerting a weaker force on distant molecules and thereby not affecting nonlocal manipulation.

Chapter 10

Summary and conclusions

The nonlocal manipulation of benzene derivatives on Si(111)-7 $\times$ 7 due to charge injection from the tip of an STM can be separated into three distinct steps, which are shown in figure 10-1 for a positive sample bias injection, however occur identically (with only the threshold biases and outcome probabilities varying) for a negative bias injection;

- charge injection from the STM tip,
- nonlocal charge transport,
- and manipulation of the local molecule.

Each of the steps in this process occurs independently for each individual charge carrier and is characterised by relaxation of the charge into a lower lying state, with associated energy thresholds. Within this thesis we have primarily focused on the latter two steps, after the initial charge injection but prior to capture within the nonlocal transport state. Here we provide an overview of the nonlocal manipulation process, with a focus on the work presented within this thesis.

Through measurement of the radial extent of nonlocal manipulation across a range of injection times, we have aimed to isolate the charge transport step. The results agree with a two-step charge transport process; an initial $\sim$ 10 fs ballistic transport followed by a longer range $\sim$ 200 fs diffusive process. The ballistic transport is non-manipulative, and hence we observe a physical limit on the minimum radius of nonlocal manipulation at the radius of the ballistic process; with only the probability of manipulation decreasing for the shortest duration injections. The minimum radius is itself determined by the surface as well as the injection parameters; for a -1.6 V injection a

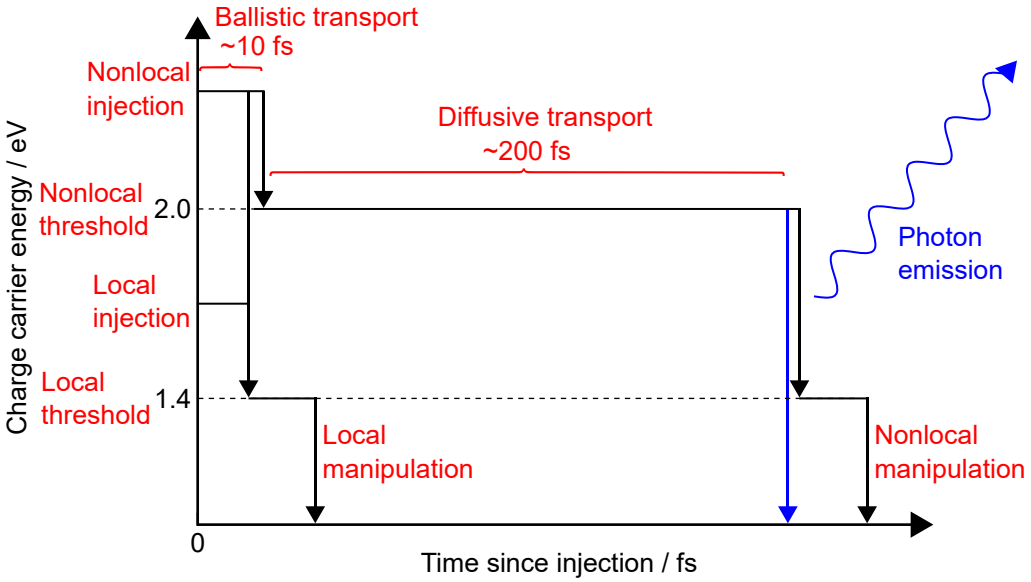

Figure 10-1: The energy of an injected charge carrier prior to a local or nonlocal manipulation event as a function of the time since injection. The threshold energies here (2.0 eV for nonlocal manipulation and 1.4 eV for local manipulation) are those for an injected electron, corresponding with the positions of unsaturated surface states.

minimum radius of (5 ± 1) nm is observed, while at -2.1 V a larger minimum of (8 ± 1) nm is observed instead.

After the ballistic transport, the injected charge is captured in a common transport state, which sets a minimum bias threshold for nonlocal manipulation. Charge carriers with energy below this threshold are unable to enter a transport state with energy sufficient to induce manipulation. Within this state the charge will undergo longer range diffusive transport, the duration of which is determined by the lifetime of the hot charge within the state. As the transport state is invariant for a range of injection biases, each injected charge will undergo an identical diffusion process with an invariant length scale. As such, the range of nonlocal manipulation for injection within a single transport state is bound by a logarithmic dependence on the number of injected charge carriers. By altering the surface properties, for example by changing the doping level, the length scale of the diffusive transport, and thereby the range of the nonlocal manipulation itself, could be enhanced or suppressed.

Identical bias thresholds are observed for both nonlocal manipulation and light emission from the Si(111)-7×7 surface during STM charge injection, which suggest common dynamics between the two processes. Photon emission from an indirect semiconductor is possible through either electronic transitions or through the relaxation of a localised

surface plasmon. Although the latter mechanism provides a good fit to the manipulation distribution for an individual injection, it is inconsistent across a range of injection durations and is unable to predict the experimentally-observed minimum radius of manipulation for short injections. Instead, the light emission occurs during the relaxation of the charge from the diffusive transport state to a lower lying state, with the common bias threshold set by the energy level of the transport state. A similar exponential increase in both the probability of photon emission and nonlocal manipulation is observed with increasing injection bias between +2.0 V and +2.7 V. Hence, noting the common energy of the transport state, the probability of an injected charge carrier entering the transport state shows the same bias dependence for both outcomes, and thereby the outcome is undetermined prior to the relaxation step.

By comparing the result of local and nonlocal manipulation, after the charge transport step, the final manipulation step has been studied. The similar order of magnitude between both the probability of manipulation per hot charge-molecule interaction (approximately three times larger for local injections than nonlocal injections at the same nonlocal biases) and the ratio between different outcomes of the manipulation itself (with a branching ratio for electron induced manipulation of toluene of 0.24 ± 0.03 for local and 0.55 ± 0.13 for nonlocal) suggest that the final manipulation process occurs identically for both local and nonlocal manipulation. In nonlocal manipulation the charge carrier is not inducing manipulation directly from the transport state, instead, prior to manipulation the charge carrier must be in an identical state between the two regimes. Thus nonlocal manipulation, after the transport step, must itself be a two-step process; non-manipulative ultrafast relaxation from the transport state to the local manipulation state, followed by manipulation dynamics identical to local manipulation.

By varying the adsorbate molecule between lighter toluene and heavier bromobenzene we observed the difference in the final manipulation step between electron and hole injection. Hole injection leads to excitation of the adsorbate molecule preceding manipulation. In this case, a heavier adsorbate molecule results in a higher probability of diffusion events per desorption event (with a branching ratio of 0.037 ± 0.004 for toluene compare to 0.11 ± 0.06 from bromobenzene) due to a reduction in the displacement of the molecule from the neutral equilibrium position during excitation. Conversely, manipulation due to electron injection is a surface-mediated process, with excitation of the underlying adatom, to which the molecule is attached, leading to the manipulation. The surface structure is unaffected by the adsorbate, which we observe as an invariance in the branching ratio between these two species (0.24 ± 0.03 for toluene compared to 0.27 ± 0.09 for bromobenzene).

The key impact of this work is likely to be the measurement of these ultrafast processes in real space. If we can understand and control the fate of the hot-charge carriers in these experiments, there could be an impact on solar-cell technology, albeit it in the far future. We observe two key limitation on using nonlocal manipulation in nanoscale manufacturing. Firstly, the initial ballistic transport sets a lower limit on the size of features able to be produced at the minimum radius of manipulation. While, secondly, the logarithmic dependence on the injection duration constrains the maximum size of features, limited by practical injection durations. By altering surface properties, for example by changing the doping level, the length scale of the diffusive transport, and thereby the range of the nonlocal manipulation itself, could be enhanced or suppressed, allowing for larger or smaller manipulation radii at reasonable injection parameters.

This work provides further confirmation of the hot charge transport mediated nonlocal molecular manipulation process, showing that the two-step ballistic-diffusive transport model can be used to predict the results of nonlocal charge injection experiments. We additionally demonstrate a method to deconvolve the transport step from the overall injection process, noting that the final manipulation process is identical with or without the nonlocal dynamics. In this case, by comparing the results of local and nonlocal manipulation experiments, effects of the nonlocal transport can be indirectly extracted. Furthermore, this work suggests that by varying the properties of the surface or surface-molecule system, through either engineering the diffusive length scale of a charge carrier within the surface states or altering the adsorbate molecule, both the result and distribution of nonlocal manipulation can be controlled.

Appendix A

The nanometre limits of ballistic and diffusive hot-hole mediated nonlocal molecular manipulation

OPEN ACCESS
IOP Publishing
Nanotechnology

Nanotechnology **31** (2020) 105401 (6pp)
https://doi.org/10.1088/1361-6528/ab5d7c

The nanometre limits of ballistic and diffusive hot-hole mediated nonlocal molecular manipulation

H G Etheridge[1], **K R Rusimova**[1,2,3] **and P A Sloan**[1,2]

[1] Department of Physics, University of Bath, Bath, BA2 7AY, United Kingdom
[2] Centre for Nanoscience and Nanotechnology, University of Bath, Bath, BA2 7AY, United Kingdom
[3] Centre for Photonics and Photonic Materials, University of Bath, Bath, BA2 7AY, United Kingdom

E-mail: p.sloan@bath.ac.uk

Received 8 August 2019, revised 30 October 2019
Accepted for publication 29 November 2019
Published 17 December 2019

Abstract

We report an experimental investigation into the surface-specific and experimental limits of the range of STM induced nonlocal molecular manipulation. We measure the spot-size of the nonlocal manipulation of bromobenzene molecules on the Si(111)-7 × 7 surface at room temperature at two voltages and for a wide range of charge-injection times (number of hot charge-carriers) from 1 s up to 500 s. The results conform to an initially ballistic, 6–10 nm, and then hot-hole diffusive, 10–30 nm, transport away from the localised injection site. This work gives further confirmation that nonlocal molecular manipulation by STM directly reveals the ultrafast transport properties of hot-charge carriers at surfaces.

Keywords: hot electron, ballistic transport, diffusive transport, STM, molecular manipulation

(Some figures may appear in colour only in the online journal)

Introduction

An understanding of ultra-fast hot-electron dynamics is key to, for example, controlling matter at the atomic scale by scanning tunnelling microscopy (STM) molecular manipulation, and to breaking the Shockley–Queisser efficiency limit in solar cells [1–4]. In the latter the rapid time-scale of thermalization (loss of energy) of light generated hot-carriers sets the length-scale over which hot-carriers would have to be captured before they have lost most of their energy. However, direct measurement of hot-carrier dynamics, to underpin and develop hot-charge carrier theory, is difficult owing to their short lifetimes (femtoseconds) and length-scales (nanometres).

The tip of an STM is a local source of tunable hot-charge carriers. These hot-charges can lead to manipulation of individual atoms and molecules on a surface with atomic precision. Such molecular level control is the cutting edge of bottom-up nanoscience and in conventional STM manipulation is restricted to the tunnel junction [5–12]. Although these manipulations are driven by the hot-charges, since the only measurable outcome is whether the manipulation was successful or not, they give little information as to the underlying hot-charge carrier dynamics.

In nonlocal manipulation, however, charge injected from the tip of an STM results in the manipulation of many molecules within a distance, typically a few nm, of the tip injection site. Critically the distant molecules only react to the charge if it still has energy above a certain threshold, that is, they only react to charge carriers while they remain hot. Nonlocal molecular manipulation, therefore, has the signature of hot-charge dynamics directly imprinted in real-space on the pattern of the manipulation. Such nonlocal manipulation by STM has been reported in noble metals [13–18] and on the Si(111)-7 × 7 surface [19–21], the surface of primary interest for this research.

The surface and molecule were chosen as they exhibit a large and easily measured nonlocal manipulation signal. This system is well characterised and has been extensively studied by us and others and is therefore the ideal testbed for developing a surface-specific theory of hot-charge carrier dynamics that underlies the nonlocal manipulation.

Combining automated experimental and analysis techniques has allowed us to explore the parameter space of both local [22, 23] and nonlocal [24–28] manipulation with unprecedented range and resolution revealing the hot-electron dynamics that govern both modes of manipulation on the Si(111)-7 × 7 surface.

Here we show that the hot-charge carrier transport model developed in [27, 28] is more general than those reports. We explicitly deconvolve the measured raw signal (image) of nonlocal manipulation into its three constituent parts: molecular properties, experimentally set properties and, crucially, the hot-charge carrier dynamics. This work is therefore an important step towards robustly linking STM mediated molecular manipulation to hot-charge carrier dynamics. It should now be possible to engineer the properties of this model system to directly measure the effect on the hot-charge dynamics so that nonlocal manipulation can act as a test-bed for controlling, measuring, and understanding hot-charge dynamics.

Experimental

Experiments were performed with a room temperature Omicron STM1 at a base pressure of ∼1 × 10^{-10} mbar. Si(111)-7 × 7 samples (n-type, phosphorous doped, 0.001–0.002 Ωcm) were prepared upon entering the vacuum chamber by an initial degassing at ∼660 °C for several hours, as well as daily automatic heating to ∼1250 °C 10 times followed by a slower reconstructive cooling from 960 °C prior to scanning. Tungsten tips were electrochemically etched using a 2 M NaOH solution and degassed via resistive heating. Sample dosing of bromobenzene gas was controlled by an automated leak valve, providing an accurate and reproducible dose of 2 Langmuirs. Bromobenzene was purified by a freeze-pump-thaw routine and verified by mass spectrometry.

Results

Figure 1 shows a set of STM images taken before (left hand side) and after (right hand side) hole injection (−2.1 V, 900 pA) at the location indicated and at increasing injection times from 5 to 500 s corresponding to 10^{10} to 10^{12} injected holes. In these relatively large-scale images, the speckled dark-spots are in fact individual bromobenzene molecules chemisorbed to neighbouring adatom-restatom pairs with a binding energy of 1.4 eV [29, 30]. They are stable at room temperature and unreactive to the imaging parameters used to capture these large scale and high resolution STM images, yet are highly reactive to hot-charge carriers.

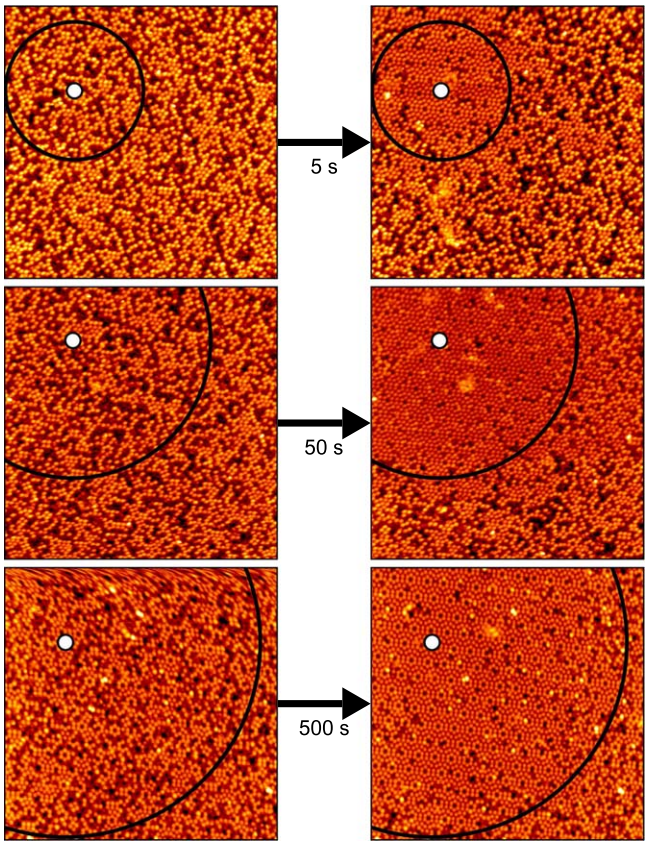

Figure 1. 50 × 50 nm STM images of Si(111)-7 × 7 dosed with bromobenzene at passive scanning parameters (+1 V, 100 pA) before (left) and after (right) a −2.1 V 900 pA injection of duration 5 s (top), 50 s (middle) and 500 s (bottom) located at the white circle. The black circles indicate the radius at which the probability of desorption is 0.5 in the after image. To allow easy visual comparison the circle is also superimposed on the before images.

Injections occur at a position towards the top left corner of the scanned area in order to maximise the possible observed radial distance from the injection site. A thermal drift-correction program minimised the drift to <1 nm during the longest 500 s injections—much less than the resulting nonlocal area of manipulation. For a 5 s injection of hot-holes the immediate area surrounding the injection site is cleaned of molecules. Some manipulated molecules appear as new adsorbates further away, but the majority desorb from the surface completely. In our site-by-site analysis we can filter out such re-adsorption to focus purely on the number of molecules that were manipulated. At 50 s injection time the radius of this nonlocal manipulation is evidently increased, and at our longest injection times of 500 s we find a large radius of ∼30 nm has been cleared of its original molecular coverage.

The 'spot-size' of the clean area has been shown to be invariant to the presence of multiple steps within the region [31]. Assuming a tunnel gap of ∼10 Å, and with a step height of 3.14 Å there would be significant variation in the strength of the tip-surface E-field at the top of a step or the bottom of multiple steps. Yet no change in the nonlocal manipulation

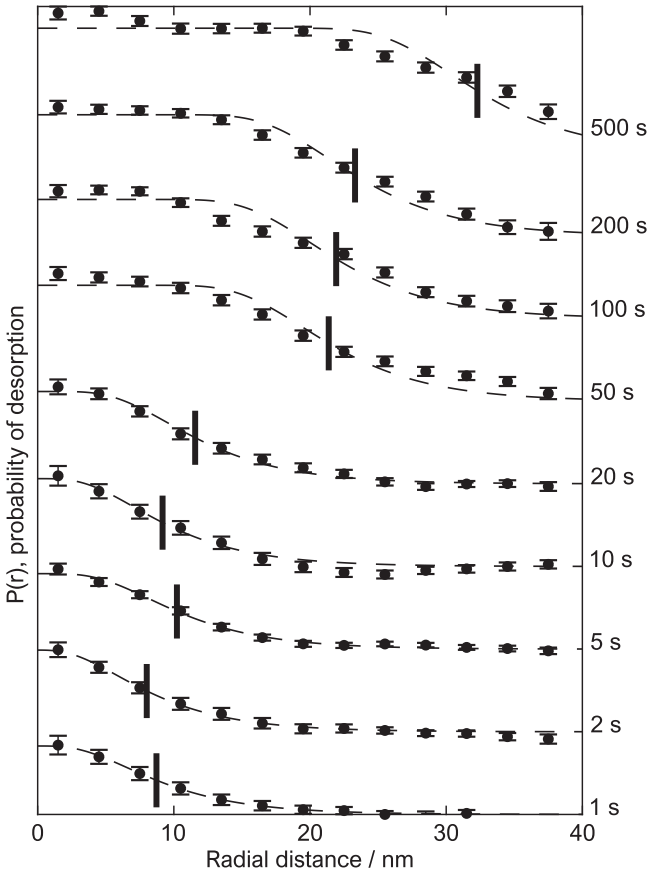

Figure 2. $P(r)$ as function of radius from tip site after an injection of −2.1 V and 900 pA. Circles mark experimental data-points, see main text for fitted curve. Each set of data-points/curve-fit has been offset vertically for ease of viewing—labels on right-hand side indicate the monotonically increasing injection time. Vertical black markers indicate the radius $r_{1/2}$ at which the probability of desorption is half the maximum probability.

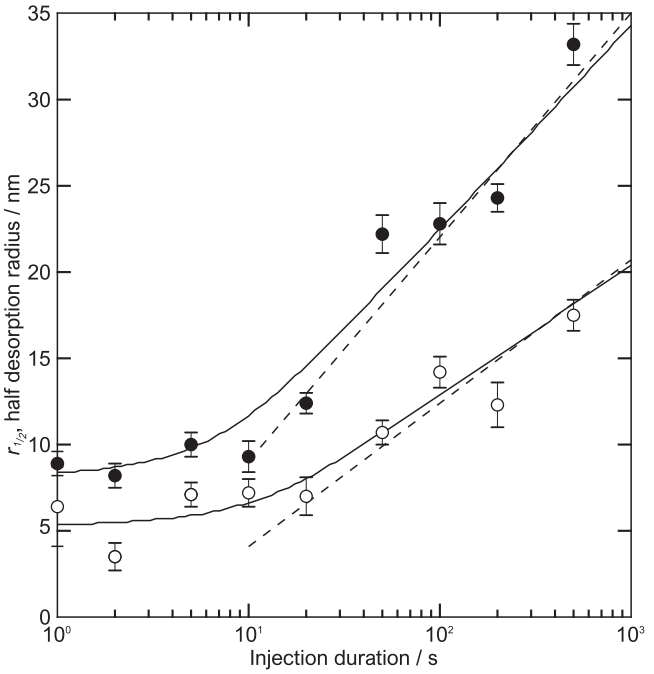

Figure 3. Half-desorption radius as function of injection duration for −2.1 V (filled) and −1.6 V (unfilled) injections at 900 pA. Dashed lines are logarithmic fits to $r_{1/2}$ for injection duration greater than 10 s. Solid lines are fits to all data-points to a ballistic-diffusive model with an initial disc of charge density. All fit parameters presented in the main text. Error bars show standard deviation of the mean for each injection time.

spot-size was observed. Therefore we ruled out any active role for the tip-sample E-field in the manipulation process.

To quantify the nonlocal manipulation the precise crystallographic locations of all the molecules and the injection sites are found using a suite of in-house written computer programs to analyse pairs of 'before' and 'after' STM images. Further analysis compares the occupation of the same individual adsorption sites before and after qinjection to determine the probability of manipulation $P(r) = N(r)/N_0(r)$: the ratio of the number of molecules manipulated $N(r)$ to the number of original molecules $N_0(r)$ within an annulus at radius r.

Figure 2 shows a series of measured $P(r)$ data-sets as a function of the injection time. Each data-set at a particular injection-time is the average from at least two 'before' and 'after' experiments (∼34 000 manipulation events were recorded in total during this work). To quantify the size of the nonlocal manipulation we define the half-radius, $r_{1/2}$, as the radius at which the probability of manipulation is half that of the maximum measured manipulation probability. For each data-set $r_{1/2}$ is indicated by the short vertical black line. For long enough injections, the maximum probability reaches a consistent maximum at ∼0.8. This upper threshold is due to the presence of immovable contaminants on the surface which are included in the $P(r)$ analysis. At short duration injections the maximum probability may be less—not all molecules in an annulus, even near the injection site, are driven to desorb. For short injection-times at −2.1 V, the nonlocal manipulation occurred near the injection site with $r_{1/2} = (9 \pm 2)$ nm. At longer injection-times the size of the nonlocal effect increased with a corresponding increase in the half-radius. For 500 s injections $r_{1/2} = (34 \pm 2)$ nm, the longest injection and largest half-radius of our −2.1 V experiments. Although the increase in half-radius with injection duration is monotonic, it is not linear.

Figure 3 shows the main result of this work, the injection-time dependence of $r_{1/2}$ for two injection voltages, −1.6 and −2.1 V. These voltages were chosen to be near threshold (−1.6 V) of a surface-state (labelled s_4 in [28]) in order to minimise any possible ballistic transport, and well beyond the threshold (−2.1 V) to maximise any ballistic transport. Using site-specific STS we previously showed that each manipulation voltage threshold corresponds to the onset of a site-specific surface state. With each state having slightly different diffusive and ballistic transport ranges [28, 32]. Here, for both voltages, below ∼10 s there is an initial constant minimum region in $r_{1/2}$, (4 ± 2) nm and (9 ± 2) nm respectively, followed by a logarithmic increase. Does our model, developed from the voltage and temperature dependence of nonlocal manipulation, extend to explain this injection-duration $r_{1/2}$ dependence?

Discussion

The model for nonlocal manipulation has the stepwise form: (i) an electron (or hole) is injected from the STM tip into a specific surface electronic state at a specific atomic site of the surface; (ii) it evolves for a few fs in that state from its initial conditions that are set by the properties of the band (dispersion etc.) and the quantum tunnelling process. This is simply ballistic transport; (iii) the electron (or hole) undergoes multiple scattering events to become quasi-thermally equilibrated at the bottom (or top) of the band and from there undergoes isotropic 2D diffusive transport with a lifetime of, here, 200 fs; (iv) during this diffusive phase the charge has a chance to localise on a molecule and, by a desorption induced by an electronic transition process, induce the molecule to detach from the surface and desorb. Given the mismatch of the time between tunnelling charges, ~100 ps, and the life-time of the hot-charge of ~100 fs, we can assume that this process repeats identically and independently for each charge carrier injected into the surface during the current-pulse. This results in the probability of manipulation per charge carrier being independent of the tunnelling current, as previously observed [28, 33].

The probability of manipulation $P(r) = N(r)/N_0(r)$ derived for this model is

$$P(r) = 1 - \exp\left[-\left(\frac{\sigma\kappa_e}{\tau_s}\right) \times \left(\frac{sIt}{e}\right) \times C(r)\right]. \quad (1)$$

This expression highlights the three factors that control the shape of the nonlocal manipulation: (i) molecular manipulation properties through κ_e the probability per injected charge carrier of inducing molecular desorption, σ the molecular cross-section (taken as (1.5 Å)^2 [34]) and τ_s the lifetime of an electron in the surface-state here taken as 200 fs [35] (Note, in comparison with our earlier work, here we have introduced this additional τ_s term for the lifetime of the charge in the surface-state. This allows us to express κ_e as a probability of manipulation per injected electron. This minor (book keeping) correction does not change the form of the results here or earlier, but is a more correct form for the expression); (ii) experimental conditions that determine the number of injected electrons $n_e = sIt/e$ where t is the injection duration, I the injection (tunnelling) current and s the fraction of the current injected into the surface state (taken as unity); and (iii) the hot-charge carrier dynamics themselves through $C(r)$, the time-integrated charge density of a single carrier. It is this last term that describes the underlying hot-electron dynamics that drives the nonlocal manipulation.

Diffusive model

A single-electron 2D diffusive model with a single unreactive decay channel gives

$$C(r) = \frac{2\tau_s}{\pi\lambda^2} \mathrm{K}_0\left(\frac{2r}{\lambda}\right), \quad (2)$$

see [27] for derivation. The 2D charge diffusion is described by the diffusion length λ and the diffusion time τ_s. These are related as usual for 2D diffusion through $\lambda = \sqrt{4D\tau_s}$ with D the diffusion coefficient. Furthermore, combining equations (1) and (2), for $r > \lambda$ the half-desorption radius as a function of injection duration can be approximated as

$$r_{1/2} \approx \frac{\lambda}{2} \log\left(\frac{t}{t_0}\right). \quad (3)$$

With the characteristic time-scale given by $t_0 = (\pi e\lambda^2/2\sigma\kappa_e Is)$.

We perform an iterative fitting routine to determine robust values for λ and κ_e. We initially find these parameters (and a contamination scaling factor) by fitting the model given by equations (1) and (2) to the data as shown in figure 2. Each injection time generates unique fitting parameters λ, κ_e and a contamination scaling factor.

From these values we determine the half-radius for each injection time, shown in figure 3. We then fit the logarithmic dependence given by equation (3) and so extract another measure of λ but here this value is fitted across all the data (injection times) for a particular voltage. The dashed lines of figure 3 show the excellent fit of this logarithmic model to the experimental results, resulting in $\lambda = 7 \pm 2$ nm for -1.6 V and $\lambda = 11 \pm 3$ nm for -2.1 V in agreement with [28].

We use this value of λ to refit the data of figure 2 but now with just κ_e and the contamination scaling factor as fitting parameters. By this route we minimise the effect of the inherent statistical variation we have in our experimental results and extract the best values for hot-charge carrier dynamics. We find that the half-radii extracted from figure 2 are relatively insensitive to variations in λ, and so further iterative fitting does not significantly affect our final values. A weighted average over all injection times gives the probability per electron of manipulation $\kappa_e = (2 \pm 2) \times 10^{-7}$ at -1.6 V and $\kappa_e = (8 \pm 5) \times 10^{-7}$ at -2.1 V.

The local manipulation probability of toluene molecules on the same surface with -1.3 V holes is remarkably similar at $k_e = 3 \times 10^{-7}$ [23]. Both bromobenzene and toluene are simple derivatives of benzene and bond in near identical fashion onto the Si(111)-7 × 7 surface and exhibit near identical molecular manipulation properties. For local injections the molecule 'experiences' the whole injected charge interaction, whereas for nonlocal manipulation the charge is spread out and so only a fraction of any one charge interacts with any one adsorbate. To relate the local manipulation probability k_e to the nonlocal probability κ_e we note that κ_e is the probability of inducing any desorption and that the fraction of the spread-out charge that interacts with the molecule will simply be the geometric fraction of the spot-size that was covered by molecules, here ~0.4. Additionally, nonlocal manipulation has a longer interaction lifetime than local manipulation, ~200 fs to ~10 fs respectively, and so we assume a linear increase [23] in probability of about an order of magnitude giving the approximate relationship $k_e \times 0.4 \times 200/10 \sim \kappa_e$. It is therefore reasonable, in our case, for the nonlocal probability per injected charge carrier to be of the same order as its local counterpart, just as we find.

At room temperature, thermal drift plays more of a role and the maximum time of a single-position experiment is set by the mechanical stability of the microscope. We go to great

experimental lengths to perform stable injections up to 500 s at room temperature. Due to the logarithmic nature of the manipulation spot-size, attaining a spot-size larger than 35 nm would require unfeasibly long injections. At cryogenic temperatures STMs are more stable, but the thermally driven (though still hot) diffusive charge transport is slowed reducing λ and hence ultimately the spot-size [27].

At injection times lower than 10 s this purely diffusive model does not fit the experimental data. This is partly due to approximations taken in the derivation of equation (3), but even the full diffusive expression does not generate the observed plateau region at small injection duration.

Ballistic model

In [28] we developed the diffusive transport model further, whereby injected charge carriers were modelled to undergo an initial ballistic (unperturbed) transport away from the injection site before intra-band thermalization and diffusion (as above). In this ballistic region the charge carriers are not observed to interact with adsorbed molecules and so, for certain injection voltages, can result in a reduction in the measured probability $P(r)$ of manipulated molecules close to the injection site. In essence, the charge only becomes 'active' some short distance from the injection site.

Consequently, the initial spatial distribution of charge density before diffusion is not a Dirac delta function at the injection site, as is assumed in the purely diffusive case described by equation (2). Instead, for the initial ballistic transport a simple 2D cylindrical Schrödinger model (and an equivalent 2D tight-binding model) predicted nearly a constant charge carrier density out to a distance R set by the properties of the surface-state and the ballistic lifetime. Values for R typically ranged from 5 to 15 nm [28]. For the half-radius desorption measurement in figure 3 this implies a lower limit, just as we observe, set by the physical properties of the surface electronic state as the electrons undergo this ultrafast ballistic transport.

To model this initial ballistic phase and its effect on the nonlocal spot-size $r_{1/2}$ we calculate the diffusion, again with a single decay channel, from an initial constant charge density across a disc of radius R centred on the injection site. Due to its linear and separable properties we use the superposition principle to calculate the total charge density $C(r)$ that feeds into equation (1)

$$C(r) = \frac{1}{\pi R^2}\int_R \frac{2\tau_s}{\pi\lambda^2} K_0\left(\frac{2r'}{\lambda}\right) dA, \qquad (4)$$

where r' is the distance between a point on the initial disc and the radial distance from the injection site r. The solid lines in figure 3 show the excellent fit to this ballistic-diffusive model for all of the data, giving for -1.6 V injections $R = (5 \pm 1)$ nm, and for -2.1 V injections $R = (8 \pm 1)$ nm. These are in good agreement with our earlier work [28].

Conclusions

This work supports the ballistic-diffusive model for hot-charge carrier transport developed to model nonlocal STM manipulation. It sets physical limits on the maximum and minimum size of the nonlocal manipulation effect and demonstrates that molecular, experimental and surface factors can be distinguished and measured. It opens the way to engineering and altering surface properties, for example doping level, to enhance (or suppress) the ultra-fast hot-charge carrier dynamics and hence the nonlocal manipulation itself.

Acknowledgments

PAS gratefully acknowledges support from the EPSRC Grant EP/K00137X/1. HE acknowledges funding and support from the Engineering and Physical Sciences Research Council (EPSRC). All data supporting this study are openly available from the University of Bath data archive at https://doi.org/10.15125/BATH-00722.

ORCID iDs

K R Rusimova https://orcid.org/0000-0002-3679-9948
P A Sloan https://orcid.org/0000-0002-0810-8468

References

[1] Bernardi M 2016 *Eur. Phys. J.* B **89** 239
[2] Guo Z, Wan Y, Yang M, Snaider J, Zhu K and Huang L 2017 *Science* **356** 59
[3] Ma J, Nissimagoudar A S and Li W 2018 *Phys. Rev.* B **97** 045201
[4] Jang Y J, Chung K, Lee J S, Choi C H, Lim J W and Kim D H 2018 *ACS Photonics* **5** 4711
[5] Lu P H, Polanyi J C and Rogers D 1999 *J. Chem. Phys.* **111** 9905
[6] Hla S-W, Bartels L, Meyer G and Rieder K-H 2000 *Phys. Rev. Lett.* **85** 2777
[7] Repp J, Meyer G, Paavilainen S, Olsson F E and Persson M 2006 *Science* **312** 1196
[8] Schull G, Frederiksen T, Arnau A, Sánchez-Portal D and Berndt R 2011 *Nat. Nanotechnol.* **6** 23
[9] Cai Z-F, Dong W-L, Chen T, Yan H-J, Wang D, Xu W and Wan L-J 2018 *Chem. Commun.* **54** 8052
[10] Gao J, Fard M R, Palmer R E, Guo Q, Kaya D and Palmer R E 2018 *Langmuir* **34** 8388
[11] Piva P G, DiLabio G A, Pitters J L, Zikovsky J, Rezeq M, Dogel S, Hofer W A and Wolkow R A 2005 *Nature* **435** 658
[12] Borca B *et al* 2015 *ACS Nano* **9** 12506
[13] Morgenstern K and Rieder K-H 2002 *Chem. Phys. Lett.* **358** 250
[14] Sicot M, Kurnosikov O, Adam O A O, Swagten H J M and Koopmans B 2008 *Phys. Rev.* B **77** 035417
[15] Chen L, Li H and Wee A T S 2009 *ACS Nano* **3** 3684
[16] MacLeod J M, Lipton-Duffin J, Fu C and Rosei F 2009 *ACS Nano* **3** 3347

[17] Schendel V, Borca B, Pentegov I, Michnowicz T, Kraft U, Klauk H, Wahl P, Schlickum U and Kern K 2016 *Nano Lett.* **16** 93
[18] Hahn J R, Jang S H, Kim K W and Son S B 2013 *J. Chem. Phys.* **139** 074707
[19] Stipe B C, Rezaei M A and Ho W 1997 *Phys. Rev. Lett.* **79** 4397
[20] Nouchi R, Masunari K, Ohta T, Kubozono Y and Iwasa Y 2006 *Phys. Rev. Lett.* **97** 196101
[21] Nakamura Y, Mera Y and Maeda K 2007 *Surf. Sci.* **601** 2189
[22] Rusimova K R and Sloan P A 2017 *Nanotechnology* **28** 1
[23] Rusimova K R, Purkiss R M, Howes R, Lee F, Crampin S and Sloan P A 2018 *Science* **361** 1012
[24] Sloan P A, Sakulsermsuk S and Palmer R E 2010 *Phys. Rev. Lett.* **105** 048301
[25] Pan T, Sloan P A and Palmer R E 2014 *Chem. Rec.* **14** 841
[26] Pan T L, Sloan P A and Palmer R E 2014 *J. Phys. Chem. Lett.* **5** 3551
[27] Lock D, Rusimova K R, Pan T L, Palmer R E and Sloan P A 2015 *Nat. Commun.* **6** 8365
[28] Rusimova K R, Bannister N, Harrison P, Lock D, Crampin S, Palmer R E and Sloan P A 2016 *Nat. Commun.* **7** 1
[29] Lock D, Sakulsermsuk S, Palmer R and Sloan P 2014 *J. Phys.: Condens. Matter.* **27** 054003
[30] Utecht M, Gaebel T and Klamroth T 2018 *J. Comput. Chem.* **39** 2517
[31] Pan T, Sloan P A and Palmer R E 2014 *Chem. Rec.* **14** 841
[32] Purkiss R M, Etheridge H G, Sloan P A and Rusimova K R 2019 *J. Phys. Commun.* **3** 095010
[33] Sloan P, Hedouin M, Palmer R and Persson M 2003 *Phys. Rev. Lett.* **91** 118301
[34] Alavi S, Rousseau R, Patitsas S N, Lopinski G P, Wolkow R A and Seideman T 2000 *Phys. Rev. Lett.* **85** 5372
[35] Ichibayashi T, Tanaka S, Kanasaki J, Tanimura K and Fauster T 2011 *Phys. Rev.* B **84** 235210

Appendix B

Common source of light emission and nonlocal molecular manipulation on the Si(111)-7×7 surface

Journal of Physics Communications

OPEN ACCESS

RECEIVED
26 July 2019

REVISED
23 August 2019

ACCEPTED FOR PUBLICATION
5 September 2019

PUBLISHED
17 September 2019

PAPER

Common source of light emission and nonlocal molecular manipulation on the Si(111)−7 × 7 surface

Rebecca M Purkiss[1], **Henry G Etheridge**[1], **Peter A Sloan**[1,2,4] **and Kristina R Rusimova**[1,2,3,4]

[1] Department of Physics, University of Bath, Bath, BA2 7AY, United Kingdom
[2] Centre for Nanoscience and Nanotechnology, University of Bath, Bath BA2 7AY, United Kingdom
[3] Centre for Photonics and Photonic Materials, University of Bath, Bath BA2 7AY, United Kingdom
[4] Author to whom any correspondence should be addressed.

E-mail: p.sloan@bath.ac.uk **and** k.r.rusimova@bath.ac.uk

Keywords: luminescence, scanning probe microscopy, Si(111)−7 × 7, desorption, nonlocal, hot electrons

Supplementary material for this article is available online

Abstract

The tip of a scanning tunnelling microscope can inject hot electrons into a surface with atomic precision. Their subsequent dynamics and eventual decay can result in atomic manipulation of an adsorbed molecule, or in light emission from the surface. Here, we combine the results of these two near identical experimental techniques for the system of toluene molecules chemisorbed on the Si(111)−7 × 7 surface at room temperature. The radial dependence of molecular desorption away from the tip injection site conforms to a two-step ballistic-diffusive transport of the injected hot electrons across the surface, with a threshold bias voltage of +2.0 V. We find the same threshold voltage of +2.0 V for light emission from the bare Si(111)−7 × 7 surface. Comparing these results with previous published spectra we propose that both the manipulation (here, desorption or diffusion) and the light emission follow the same hot electron dynamics, only differing in the outcome of the final relaxation step which may result in either molecular displacement, or photon emission.

Introduction

The scanning tunnelling microscope (STM) in combination with an optical detection system can measure the light emission induced by charge tunnelling from the STM tip—an experiment called scanning tunnelling luminescence (STL) [1–3]. In recent years, STL has been used to detect the light emission from single molecules [4–10], the radiative decay of nano-cavity generated surface plasmons [1, 11, 12], and even the production of pure single photons from molecular monolayers [13]. By employing the key capabilities of the STM for imaging with submolecular resolution and selectively exciting surface electronic states, STL has rendered itself the only far-field optical technique capable of circumventing the diffraction limit. By studying the interaction of light with individual molecules it has uncovered properties fundamentally different to those of molecular ensembles [5, 8–10, 13]. The three main mechanisms via which light is generated in the STL tunnel junction are (i) through the relaxation of a localised surface plasmon (LSP) in the region underneath the tip, (ii) by recombination of an electron-hole exciton [14, 15], or (iii) by electronic transitions [6, 7, 16–19]. The LSP model applies to metal surfaces, typically excited with a plasmonic (e.g. silver) STM tip, where the plasmon decays radiatively [1, 4, 11, 12]. On the other hand, the exciton model commonly applies to decoupled single-molecule systems, where a molecular exciton can be excited either indirectly by the coherent coupling of a nanocavity plasmon [5, 8, 9], or directly by the tunnelling electrons from the STM tip [10, 13]. However, there are conflicting reports over the STL emission mechanism for semiconductor surfaces. In direct bandgap semiconductors, luminescence is caused by the recombination of tunnelling electrons with holes in the conduction band of the material [18, 19]. In indirect bandgap semiconductors, where such recombination is forbidden, light emission is discussed in the context of a direct dipole transition of an electron from a tip state into a surface state [16, 17], or a radiative relaxation of a surface plasmon [12, 20], but the experimental evidence is contradictory.

Here we report both STL measurements and nonlocal molecular manipulation (desorption or diffusion) measurements on the Si(111)−7 × 7 semiconducting surface. Both experiments follow exactly the same experimental procedure, except that for STL we measure the light output of the hot-electron injection into the bare silicon surface, and for the atomic-manipulation we measure the reaction of adsorbed molecules on the surface. In the latter case, toluene molecules adsorbed on the surface up to 20 nm distant from the STM tip are induced to leave the surface by an injection of electrons from the tip into the surface. We show that the voltage threshold of +2.0 V for such STM electron induced nonlocal molecular manipulation matches the voltage threshold for STL electron induced light emission. Building on our prior nonlocal manipulation work [21–23] and other group's STL work [20, 24], we suggest a common mechanism for these electron induced events. Namely, a fast inelastic relaxation of the injected charge to the bottom of a high-lying electronic surface-resonance, followed by elastic diffusive transport away from the injection site and eventual inelastic decay to a lower lying surface state with possible outcomes of molecule displacement, or of light emission.

Experimental details

UHV STM System

Experiments were carried out on an Omicron STM1 under ultra-high vacuum with a base pressure less than 10^{-10} mbar and operated at room temperature. Si(111) wafers (n-type, phosphorus doped, 0.001 to 0.002 Ω.cm) were prepared by repeated resistively heating to 1200 °C followed by a slow cooling from 960 °C to allow the surface to form 7 × 7 reconstruction [25]. Tungsten STM tips were produced by electrochemical etching of W-wire in 2 M NaOH solution followed by heat treatment in vacuum to remove any tungsten oxide . The STM was controlled by Nanonis digital control electronics [26]. Liquid toluene was purified by the freeze-pump-thaw technique with liquid nitrogen and checked for purity with a quadrupole mass spectrometer. To prepare a partially toluene covered surface (~3 molecules per unit cell) the Si(111)−7 × 7 surface was dosed through a computer-controlled leak valve. Automated drift tracking combined with a feature locking technique was used to ensure stability during charge carrier injection [22, 23, 27, 28]. Typical values of the drift compensation ranged from 100 fm s^{-1} up to 2 pm s^{-1} in all three directions.

Scanning tunnelling spectroscopy

Scanning tunnelling spectra were obtained by modulating the tunnelling voltage and recording dI/dV directly with a lockin amplifier from 0 V to 3.5 V. The tunnel gap was varied linearly with voltage at a rate of 150 pm V^{-1}. Each spectrum contains 200 data points, collected at an integration time of 150 ms and lock-on modulation of 20 mV at 521 Hz.

Luminescence measurement

The Andor Luca R camera had 1004 (H) × 1002 (V) pixels with a pixel size 8 × 8 μm. To maximise the signal, but prevent pixel saturation, we used an exposure time t of 40 s and a gain G of 833. The camera was mounted at 80° to the surface normal and at a distance of ~20 cm, giving a solid angle of ~0.024 Sr This solid angle is much lower, by at least an order of magnitude, than that typically used for STL experiments [29], but given the single-photon sensitivity of the camera the solid angle was adequate. The angle is also appreciably away from the ideal 60° emission angle [30].

Results

STM Induced Light Emission

Figure 1(a) shows a typical STM image of the Si(111)−7 × 7 surface (+1 V, 100 pA, 25 × 25 nm). The repeating crystal structure is evident, as are several surface defects. The unit cell, outlined in figure 1(a), contains six silicon adatom sites that correspond to the bright spots in the STM images. Due to a stacking fault of the surface, the unit cell has two sides: the faulted (F) and the unfaulted (U), each with two distinct adatom sites, the corner (C) and the middle (M). Hence we address, for example, the faulted corner silicon adatom site as FC. To measure the light emission we photographed the STM and sample system while the STM was in tunnelling position. Photographs of the tunnel junction were taken using an Andor Luca R camera, an electron multiplying CCD camera with near single photon sensitivity and a wavelength range of 400 nm to 900 nm (3.10 eV to 1.38 eV). Figure 1(b) shows a photograph of the STM tip and sample with background illumination. This photograph allows us to identify a small region of the camera image that contains the tunnel junction between tip and sample. With the background illumination switched off and light-tight covering applied to the UHV system we were able to record the light emission from the tunnel junction. Figure 1(c) shows the same camera region as the marked square of figure 1(b), but with active STM tunnelling parameters of +3 V, 1 nA and no

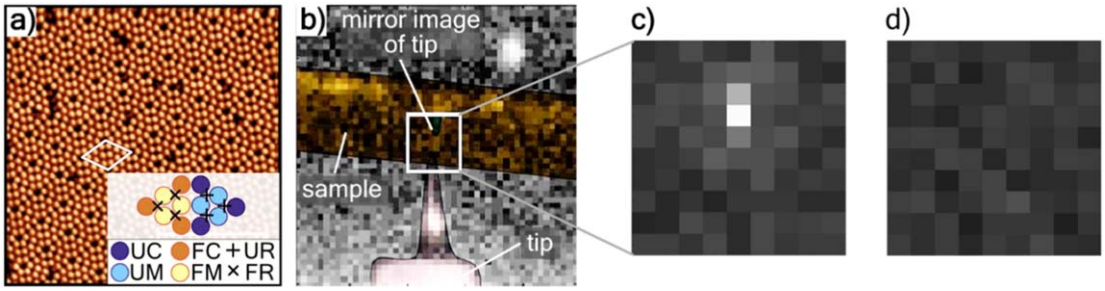

Figure 1. Detection of scanning tunnelling luminescence from the Si(111)-7 × 7 surface. (a) STM image of the Si(111)-7 × 7 surface (+1 V, 100 pA, 25 × 25 nm) with a unit cell outlined in white. Inset: Schematic of the outlined unit cell, showing all adatom and restatom sites as follows: unfaulted corner (UC); unfaulted middle (UM); faulted corner (FC); faulted middle (FM); unfaulted restatom (UR); faulted restatom (FR). A negative bias image (−1 V, 100 pA) of Si(111)−7 × 7 is used to determine the faulted half of the unit cell, which appears brighter than the unfaulted half. (b) Camera image, with background lighting on, of the tunnel junction with silicon sample shaded orange, and the tip purple. The reflection of the tip can just be seen in the sample (best viewed online). The boxed region of interest contains the tip-apex/sample tunnel junction. (c) An STL-photograph (injection at +3 V, 1 nA, 40 s) of the boxed region of (b) with background light off, clearly indicating the enhanced light signal associated with the tunnel junction. (d) A dark-photograph (injection at +3 V, 0 nA, 40 s) of the boxed region of (b) also with background light off.

background illumination. A single pixel at the location associated with the tunnel junction has a much elevated photon count. We label this pixel as the 'tunnel junction pixel' and describe these measurements as STL-photographs. We repeat the measurement directly after, but with the STM tip withdrawn by 10 nm away from the surface, thus ensuring no tunnelling current. These images we label as dark-photographs and they give a combined camera-bias and dark-count measurement. Here we present the raw camera counts, and in the final discussion we convert these counts to photons per injected electron.

For each set of tunnelling parameters we typically record 11 pairs of STL and dark photographs. Figure 2(a) shows the number of camera-counts of the tunnel junction pixel over the course of 11 pairs of STL/dark photographs. There is an obvious elevation of the number of camera-counts when the tip is in tunnelling contact, but also a reasonable spread of camera-counts for both photographs: STL 1435 ± 98 and dark 642 ± 48 (error is one standard deviation of the mean, N = 11). The camera-counts of a pixel some distance remote from the emission-pixel, figure 2(b), shows little difference between STL (606 ± 46, N = 11) and dark (660 ± 73, N = 11) camera-counts. The fluctuation in the tunnel junction STL signal may be due to the high tunnelling current used in this experiment of 1 nA. At this relatively high tunnelling current the tip-apex can become unstable and change state during the tunnelling experiment leading to the degree of variation measured in the camera signal. It may also reflect the typically Poisson noise for our low photon count rate (see final discussion section).

Figure 2(c) presents the main STL result of this work, the voltage dependence of the light emission for electron injections from +1.5 V to +3 V. Each data point represents the average taken over typically 11 sets of STL/dark photographs. What is striking is the sharp voltage threshold at +2 V STM bias voltage. Below +2 V we find no light emission; above this threshold we find a near monotonically increasing light emission signal.

Previous STL reports on the Si(111)−7 × 7 surface have invoked both LSP and direct dipole transition mechanisms. In the work of Downes and Welland they reported a STL signal that lacked atomic-resolution and instead indicated a light emission region of ~2 nm surrounding their STM tip [20]. The light emission was modelled with a LSP in the tip/surface junction. Such a model would imply a photon-emission spectrum that was dependent on the geometric shape of the tunnel junction and its elemental identity [29]. On the other hand, the STL-spectroscopy work of Imada and co-workers [24], showed atomic spacial resolution in the STL signal and no energy shift of the detected photon emission peaks with increasing tip-sample bias voltage. This lack of energy shift also rules out the previously proposed mechanism of a direct dipole transition between a tip state and a sample state [17], which would produce a voltage dependence of the emission peak.

STM induced nonlocal atomic manipulation

There is no fundamental difference between an STL experiment and an atomic-manipulation experiment, except the measured outcome. In STL we measure the light emission generated by the hot-electrons injected from the tip of the STM. In atomic-manipulation we measure the response of molecules on the surface to the hot-electrons injected from the tip of the STM.

For each nonlocal atomic-manipulation experiment a large STM image was recorded with passive parameters (no molecular displacement) [31] of a surface partly covered with chemisorbed toluene molecules which appear as dark-spots, see figure 3(a). The tip was positioned at the centre of the image and a current injection performed with set voltage, current and time (here +2.8 V, 750 pA and 10 s). A second large STM

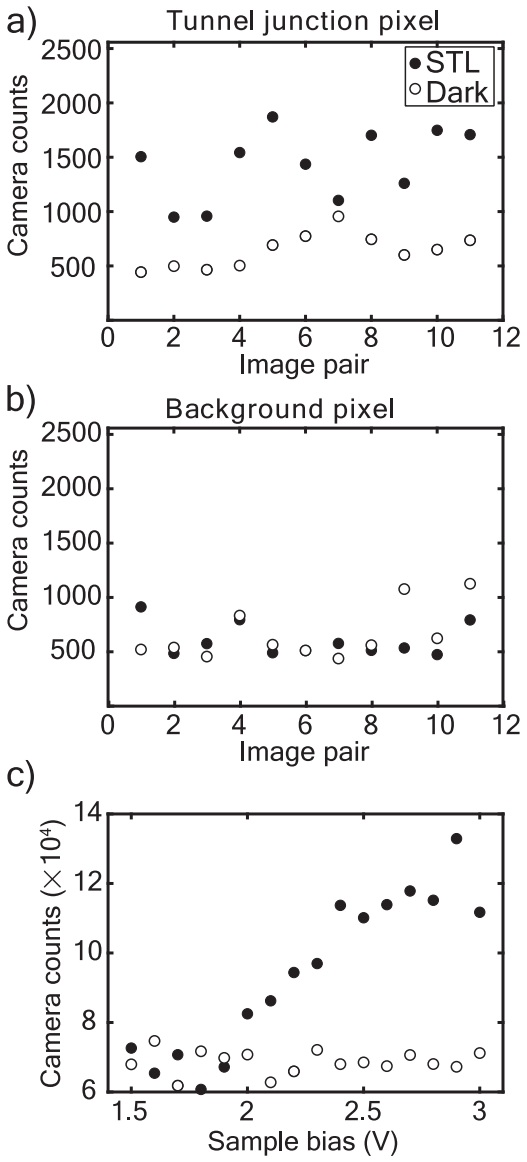

Figure 2. Light emission from the tunnelling junction pixel. (a) Camera-counts for the tunnel junction pixel over 11 pairs of STL photographs (Injection: +3 V, 1 nA, 40 s. Camera gain ×333) and dark photographs (Injection: +3 V, 0 nA, 40 s. Camera gain ×333). (b) Camera-counts taken from the same photographs as (a), but from a pixel some distance away from the tunnel junction pixel. (c) Voltage dependence of the STL and dark camera-counts (summed over 11 photographs) from the tunnel junction (Injections: 40 s. Camera gain ×833).

image is then recorded, figure 3(b), revealing a central region that has fewer molecular adsorbates (dark-spots) indicating a region of the surface that has undergone nonlocal molecular manipulation. That is, molecules some distance from the tunnel junction, i.e. injection site, have been induced to desorb from the surface.

We have previously reported on nonlocal manipulation of chlorobenzene and toluene from the Si(111) -7×7 surface [21–23, 32]. See [33] for a general review of nonlocal manipulation. Here we use our ballistic-diffusive model, developed in [22, 23] to model hole-induced (negative bias voltage) nonlocal desorption, and apply it to electron-induced (positive bias voltage) nonlocal desorption. Our simple step-wise model proceeds as follows: (i) An electron tunnels from tip to surface and populates a 2D surface resonance; (ii) The wavefunction of this state evolves ballistically unperturbed for a certain time τ_i (of order 10 fs); (iii) The electron thermalises and relaxes to the bottom of the surface resonance band; (iv) it then undergoes a 2D random walk, i.e. 2D isotropic diffusion for ~200 fs; (v) the charge inelastically relaxes towards the Fermi level leading to the possible desorption of a molecule.

Figure 3(c) presents a series of curves showing the probability of displacement as a function of distance from the injection site. From each curve we extract three key parameters: β the probability per injected electron of inducing desorption; λ the diffusive length-scale; and R the region close to the tip where there appears to be a suppression of desorption. Here, in the 'suppression' region, a purely diffusive model fails and the full ballistic-

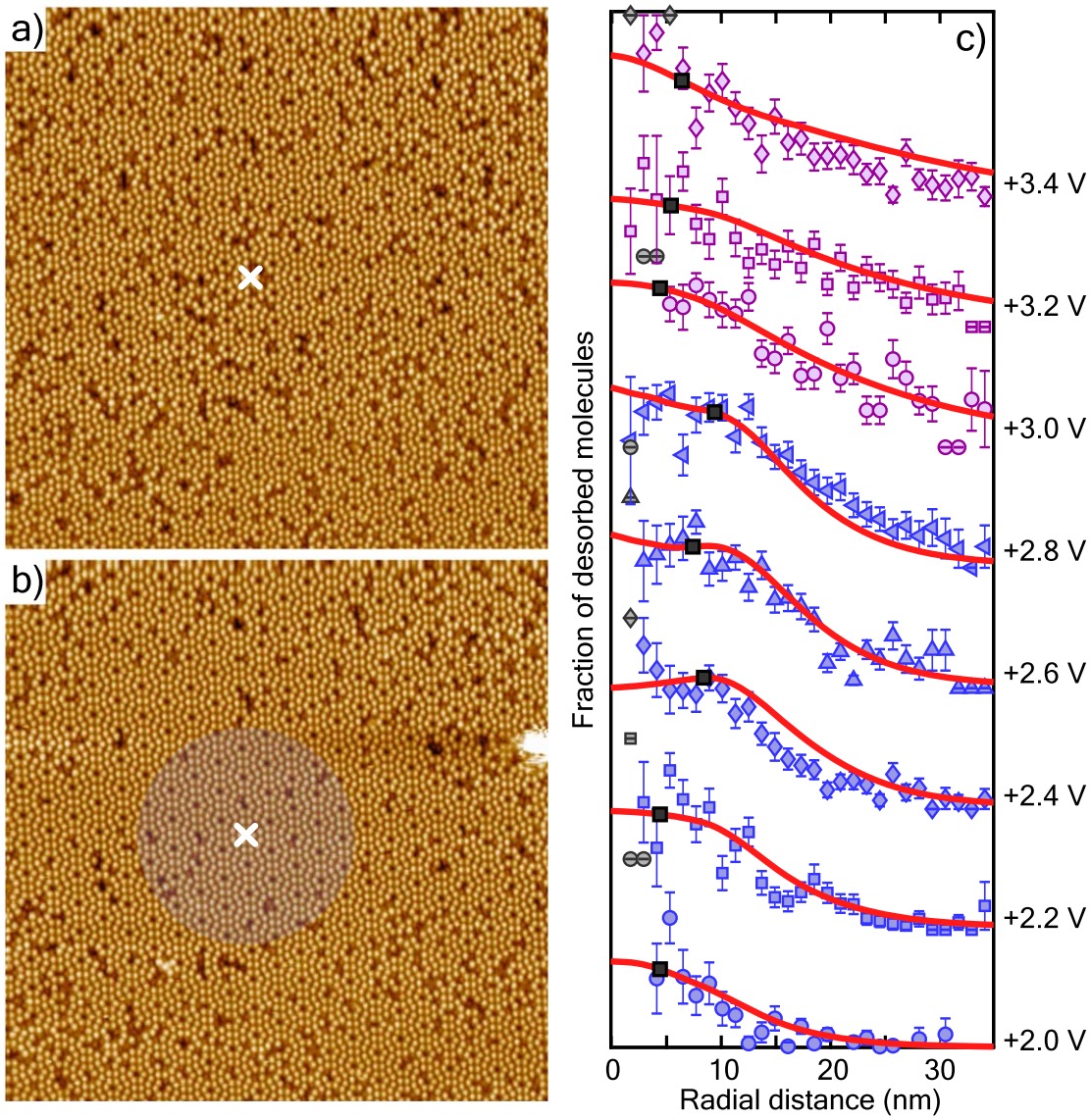

Figure 3. Nonlocal atomic manipulation with the STM. (a) Passive STM image (+1 V, 100 pA, 50 nm × 50 nm) taken before current injection. (b) STM image, with same parameters as (a), but taken after a current injection of +2.8 V, 750 pA and duration of 10 s located at the white ×. The shaded region indicates the measured hot electron diffusion length-scale of 10 nm for manipulation experiments at +2.8 V. (c) Injection voltage dependence of nonlocal manipulation of FM toluene molecules with a corner-hole injection site. Radial distribution curves have been vertically offset to aid clarity and match STS energy axis. Solid red lines show the inflation-diffusion model fitted to each dataset (light grey data points were omitted from the fits). Black markers indicate the range of the inflation region determined from the experimental data. Details of the fitting model are given in the main text and methods section. Data in blue/purple corresponds to electron transport by state U_3/U_4, respectively.

diffusive model is required. Figure 4 presents, in identical fashion to [23], these parameters as a function of the injection voltage as extracted from the experimental data curves of figure 3(c).

Below +2.0 V we found no evidence of nonlocal manipulation. The same threshold we found for light emission. Between (+2.0 ± 0.1) V and (+2.9 ± 0.1) V we have a manipulation region of near constant diffusion length $\lambda = (14 \pm 2)$ nm. Above this we enter into a second manipulation region with a diffusive length of $\lambda = (34 \pm 4)$ nm. As in [23] we find a sharp reduction in the suppression region R upon a change from one nonlocal regime to another. This is rationalised as the nonlocal transport changing from one surface electronic state to another. Hence, at the threshold voltage of +2.0 V, the electron wavepacket is generated at the bottom of a band and so has little or no group velocity and does not undergo any significant ballistic transport from the injection site before undergoing diffusive transport.

Scanning tunnelling spectroscopy (STS) measurements of a clean FM adatom, figure 4(d), reveal the usual U_3 state at (+2.3 ± 0.5) eV with its onset responsible for the +2 V threshold for nonlocal manipulation. It also shows a higher-lying state at (+3.4 ± 0.3) eV, that we simply label for consistency as U_4. Hence, we label the first region as transport though the U_3 state as T_{U_3}, and the higher-lying region as T_{U_4}.

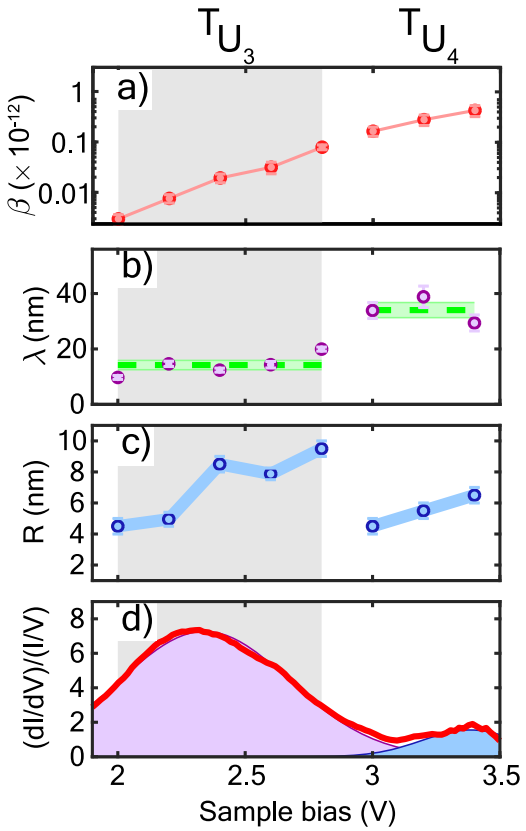

Figure 4. Injection bias dependence for electron injections into CH sites. Nonlocal manipulation of FM toluene molecules. (a) The probability β of manipulation per injected hole. (b) Diffusion length-scale λ with the average length-scale for each transport region indicated with green bar with uncertainty given by the width of the bar. (c) The range of the suppression region R. (d) Red curve, normalized STS spectrum taken on a clean FM site. Shaded areas show Gaussian fits to the two peaks with peak position and FWHM of (2.3 $\pm$ 0.5) eV and (3.4 $\pm$ 0.3) eV.

Using these STS parameters for the two regimes we can test whether our ballistic-diffusive model developed to model hole-injection, also describes electron-injection (see methods and [23] for detailed discussion and further justification). The fitted curves of figure 3(c) show a good fit for radial distances greater than 10 nm away from the injection site, the length-scale dominated by diffusive transport. Below 10 nm we also find a good fit that describes the suppression of manipulation at these short ranges governed by the ballistic process. From a global fit to all the radial desorption curves within a region we extract an initial ballistic time for T_{U_3} of $\tau_i = 5$ fs and the same for T_{U_4} with $\tau_i = 5$ fs. We estimate a fitting error on the ballistic time of ~2 fs.

Discussion

The invariance of the nonlocal diffusive length-scale, figure 4(b), to the injection voltage shows that once above a voltage threshold, all injected electrons are transported in the same fashion. That is, no matter their injection energy (voltage), the injected electrons are identical upon initiating the diffusive transport step of the nonlocal manipulation. Hence, after the initial ballistic step and before the diffusion, there must be an ultrafast relaxation of the charge to the bottom of its surface band [34, 35]. As the STS of figure 4(d) shows, for injections between +2 V and +3 V this surface band is the U_3 state, and above +3 V it is the U_4 state. The STL threshold found here of +2 V therefore suggests that if the same electron dynamics occur, then the light emission for injections above +2 V would be from the bottom of the U_3 state. We therefore propose that after the injected electron has undergone diffusion for 200 fs [36], it decays out of the state and may emit a photon, or manipulate a molecule.

Therefore there are at least 3 decay channels: one leading to manipulation, one leading to light emission, and one that is inactive. Hence, within a transport regime, T_{U_3} or T_{U_4}, the energy of the emitted photon should be voltage independent. Imada *et al* [24]. report just such a spectral invariance to the STL injection voltage. For electron injection at +2 V Imada *et al* measure photon energy peaks at 1.4 eV and at 1.85 eV, and for electron injection at +3 V they measure photon energy peaks at 1.4 eV, 1.85 eV, and 2.4 eV, respectively. The invariance of the STL peaks to injection energy is analogous to our invariant nonlocal length scale λ and agrees with having a common underlying physical process.

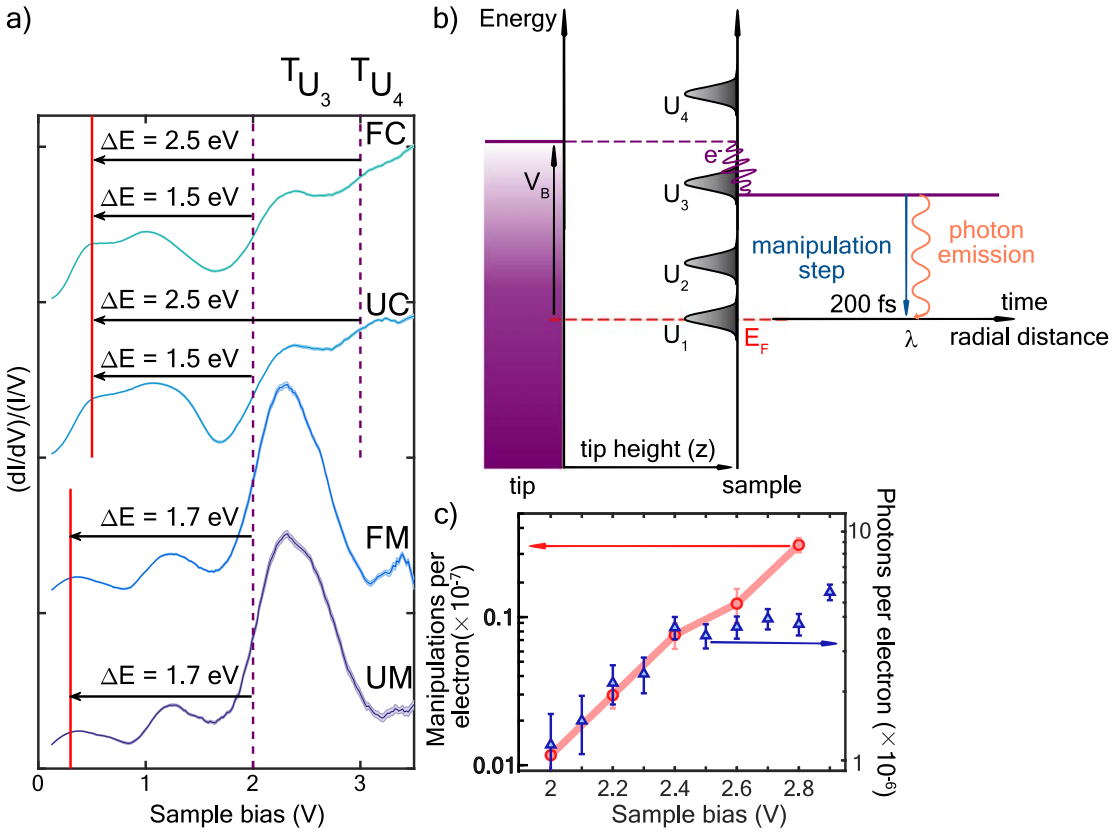

Figure 5. Proposed model for the energy relaxation of an electron injected from the STM tip into the sample. (a) Normalised density of states of the empty states. Each spectrum is the average of: 10, UM; 14, FM; 21, UC; 25, FC individual spectra, respectively. Spectra are offset vertically for clarity. Shaded area (barely visible) represents the standard error on each spectrum. Black arrows show the possible energy transitions for electrons on each site of the silicon surface. (b) Schematic showing the proposed energy relaxation mechanism for electrons tunnelling from the STM tip into the sample. An electron of energy higher than the nonlocal manipulation threshold first relaxes to the bottom of the U_3 state [23]. There it lives for ~200 fs, during which time it diffuses across the sample surface to a distance λ [22]. Next, the electron drops in energy into the U_1 state. During this final transition the electron may manipulate a molecule, or emit a photon. (c) Probability per electron of molecular manipulation (red circles) and probability per electron of photon emission (blue triangles) as a function of sample bias voltage.

These results suggest that STL on the Si(111)-7×7 has the same initial ballistic-diffusive electron dynamics and that the electron has relaxed to the bottom of the high lying electronic band before decaying with the emission of a photon.

Taking the pre-photon emission energy as the energy threshold of our nonlocal manipulation we use the discrete energy losses observed in the spectra of Imada *et al* to determine the final state of the injected electron upon its relaxation step. Figure 5 shows scanning tunnelling spectra, from 0 V to +3.5 V, of all four silicon adatom species of the surface. The U_3 state centred at $(+2.3 \pm 0.5)$ eV has a clear amplitude at each adatom site. The minimum energy required to manipulate a toluene molecule is +1.4 eV [22, 27], and the energy range of photons detectable by our camera is ≈1.4 to 3.1 eV. Thus, we would be insensitive to any transition between the bottom of the U_3 state and next state, U_2, observed at +1.3 V in the STS ($\Delta E = 0.7$ eV). The next and lowest energy state is the dangling bond state U_1 which has slightly different values depending on the adatom species [37]. For middle adatoms the U_1 state lies at +0.3 eV. Hence a transition from the bottom of the U_3 band to the peak of the U_1 state gives an energy difference of $\Delta E = 1.7$ eV. For corner adatoms, the U_1 state lies slightly higher at +0.5 eV giving an energy difference of $\Delta E = 1.5$ eV.

Above +3 V injection bias we enter a new electron transport state T_{U_4} which is predominantly located on the corner adatom sites, as STS shows in figure 5. A transition to the U_1 state gives $\Delta E = 2.5$ eV. For STL with +3 V injection Imada *et al* find a spectral peak at 2.4 eV photon energy. We can therefore interpret the STL spectra of Imada *et al* in terms of electron relaxation at particular adatom sites with initial energy at the bottom of the U_3 band, or as a cascade of relaxation steps from the U_4 band for electron injections above +3 V.

To quantitatively compare the two outcomes we recast both the manipulation and the light emission results into the probability of displacement or photon emission per electron. The conversion from camera counts follows standard practice (see methods section). However, since the models used to describe the nonlocal manipulation [21–23] are based on individual electron-molecule interactions, we develop the following

procedure to convert to the total manipulation probability. For simplicity we consider a purely diffusive model [22] and so the probability P_m of manipulating a single molecule at radius r is

$$P_m(r) = 1 - \exp\left[-\frac{2n_i\beta\tau_D}{\pi\lambda^2}K_0\left(\frac{2r}{\lambda}\right)\right], \quad (1)$$

where n_i is the number of injected electrons, β is related to the probability of a single electron manipulating a single molecule, λ the diffusive length-scale, τ_D the lifetime of the diffusive state, and K_0 a modified Bessel function of the second kind with argument $2r/\lambda$. Note in references [22, 38] we used $\lambda = \sqrt{D\tau_D}$, here we use the correct form relating to 2D isotropic diffusion of $\lambda = \sqrt{4D\tau_D}$. Hence, equation (1) is slightly modified from the version presented in [22, 38]. For a single electron we can simply expand the exponential about zero to give $P_m(r) = \frac{2n_i\beta\tau_D}{\pi\lambda^2}K_0\left(\frac{2r}{\lambda}\right)$. Experimentally $P_m(r)$ is simply the ratio of the measured number of molecules in an annulus of radius r before $N_0(r)$ and after $N(r)$ the electron injection, $P_m(r) = N(r)/N_0(r)$. Here, to compute the total number of manipulations that could happen in a single electron event we assume that each adatom site is manipulation 'active' and hence $N_0(r) = \rho 2\pi r\Delta r$ for an annulus Δr, and with $\rho = 1.92 \times 10^{18}$ the number of adatoms per m^2. Therefore the total number of possible manipulation events N for a single electron injection ($n_i = 1$) is $N = \int_0^\infty \rho\frac{2\beta\tau_D}{\pi\lambda^2}K_0\left(\frac{2r}{\lambda}\right)2\pi r dr$. In the limit of $r \to \infty$ the integral $\int rK_0(2r/\lambda)dr \to \lambda^2/4$, hence $N = \rho\beta\tau_D$. We take $\tau_D =$ 200 fs [36] and so convert the β values of figure 4 to the total probability of manipulation per injected electron N as displayed in figure 5(c). This form of analysis should be identical to the original 'scanning' manipulation work and indeed we find our results here match qualitatively and quantitatively with that earlier work [32, 39].

Figure 5(c) shows the voltage dependence of both the probability per electron of molecular displacement and the probability per electron of photon emission. Both have a common +2 V threshold and then near exponential increase demonstrating near constant branching ratio between these two decay channels over the range from the threshold +2 V up to ~+2.8 V. This similarity again suggests that, within a transport region, the state before molecular manipulation or light emission is the same common state no matter the injection voltage. This common state thus conforms to the proposal of a rapid relaxation of the injected charge to the bottom of a high lying state, before diffusive transport across the surface, and eventual decay out of that state with the possible outcomes of molecular manipulation or light emission.

As we demonstrated in an earlier work the actual molecular displacement is in fact driven by excitation of the underlying silicon surface [27]. It is possible to manipulate the silicon adatoms of the surface in exactly the same fashion as reported here for the toluene adsorbates [40, 41]. The main difference is whereas desorption of toluene is an irreversible process, the manipulated silicon adatoms are meta-stable at room temperature and drop back to their original sites before they can be imaged by an STM. We have also reported that the low lying state at ~+0.5 V is reduced in intensity but still present at the location of the bonding adatom to a chlorobenzene adsorbate [32]. Toluene and chlorobenzene both bond and are manipulated in near identical fashion on the Si(111)-7 × 7 surface. Therefore, it is plausible that an inelastic transition from the surface state at +2 V to the dangling bond state at +0.5 V is responsible for both the light emission and the molecular displacement. Figure 5(b) shows schematically our proposed relaxation process for electrons tunnelling from the STM tip into the sample. If the injected electrons have energy above the threshold for nonlocal manipulation, they first undergo ultrafast relaxation to the bottom of the U_3 state [21, 23]. There they live for ~200 fs, during which they spread diffusively away from the STM injection site on the Si(111)−7 × 7 surface [22]. Finally, the electrons undergo relaxation to the dangling bond state (U_1). It is during this transition that photon emission, or molecular displacement, may take place.

Conclusion

The agreement between our luminescence threshold, our nonlocal manipulation thresholds, our STS and Imada *et al*'s [24] spectroscopy suggest a common origin for STL and nonlocal manipulation on the Si(111)−7 × 7 surface, namely the decay of an electron from the bottom of a high-lying band.

The combination of nonlocal manipulation with STL is a powerful experimental technique, which can be used to provide a deeper and more accurate understanding of the relaxation dynamics of hot electrons on a semiconducting surface. For the first time, we can access information about the final state of the relaxation dynamics of electrons injected from the tip of an STM. As a result, this technique opens up the possibility for tuning the density of surface states/resonances of a given semiconducting surface, which could lead to control over the lifetime of the excited state, and as a result over the size of the nonlocal effect. Thereby, we may be able to extend the lifetime (hence, the range) of hot electron transport, crucial to optimising both light harvesting devices and surface photochemical processes.

Methods

Experimental stability

Stability during injection was ensured by an in-house drift tracking programme, combined with a feature locking technique. Figure S1 (available online at stacks.iop.org/JPCO/3/095010/mmedia) demonstrates the stability in all 3 directions during the charge injection experiment from figures 3(a) and (b). As seen in figure S1(a), the shift in the tip position after the 10 s injection is smaller much smaller than an adatom in the x and y directions. Figure S1(b) further demonstrates that STM tip height (z direction) fluctuates by less than 10 pm during the 10 s injection.

Scanning tunnelling luminescence

To convert from measured signal to emission probability per electrons P_p we use the following conversion

$$P_p = \frac{(STL - Dark) \times W}{11 \times G \times t \times Q \times T \times S \times A \times n_e}, \tag{2}$$

where: STL is the raw camera counts summed over 11 single photographs; $Dark$ is the raw camera counts over 11 dark-photographs; $W = 50$ is a tip-material factor to account for the low yield associated with tungsten; G is the camera gain; $Q = 0.5$ is the mean quantum efficiency of the camera; $T = 0.9$ is the typical transmission of a glass UHV view port; S is the ratio of camera solid angle to 4π; $A = 0.3$ is a correction for the angle of the camera away from the maximum light emission angle; $n_e = I/e$ is the number of electrons per second, which is simply related to the tunnelling current I and the charge on an electron e. Although approximate this conversion should be within an order of magnitude or so of the true value. The critical conversion factor to allow quantitative comparison with other STL measurements is W. Here we take a conservative value.

The camera had a measured bias of 490 ± 30 counts and a dark count of 0.009 ± 0.001 per second per unit gain, giving a raw single dark-photograph camera-count of $490 + 0.009 \times t \times G$.

Ballistic-diffusive model

We employ the model from [23], which relates the magnitude of the suppression region R to the surface band-structure. This allows us to extract the characteristic ballistic lifetime for each transport state. For each site, we have site-specific transport properties (λ, β, R) and spectroscopy measurements. This allows us to determine the site-specific transport region energy thresholds and band-widths. Using the s-band tight-binding model, the energy dispersion of the transport state is described by

$$E = E_0 + \frac{\Delta E}{2}(\cos(ka) - 1), \tag{3}$$

where E_0 is the energy threshold, ΔE is the state band-width and a is the 7×7 unit cell size $a = 2.69$ nm. From the site-specific plateau regions in λ, we determine energy onsets of the 2 transport states measured on FM's at $(+2.0 \pm 0.1)$ eV for the U_3 state and $(+2.85 \pm 0.1)$ eV for the U_4 state. The first threshold matches well with the position of the U_3 reported previously in [21, 22, 36]. The U_3 state has upwards dispersion [42–44].

Previously, it has been measured that the S_3 state has a width of ~0.35 eV between the $\overline{M}$ point and half-way to the $\overline{\Gamma}$ point [42, 44], giving a full dispersion width of ~0.7 eV. The average FWHM of the S_3 state from our STS measurements [23] is 0.49 eV (0.54 eV for U_3; 1.08 eV for U_4). Based on the angle-resolved ultraviolet photoemission spectroscopy results, we calculate a conversion factor for the FWHM of the S_3 state [42], giving a band-width of 0.7 eV for S_3 (and 0.8 eV for U_3; 1.5 eV for U_4). The state occupancy is then described with the standard equation for the tunnelling probability [23, 45].

Acknowledgments

PAS gratefully acknowledges support from the EPSRC grant EP/K00137X/1. RMP acknowledges funding and support from the Engineering and Physical Sciences Research Council (EPSRC) Centre for Doctoral Training in Condensed Matter Physics (CDT-CMP), Grant No. EP/L015544/1. The authors thank Dr. Peter J Mosley and Dr. Kei Takashina for fruitful discussions. We thank Dr. Peter J Mosley for the use of the Andor Luca R camera. All data supporting this study are openly available from the University of Bath data archive at https://doi.org/10.15125/BATH-00622.

ORCID iDs

Peter A Sloan https://orcid.org/0000-0002-0810-8468
Kristina R Rusimova https://orcid.org/0000-0002-3679-9948

References

[1] Berndt R, Gimzewski J K and Johansson P 1991 *Phys. Rev. Lett.* **67** 3796–9
[2] Kuhnke K, Große C, Merino P and Kern K 2017 *Chem. Rev.* **117** 5174–222
[3] Kazuma E, Jung J, Ueba H, Trenary M and Kim Y 2018 *Science (80-.).* **360** 521–6
[4] Berndt R, Gaisch R, Gimzewski J K, Reihl B, Schlittler R R, Schneider W D and Tschudy M 1993 *Science (80-.).* **262** 1425–7
[5] Dong Z C *et al* 2010 *Nat. Photonics* **4** 50–4
[6] Chen C, Chu P, Bobisch C A, Mills D L and Ho W 2010 *Phys. Rev. Lett.* **105** 217402
[7] Imada H, Miwa K, Imai-Imada M, Kawahara S, Kimura K and Kim Y 2016 *Nature* **538** 364–7
[8] Imada H, Miwa K, Imai-Imada M, Kawahara S, Kimura K and Kim Y 2017 *Phys. Rev. Lett.* **119** 013901
[9] Chong M C, Reecht G, Bulou H, Boeglin A, Scheurer F, Mathevet F and Schull G 2016 *Phys. Rev. Lett.* **116** 036802
[10] Zhang Y *et al* 2016 *Nature* **531** 623–7
[11] Große C, Kabakchiev A, Lutz T, Froidevaux R, Schramm F, Ruben M, Etzkorn M, Schlickum U, Kuhnke K and Kern K 2014 *Nano Lett.* **14** 5693–7
[12] Iwami M, Uehara Y and Ushioda S 2001 *Appl. Surf. Sci.* **169–170** 188–92
[13] Merino P, Große C, Rosławska A, Kuhnke K and Kern K 2015 *Nat. Commun.* **6** 8461
[14] Nian L, Wang Y and Lü J-T 2018 *Nano Lett.* **18** 6826–31
[15] Miwa K, Sakaue M, Gumhalter B and Kasai H 2014 *J. Phys. Condens. Matter* **26** 222001
[16] Sakurai M, Thirstrup C and Aono M 2004 *Phys. Rev. Lett.* **93** 046102
[17] Thirstrup C, Sakurai M, Stokbro K and Aono M 1999 *Phys. Rev. Lett.* **82** 1241–4
[18] Imada H, Miwa K, Jung J, Shimizu T K, Yamamoto N and Kim Y 2015 *Nanotechnology* **26** 365402
[19] Abraham D L, Veider A, Schönenberger C, Meier H P, Arent D J and Alvarado S F 1990 *Appl. Phys. Lett.* **56** 1564–6
[20] Downes A and Welland M E 1998 *Phys. Rev. Lett.* **81** 1857–60
[21] Sloan P A, Sakulsermsuk S and Palmer R E 2010 *Phys. Rev. Lett.* **105** 048301–4
[22] Lock D, Rusimova K R, Pan T L, Palmer R E and Sloan P A 2015 *Nat. Commun.* **6** 8365
[23] Rusimova K R, Bannister N, Harrison P, Lock D, Crampin S, Palmer R E and Sloan P A 2016 *Nat. Commun.* **7** 12839
[24] Imada H, Ohta M and Yamamoto N 2010 *Appl. Phys. Express* **3** 045701
[25] Sakulsermsuk S, Sloan P A, Theis W and Palmer R E 2010 *J. Phys. Condens. Matter* **22** 84002
[26] Lucier A-S, Mortensen H, Sun Y and Grütter P 2005 *Phys. Rev. B* **72** 235420
[27] Rusimova K R and Sloan P A 2017 *Nanotechnology* **28** 054002
[28] Rusimova K R, Purkiss R M, Howes R, Lee F, Crampin S and Sloan P A 2018 *Science (80-.).* **361** 1012–6
[29] Rossel F, Pivetta M and Schneider W-D 2010 *Surf. Sci. Rep.* **65** 129–44
[30] Rendell R W and Scalapino D J 1981 *Phys. Rev. B* **24** 3276–94
[31] Lock D, Sakulsermsuk S, Palmer R E and Sloan P A 2015 *J. Phys. Condens. Matter* **27** 054003
[32] Pan T, Sloan P A and Palmer R E 2014 *Chem. Rec.* **14** 841–7
[33] Rusimova K R and Sloan P A 2018 *Encycl. Interfacial Chem.* 511–24
[34] Bernardi M, Vigil-Fowler D, Lischner J, Neaton J B and Louie S G 2014 *Phys. Rev. Lett.* **112** 257402
[35] Mauerer M, Shumay I L, Berthold W and Höfer U 2006 *Phys. Rev. B* **73** 245305
[36] Ichibayashi T, Tanaka S, Kanasaki J, Tanimura K and Fauster T 2011 *Phys. Rev. B* **84** 235210
[37] Mysliveček J, Stróżecka A, Steffl J, Sobotík P, Ošťádal I and Voigtländer B 2006 *Phys. Rev. B* **73** 161302
[38] Rusimova K R, Bannister N, Harrison P, Lock D, Crampin S, Palmer R E and Sloan P A 2016 *Nat. Commun.* **7** 1–7
[39] Sloan P, Hedouin M, Palmer R and Persson M 2003 *Phys. Rev. Lett.* **91** 118301
[40] Stipe B C, Rezaei M A and Ho W 1997 *Phys. Rev. Lett.* **79** 4397–400
[41] Sagisaka K, Luce A and Fujita D 2010 *Nanotechnology* **21** 045707
[42] Uhrberg R I G, Hansson G V, Nicholls J M, Persson P E S and Flodström S A 1985 *Phys. Rev. B* **31** 3805–10
[43] Northrup J E 1986 *Phys. Rev. Lett.* **57** 154–154
[44] Martensson P, Ni W-X, Hansson G V, Nicholls J M and Reihl B 1987 *Phys. Rev. B* **36** 5974–81
[45] Wiesendanger R 1994 *Scanning Probe Microscopy and Spectroscopy: Methods and Applications* (Cambridge University Press) (https://doi.org/10.1017/CBO9780511524356)

Bibliography

[1] Y. Xu, T. Gong, and J. N. Munday. The generalized Shockley-Queisser limit for nanostructured solar cells. *Scientific Reports*, 5(13536), 2015.

[2] Z. Guo, Y. Wan, M. Yang, J. Snaider, K. Zhu, and L. Huang. Long-range hot-carrier transport in hybrid perovskites visualized by ultrafast microscopy. *Science*, 356(6333):59–62, 2017.

[3] T. C. Shen and P. Avouris. Electron stimulated desorption induced by the scanning tunneling microscope. *Surface Science*, 390(1-3):35–44, 1997.

[4] D. M. Eigler and E. K. Schweizer. Positioning single atoms with a scanning tunnelling microscope. *Nature*, 344(6266):524–526, 1990.

[5] S. W. Hla, L. Bartels, G. Meyer, and K. H. Rieder. Inducing all steps of a chemical reaction with the scanning tunneling microscope tip: Towards single molecule engineering. *Physical Review Letters*, 85(13):2777–80, 2000.

[6] P. A. Sloan, M. F. G. Hedouin, R. E. Palmer, and M. Persson. Mechanisms of Molecular Manipulation with the Scanning Tunneling Microscope at Room Temperature: Chlorobenzene/Si(111)-(7×7). *Physical Review Letters*, 91(11):118301, 2003.

[7] P. A. Sloan, S. Sakulsermsuk, and R. E. Palmer. Nonlocal desorption of chlorobenzene molecules from the Si(111)-(7×7) surface by charge injection from the tip of a scanning tunneling microscope: Remote control of atomic manipulation. *Physical Review Letters*, 105(4):048301, 2010.

[8] K. R. Rusimova, N. Bannister, P. Harrison, D. Lock, S. Crampin, R. E. Palmer, and P. A. Sloan. Initiating and imaging the coherent surface dynamics of charge carriers in real space. *Nature Communications*, 7:12839, 2016.

[9] K. R. Rusimova and P. A. Sloan. Molecular and atomic manipulation mediated by electronic excitation of the underlying Si(111)-7x7 surface. *Nanotechnology*, 28(5):054002, 2017.

[10] H. G. Etheridge, K. R. Rusimova, and P. A. Sloan. The nanometre limits of ballistic and diffusive hot-hole mediated nonlocal molecular manipulation. *Nanotechnology*, 31(10):105401, 2020.

[11] R. M. Purkiss, H. G. Etheridge, P. A. Sloan, and K. R. Rusimova. Common source of light emission and nonlocal molecular manipulation on the Si(111)-7 $\times$ 7 surface. *Journal of Physics Communications*, 3(9):095010, 2019.

[12] K. R. Rusimova, R. M. Purkiss, R. Howes, F. Lee, S. Crampin, and P. A. Sloan. Regulating the femtosecond excited-state lifetime of a single molecule. *Science*, 361(6406):1012–16, 2018.

[13] G. Binning, H. Rohrer, C. Gerber, and E. Weibel. Surface studies by scanning tunneling microscopy. *Physical Review Letters*, 49(1):57–61, 1982.

[14] G. Binnig, H. Rohrer, C. Gerber, and E. Weibel. 7 $\times$ 7 Reconstruction on Si(111) Resolved in Real Space. *Physical Review Letters*, 50(2):120–123, 1983.

[15] C. J. Chen. *Introduction to Scanning Tunneling Microscopy.* Oxford University Press, 1993.

[16] P. J. De Pablo. Introduction to atomic force microscopy. In E. Peterman and G. Wuite, editors, *Single Molecule Analysis. Methods in Molecular Biology (Methods and Protocols)*, volume 783, pages 197–212. Humana Press, 2011.

[17] O. Custance, R. Perez, and S. Morita. Atomic force microscopy as a tool for atom manipulation. *Nature Nanotechnology*, 4(12):803–810, 2009.

[18] S. Kawai, A. S. Foster, F. F. Canova, H. Onodera, S. I. Kitamura, and E. Meyer. Atom manipulation on an insulating surface at room temperature. *Nature Communications*, 5:4403, 2014.

[19] F. J. Giessibl. Principles and Applications of the qPlus Sensor. In S. Morita, F. J. Giessibl, and R. Wiesendanger, editors, *Noncontact Atomic Force Microscopy*, pages 121–142. Springer, Berlin, Heidelberg, 2009.

[20] B. De La Torre, M. Švec, G. Foti, O. Krejčí, P. Hapala, A. Garcia-Lekue, T. Frederiksen, R. Zbořil, A. Arnau, H. Vázquez, and P. Jelínek. Submolecular Resolution by Variation of the Inelastic Electron Tunneling Spectroscopy Amplitude and

its Relation to the AFM/STM Signal. *Physical Review Letters*, 119(16):166001, 2017.

[21] M. Herz, C. Schiller, F. J. Giessibl, and J. Mannhart. Simultaneous current-, force-, and work-function measurement with atomic resolution. *Applied Physics Letters*, 86:153101, 2005.

[22] L. L. Patera, F. Queck, P. Scheuerer, and J. Repp. Mapping orbital changes upon electron transfer with tunnelling microscopy on insulators. *Nature*, 566(7743):245–248, 2019.

[23] J. Hellerstedt, A. Cahlík, M. Švec, B. De La Torre, M. Moro-Lagares, T. Chutora, B. Papoušková, G. Zoppellaro, P. Mutombo, M. Ruben, R. Zbořil, and P. Jelinek. On-surface structural and electronic properties of spontaneously formed Tb2Pc3 single molecule magnets. *Nanoscale*, 10(33):15553–63, 2018.

[24] P. Scheuerer, L. L. Patera, and J. Repp. Manipulating and Probing the Distribution of Excess Electrons in an Electrically Isolated Self-Assembled Molecular Structure. *Nano Letters*, 20(3):1839–45, 2020.

[25] B. Voigtländer. Scanning Tunneling Microscopy. In *Scanning Probe Microscopy*, pages 279–308. Springer, Berlin, Heidelberg, 2015.

[26] J. R. Rumble, D. R. Lide, and T. J. Bruno. Physical Constants of Organic Compounds. In J. R. Rumble, editor, *CRC handbook of chemistry and physics*. CRC Press/Taylor & Francis, Boca Raton, Fl., 100th edition, 2019.

[27] S. Gasiorowicz. *Quantum physics*. Wiley, 3rd edition, 2003.

[28] K. Palotás, G. Mándi, and W. A. Hofer. Three-dimensional Wentzel-Kramers-Brillouin approach for the simulation of scanning tunneling microscopy and spectroscopy. *Frontiers of Physics*, 9(6):711–747, 2014.

[29] J. P. Ibe, P. P. Bey, S. L. Brandow, R. A. Brizzolara, N. A. Burnham, D. P. DiLella, K. P. Lee, C. R. K. Marrian, and R. J. Colton. On the electrochemical etching of tips for scanning tunneling microscopy. *Journal of Vacuum Science & Technology A: Vacuum, Surfaces, and Films*, 8(4):3570–75, 1990.

[30] R. Boulton. Optimisation of the One-Step Electrochemical Etching Process of Tungsten Scanning Tunnelling Microscope Tips, MPhys dissertation, Department of Physics, University of Bath, Bath, 2013.

[31] F. J. Giessibl. Atomic resolution of the silicon (111)-(7x7) surface by atomic force microscopy. *Science*, 267(5194):68–71, 1995.

[32] Z. Majzik, B. Drevniok, W. Kamiński, M. Ondráček, A. B. McLean, and P. Jelínek. Room Temperature Discrimination of Adsorbed Molecules and Attachment Sites on the Si(111)–7 × 7 Surface Using a qPlus Sensor. *ACS Nano*, 7(3):2686–92, 2013.

[33] J. Villain, M. Lavagna, and P. Bruno. Jacques Friedel and the physics of metals and alloys. *Comptes Rendus Physique*, 17(3-4):276–290, 2016.

[34] M. F. Crommie, C. P. Lutz, and D. M. Eigler. Imaging standing waves in a two-dimensional electron gas. *Nature*, 363(6429):524–527, 1993.

[35] P. Sessi, V. M. Silkin, I. A. Nechaev, T. Bathon, L. El-Kareh, E. V. Chulkov, P. M. Echenique, and M. Bode. Direct observation of many-body charge density oscillations in a two-dimensional electron gas. *Nature Communications*, 6:8691, 2015.

[36] T. Ardhuin, O. Guillermet, C. J. Villagómez, A. Gourdon, and S. Gauthier. Observation of electron two-dimensional standing-wave patterns at the surface of an insulating layer by scanning tunneling microscopy. *Physical Review B*, 99:35410, 2019.

[37] M. F. Crommie, C. P. Lutz, and D. M. Eigler. Confinement of electrons to quantum corrals on a metal surface. *Science*, 262(5131):218–220, 1993.

[38] A. D. Gottlieb and L. Wesoloski. Bardeen's tunnelling theory as applied to scanning tunnelling microscopy: A technical guide to the traditional interpretation. *Nanotechnology*, 17(8):R57, 2006.

[39] H. C. Manoharan, C. P. Lutz, and D. M. Eigler. Quantum mirages formed by coherent projection of electronic structure. *Nature*, 403(6769):512–515, 2000.

[40] E. Inami, I. Hamada, K. Ueda, M. Abe, S. Morita, and Y. Sugimoto. Room-temperature-concerted switch made of a binary atom cluster. *Nature Communications*, 6:6231, 2015.

[41] G. Lovat, B. Choi, D. W. Paley, M. L. Steigerwald, L. Venkataraman, and X. Roy. Room-temperature current blockade in atomically defined single-cluster junctions. *Nature Nanotechnology*, 12(11):1050–54, 2017.

[42] A. C. Aragonès, N. Darwish, S. Ciampi, F. Sanz, J. J. Gooding, and I. DIéz-Pérez. Single-molecule electrical contacts on silicon electrodes under ambient conditions. *Nature Communications*, 8:15056, 2017.

[43] P. A. Sloan. Tunnel-Current Induced STM Atomic Manipulation. In A. J. Mayne and G. Dujardin, editors, *Frontiers of Nanoscience*, volume 2, pages 121–150. Elsevier Ltd, 2011.

[44] G. P. Salam, M. Persson, and R. E. Palmer. Possibility of coherent multiple excitation in atom transfer with a scanning tunneling microscope. *Physical Review B*, 49(15):10655–62, 1994.

[45] P. A. Redhead. INTERACTION OF SLOW ELECTRONS WITH CHEMISORBED OXYGEN. *Canadian Journal of Physics*, 42(5):886–905, 1964.

[46] P. R. Antoniewicz. Model for electron- and photon-stimulated desorption. *Physical Review B*, 21(9):3811–15, 1980.

[47] P. Saalfrank, G. Boendgen, C. Corriol, and T. Nakajima. Direct and indirect DIET and DIMET from semiconductor and metal surfaces: What can we learn from 'toy models'? In *Faraday Discussions*, volume 117, pages 65–83. Royal Society of Chemistry, 2000.

[48] A. Groß. *Theoretical surface science: A microscopic perspective*. Springer Berlin Heidelberg, 2009.

[49] B. C. Stipe, M. A. Rezaei, W. Ho, S. Gao, M. Persson, and B. I. Lundqvist. Single-molecule dissociation by tunneling electrons. *Physical Review Letters*, 78(23):4410–13, 1997.

[50] S. Alavi, R. Rousseau, S. N. Patitsas, G. P. Lopinski, R. A. Wolkow, and T. Seideman. Inducing desorption of organic molecules with a scanning tunneling microscope: theory and experiments. *Physical Review Letters*, 85(25):5372–75, 2000.

[51] D. M. Eigler, C. P. Lutz, and W. E. Rudge. An atomic switch realized with the scanning tunnelling microscope. *Nature*, 352(6336):600–603, 1991.

[52] P. A. Sloan and R. E. Palmer. Two-electron dissociation of single molecules by atomic manipulation at room temperature. *Nature*, 434(7031):367–371, 2005.

[53] P. Maksymovych, D. C. Sorescu, K. D. Jordan, and J. T. Yates. Collective reactivity of molecular chains self-assembled on a surface. *Science*, 322(5908):1664–67, 2008.

[54] B. C. Stipe, M. A. Rezaei, and W. Ho. Site-specific displacement of Si adatoms on Si(111)-(7 × 7). *Physical Review Letters*, 79(22):4397–400, 1997.

[55] T. Komeda, Y. Kim, Y. Fujita, Y. Sainoo, and M. Kawai. Local chemical reaction of benzene on Cu(10) via STM-induced excitation. *Journal of Chemical Physics*, 120(11):5347–52, 2004.

[56] L. Soukiassian, A. J. Mayne, M. Carbone, and G. Dujardin. Atomic-scale desorption of H atoms from the Si(100)-2×1:H surface: Inelastic electron interactions. *Physical Review B*, 68(3):035303, 2003.

[57] P. Liljeroth, J. Repp, and G. Meyer. Current-induced hydrogen tautomerization and conductance switching of naphthalocyanine molecules. *Science*, 317(5842):1203–06, 2007.

[58] F. Mohn, J. Repp, L. Gross, G. Meyer, M. S. Dyer, and M. Persson. Reversible bond formation in a gold-atom-organic-molecule complex as a molecular switch. *Physical Review Letters*, 105(26):266102, 2010.

[59] P. Maksymovych, D. B. Dougherty, X.-Y. Zhu, and J. T. Yates. Nonlocal dissociative chemistry of adsorbed molecules induced by localized electron injection into metal surfaces. *Physical Review Letters*, 99(1):016101, 2007.

[60] M. Sicot, O. Kurnosikov, O. A. Adam, H. J. Swagten, and B. Koopmans. STM-induced desorption of hydrogen from Co nanoislands. *Physical Review B*, 77(3):035417, 2008.

[61] J. R. Hahn, S. H. Jang, K. W. Kim, and S. B. Son. Hot carrier-selective chemical reactions on Ag(110). *Journal of Chemical Physics*, 139(7):74707, 2013.

[62] J. N. Ladenthin, L. Grill, S. Gawinkowski, S. Liu, J. Waluk, and T. Kumagai. Hot Carrier-Induced Tautomerization within a Single Porphycene Molecule on Cu(111). *ACS Nano*, 9(7):7287–95, 2015.

[63] H. Yang, A. J. Mayne, C. Cejas, G. Dujardin, and Y. Kuk. Manipulation at a distance: Atomic-scale observation of ballistic electron transport in single layer graphene. *Applied Physics Letters*, 102(22):223104, 2013.

[64] Y. Takagi, Y. Yoshimoto, K. Nakatsuji, and F. Komori. Nonlocal manipulation of dimer motion at Ge(001) clean surface via hot carriers in surface states. *Journal of the Physical Society of Japan*, 74(12):3143–46, 2005.

[65] R. Nouchi, K. Masunari, T. Ohta, Y. Kubozono, and Y. Iwasa. Ring of C60 polymers formed by electron or hole injection from a scanning tunneling microscope tip. *Physical Review Letters*, 97(19):196101, 2006.

[66] A. Bellec, D. Riedel, G. Dujardin, O. Boudrioua, L. Chaput, L. Stauffer, and P. Sonnet. Nonlocal activation of a bistable atom through a surface state charge-transfer process on Si(100)-(2×1):H. *Physical Review Letters*, 105(4):048302, 2010.

[67] S. Titmuss, A. Wander, and D. A. King. Reconstruction of clean and adsorbate-covered metal surfaces. *Chemical Reviews*, 96(4):1291–1305, 1996.

[68] H. Lüth. *Solid Surfaces, Interfaces and Thin Films*. Graduate Texts in Physics. Springer International Publishing, Cham, 2015.

[69] Y. Takagi, K. Nakatsuji, Y. Yoshimoto, and F. Komori. Superstructure manipulation on a clean Ge(001) surface by carrier injection using an STM. *Physical Review B*, 75(11):115304, 2007.

[70] Y. Takagi, Y. Yoshimoto, K. Nakatsuji, and F. Komori. Reversible local-modification of surface structure on clean Ge(0 0 1) by scanning tunneling microscopy below 80 K. *Surface Science*, 559(1):1–15, 2004.

[71] H. Kawai and O. Narikiyo. Vibration of dimer on Ge(001) surface excited coherently by tunneling current of scanning tunneling microscopy. *Journal of the Physical Society of Japan*, 73(9):2362–65, 2004.

[72] Y. Takagi, K. Tomatsu, K. Nakatsuji, and F. Komori. Multiple electronic excitation using scanning tunneling microscopy on Ge(001). *Journal of the Physical Society of Japan*, 78(6):063601, 2009.

[73] K. Takayanagi, Y. Tanishiro, S. Takahashi, and M. Takahashi. Structure analysis of Si(111)-7 × 7 reconstructed surface by transmission electron diffraction. *Surface Science*, 164(2-3):367–392, 1985.

[74] M. Smeu, H. Guo, W. Ji, and R. A. Wolkow. Electronic properties of Si(111)-7×7 and related reconstructions: Density functional theory calculations. *Physical Review B*, 85(19):195315, 2012.

[75] J. Ortega, F. Flores, and A. L. Yeyati. Electron correlation effects in the Si(111) surface. *Physical Review B*, 58(8):4584–88, 1998.

[76] R. Losio, K. Altmann, and F. Himpsel. Fermi surface of Si(111)7x7. *Physical Review B*, 61(16):10845–53, 2000.

[77] R. Schillinger, C. Bromberger, H. J. Jänsch, H. Kleine, O. Kühlert, C. Weindel, and D. Fick. Metallic Si(111)-(7x7)-reconstruction: A surface close to a Mott-Hubbard metal-insulator transition. *Physical Review B*, 72(11):115314, 2005.

[78] F. J. Himpsel, G. Hollinger, and R. A. Pollak. Determination of the Fermi-level pinning position at Si(111) surfaces. *Physical Review B*, 28(12):7014–18, 1983.

[79] K. Yoo and H. H. Weitering. Electrical conductance of reconstructed silicon surfaces. *Physical Review B*, 65(11):115424, 2002.

[80] I. Barke, F. Zheng, A. R. Konicek, R. C. Hatch, and F. J. Himpsel. Electron-phonon interaction at the Si(111)-7×7 surface. *Physical Review Letters*, 96(21):216801, 2006.

[81] M. Mauerer, I. L. Shumay, W. Berthold, and U. Höfer. Ultrafast carrier dynamics in Si(111)7×7 dangling bonds probed by time-resolved second-harmonic generation and two-photon photoemission. *Physical Review B*, 73(24):245305, 2006.

[82] J. E. Northrup. Origin of surface states on Si(111)(7×7). *Physical Review Letters*, 57(1):154, 1986.

[83] R. J. Hamers, R. M. Tromp, and J. E. Demuth. Surface electronic structure of Si (111)-(7×7) resolved in real space. *Physical Review Letters*, 56(18):1972–75, 1986.

[84] Y. L. Wang, H. J. Gao, H. M. Guo, H. W. Liu, I. G. Batyrev, W. E. McMahon, and S. B. Zhang. Tip size effect on the appearance of a STM image for complex surfaces: Theory versus experiment for Si(111)-(7 X 7). *Physical Review B*, 70(7):073312, 2004.

[85] R. M. Tromp, R. J. Hamers, and J. E. Demuth. Quantum states and atomic structure of silicon surfaces. *Science*, 234(4774):304–309, 1986.

[86] J. Mysliveček, A. Strózecka, J. Steffl, P. Sobotík, I. Ošt'ádal, and B. Voigtländer. Structure of the adatom electron band of the Si (111)-7×7 surface. *Physical Review B*, 73(16):161302, 2006.

[87] Y. Taguchi, M. Fujisawa, and M. Nishijima. Adsorbed state of benzene on the Si(111) (7×7) surface. *Chemical Physics Letters*, 178(4):363–368, 1991.

[88] X. H. Chen, Q. Kong, J. C. Polanyi, D. Rogers, and S. So. The adsorption of C6H5Cl on Si(111)7 × 7 studied by STM. *Surface Science*, 340(3):224–230, 1995.

[89] R. A. Wolkow and D. J. Moffatt. The frustrated motion of benzene on the surface of Si(111). *The Journal of Chemical Physics*, 103(24):10696–700, 1995.

[90] Y. Cao, J. F. Deng, and G. Q. Xu. Stereo-selective binding of chlorobenzene on Si(111)-7×7. *Journal of Chemical Physics*, 112(10):4759–67, 2000.

[91] S. A. Horn and S. N. Patitsas. STM study of charge transfer and the role of rest-atoms in the binding of benzene to Si(1 1 1)7 × 7. *Surface Science*, 602(2):630–637, 2008.

[92] S. Sakulsermsuk, P. A. Sloan, and R. E. Palmer. A New Mechanism of Atomic Manipulation: Bond-Selective Molecular Dissociation via Thermally Activated Electron Attachment. *ACS Nano*, 4(12):7344–48, 2010.

[93] I. Petsalakis, J. C. Polanyi, and G. Theodorakopoulos. Theoretical study of benzene, toluene, and dibromobenzene at a Si(111)7×7 surface. *Israel Journal of Chemistry*, 45:111 – 126, 2010.

[94] M. Utecht, T. Pan, T. Klamroth, and R. E. Palmer. Quantum chemical cluster models for chemi- and physisorption of chlorobenzene on Si(111)-7×7. *Journal of Physical Chemistry A*, 118(33):6699–704, 2014.

[95] D. Lock, K. R. Rusimova, T. L. Pan, R. E. Palmer, and P. A. Sloan. Atomically resolved real-space imaging of hot electron dynamics. *Nature Communications*, 6:8365, 2015.

[96] M. Utecht, R. E. Palmer, and T. Klamroth. Quantum chemical approach to atomic manipulation of chlorobenzene on the Si(111)- 7×7 surface: Resonance localization, vibrational activation, and surface dynamics. *Physical Review Materials*, 1(2):026001, 2017.

[97] M. Utecht, T. Gaebel, and T. Klamroth. Desorption induced by low energy charge carriers on Si(111)-7 × 7: First principles molecular dynamics for benzene derivates. *Journal of Computational Chemistry*, 39(30):2517–25, 2018.

[98] M. Utecht and T. Klamroth. Local resonances in STM manipulation of chlorobenzene on Si(111)-7×7: performance of different cluster models and density functionals. *Molecular Physics*, 116(13):1687–96, 2018.

[99] I. D. Petsalakis and G. Theodorakopoulos. Theoretical study of halogen-substituted benzene at a Si(111)7×7 surface. *Israel Journal of Chemistry*, 45(1-2):127–136, 2005.

[100] H. Tomimoto, T. Takehara, K. Fukawa, R. Sumii, T. Sekitani, and K. Tanaka. Study of benzene and toluene on Si(111)7×7 surface by scanning tunneling microscopy. *Surface Science*, 526(3):341–350, 2003.

[101] H. Tomimoto, T. Sekitani, R. Sumii, E. O. Sako, S. I. Wada, and K. Tanaka. Study of adsorption structure of benzene and toluene on Si(1 1 1)7 × 7 surfaces. In *Surface Science*, volume 566-568, pages 664–670, 2004.

[102] T. Pan, P. A. Sloan, and R. E. Palmer. Non-local atomic manipulation on semiconductor surfaces in the STM: the case of chlorobenzene on Si(111)-7×7. *Chemical record*, 14(5):841–847, 2014.

[103] P. A. Sloan and R. E. Palmer. Manipulation of polyatomic molecules with the scanning tunnelling microscope at room temperature: Chlorobenzene adsorption and desorption from Si(111)-(7 × 7). *Journal of Physics: Condensed Matter*, 18(33):S1873, 2006.

[104] J. Boland and J. Villarrubia. Formation of Si(111)-(1 x 1)Cl. *Physical Review B*, 41(14):9865–70, 1990.

[105] P. A. Sloan and R. E. Palmer. Tip-State Control of Rates and Branching Ratios in Atomic Manipulation. *Nano Letters*, 5(5):835–839, 2005.

[106] D. E. Brown, D. J. Moffatt, and R. A. Wolkow. Isolation of an intrinsic precursor to molecular chemisorption. *Science*, 279(5350):542–544, 1998.

[107] S. Dobrin, K. Harikumar, and J. C Polanyi. An STM study of the localized atomic reaction of 1,2- and 1,4-dibromobenzene at Si(1 1 1)-7 × 7. *Surface Science*, 561(1):11–24, 2004.

[108] D. Lock, S. Sakulsermsuk, R. Palmer, and P. Sloan. Mapping the site-specific potential energy landscape for chemisorbed and physisorbed aromatic molecules on the Si(1 1 1)-7 × 7 surface by time-lapse STM. *Journal of Physics: Condensed Matter*, 27(5):054003, 2014.

[109] M. Carbone, M. N. Piancastelli, R. Zanoni, G. Comtet, G. Dujardin, and L. Hellner. A low symmetry adsorption state of benzene on Si(111)7 × 7 studied by photoemission and photodesorption. *Surface Science*, 407(1-3):275–281, 1998.

[110] S. Sakulsermsuk, P. A. Sloan, W. Theis, and R. E. Palmer. Calibrating thermal and scanning tunnelling microscope induced desorption and diffusion for the chemisorbed chlorobenzene/Si(111)7 $\times$ 7 system. *Journal of Physics: Condensed Matter*, 22(8):084002, 2010.

[111] T. L. Pan, P. A. Sloan, and R. E. Palmer. Concerted thermal-plus-electronic nonlocal desorption of chlorobenzene from Si(111)-7 $\times$ 7 in the STM. *Journal of Physical Chemistry Letters*, 5(20):3551–54, 2014.

[112] K. I. Shudo, S. Takeda, and T. Munakata. Resonant surface-state transitions of Si(111)-7×7 measured with two-photon photoemission spectroscopy. *Physical Review B*, 65(7):075302, 2002.

[113] T. Ichibayashi, S. Tanaka, J. Kanasaki, K. Tanimura, and T. Fauster. Ultrafast relaxation of highly excited hot electrons in Si: Roles of the L-X intervalley scattering. *Physical Review B*, 84(23):235210, 2011.

[114] R. J. Wilson and S. Chiang. Surface modifications induced by adsorbates at low coverage: A scanning tunneling microscopy study of the Ni/Si(111) $\sqrt{19}$ surface. *Physical Review Letters*, 58(24):2575–78, 1987.

[115] S. A. Parikh, M. Y. Lee, and P. A. Bennett. Formation conditions and atomic structure of the Si(111)-$\sqrt{19}$ Ni surface. *Surface Science*, 356(1-3):53–58, 1996.

[116] T. Yao, S. Shinabe, and M. Yoshimura. Atomistic study of the formation process of Ni silicide on the Si(111)-7 $\times$ 7 surface with scanning tunneling microscopy. *Applied Surface Science*, 104-105:213–217, 1996.

[117] A. Ishizaka and Y. Shiraki. Low temperature surface cleaning of silicon and its application to silicon MBE. *Journal of the Electrochemical Society*, 133(4):666–671, 1986.

[118] N. M. Ravindra, B. Sopori, O. H. Gokce, S. X. Cheng, A. Shenoy, L. Jin, S. Abedrabbo, W. Chen, and Y. Zhang. Emissivity Measurements and Modeling of Silicon-Related Materials: An Overview. *International Journal of Thermophysics*, 22(5):1593–1611, 2001.

[119] J. L. Lin, D. Y. Petrovykh, J. Viernow, F. K. Men, D. J. Seo, and F. J. Himpsel. Formation of regular step arrays on Si(111)7×7. *Journal of Applied Physics*, 84(1):255–260, 1998.

[120] J. Tersoff and D. R. Hamann. Theory of the scanning tunneling microscope. *Physical Review B*, 31(2):805, 1985.

[121] W. T. Chang, I. S. Hwang, M. T. Chang, C. Y. Lin, W. H. Hsu, and J. L. Hou. Method of electrochemical etching of tungsten tips with controllable profiles. *Review of Scientific Instruments*, 83(8):083704, 2012.

[122] S. Qin and H. Deng. Electrochemical Etching of Tungsten for Fabrication of Sub-10-nm Tips with a Long Taper and a Large Shank. *Nanomanufacturing and Metrology*, 2:235–240, 2019.

[123] S. B. Chikkamaranahalli, R. R. Vallance, B. N. Damazo, and R. M. Silver. Damping mechanisms for precision applications in UHV environment. In *American Society for Precision Engineering 2006 Spring Topical Meeting: Challenges at the Intersection of Precision Engineering and Vacuum Technology*. NIST, 2006.

[124] R. Rennie and J. Law, editors. *A dictionary of chemistry*. Oxford University Press, Oxford, seventh edition, 2016.

[125] NIST Mass Spectrometry Data Center and W. E. Wallace (Director). Mass spectra 291408. In P.J. Linstrom and W.G. Mallard, editor, *NIST Chemistry WebBook, NIST Standard Reference Database Number 69*. National Institute of Standards and Technology, Gaithersburg, MD., 20899, 2018.

[126] P. Hidnert. THERMAL EXPANSION OF SOME CHROMIUM-VANADIUM STEELS. Technical report, U.S. Department of Commerce, 1940.

[127] K. G. Lyon, G. L. Salinger, C. A. Swenson, and G. K. White. Linear thermal expansion measurements on silicon from 6 to 340 K. *Journal of Applied Physics*, 48(3):865–868, 1977.

[128] S. Vieira. BEHAVIOR AND CALIBRATION OF SOME PIEZOELECTRIC CERAMICS USED IN THE STM. *IBM Journal of Research and Development*, 30(5):553–556, 1986.

[129] M. Markus, A. Schwarz, and U. D. Schwarz. Low-Temperature Scanning Probe Microscopy. In B. Bhushan, editor, *Springer Handbook of Nanotechnology*, pages 663–709. Springer Berlin Heidelberg, Berlin, Heidelberg, 2010.

[130] A. J. Fleming and K. K. Leang. Position Sensors for Nanopositioning. In C. Ru, X. Liu, and Y. Sun, editors, *Nanopositioning Technologies: Fundamentals and Applications*, pages 245–294. Springer International Publishing, 2015.

[131] J. Lyding. Fabrication challenges to overcome - precision, scale. In W. P. Kirk, J. N. Randall, and J. H. G. Owen, editors, *2D Quantum Metamaterials: 2018 NIST Workshop*, pages 25–26. World Scientific Publishing Company Pte Limited, 2019.

[132] K. R. Rusimova. *Mechanisms of local and nonlocal atomic manipulation with a scanning tunnelling microscope.* PhD thesis, University of Bath, 2016.

[133] D. Lock. *Scanning tunnelling microscopy studies of nonlocal atomic manipulation and molecular kinetics on the Si(111)-7x7 surface.* PhD thesis, University of Bath, 2015.

[134] L. C. Evans. *Partial Differential Equations (Graduate Studies in Mathematics).* American Mathematical Society, University of California, Berkeley, 2nd edition, 2010.

[135] W. H. Press, B. P. Flannery, S. A. Teukolsky, and W. T. Vetterling. *Numerical Recipes in C: The Art of Scientific Computing.* Cambridge University Press, New York, NY, USA, 1988.

[136] K. Kaiser, L. Gross, and F. Schulz. A Single-Molecule Chemical Reaction Studied by High-Resolution Atomic Force Microscopy and Scanning Tunneling Microscopy Induced Light Emission. *ACS Nano*, 13(6):6947–54, 2019.

[137] R. J. Peña Román, Y. Auad, L. Grasso, F. Alvarez, I. D. Barcelos, and L. F. Zagonel. Tunneling-current-induced local excitonic luminescence in p-doped WSe2 monolayers. *Nanoscale*, 12(25):13460–70, 2020.

[138] H. Imada, M. Ohta, and N. Yamamoto. Atom-resolved luminescence of Si(111)-7×7 induced by scanning tunneling microscopy. *Applied Physics Express*, 3(4):045701, 2010.

[139] C. Chen, P. Chu, C. A. Bobisch, D. L. Mills, and W. Ho. Viewing the interior of a single molecule: Vibronically resolved photon imaging at submolecular resolution. *Physical Review Letters*, 105(21):217402, 2010.

[140] R. Berndt, J. K. Gimzewski, and P. Johansson. Inelastic tunneling excitation of tip-induced plasmon modes on noble-metal surfaces. *Physical Review Letters*, 67(27):3796–99, 1991.

[141] P. Johansson and R. Monreal. Theory for photon emission from a scanning tunneling microscope. *Zeitschrift für Physik B Condensed Matter*, 84(2):269–275, 1991.

[142] K. Edelmann, L. Wilmes, V. Rai, L. Gerhard, L. Yang, M. Wegener, T. Repän, C. Rockstuhl, and W. Wulfhekel. Influence of Co bilayers and trilayers on the plasmon-driven light emission from Cu(111) in a scanning tunneling microscope. *Physical Review B*, 101(20):205405, 2020.

[143] R. H. Ritchie. Surface plasmons in solids. *Surface Science*, 34(1):1–19, 1973.

[144] J. Lambe and S. L. McCarthy. Light emission from inelastic electron tunneling. *Physical Review Letters*, 37(14):923–925, 1976.

[145] B. Laks and D. L. Mills. Photon emission from slightly roughened tunnel junctions. *Physical Review B*, 20(12):4962–80, 1979.

[146] R. W. Rendell, D. J. Scalapino, and B. Mühlschlegel. Role of local plasmon modes in light emission from small-particle tunnel junctions. *Physical Review Letters*, 41(25):1746–50, 1978.

[147] K.-D. Zhu and S.-W. Gu. Quantum Theory of Surface Polaritons on a Rough Surface. *Communications in Theoretical Physics*, 17(3):291, 1992.

[148] H. Raether. Surface plasmons on smooth surfaces. In *Surface Plasmons on Smooth and Rough Surfaces and on Gratings*, volume 111, pages 4–39. Springer-Verlag Berlin Heidelberg, 1st edition, 1988.

[149] B. N. Persson and A. Baratoff. Theory of photon emission in electron tunneling to metallic particles. *Physical Review Letters*, 68(21):3224–27, 1992.

[150] R. Berndt, R. Gaisch, J. K. Gimzewski, B. Reihl, R. R. Schlittler, W. D. Schneider, and M. Tschudy. Photon Emission at Molecular Resolution Induced by a Scanning Tunneling Microscope. *Science*, 262(5138):1425–27, 1993.

[151] K. Kuhnke, C. Große, P. Merino, and K. Kern. Atomic-scale imaging and spectroscopy of electroluminescence at molecular interfaces. *Chemical Reviews*, 117(7):5174–222, 2017.

[152] H. Reddy, K. Wang, Z. Kudyshev, L. Zhu, S. Yan, A. Vezzoli, S. J. Higgins, V. Gavini, A. Boltasseva, P. Reddy, V. M. Shalaev, and E. Meyhofer. Determining plasmonic hot-carrier energy distributions via single-molecule transport measurements. *Science*, 369(6502):423–426, 2020.

[153] A. Downes and M. E. Welland. Photon Emission from Si(111)- (7×7) Induced by Scanning Tunneling Microscopy: Atomic Scale and Material Contrast. *Physical Review Letters*, 81(9):1857–60, 1998.

[154] T. J.-Y. Derrien, J. Krüger, and J. Bonse. Properties of surface plasmon polaritons on lossy materials: lifetimes, periods and excitation conditions. *Journal of Optics*, 18(11):115007, 2016.

[155] P. Johansson. Light emission from a scanning tunneling microscope: Fully retarded calculation. *Physical Review B*, 58(16):10823–34, 1998.

[156] J. K. Gimzewski, J. K. Sass, R. R. Schlitter, and J. Schott. Enhanced Photon Emission in Scanning Tunnelling Microscopy. *Europhysics Letters*, 8(5):435, 1989.

[157] C. Zhang, L. Chen, R. Zhang, and Z. Dong. Scanning tunneling microscope based nanoscale optical imaging of molecules on surfaces. *Japanese Journal of Applied Physics*, 54(8):08LA01, 2015.

[158] Y. Khang, Y. Park, M. Salmeron, and E. R. Weber. Low temperature ultrahigh vacuum cross-sectional scanning tunneling microscope for luminescence measurements. *Review of Scientific Instruments*, 70(12):4595–99, 1999.

[159] N. J. Watkins, J. P. Long, Z. H. Kafafi, and A. J. Mäkinen. Fiber optic light collection system for scanning-tunneling-microscope- induced light emission. *Review of Scientific Instruments*, 78(5):053707, 2007.

[160] R. M. Purkiss. *Scanning Tunnelling Microscopy of Si(111)-7x7: Local Atomic Manipulation and Light Emission.* PhD thesis, University of Bath, 2018.

[161] P. H. Lu, J. C. Polanyi, and D. Rogers. Electron-induced "localized atomic reaction" (LAR): Chlorobenzene adsorbed on Si(111) 7×7. *The Journal of Chemical Physics*, 111(22):9905–07, 1999.

[162] Z. H. Li, Y. C. Li, W. N. Wang, Y. Cao, and K. N. Fan. A density functional theory study on the adsorption of chlorobenzene on the Si(111)-7 × 7 surface. *Journal of Physical Chemistry B*, 108(37):14049–55, 2004.

[163] J. S. Chickos, W. E. Acree Jr., and J. F. Liebman. Heat of Fusion data. In P. J. Linstrom and W. G. Mallard, editors, *NIST Chemistry WebBook, NIST Standard Reference Database Number 69.* National Institute of Standards and Technology, Gaithersburg MD, 20899, 2020.

[164] R. Sanders. Henry's Law Constants. In P. J. Linstrom and W. G. Mallard, editors, *NIST Chemistry WebBook, NIST Standard Reference Database Number 69*. National Institute of Standards and Technology, Gaithersburg MD, 20899, 2020.

[165] Y. Cao, X. M. Wei, W. S. Chin, Y. H. Lai, J. F. Deng, S. L. Bernasek, and G. Q. Xu. Formation of Di-σ Bond in Benzene Chemisorption on Si(111)-7×7. *Journal of Physical Chemistry B*, 103(27):5698–702, 1999.

[166] A. Mclean, A. Weymouth, G. J. A. Edge, R. Miwa, and G. P. Srivastava. Using steric constraints to template an organic array on Si(111)-7 × 7. *Physica Status Solidi Applied Research*, 209:647–652, 2012.

[167] P. H. Lu, J. C. Polanyi, and D. Rogers. Photoinduced localized atomic reaction (LAR) of 1,2- and 1,4-dichlorobenzene with Si(111) 7×7. *Journal of Chemical Physics*, 112(24):11005–10, 2000.

[168] M. Ebrahimi, K. Huang, X. Lu, I. Mcnab, J. C Polanyi, Z. Waqar, J. S. Y. Yang, H. Lin, and W. Hofer. Facile Charge-Displacement at Silicon Gives Spaced-out Reaction. *Journal of the American Chemical Society*, 133(41):16560–65, 2011.

[169] K. R. Harikumar, I. D. Petsalakis, J. C. Polanyi, and G. Theodorakopoulos. Parent- and daughter-mediated halogenation reactions modeled for 1,2- and 1,4-dibromobenzene at Si(1 1 1)-7 × 7. *Surface Science*, 572(2-3):162–178, 2004.

[170] X. Chen, J. Polanyi, and D. Rogers. Photoetching of Si(111)-(7 × 7) studied by STM. *Surface Science*, 376(1-3):77–86, 1997.

[171] K. Mochiji and M. Ichikawa. Atomic structural study of a Br-chemisorbed Si(111)-7×7 surface by using scanning tunneling microscopy. *Journal of Applied Physics*, 86(2):841–844, 1999.

[172] J. Kanasaki, T. Ishida, K. Ishikawa, and K. Tanimura. Laser-induced electronic bond breaking and desorption of adatoms on Si(111)-(7 × 7). *Physical Review Letters*, 80(18):4080–83, 1998.

[173] J. Kanasaki, K. Iwata, and K. Tanimura. Translational energy distribution of Si atoms desorbed by laser-induced electronic bond breaking of adatoms on Si(111)-(7×7). *Physical Review Letters*, 82(3):644–647, 1999.

[174] H. Sumi. Theory on laser sputtering by high-density valence-electron excitation of semiconductor surfaces. *Surface Science*, 248(3):382–410, 1991.

[175] J. Kanasaki and K. Tanimura. Laser-induced electronic desorption of Si atoms from Si(111)-(7×7). *Physical Review B*, 66(12):125320, 2002.

[176] K. Sagisaka, A. Luce, and D. Fujita. Silicon adatom switching and manipulation on Si(111)- 7 × 7. *Nanotechnology*, 21(4):045707, 2010.